

***Ab initio* All-electron Full-potential Linearized
Augmented
Plane-wave Method for One-dimensional Systems**

Von der Fakultät für Mathematik, Informatik und Naturwissenschaften der
Rheinisch-Westfälischen Technischen Hochschule Aachen
zur Erlangung des akademischen Grades eines Doktors der Naturwissenschaften
genehmigte Dissertation

vorgelegt von

Master of Science

Yuriy Mokrousov

aus Kiev (Ukraine)

Berichter: Universitätsprofessor Dr. Stefan Blügel
Universitätsprofessor Dr. Peter Heinz Dederichs

Tag der mündlichen Prüfung: 24.05.2005

Diese Dissertation ist auf den Internetseiten der Hochschulbibliothek online verfügbar

Abstract

In recent years we witnessed an enormous progress in the chemical synthesis, growth and the development of technology allowing the fabrication of a rich variety of one-dimensional (1D) structures. They include single walled (SWNT) and multi-walled (MWNT) one-dimensional tubular structures, made of carbon, GaN, BN, TiO, VO and other compounds, thin metallic quantum wires, quasi-1D molecular magnets etc. They involve elements from the entire periodic table and show new physical phenomena such as quantized conductance, charge and spin separation, intriguing structural and magnetic properties such as high spin-polarization and large spin-scattering lengths. In many cases the transport properties of these systems can be easily tuned by choosing suitable structural parameters such as the diameter or chirality. Moreover, the diameters of many experimentally observed 1D structures are much smaller than most semiconductor devices obtained so far, and thus one can imagine that the smallest possible transistors are likely to be based on them. In order to understand the structure-property relation in these new materials on the basis of the electronic structure, *ab initio* calculations based on the density functional theory play an important role.

In this work we have presented an extension of the full-potential linearized augmented plane-wave (FLAPW) method to truly one-dimensional systems. The space is partitioned into three regions, the muffin-tin sphere around the atom, a vacuum region surrounding a cylinder and the interstitial region between the atoms and the vacuum region. In each region optimal basis functions for the wavefunctions, charge density and potential are used. The spin-orbit interaction is included to investigate the orbital moments and the magnetic anisotropy. Despite the plane-wave representation in the interstitial region we were able to include a wide class of chiral symmetries, characteristic for one-dimensional systems. The one-dimensional FLAPW method was implemented as extension of the FLAPW code FLEUR and parallelized for supercomputing applications. Due to the efficiently adjusted basis functions and partitioning of space, 1D code allows to achieve a significant speed-up, for instance, approximately by a factor of 150 for monowires, as compared to the super-cell approach in the bulk code.

The accuracy, precision and correctness of the code was validated on a set of 1D structures, already calculated previously with other methods. We focused on the systems of a large current interest in the field of nanophysics. We reported on the calculations of 3*d*- and 4*d*- monowires (Ti; Y, Zr, Nb, Mo, Tc, Ru, Rh and Pd). For these monowires we investigated the ferro- and antiferromagnetic instability, calculated equilibrium interatomic distances, magnetic and orbital moments, magnetocrystalline anisotropy energies. We found that across the 4*d*-transition-metal series, Y and Nb exhibit a nonmagnetic ground-state, Mo and Tc are antiferromagnetic and Zr, Ru, Rh and Pd are ferromagnetic at equilibrium lattice constants. For the Ru, Rh and Pd system it was found that the easy axis is perpendicular to the wire for Ru and Pd and along-the-wire for Rh.

Further we considered a (6,0) nanowire of gold atoms, and a hybrid structure of an iron monowire inside a gold (6,0) tube, showing that the Fe monowire is prone to the Peierls dimerization. For the hybrid system Fe@Au(6,0) we found a high spin-polarization at the

Fermi level, proposing, therefore, this system as a possible candidate for spin-dependent transport applications.

Using a super-cell approach within the one-dimensional FLAPW method we investigated a set of one-dimensional multiple-decker sandwiches of benzene and vanadium, which are for the past 20 years of great interest in the field of organometallics. The calculated structural results obtained are in good agreement with experimental and theoretical results. After the calculation of total energies, magnetic moments, orbital interaction schemes, one can finally conclude, that with the increasing number of the vanadium atoms in the molecule, the magnetic moments of vanadium prefer to order ferromagnetically, which was recently observed experimentally.

"Using an equality due to Bogolyubov, Mermin and Wagner have proved rigorously the absence of both ferromagnetism and antiferromagnetism in one-dimensional spin systems."

M.B. Walker and T.W. Ruijgrak, *Physical Review*, **171**, 513 (1968)

"still... still... still... still..."

Miles Davis to his musicians in
Gingerbread Boy, album "*Miles Smiles*", Columbia **CL 2601** (1966)

Contents

1	Introduction	9
2	Density Functional Theory	13
2.1	Density Functional Theory	13
2.2	Spin Density Functional Theory	16
2.3	The Local Spin Density Approximation	17
2.4	The Generalized Gradient Approximation (GGA)	18
3	FLAPW Approach to One-Dimensional Systems	21
3.1	FLAPW Method	21
3.1.1	The APW Method	22
3.1.2	The Concept of LAPW	23
3.1.3	The Concept of FLAPW	25
3.2	Chiral Symmetries	26
3.2.1	Hexagonal In-Plane Lattice	27
3.2.2	Triangular In-Plane Lattice	29
3.3	Implementation	30
3.3.1	Geometry	31
3.3.2	Symmetries	32
3.3.3	Charge Density and Potential	34
3.3.4	Coulomb Potential	35
3.3.5	Basis Functions	37
3.3.6	Eigenvalue Problem	38
3.3.7	Timing	38
4	Eigenvalue Problem	41
4.1	Relativity in Valence Electron Calculations	42
4.1.1	The Kohn-Sham-Dirac Equation	43
4.1.2	The Scalar Relativistic Approximation	44
4.2	Construction of the Hamiltonian Matrix	46
4.2.1	Hamiltonian and Overlap Matrices in the Spheres	47
4.2.2	Inversion Symmetry	50
4.2.3	Hamiltonian and Overlap Matrices in the Interstitial	52

4.2.4	Hamiltonian and Overlap Matrices in the Vacuum	54
4.3	Fermi Energy and Brillouin Zone Integration	58
5	Charge Density	61
5.1	Generation of the Starting Density	61
5.2	Generation of the Charge Density	63
5.2.1	“ <i>l</i> -like” Charge	64
5.2.2	Determination of the Optimal Energy Parameters	65
5.2.3	Generation of the Charge Density in the Spheres	65
5.2.4	Generation of the Charge Density in the Interstitial	66
5.2.5	Generation of the Charge Density in the Vacuum	67
6	Potential	69
6.1	Coulomb Potential	69
6.1.1	The Pseudo-Charge Scheme	69
6.1.2	Solution of the Poisson Equation in the Vacuum and Interstitial	71
6.2	Exchange–Correlation Potential	79
6.2.1	Calculation of ϵ_{xc}^σ and V_{xc}^σ in the Interstitial	79
6.2.2	Calculation of ϵ_{xc}^σ and V_{xc}^σ in the Spheres	80
6.2.3	Calculation of ϵ_{xc}^σ and V_{xc}^σ in the Vacuum	80
7	Results	83
7.1	Monowires of Ti and <i>4d</i> transition elements	83
7.1.1	Ti Monowire	85
7.1.2	Monowires of <i>4d</i> transition elements	88
7.2	Gold (6,0) Nanowire	99
7.2.1	Computational Details	99
7.2.2	Geometrical Structure	101
7.2.3	Electronic Structure	101
7.2.4	Charge Density	102
7.3	Hybrid Structure Fe@Au(6,0)	103
7.3.1	Geometrical Structure	104
7.3.2	Magnetic Properties	105
7.3.3	Electronic Structure	106
7.3.4	Charge Density	108
7.4	One-Dimensional Multiple Benzene-Vanadium Sandwiches	108
7.4.1	Computational Details	112
7.4.2	$V(Bz)$ Complex	113
7.4.3	$V_1(Bz)_2$ Complex	118
7.4.4	$V_2(Bz)_3$ Complex	122
7.4.5	$V_3(Bz)_4$ Complex	126
7.4.6	Conclusions	129

<i>CONTENTS</i>	7
8 Conclusions	131

Chapter 1

Introduction

During the last decade research on the nanoscale developed to one of the most innovative and fastest growing fields of modern physics. One reason is certainly the enormous progress witnessed in the chemical synthesis, growth and the development of technology allowing the fabrication of a rich variety of nanomaterials with unprecedented new properties. As the scale of nanomaterials continue to decrease from the mesoscopic regime to the atomic scale, one-dimensional (1D) nanometer scale systems such as carbon nanotubes [38], radially and axially modulated semiconductor nanowires [71], and thin metallic quantum wires [49, 29, 113] moved into the focus of attention. The excitement in these one-dimensional structures is fueled by their wealth of new physical phenomena such as quantized conductance, charge and spin separation, intriguing structural and magnetic properties such as high spin-polarization and large spin-scattering lengths [115]. Today, there is a general consensus on the expectation that the quantum nature in materials is much richer in one-dimensional systems than in bulk materials.

One-dimensional systems are also important from a technological point of view. For example, the ability to fabricate thin metallic interconnects with favorable properties is an important factor determining the progress of ultra-large scale integrated circuits. In many cases the transport properties of these systems can be easily tuned by choosing suitable structural parameters such as the diameter or chirality. Moreover, the diameters of many experimentally observed 1D structures are much smaller than most semiconductor devices obtained so far, and thus one can imagine that the smallest possible transistors are likely to be based on them [110, 63, 33].

Today a large variety of one-dimensional structures are known and continue to be synthesized. First and foremost are the single walled (SWNT) and multi-walled (MWNT) one-dimensional tubular structures, which exist not only for carbon [38], but also for GaN [27], BN [34], TiO [42], VO [53] and other compounds. A further large class are quasi-1D crystals, a family of structures with different diameters and chiralities, chemical and physical properties [17]. They involve elements from the entire periodic table.

In the context of magneto-electronics and spintronics we witness two important trends in the synthesis of one-dimensional magnetic hybrid structures. One is based on the development of new nanotube production technologies which for example allow to fill

carbon nanotubes [28, 70] and other nanotubes with metals [26] with magnetic atoms. The other one rests in the field of organometallics. Molecular magnets with a tendency towards one-dimensionalization are synthesized and experimentally observed as quasi-1D structures showing intriguing magnetic and structural properties [69, 68].

Understanding the structure-property relation in these new materials on the basis of the electronic structure becomes possible due to the established success of the the density functional theory. Powerful and at the same time numerically simple approximations to the density functional theory such as the local density approximation (LDA) and the generalized gradient approximation (GGA) open the gate to the investigations of these low-dimensional with predictive power. The low-dimensionality, the chemical complexity, the open structure, and the large variety of chemical elements in these systems ask for flexible first-principles methods able to solve the density functional equations with required precision and efficiency. Methods employed for density-functional calculations of one-dimensional systems include the tight-binding [116], pseudopotential [126], linearized muffin-tin orbital LMTO [107], and the PAW [104] and full-potential linearized augmented plane-wave (FLAPW) [14, 15] super-cell formalism. Although applicable to a range of materials, the first two methods are usually not optimal for a highly precise description of the electronic properties of low-dimensional systems containing, for instance, (magnetic) transition elements. From this point of view FLAPW would be an optimal calculating scheme, although, as for the pseudopotential and PAW method, one-dimensional structures are treated in a the super-cell geometry, i.e. in a two-dimensional lattice of one-dimensional structures. Obviously, either one has to deal with very large super-cells or one has to accept a degree of interactions coming from the neighboring unit cells at finite distance. Further, in the super-cell geometry the symmetries characteristic for the 1D systems are not naturally included.

In this thesis we present a new efficient and very precise all-electron method for carrying out *ab initio* calculations based on density functional theory of electronic ground state properties for systems having a one-dimensional periodicity, in particular, metallic wires and nanotubes. The method is truly one-dimensional, i.e. it is applied for calculations of single wires or tubes surrounded by infinite vacuum, avoiding any interaction due to the presence of the neighboring unit-cells. The truly one-dimensional structure model can lead to a large computational speed-up over the conventional super-cell approach opening opportunities to study more complex systems. Including the symmetries allows to achieve a further significant speed-up, increased accuracy as well as a simplified analysis of the results. This new approach, which makes use of the chiral symmetries for a considered system, allows to carry out calculations of the total energies, forces and atomic relaxations, band structures, and densities of states including spin-orbit coupling effects. A particular emphasis was put on the investigation of magnetic properties such as the spin and orbital moment, magnetization direction and the magnetic structure.

In the thesis we applied the new method basically to three classes of materials: *4d* transition-metal monowires, a Au covered Fe wire, and metallorganic V-benzene multi-decker sandwiches of finite size. The emphasis of the work is on the geometrical structure, electronic structure and magnetism of these systems.

At first, the accuracy, correctness and precision of the code was validated on a set of 1D structures, already calculated previously with other methods. We focus on the systems of large current interest in the field of nanophysics. We report on the calculations of $3d$ - and $4d$ -transition-metal monowires (Ti; Y, Zr, Nb, Mo, Tc, Ru, Rh and Pd). For these monowires we investigated the chemical and physical trend of the ferro- and antiferromagnetic instability, calculated equilibrium interatomic distances, magnetic and orbital moments, and magnetocrystalline anisotropy energies. We found that across the $4d$ -transition-metal series, Y exhibits a nonmagnetic ground-state, Zr is ferromagnetic, Nb is nonmagnetic again, Mo and Tc are antiferromagnetic and Ru, Rh and Pd are ferromagnetic at equilibrium lattice constants. For the Ru, Rh, and Pd monowire, we investigated the easy axis of the magnetization. We found that the easy axis is perpendicular to the wire for Ru and Pd but along-the-wire for Rh.

We also investigate the electronic properties, geometrical and magnetic structure of an Au(6,0) and an Fe@Au(6,0) nanowire. The results show, that the bare Fe monowire and the Fe monowire inside the Au(6,0) are ferromagnetic. The Au coverage of the Fe monowire causes a change of the easy magnetization axis, which is along the wire for the single Fe monowire and perpendicular to the wire for the Au covered Fe wire. This is explained by the magnetic proximity effect of Fe on the Au and the large spin-orbit interaction of Au. The Fe@Au(6,0) hybrid structure exhibits a large negative polarization at the Fermi energy, which makes this system interesting as a potential candidate for spin-dependent transport applications. The structural investigation shows that this system is prone to a Peierls dimerization.

Using a super-cell approach within the one-dimensional FLAPW method we investigated a set of one-dimensional but finite multiple-decker sandwiches of benzene and vanadium. These organometallic compounds raise much interest due to the unusual magnetism of V. The magnetism of V is reproduced in the thesis. It is concluded, that V atoms couple ferromagnetically within the multi-decker and the coupling strength increases with increasing number of V atoms.

The thesis is organized as following: in chapter 3 an overview of the one-dimensional FLAPW method is presented. This includes the definition of the one-dimensional symmetry, the LAPW basis function, charge density and potential representation in different regions of space. In sections 4–6 the implementational details of the method are given, including the eigenvalue problem, construction of the charge density and Coulomb and exchange-correlation parts of the potential. Chapter 7 includes the results on the $3d$ - and $4d$ -monowires, gold tube Au(6,0) and hybrid structure Fe@Au(6,0), and one-dimensional multiple-decker vanadium-benzene sandwiches. The thesis is concluded in chapter 8.

Chapter 2

Density Functional Theory

2.1 Density Functional Theory

As far as our main aim is to understand and investigate the properties of real materials, we come to the problem of an appropriate quantum-mechanical description of these systems. From the basic quantum mechanical point of view we should necessarily consider the many-body problem: the problem of describing a system containing an enormously large number of interacting electrons and ions. Due to the complexity of this problem it cannot be solved even nowadays nor analytically neither numerically. First attempts to find some simplifications took place a long time ago. The most essential among them is the Born-Oppenheimer approximation, which is employed by the majority of first-principle calculations. It states that as the electrons are very light compared with the nuclei, they move much more rapidly and one can neglect all the quantum effects due to the motion of the nuclei. In other words, in this approximation the positions of ions are fixed, and the Hamiltonian of the system becomes:

$$\mathcal{H} = \sum_{i=1}^N -\frac{\hbar^2}{2m} \nabla_i^2 + \frac{1}{2} \sum_{i,j} \frac{e^2}{|\mathbf{r}_i - \mathbf{r}_j|} - \sum_{i,I} \frac{Z_I e^2}{|\mathbf{r}_i - \mathbf{R}_I|} + \frac{1}{2} \sum_{I,J} \frac{Z_I Z_J}{|\mathbf{R}_I - \mathbf{R}_J|}, \quad (2.1)$$

where Z_I denotes the charge of the nucleus I and \mathbf{R}_I is the position of the nucleus I . But even with this simplification there is not an analytical or numerical solution, i.e. many-body eigen wavefunction for this Hamiltonian, if more than a few electrons are considered.

A reduction of the complicated many-body problem to an effective single-particle theory which can be applied for the numerical prediction of the different properties for different types of materials and also supplies deeper physical insight is the density functional theory by Hohenberg, Kohn and Sham [35, 47].

We start with writing the Hamiltonian of N interacting electrons as:

$$\mathcal{H} = T + V + U,$$

where T is kinetic energy operator:

$$T = -\frac{\hbar^2}{2m} \sum_i \nabla_i^2,$$

the quantity V denotes the external potential, which in the Born-Oppenheimer approximation consists of the potential due to the fixed ions, and possibly other external fields:

$$V = \sum_i \left(V_{field}(\mathbf{r}_i) + \sum_j V_{ion}(\mathbf{r}_i - \mathbf{R}_j) \right). \quad (2.2)$$

The last term is the Coulomb electron-electron interaction:

$$U = \sum_{ij, i \neq j} \frac{e^2}{|\mathbf{r}_i - \mathbf{r}_j|}. \quad (2.3)$$

This Hamiltonian has generated the truly immense literature and numerous techniques to extract physically interesting approximate solutions. Now we focus our attention on the electron density. The electron density operator is defined as:

$$\hat{n}(\mathbf{r}) = \sum_{i=1}^N \delta(\mathbf{r} - \mathbf{r}_i), \quad (2.4)$$

from which the electron density is given by:

$$n(\mathbf{r}) = \langle \Phi | \hat{n}(\mathbf{r}) | \Phi \rangle,$$

where Φ is a many-body state. Hohenberg and Kohn discovered that this quantity is actually a crucial variable. This is reflected in two famous theorems.

1. The total ground-state energy, E , of any many-electron system is a functional of the density $n(\mathbf{r})$:

$$E[n] = F[n] + \int n(\mathbf{r}) V_{ext}(\mathbf{r}) d\mathbf{r}, \quad (2.5)$$

where $F[n]$ is a functional of the density, but independent of the external potential.

2. For any many-electron system the functional $E[n]$ for the total energy has a minimum equal to the total ground-state energy at the ground-state density.

The second theorem is of great importance because it leads to a variational principle. This was given by Kohn and Sham who used the variational principle implied by the minimal properties of the energy functional to derive a single-particle Schrödinger equation. For this they split the functional $F[n]$ into three parts:

$$F[n] = T[n] + \int \int \frac{n(\mathbf{r})n(\mathbf{r}')}{|\mathbf{r} - \mathbf{r}'|} d\mathbf{r} d\mathbf{r}' + E_{xc}[n], \quad (2.6)$$

which describe the kinetic, Hartree and exchange-correlation energy. In contrast to the Hartree integral, an explicit form of the other functionals, T and E_{xc} is not known in general. Ignoring this problem at the moment, we use the variational principle and write:

$$\frac{\delta E[n]}{\delta n(\mathbf{r})} + \mu \frac{\delta(N - \int n(\mathbf{r}) d\mathbf{r})}{\delta n(\mathbf{r})} = 0, \quad (2.7)$$

where μ is a Lagrange multiplier taking care of particle conservation. We now split up the kinetic energy into a term T_0 reflecting the kinetic energy of noninteracting particles and T_{ex} which stands for the rest, i.e. we write:

$$T = T_0 + T_{ex}.$$

Here we are making an important step, we represent the density in the following form:

$$n(\mathbf{r}) = \sum_{i=1}^N |\psi_i(\mathbf{r})|^2, \quad (2.8)$$

where we assume that we can determine the 'single-particle' wave-functions ψ_i so that the density can be represented in this form. One might indeed question whether the desired densities can be written in this form, but we simply accept this form. Then we are writing the kinetic energy of noninteracting particles as:

$$T_0[n] = -\frac{\hbar^2}{2m} \sum_{i=1}^N \int \nabla \psi_i^*(\mathbf{r}) \nabla \psi_i(\mathbf{r}) d\mathbf{r}. \quad (2.9)$$

Since the Schödinger equation is just an Euler-Lagrange equation obtained by varying $T_0[n]$ plus a potential energy term we come to:

$$\left(-\frac{\hbar^2}{2m} \nabla^2 + V_{eff}(\mathbf{r}) \right) \psi_i(\mathbf{r}) = \epsilon_i \psi_i(\mathbf{r}). \quad (2.10)$$

Now we will try to determine the effective potential which the i th 'single particle' feels, such that the density $n(\mathbf{r})$ minimizes the energy functional. Thus, requiring the functions ψ_i to be normalized, multiplying the last equation with ψ_i^* , integrating and adding we obtain:

$$T_0[n] = \sum_{i=1}^N \epsilon_i - \int V_{eff}(\mathbf{r}) n(\mathbf{r}) d\mathbf{r}. \quad (2.11)$$

The variation of the energy functional is now easily carried out, and noting that terms containing $\delta\epsilon_i$ cancel δV_{eff} we get:

$$V_{eff}(\mathbf{r}) = V_{ext}(\mathbf{r}) + 2 \int \frac{n(\mathbf{r}')}{|\mathbf{r} - \mathbf{r}'|} d\mathbf{r}' + V_{xc}(\mathbf{r}) \quad (2.12)$$

with

$$V_{xc}(\mathbf{r}) = \frac{\delta(E_{xc} + T_{xc})}{\delta n(\mathbf{r})}. \quad (2.13)$$

The effective single-particle equation,

$$\left(-\frac{\hbar}{2m}\nabla^2 + V_{eff}(\mathbf{r})\right)\psi_i(\mathbf{r}) = \epsilon_i\psi_i(\mathbf{r}) \quad (2.14)$$

is called the Kohn-Sham equation. It is a Schrödinger equation with the external potential replaced by the effective potential which depends on the density. The density itself depends on the single-particle states ψ_i . The Kohn-Sham equation thus constitutes a self-consistent field problem. By choosing some reasonable starting density, which is usually constructed from the densities of isolated atoms, the starting potentials are defined. Then by solving the Kohn-Sham equations the output density is constructed. The output density is mixed with the input density afterward thus becoming a starting density for the next iteration. This iterative process is repeated until the distance between the output and starting density becomes small. In this case the calculation is converged and the ground-state density is found.

The Kohn-Sham equation furthermore allows us to derive an alternative expression for the total energy:

$$E[n] = \sum_{i=1, \epsilon_i \leq E_F}^N \epsilon_i - \int \int \frac{n(\mathbf{r})n(\mathbf{r}')}{|\mathbf{r} - \mathbf{r}'|} d\mathbf{r} d\mathbf{r}' - \int V_{xc}(\mathbf{r})n(\mathbf{r}) d\mathbf{r} + E_{xc}[n]. \quad (2.15)$$

The total energy thus consists of the sum over the eigenvalues, ϵ_i , minus the so-called 'double-counting' terms. Note that in the term E_{xc} we also included the exchange-correlation kinetic energy T_{xc} .

Although density-functional theory provides the scheme to reduce the entire many-body problem to a Schrödinger-like effective single-particle equation, the physical meaning of the eigenvalues ϵ_i is not clear. These eigenvalues have been used very often and with success to interpret excitation spectra. But there also some problematic cases.

2.2 Spin Density Functional Theory

In order to describe magnetic effects the density functional theory has to be extended to the case of spin polarized electrons. This is important for systems that possess non-zero ground state magnetization, which is the case for most atoms, magnetic solids and surfaces and electronic systems exposed to an external magnetic field. The necessary extension to the Hohenberg-Kohn theory can be formulated replacing the electron density by the electron density plus the magnetization density as fundamental variables. In this case, the variational principle becomes

$$E[n(\mathbf{r}), \mathbf{m}(\mathbf{r})] \geq E[n_0(\mathbf{r}), \mathbf{m}_0(\mathbf{r})]. \quad (2.16)$$

An alternative, but completely equivalent, formulation can be obtained using a four component density matrix $\rho_{\alpha\beta}$ instead of $n(\mathbf{r})$ and $\mathbf{m}(\mathbf{r})$ [117]. In order to gain a generalized

form of the Kohn-Sham equations, it is necessary at least to introduce two component Pauli wavefunctions, that reproduce the electron and magnetization density.

$$\psi_i(\mathbf{r}) = \begin{pmatrix} \psi_{1,i}(\mathbf{r}) \\ \psi_{2,i}(\mathbf{r}) \end{pmatrix} \quad (2.17)$$

$$n(\mathbf{r}) = \sum_{i=1}^N |\psi_i(\mathbf{r})|^2$$

$$\mathbf{m}(\mathbf{r}) = \sum_{i=1}^N \psi_i^*(\mathbf{r}) \vec{\sigma} \psi_i(\mathbf{r}) \quad (2.18)$$

Applying the variational principle again yields the Kohn-Sham equations, which now have the form of Schrödinger-Pauli equations.

$$\left\{ -\frac{\hbar^2}{2m} \nabla^2 + V_{eff}(\mathbf{r}) + \vec{\sigma} \cdot \mathbf{B}_{eff}(\mathbf{r}) \right\} \psi_i(\mathbf{r}) = \epsilon_i \psi_i(\mathbf{r}) \quad (2.19)$$

The additional effective magnetic field consists of two terms. One of them is due to the variation of the exchange correlation energy with respect to the magnetization density. The second term is the external B-field, if present.

$$\mathbf{B}_{eff}(\mathbf{r}) = \mathbf{B}_{xc}(\mathbf{r}) + \mathbf{B}_{ext}(\mathbf{r})$$

$$\mathbf{B}_{xc}(\mathbf{r}) = \frac{\delta E_{xc}[n(\mathbf{r}), \mathbf{m}(\mathbf{r})]}{\delta \mathbf{m}(\mathbf{r})} \quad (2.20)$$

In many applications, like for example ferromagnetic and antiferromagnetic solids, the magnetization is orientated along one particular direction. For these collinear cases the problem can be simplified further. The z-axis can be chosen along the direction of the magnetic field. Therefore, the Hamiltonian of equation (2.19) becomes diagonal in the two spin components of the wavefunction, i.e. the spin-up and -down problems become completely decoupled and can be solved independently. The energy and all other physical observables become functionals of the electron density and the magnitude of the magnetization density $m(\mathbf{r}) = |\mathbf{m}(\mathbf{r})|$ rather than $\mathbf{m}(\mathbf{r})$, or, equivalently, of the spin-up and spin-down electron densities $n_{\uparrow}(\mathbf{r})$ and $n_{\downarrow}(\mathbf{r})$ which are given by

$$n_{\sigma}(\mathbf{r}) = \sum_{i=1}^N |\psi_{i\sigma}(\mathbf{r})| \quad (2.21)$$

The vast majority of the spin-polarized density functional calculations have been performed using this formalism.

2.3 The Local Spin Density Approximation

So far, no approximations have been made. The density functional formalism, outlined in the previous sections, could in principle reproduce all ground state properties of any

complex many-electron system exactly, if the exchange correlation energy E_{xc} was known. Unfortunately, no explicit representation of this functional, that contains all many-body effects, has been found yet. Thus, approximations to E_{xc} have to be used. The most widely used and very successful approximation is the local spin density approximation (LSDA). The underlying idea is very simple. At each point of space E_{xc} is approximated locally by the exchange correlation energy of a homogeneous electron gas with the same electron and magnetization density. Hence, the approximate functional E_{xc} is of the form

$$E_{xc}[n(\mathbf{r}), |\mathbf{m}(\mathbf{r})|] = \int n(\mathbf{r}) \epsilon_{xc}(n(\mathbf{r}), |\mathbf{m}(\mathbf{r})|) d^3r \quad (2.22)$$

It is important to note, that ϵ_{xc} is not a functional, but a function of $n(\mathbf{r})$ and $|\mathbf{m}(\mathbf{r})|$ at a particular point of space. As a consequence of its local definition ϵ_{xc} and thus E_{xc} depend only of the magnitude of the magnetization. This, in terms, leads to the fact that $\mathbf{B}_{xc}(\mathbf{r})$ and $\mathbf{m}(\mathbf{r})$ do always have the same direction. Therefore, the exchange correlation potential and magnetic field derived from (2.22) become

$$\begin{aligned} V_{xc}(\mathbf{r}) &= \epsilon_{xc}(n(\mathbf{r}), |\mathbf{m}(\mathbf{r})|) + n(\mathbf{r}) \frac{\delta \epsilon_{xc}(n(\mathbf{r}), |\mathbf{m}(\mathbf{r})|)}{\delta n(\mathbf{r})} \\ \mathbf{B}_{xc}(\mathbf{r}) &= n(\mathbf{r}) \frac{\delta \epsilon_{xc}(n(\mathbf{r}), |\mathbf{m}(\mathbf{r})|)}{\delta |\mathbf{m}(\mathbf{r})|} \hat{\mathbf{m}}(\mathbf{r}). \end{aligned} \quad (2.23)$$

Using the LSDA the Kohn-Sham equations take exactly the same form as the Hartree equations, and they are no more difficult to solve. In particular, they are far easier to deal with than the Hartree-Fock equations because of the local effective potential. Intuitively one should expect, that the LSDA is valid only for slowly varying densities. Nevertheless, it has been applied successfully to inhomogeneous systems.

Explicit parameterizations of ϵ_{xc} can be obtained for example from Hartree-Fock calculations for the homogeneous electron gas. Of course, such calculations do only take into account the exchange effects, but neglect correlation. Modern parameterizations of ϵ_{xc} are based on quantum-mechanical many-body calculations. Most commonly used are the parameterizations of v. Barth and Hedin [117] and Moruzzi, Janak and Williams [72], which have been obtained applying the random phase approximation (RPA), the parameterization of Vosko, Wilk and Nusair [118], that is based on Quantum-Monte-Carlo simulations by Ceperley and Alder [9], and goes beyond the RPA, and the parameterization of Perdew and Zunger [88], which is, in a certain sense, a mixture of the previous two.

2.4 The Generalized Gradient Approximation (GGA)

In the LSDA approximation the exchange-correlation energy functional is written in terms of $\epsilon_{xc}(n_{\uparrow}, n_{\downarrow})$, the exchange-correlation energy per particle of an electron gas with uniform spin densities $n_{\uparrow}, n_{\downarrow}$ and $n = n_{\uparrow} + n_{\downarrow}$. This approximation is clearly valid when the spin densities vary slowly over space. However, this condition does not really seem appropriate

for real atoms, molecules and solids, temporarily setting aside the surprisingly successful applications of the LSDA.

The next step would be the generalized gradient approximation (GGA) and is written as:

$$E_{xc}^{GGA}[n_{\uparrow}, n_{\downarrow}] = \int f(n_{\uparrow}, n_{\downarrow}, \nabla n_{\uparrow}, \nabla n_{\downarrow}) d\mathbf{r}. \quad (2.24)$$

While the input quantity $\varepsilon_{xc}(n_{\uparrow}, n_{\downarrow})$ in LSDA is in principal unique - there is the electron gas in which n_{\uparrow} and n_{\downarrow} are constant and for which LSDA is exact - there is no unique input quantity $f(n_{\uparrow}, n_{\downarrow}, \nabla n_{\uparrow}, \nabla n_{\downarrow})$ to construct the GGA. However, due to the work of Perdew and his collaborators (1986-1998) [87], Burke [7], etc., it is possible to construct a nearly unique GGA possessings all the known correct formal features of LSDA.

Since the construction of GGA is not unique, one must in the end compare results of calculations for realistic systems with experimental data, such as atomization energies for molecules. This was done with great success by Perdew et al [85, 86] for a large selection of different molecules.

One should remember, however, that GGA is not a remedy for all ills. Different cases require different corrections, a list of those being SIC, orbital-polarization corrections, LDA+U, and exact exchange. SIC, the self-energy correction, is important for localized electron states [88, 111]. Orbital-polarization correction becomes a necessity mainly in relativistic systems [94]. LDA+U is of importance whenever correlation effects play a dominant role [3], and an exact treatment of exchange is asked for in insulators when the band gap is to be treated correctly [108].

Chapter 3

FLAPW Approach to One-Dimensional Systems

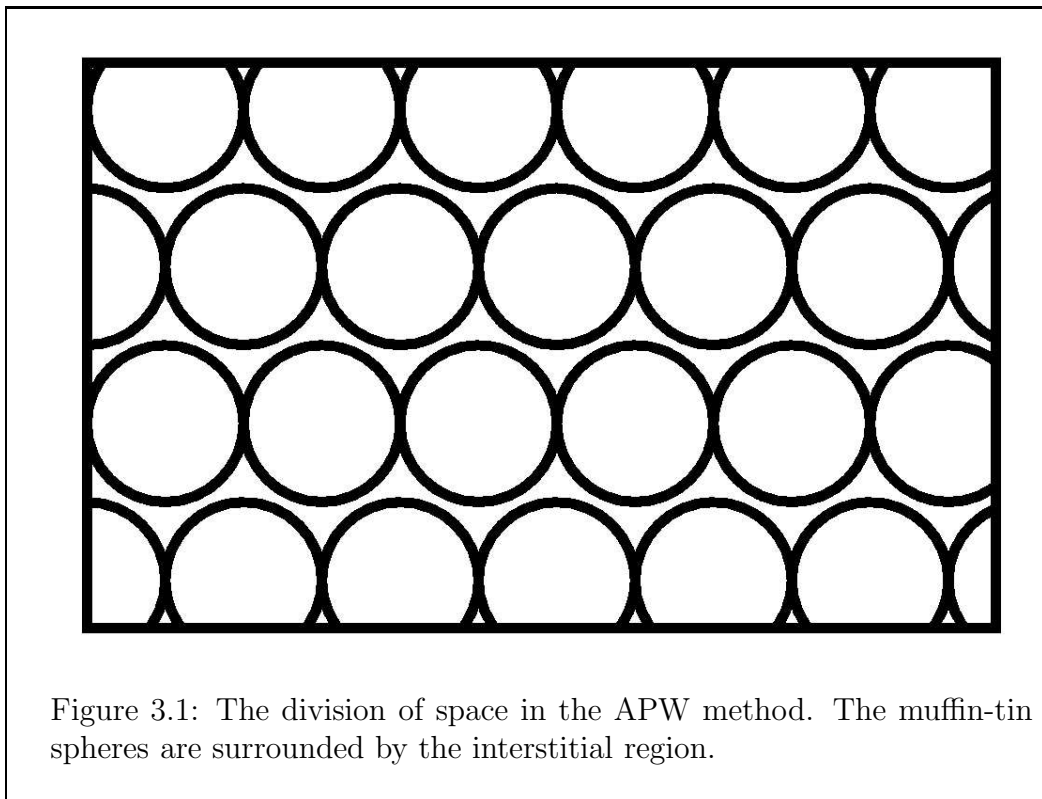
In this section we are going to present a small introduction into a newly developed scheme for treating systems of one-dimensional nature within the FLAPW formalism. We introduce the geometrical setup, briefly describe the construction of the basis set, representation of the charge density and potential, solution of the Poisson equation, general description of the eigenvalue problem we solve, and the way of implementing the symmetries, characteristic for one-dimensional systems. More detailed description of the listed implementational aspects of the method is presented in the first part of the thesis.

3.1 FLAPW Method

The Kohn-Sham equations can be solved in many different ways. One of the most common strategies is to expand the single-particle wavefunctions in terms of suitable, problem-adopted basis functions. Then the Kohn-Sham equations are written and solved in terms of these basis functions. One of the best choices for a set of basis functions in solid state physics is a set of plane-waves. Plane-waves are diagonal for the Laplace operator, which appears in the kinetic energy of the Hamiltonian as well as the Poisson equation. They are analytically simple, orthogonal to each other, as well as their derivatives of any order. Moreover, plane-waves are suggested by the Bloch theorem. However, around the atoms oscillations of the charge density and wave-functions become too rapid, and in order to achieve a precise description a large number of plane-waves is required. One way to cope with problem is to use modified potential around the atoms in order to avoid the fast oscillations of the charge density, which recalls a group of pseudopotential methods. Another way is based on the space separation and use of suitably modified basis functions for different regions of space. This has already been suggested by Slater [100]. The corresponding technique is called the augmented plane-wave method (APW).

3.1.1 The APW Method

Within the APW approach, space is divided into spheres centered at each atom site, the so-called muffin-tins, and the remaining interstitial region (cf. Fig. 3.1).



Inside the muffin-tins the potential is approximated by a spherically symmetric shape, and in many implementations the interstitial potential is set to a constant. The restrictions to the potential are commonly called shape-approximations. Noting that plane-waves solve the Schrödinger equation in a constant potential, while spherical harmonics times radial functions are the solutions in a spherical potential, suggests to expand the single particle wavefunctions¹ $\phi_\nu(\mathbf{k}, \mathbf{r})$ in terms of the following basis functions:

$$\varphi_{\mathbf{G}}(\mathbf{k}, \mathbf{r}) = \begin{cases} \frac{1}{\sqrt{\Omega}} e^{i(\mathbf{G}+\mathbf{k})\mathbf{r}} & \text{interstitial region} \\ \sum_{lm} A_L^{\mu\mathbf{G}}(\mathbf{k}) u_l(r) Y_L(\hat{\mathbf{r}}) & \text{muffin-tin } \mu \end{cases} \quad (3.1)$$

¹In the section 3.1 we deal only with the systems, having 3-dimensional translational symmetry, i.e. bulk

Where \mathbf{k} is the Bloch vector, Ω is the cell volume, \mathbf{G} is a reciprocal lattice vector, L abbreviates the quantum numbers l and m and u_l is the regular solution of the radial Schrödinger equation

$$\left\{ -\frac{\hbar^2}{2m} \frac{\partial^2}{\partial r^2} + \frac{\hbar^2}{2m} \frac{l(l+1)}{r^2} + V(r) - E_l \right\} r u_l(r) = 0, \quad (3.2)$$

for a given energy parameter E_l . $V(r)$ is the spherical component of the potential. The coefficients $A_L^{\mu\mathbf{G}}(\mathbf{k})$ are determined from the requirement, that the wavefunctions have to be continuous at the boundary of the muffin-tin spheres.

Hence, the APW's form a set of continuous basis functions that cover all space. Each basis function consists of a plane-wave in the interstitial region plus a sum of functions, which are solutions of the Schrödinger equation for a given set of angular momentum quantum numbers (lm) and a given parameter E_l inside the muffin-tin spheres.

If the E_l 's were fixed, used only as a parameter during the construction of the basis, the Hamiltonian could be set up in terms of this basis. This would lead to a standard secular equation for the band energies. Unfortunately, it turns out, that the APW basis does not offer enough variational freedom if the E_l 's are kept fixed. An accurate description can only be achieved if they are set to the corresponding band energies. However, requiring the E_l 's to be equal to the band energies, the latter can no longer be determined by a simple diagonalization of the Hamiltonian matrix. Since the u_l 's depend on the band energies, the solution of the secular equation becomes a nonlinear problem, which is computationally much more demanding than a secular problem.

Another disadvantage of the APW method is, that it is difficult to extend beyond the spherically averaged muffin-tin potential approximation, because in the case of a general potential the optimal choice of E_l is no longer the band energy. And finally, but less serious, if, for a given choice of E_l 's, the radial functions u_l vanish at the muffin tin radius, the boundary conditions on the spheres cannot be satisfied, i.e. the plane-waves and the radial functions become decoupled. This is called the asymptote problem. It can already cause numerical difficulties if u_l becomes very small at the sphere boundary. Further information about the APW method can be found in the book by Loucks [60], which also reprints several early papers including Slater's original publication [100].

3.1.2 The Concept of LAPW

The basic idea of the linearized augmented plane-wave method (LAPW) is to add extra variational freedom to the basis inside the muffin-tins, so that it is not necessary to set the E_l 's equal to the band energies. This is done by using not only the radial solution of the Schrödinger equation, but also its derivative with respect to the energy. This construction, which was first suggested by Andersen [1], and independently by Koelling and Arbman [45], can be regarded as a linearization of the APW. To understand this we remind that in the APW method the u_l 's depend on the band energies and can thus be understood as functions of r and ϵ . Hence, u_l can be expanded into a Taylor-series around

E_l .

$$u_l(\epsilon, r) = u_l(E_l, r) + \dot{u}_l(E_l, r)(\epsilon - E_l) + O[(\epsilon - E_l)^2] \quad (3.3)$$

Here \dot{u}_l denotes the energy derivative of u_l , $\partial u_l(\epsilon, r)/\partial \epsilon$, and $O[(\epsilon - E_l)^2]$ denotes errors that are quadratic in the energy difference. Ergo, the LAPW method introduces an error of order $(\epsilon - E_l)^2$ in the wavefunction. Therefore, according to the variational principle the error in the calculated band energies is of the order $(\epsilon - E_l)^4$. Because of this high order, the linearization works very well even over rather broad energy regions. In most cases a single set of energy parameters is sufficient for the whole valence band. However, sometimes the energy region has to be split up in two or more windows with separate sets of energy parameters.

But let us turn to some important properties of the LAPW basis first, before discussing its quality and accuracy. The LAPW basis functions are of the form

$$\varphi_{\mathbf{G}}(\mathbf{k}, \mathbf{r}) = \begin{cases} \frac{1}{\sqrt{\Omega}} e^{i(\mathbf{G}+\mathbf{k})\mathbf{r}} & \text{interstitial region} \\ \sum_L A_L^{\mu\mathbf{G}}(\mathbf{k}) u_l(r) Y_L(\hat{\mathbf{r}}) + B_L^{\mu\mathbf{G}}(\mathbf{k}) \dot{u}_l(r) Y_L(\hat{\mathbf{r}}) & \text{muffin-tin } \mu \end{cases} \quad (3.4)$$

with the extra term $B_L^{\mu\mathbf{G}} \dot{u}_l(r) Y_L(\hat{\mathbf{r}})$ compared to the APW method. The additional coefficient is determined by requiring that not only the basis functions, but also their derivatives with respect to r are continuous at the sphere boundaries. It is useful to require the following normalization:

$$\langle u|u \rangle = \int_0^{R_{MT}} u_l^2(r) r^2 dr = 1, \quad (3.5)$$

where R_{MT} is the muffin-tin radius. Taking the derivative of (3.5) with respect to the energy it can easily be shown, that u_l and \dot{u}_l are orthogonal. \dot{u}_l is calculated from a Schrödinger-like equation, derived by taking the energy derivative of (3.2) with respect to E_l :

$$\left\{ -\frac{\hbar^2}{2m} \frac{\partial^2}{\partial r^2} + \frac{\hbar^2}{2m} \frac{l(l+1)}{r^2} + V(r) - E_l \right\} r \dot{u}_l(r) = r u_l(r). \quad (3.6)$$

The solution of this equation still has to be made orthogonal to u_l , since any linear combination of \dot{u}_l and u_l also solves the equation. Once the u_l and \dot{u}_l are made orthogonal the basis functions inside the spheres form a completely orthogonal basis set, since the angular functions $Y_{lm}(\hat{\mathbf{r}})$ are also orthogonal. However, the LAPW functions are in general not orthogonal to the core states, which are treated separately in the LAPW method. This fact can cause problems in the presence of high lying core states. A detailed discussion of these problems and strategies to cure them can be found in the book by Singh [98], which includes a very comprehensive review of many aspects of the LAPW method. With the construction of the LAPW basis the main problems of the APW method are solved:

- Since it is no longer necessary to set the energy parameters equal the band energies, the later can be determined by a single diagonalization of the Hamiltonian matrix.

- The LAPW method can be extended to non-spherical muffin-tin potentials with little difficulty, because the basis offers enough variational freedom. This leads then to the full-potential linearized augmented plane-wave method (FLAPW).
- If u_l is zero at the sphere boundary, its radial derivative and \dot{u}_l are in general nonzero. Hence, the boundary conditions can always be satisfied and there is no asymptote problem.

As a final remark it is worth mentioning, that the nonlinearity inherent to the APW method can only be circumvented at the expense of a larger eigenvalue problem. To see this, recall that within LAPW (and also within APW) the basis functions are represented by plane-waves. The functions inside the muffin-tins are coupled to the plane-waves via the boundary conditions, and can only be varied indirectly by a variation of the plane-wave coefficients. Clearly, with a finite number of plane-waves, at maximum the same number of functions inside the spheres can be varied independently. Hence, to make use of the extra variational freedom, that the LAPW basis set allows compared to the APW basis, i.e. to vary the u_l 's and the \dot{u}_l 's independently, more plane-waves have to be used.

For completeness it is worth mentioning that recently independently by two authors [51, 99] local orbitals (lo) had been suggested to amend the LAPW and APW basis set, to improve the speed of convergence with respect to the number of basis functions, and to increase the energy width of appropriate energy minimization.

3.1.3 The Concept of FLAPW

In the past the majority of applications of APW and LAPW² method employed shape-approximations on the potential used in the Hamiltonian. Typically, the potential in the unit cell $V(\mathbf{r})$ is approximated by $V_0(\mathbf{r})$,

$$V(\mathbf{r}) = \begin{cases} V_I^0 = \text{const.} & \text{interstitial region} \\ V_{MT}^0(r) & \text{muffin-tin} \end{cases} \quad (3.7)$$

using a constant potential in the interstitial region and a spherically symmetric potential inside each sphere.

While the LAPW method yields accurate results for close-packed metal systems the shape-approximation becomes difficult to justify for crystals with open structures such as silizides, perovskides, surfaces or clusters.

In the full-potential LAPW method (FLAPW), developed by Hamann and Wimmer in [32, 125], any shape-approximations in the interstitial region and inside the muffin-tins are dropped. This generalization is achieved by relaxing the constant interstitial potential V_I^0 and the spherical muffin-tin approximation $V_{MT}^0(r)$ due to the inclusion of a warped

²There are APW and LAPW methods available which include the warped interstitial potential [44].

interstitial $\sum V_I^{\mathbf{G}} e^{i\mathbf{G}\mathbf{r}}$ and the non-spherical terms inside the muffin-tin spheres:

$$V(\mathbf{r}) = \begin{cases} \sum_{\mathbf{G}} V_I^{\mathbf{G}} e^{i\mathbf{G}\mathbf{r}} & \text{interstitial region} \\ \sum_L V_{MT}^L(r) Y_L(\hat{\mathbf{r}}) & \text{muffin-tin} \end{cases} \quad (3.8)$$

This method became possible with the development of a technique for obtaining the Coulomb potential for a general periodic charge density without shape-approximations and with the inclusion of the Hamiltonian matrix elements due to the warped interstitial and non-spherical terms of the potential. The charge density is represented in the same way as the potential:

$$\rho(\mathbf{r}) = \begin{cases} \sum_{\mathbf{G}} \rho_I^{\mathbf{G}} e^{i\mathbf{G}\mathbf{r}} & \text{interstitial region} \\ \sum_L \rho_{MT}^L(r) Y_L(\hat{\mathbf{r}}) & \text{muffin-tin} \end{cases} \quad (3.9)$$

Detail of the solution of the Poisson equation for an arbitrarily shaped periodic potential are described in section 6.1.

3.2 Chiral Symmetries

Since our main purpose is to derive an FLAPW method for one-dimensional systems, we face the problem of dealing with the world of symmetries, 1D systems possess. Within the applications of the FLAPW method to the bulk and film structures, the symmetries of the considered systems were naturally included, allowing to achieve a significant speed-up and increasing the efficiency of analysis of the obtained results [125]. However, symmetries of 1D systems are very much different from those characteristic for 2D and 3D geometries. The complexity of the problem is emphasized by the fact that the plane-wave basis set, used both for 1D and 2D-3D versions, allows symmetrization according to the film and bulk symmetrical operations more naturally, than to 1D chiral symmetries (see section 3.3.3). To look deeper into the problem, we will have to analyze chiral symmetries in more detail in order to work out a suitable concept for treating these symmetries efficiently.

Since the discovery of Ijima [38], carbon nanotubes are one of the most prominent quasi-one dimensional crystals, which have been extensively investigated both experimentally and theoretically. A carbon nanotube is a honeycomb lattice (graphene sheet) rolled into a cylinder. The nanotube diameter is much smaller in size than the most advanced semiconductor devices obtained so far. Thus the availability of the carbon nanotubes may have a large impact on semiconductor physics because of their small size and special electronic properties, which are unique. Because of the large variety of possible helical geometries known as chirality, carbon nanotubes provide a family of structures with different diameters and chiralities. One of the most significant physical properties of carbon nanotubes is their electronic structure which depends basically on their geometry. In

particular, the electronic structure of a single-walled carbon nanotube is either metallic or semiconducting, depending on its chirality and diameter.

But the world of 1D structures with the chiral geometries and specific electronic, semi-conducting or metallic, properties is not restricted to a set of carbon nanotubes based materials. First of all, there is currently a strong interest in the 1D complex materials containing not only carbon atoms, but also other elements such as B, N, Si, Ga etc. Possessing peculiar, theoretically predicted, physical properties, these materials have been successfully produced experimentally, existing in the form of quasi-one dimensional nanotubes and nanowires, with the symmetries, mostly related to the symmetries of carbon nanotubes. On the other hand, recent discoveries in the field of metallic wires and tubes, make it possible to apply the symmetry technique usually used for carbon nanotubes for a huge general class of materials of one-dimensional nature via some generalizations.

In the code the symmetry properties are formulated and included in terms of the chiral symmetry group of the considered system. This means that the symmetry group \mathcal{T} is cyclic of order N with a generator \mathcal{R} so that for every operation $n = 1, \dots, N : \mathcal{R}_n = \mathcal{R}^n$, $\mathcal{T} = \{\mathcal{R}, \mathcal{R}_2, \dots, \mathcal{R}_{N-1}\}$. In a three-dimensional space the operation \mathcal{R} is nothing else but a simultaneous rotation around the z -axis (the axis of one-dimensional periodicity) R_ψ and a translation along the z -axis τ , $\mathcal{R} = (R_\psi, \tau)$. Obviously,

$$\psi = \frac{2\pi}{N}, \text{ and } \tau = \frac{M \cdot T}{N}, \quad (3.10)$$

where M is some integer number and T is a period of the system along the z -direction.

Formulated in such a manner, the approach for describing the chiralities of the considered 1D systems seems to be the most optimal from the implementational point of view within the FLAPW approach.

This symmetrical approach, being rather abstract and general, can be easily mapped, for instance, on hexagonal and triangular classes of symmetries, which many of the 1D systems possess. We briefly show this mapping in two following sections.

3.2.1 Hexagonal In-Plane Lattice

The structure of a single-walled nanotube, obtained by rolling up a hexagonal sheet of atoms [17], can be specified by two vectors: \vec{OA} and \vec{OB} (see 3.2 (left)). Vector \vec{OB} corresponds to the direction of the nanotube and vector \vec{OA} corresponds to the circumference of a nanotube, perpendicular to the nanotube axis. A 1D nanotube is obtained by connecting the points O, A and B, B' . The vectors \vec{OA} and \vec{OB} define the chiral vector of the nanotube \mathbf{C}_h and translational vector \mathbf{T} . The chiral vector can be expressed in terms of the real space unit vectors \mathbf{a}_1 and \mathbf{a}_2 of the hexagonal lattice:

$$\mathbf{C}_h = m\mathbf{a}_1 + n\mathbf{a}_2, \text{ (} m, n \text{ are integers, } 0 \leq |m| \leq n \text{)}. \quad (3.11)$$

It is very important to remember that a nanotube can be uniquely determined by its chiral vector, and, therefore, talking about nanotubes, one always calls them by their chiral vector (m, n) .

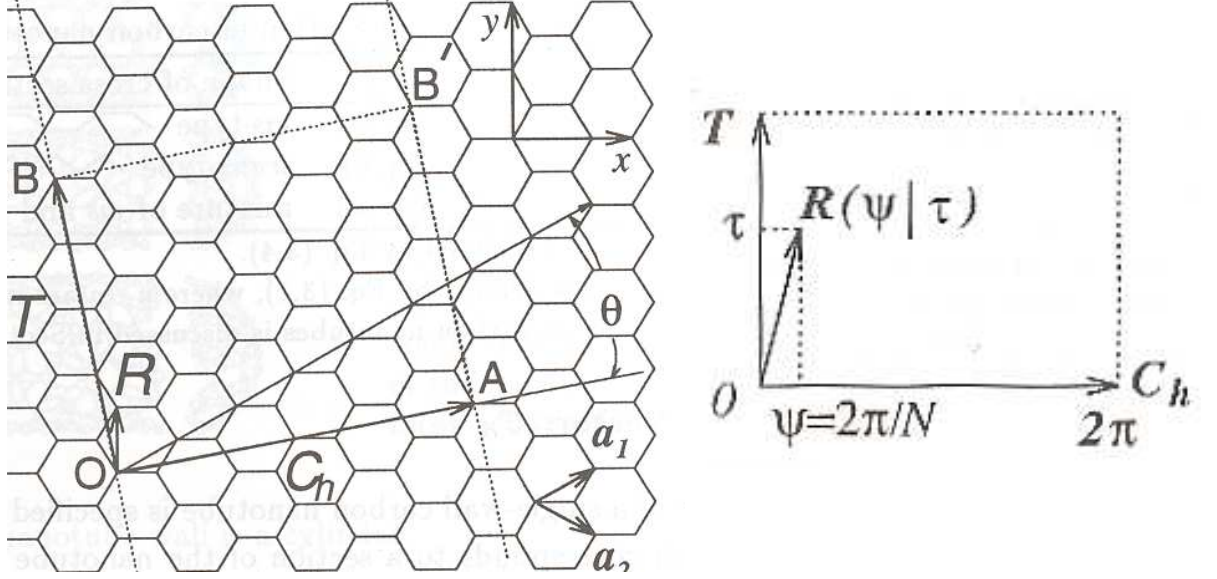


Figure 3.2: Left: the unrolled honeycomb lattice of a nanotube. When we connect sites O and A , and B and B' , a nanotube can be constructed. \vec{OA} and \vec{OB} define the chiral vector \mathbf{C}_h and the translational vector \mathbf{T} of the nanotube, respectively. The rectangle $OAB'B$ defines the unit cell for the nanotube. The vector \mathbf{R} denotes a symmetry vector. Right: space group symmetry operation $\mathcal{R} = (R_\psi, \tau)$ in which ψ denotes the angle of rotation around the nanotube axis and τ is a translation in the direction of \mathbf{T} as specified by the symmetry vector \mathbf{R} .

The diameter of the nanotube, d_t , is given by L/π , in which L is the circumferential length of the carbon nanotube:

$$d_t = L/\pi, \quad L = |\mathbf{C}_h| = a\sqrt{n^2 + m^2 + nm}, \quad \mathbf{a}_1 \cdot \mathbf{a}_1 = a. \quad (3.12)$$

The chiral angle θ is defined as the angle between the \mathbf{C}_h and \mathbf{a}_1 .

The translational vector \mathbf{T} is defined to be the unit vector of a 1D nanotube. It is parallel to the nanotube axis and normal to the \mathbf{C}_h in the unrolled honeycomb lattice. The translational vector can be expressed in terms of the planar basis vectors as:

$$\mathbf{T} = t_1\mathbf{a}_1 + t_2\mathbf{a}_2, \quad (t_1, t_2 \text{ are integers}). \quad (3.13)$$

The translational vector \mathbf{T} corresponds to the first lattice point of the 2D hexagonal sheet through which the vector \vec{OB} passes. From this fact and the fact of orthogonality of \mathbf{T} and \mathbf{C}_h the numbers t_1 and t_2 can be defined:

$$t_1 = \frac{2n + m}{d_R}, \quad t_2 = -\frac{2m + n}{d_R}, \quad (3.14)$$

where d_R is the greatest common divisor (*gcd*) of $(2n + m)$ and $(2m + n)$.

We denote the atom site vectors within the 1D nanotube unit cell by i times the vector \mathbf{R} , that is, $i\mathbf{R}$, where i is an integer: $i = 1, \dots, N$, and $2N$ is the number of atoms in the 1D unit cell of the carbon nanotube. When $i\mathbf{R}$ goes out of the unit cell, we shift it to lie within the unit cell through translation by a integer number of \mathbf{C}_h or \mathbf{T} vectors, using periodic boundary conditions. The vector \mathbf{R} connects symmetry equivalent atoms in the nanotube. It is convenient to express the \mathbf{R} vector in terms of its projections on the orthogonal vectors \mathbf{C}_h and \mathbf{T} of the nanotube unit cell, as it shown in the Fig. 3.2 (right). The symmetry vector \mathbf{R} is then defined as the site vector (shown by \vec{OR} in Fig. 3.2 (left)), having the smallest component in the direction of \mathbf{C}_h , and expressed as:

$$\mathbf{R} = p\mathbf{a}_1 + q\mathbf{a}_2, \quad (p, q \text{ are integers}). \quad (3.15)$$

From a physical standpoint, the vector \mathbf{R} consists of a rotation around the nanotube axis by an angle ψ combined with a translation τ in the direction of \mathbf{T} , and, therefore, \mathbf{R} can be treated as a generator of a symmetry group for a given nanotube $\mathcal{R} = (R_\psi, \tau)$, allowing a complete description of the system in terms of a symmetry approach, which we have formulated above.

Summarizing, having a nanotube with a unique chiral vector $\mathbf{C}_h = (m, n)$ and symmetry vector $\mathbf{R} = (p, q)$, the order of the symmetry group

$$N = \frac{2(m^2 + n^2 + nm)}{d_R} \quad (3.16)$$

is equal to the number of hexagons in the unit cell, $d_R = \text{gcd}(2m + n, m + 2n)$. The corresponding relations are:

$$\tau = \frac{(mp - nq)T}{N}, \quad M = mp - nq. \quad (3.17)$$

As an example, for the (9,0) nanotube (Fig. 3.3) we have: $\mathbf{R} = (1, -1)$, $d_R = 9$, $N = 18$, $M = 9$, $\psi = \frac{\pi}{9}$, $\tau = \frac{1}{2}$ in units of T .

3.2.2 Triangular In-Plane Lattice

Instead of rolling up a hexagonal sheet of atoms one could use a triangular lattice. Structures obtained in this way are very common for existing and experimentally observed metallic nanowires and nanotubes.

Introducing a triangular lattice instead of a hexagonal one does not cause any significant changes in the formalism (for details see [113, 82]). In the same manner the chiral vector $\mathbf{C}_h = (m, n)$, the translational vector $\mathbf{T} = (t_1, t_2)$ and symmetry vector $\mathbf{R} = (p, q)$ can be defined in terms of the two-dimensional basis vectors \mathbf{a}_1 , \mathbf{a}_2 of a triangular lattice.

The changes in the derived expressions for the chiral, translational and symmetry vectors are mainly caused by the different orientation of \mathbf{a}_1 and \mathbf{a}_2 to each other. However, the number of symmetry operations

$$N = \frac{2(m^2 + n^2 - nm)}{d_R} \quad (3.18)$$

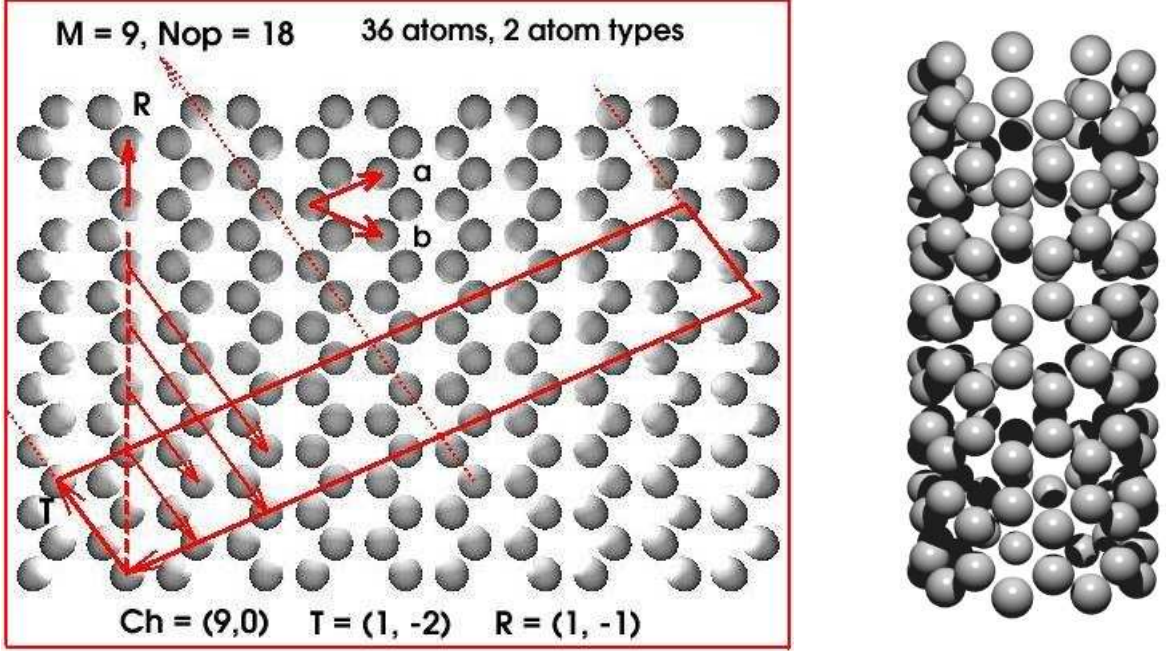


Figure 3.3: A large set of the future nanodevices are based on use of the carbon nanotubes, which can be created by rolling up of a graphene sheet. Depending on the way this sheet is rolled (or, equivalently, on the symmetry of the nanotube) physical properties show essential differences, in particular, a transition from a conducting to semiconducting behavior. As an example, in-plane representation of a (9,0) nanotube is shown, including the derived symmetry parameters. The elementary unit cell is marked with a thick red line.

is equal to the number of atoms in the unit cell, where d_R is the greatest common divisor (gcd) of $(2m - n)$ and $(m - 2n)$. The translational part of \mathcal{R} is given by

$$\tau = \frac{(mp - nq)T}{N}, \text{ with } M = mp - nq. \quad (3.19)$$

For example for the $\mathbf{C}_h = (6, 0)$ wire (see also Fig. 3.4) \mathbf{R} would be $(1, 1)$, $d_R = 6$, $N = 12$, $M = 6$, $\psi = \frac{\pi}{6}$, $\tau = \frac{1}{2}$ in units of T .

On the Fig. 3.5 we have also shown a (6,3) nanowire obtained by rolling a triangular sheet of atoms with $\mathbf{C}_h = (6, 3)$. In this case $\mathbf{R} = (1, 1)$, and $d_R = 9$, $N = 6$, $M = 3$, $\psi = \frac{\pi}{3}$, $\tau = \frac{1}{2}$ in units of T .

3.3 Implementation

In this section we give a brief outlook of the current implementation of the 1D philosophy within the FLAPW formalism. One-dimensional FLAPW model is a natural continuation

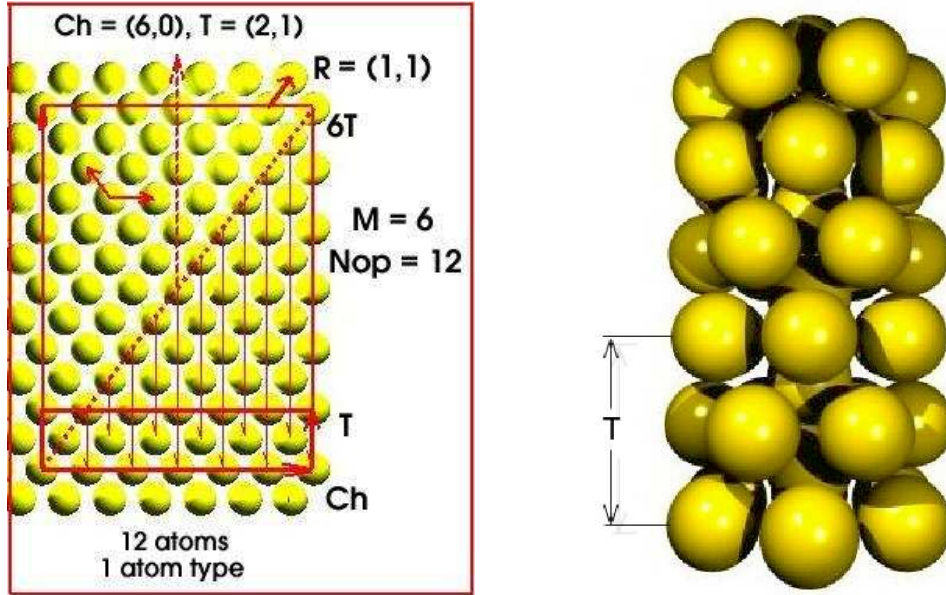


Figure 3.4: Many of the metallic nanowires (single-walled or multi-walled) are obtained by rolling up a triangular sheet of metal atoms. Figure presents a symmetrical characterization of a (6,0) nanowire in terms of a chiral vector with corresponding derived symmetry parameters. The elementary unit cell of the considered structure is marked with a thick red line.

of a film FLAPW method, where an additional region of space, besides the interstitial and muffin-tin regions, appears. This third, additional, as compared to bulk, region, which is called vacuum region, is situated outside the muffin-tins in order to describe the decay of the charge density, potential and basis functions into the vacuum at a large distance from the film surfaces. Implemented by E. Wimmer, H. Krakauer, M. Weinert, A.J. Freeman and M. Posternak 25 years ago ([50, 125, 122]), the FLAPW film model proved to be powerful, very precise and fast compared to the FLAPW super-cell approach for the calculations of the electronic properties of thin slabs. However, recent scientific interest in the structures of one-dimensional nature was our main motivation in extending the FLAPW method to 1D systems.

3.3.1 Geometry

In the FLAPW method for one-dimensional systems, presented in this thesis, the infinite three-dimensional space is partitioned into three regions: the muffin-tin spheres (MT) with the radius R_{MT} around the atoms, the interstitial region (IR) between the atoms and within a cylinder along the z -direction of the radius R_{vac} (for this parameter we will also often use R). Outside this cylinder there is an infinitely extended vacuum region (VR) (see Fig. 3.5). From here on we define the z -axis as the axis of one-dimensional translational

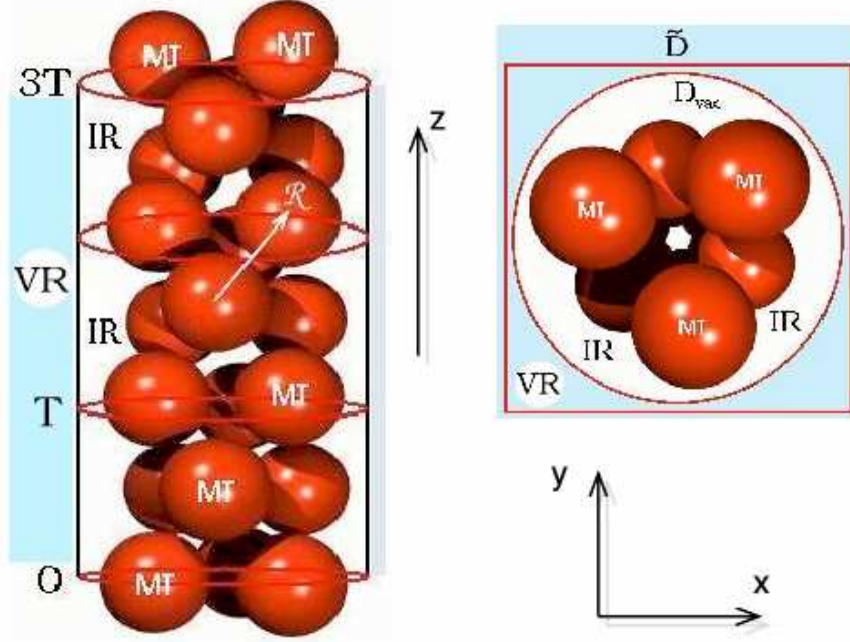
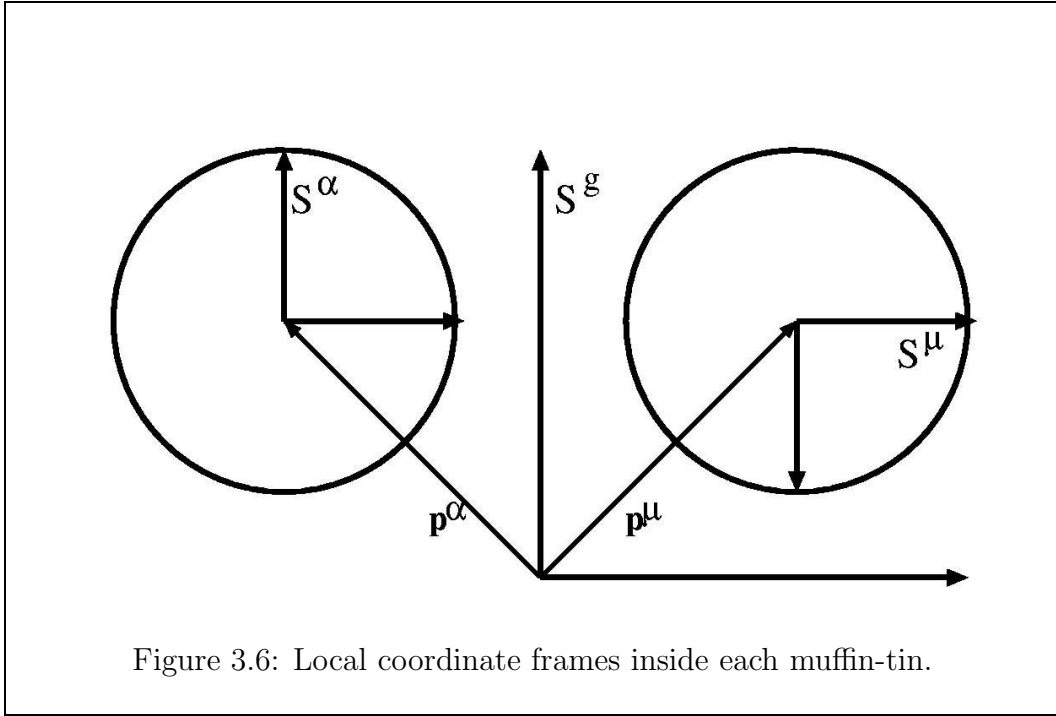


Figure 3.5: Spatial partitioning of space into muffin-tin spheres (MT), interstitial region (IR) and vacuum region (VR) (shown in blue color) is shown from aside (left) and from the top (right). The vacuum region is the infinite region outside the cylinder with the diameter D_{vac} . In-plane reciprocal vectors \mathbf{G}_{\parallel} are generated in an in-plane square lattice with the lattice constant $\tilde{D} > D_{\text{vac}}$. T is a period of the wire along the z -axis. $\mathcal{R} = (R_{\psi}, \tau)$ is a generator of the symmetry group. Here: the order of the group is $N = 6$, $\psi = \frac{\pi}{3}$, $M = 3$, $\tau = \frac{1}{2}$.

symmetry. As our method is based on the use of LAPW basis functions [1, 50, 125], the set of reciprocal vectors $\mathbf{G} = (\mathbf{G}_{\parallel}, G_z)$ is generated in a rectangular box, which reflects the translational periodicity of the system in z -direction. The corresponding Bloch number k_z (which is also often written as k in the text) lies within the first one-dimensional Brillouin zone. The in-plane reciprocal lattice vectors \mathbf{G}_{\parallel} are generated in an in-plane square lattice with the lattice constant \tilde{D} . The vacuum region is an infinite region outside the cylinder with the diameter $D_{\text{vac}} < \tilde{D}$ ($D_{\text{vac}} = 2R_{\text{vac}}$), with the axis along z -direction. Parameter \tilde{D} is chosen larger than D to gain greater variational freedom.

3.3.2 Symmetries

Introducing the symmetry for the system (see section 3.2) automatically means, that some of the atoms in the unit cell are symmetry equivalent, i.e. these atoms can be mapped onto each other by a space group operation $\mathcal{R} = \{R_{\psi} | \tau\}$. Such a group of atoms is called an atom type, represented by one of the atoms. Let $\mathcal{R}^{\mu} = \{R_{\psi_{\mu}} | \tau_{\mu}\} = \{\mathbf{R}^{\mu} | \tau^{\mu}\}$ be the



operation that maps the atom μ onto its representative. This atom can now be assigned a local coordinate frame S^μ (cf. Fig. 3.6), where the origin of S^μ is at the atom's position \mathbf{p}^μ .³

The local frame is chosen such that the unit vectors of the local frame S^μ are mapped onto those of the global frame by \mathbf{R}^g ($\mathbf{R}^\mu S^\mu = S^g$). The local frame of the representative atom S^α is only translated with respect to the global frame, i.e. the same rotation \mathbf{R}^μ maps S^μ onto S^α . The potential (and other quantities) inside the muffin-tins can now be written in terms of the local coordinate system. Due to the symmetry we find $V_{MT^\alpha}(\mathbf{r}^\alpha) = V_{MT^\mu}(\mathbf{r}^\mu)$, where \mathbf{r}^α and \mathbf{r}^μ are expanded in terms of the local frames S^α and S^μ respectively. As a consequence the radial functions $u_l(r)$ and the t -matrices (see section 4.2.1) are the same for all atoms of the same type. This way symmetry is exploited to save memory and computing time during the calculation of the t -matrices.

³The atom position is very frequently denoted by τ^μ , which would clearly cause some confusion in this context.

3.3.3 Charge Density and Potential

The charge density is represented according to the symmetries of the system in the following way:

$$\rho(\mathbf{r}) = \begin{cases} \sum_{\mathbf{G}} \rho_{\mathbf{G}} e^{i\mathbf{G}\mathbf{r}} \sim \sum_{\mathbf{G}} \rho_{\mathbf{G}} \Phi_{\mathbf{G}}(\mathbf{r}) & \text{in IR} \\ \sum_{\nu} \rho_{\nu}(r_{\alpha}) K_{\nu}(\hat{\mathbf{r}}_{\alpha}) - Z_{\alpha} \delta(\mathbf{r}_{\alpha}) & \text{in MT}^{\alpha} \\ \sum_{\mu} \rho_{\mu}(r) \Phi_{\mu}(\varphi, z) & \text{in VR} \end{cases} \quad (3.20)$$

where

$$K_{\nu}(\hat{\mathbf{r}}) = \sum_m c_m(\nu) Y_{\nu m}(\hat{\mathbf{r}}) \quad (3.21)$$

are the lattice harmonics, obtained by exploiting the point symmetry of the atom α , $\mathbf{r}_{\alpha} = \mathbf{r} - \tau_{\alpha}$, τ_{α} is the position of the atomic sphere α with the nuclear number Z_{α} . The quantities in the spheres, like radial components of the charge density, potential, and basis functions are calculated and stored only for the representative atom of type α . All necessary information on the charge density of an atom β , which is related by symmetry to the atom α can then be obtained exploiting the fact that the local coordinate frame of the atom $\mathcal{S}_{\beta} = \mathcal{R}_{\beta(\alpha)} \mathcal{S}_{\alpha}$ is related to the coordinate frame \mathcal{S}_{α} by the symmetry operation $\mathcal{R}_{\beta(\alpha)}$ which moves the representative atom α to the β th atom of the same type.

In the vacuum, symmetry can be used to reduce the number of expansion coefficients, necessary to represent the charge density by introducing star functions. For a certain $\mu = (m, G_z)$ a vacuum symmetrized two-dimensional star $\Phi_{\mu}(\varphi, z)$ looks like:

$$\Phi_{\mu}(\varphi, z) = \frac{1}{N} \sum_{n=1}^N \mathcal{R}_n e^{im\varphi} e^{iG_z z} \quad (3.22)$$

for those μ for which $\Phi_{\mu}(\varphi, z) \neq 0, r \geq R_{\text{vac}}$. For instance having a rotational symmetry of order p reduces the number of μ 's considered by factor p . The summation in (3.20) includes μ 's with m 's up to a parameter m_{max} , defined for the charge density in the vacuum as $m_{\text{max}} \approx G_{\text{max}} \cdot R_{\text{vac}}$, in analogy to the corresponding angular expansion parameter for the basis functions in the vacuum.

In the interstitial region a double representation of the charge density is used:

$$\rho(\mathbf{r}) = \sum_{\mathbf{G}} \rho_{\mathbf{G}} e^{i\mathbf{G}\mathbf{r}} \longleftrightarrow \sum_{\mathbf{G}} \rho_{\mathbf{G}} \Phi_{\mathbf{G}}(\mathbf{r}), \quad (3.23)$$

where $\Phi_{\mathbf{G}}(\mathbf{r})$ is a symmetrized three-dimensional star:

$$\Phi_{\mathbf{G}}(\mathbf{r}) = \frac{1}{N} \sum_{n=1}^N \mathcal{R}_n e^{i\mathbf{G}\mathbf{r}} = \frac{1}{N} \sum_{n=1}^N e^{iR_n \mathbf{G}(\mathbf{r} - \tau_n)} \quad (3.24)$$

The necessity of the double representation is caused by the nonorthogonality of the symmetrized stars $\Phi_{\mathbf{G}}$. This means that in contrast to the situation using usual plane-waves,

the integral of a symmetrized star $\Phi_{\mathbf{G}}(\mathbf{r})$ over the tetragonal unit cell with the in-plane lattice constant \tilde{D} is not necessarily zero in the case of $\mathbf{G} \neq 0$. Also, the product of two symmetrized stars is not a symmetrized star, which means, that it cannot be presented in the form of (3.24) anymore (although, being a symmetrical function, can be expanded in terms of symmetrized stars). The combination of the latter two facts makes it difficult to apply a technique of fast Fourier transformations, widely used in plane-wave based codes. The same representation in different regions of space, as for the charge density in (3.20), is used for the potential.

After finding the wavefunctions expansion coefficients $c_{\nu}^{\mathbf{G}}(k_z)$, the eigenvalues $\epsilon_{\nu}(k_z)$, and the Fermi energy E_F (see section 3.3.6), the charge density is determined as:

$$\rho(\mathbf{r}) = \sum_{k_z} \sum_{\nu} w(k_z) f(\nu, k_z) |\Psi_{k_z}^{\nu}(\mathbf{r})|^2, \quad (3.25)$$

where the summation goes over the one-dimensional Brillouin zone with the weighting factors $w(k_z)$ and the Fermi function $f(\nu, k_z)$.

3.3.4 Coulomb Potential

The potential used for solving the one-particle Kohn-Sham equation is divided into the Coulomb and the exchange-correlation parts. While the latter is obtained on a real-space grid in a quite straightforward manner, the Coulomb potential requires more attention.

Conceptually, the approach for solving the Poisson equation goes back to Weinert's pseudo-charge scheme for the Dirichlet problem [120] for the spheres and vacuum boundaries. The basic idea of the pseudo-charge scheme is that the charge distributions inside the spheres contribute to the potential outside the spheres only via their multipole moments. As multipole moments do not uniquely define a charge density, we replace the real charge density in the spheres by a so-called pseudo-charge density with the same multipole moments fulfilling the additional requirement of having rapidly converging Fourier components. These Fourier components together with the vacuum charge density take part in solving the Poisson equation in the vacuum. After that the Dirichlet problem for the interstitial-vacuum boundary is solved in order to find the Fourier components of the interstitial potential. Subsequently, the Coulomb potential in the spheres is found via the interstitial-spherical Dirichlet boundary problem:

$$V_{\alpha}(\mathbf{r}_{\alpha}) = \int_{S_{\alpha}} \rho_{\alpha}(\mathbf{r}) G(\mathbf{r}, \mathbf{r}_{\alpha}) d^3r - \frac{R_{\alpha}^2}{4\pi} \oint_{S_{\alpha}} V_I(\mathbf{R}_{\alpha}) \frac{\partial G}{\partial n} d\Omega, \quad (3.26)$$

where S_{α} denotes a sphere around atom α with the radius R_{α} , \mathbf{R}_{α} is a point on ∂S_{α} , V_I is the interstitial potential, and the Green function $G(\mathbf{r}, \mathbf{r}_{\alpha})$ and its normal derivative are given in [120].

The Poisson equation in the vacuum is solved in cylindrical coordinates using the boundary condition at infinity:

$$\lim_{r \rightarrow \infty} V(r) = 0, \quad \lim_{r \rightarrow \infty} \frac{\partial V(r)}{\partial r} = 0. \quad (3.27)$$

Thus, we introduce the zero energy as an absolute reference from which all energies are measured. For example, the work function is just given by the negative of the Fermi energy E_F . The radial Poisson equation which describes the (m, G_z) -component of the vacuum potential in cylindrical coordinates is given by:

$$\left(\frac{d^2}{dr^2} + \frac{1}{r} \frac{d}{dr} - G_z^2 - \frac{m^2}{r^2} \right) V_{G_z, m}(r) = -4\pi \rho_{G_z, m}(r). \quad (3.28)$$

The equation is solved using the Green function G_{m, G_z} , which satisfies above defined boundary conditions:

$$G_{m, G_z}(r, r') = \begin{cases} -4\pi \ln r_{<} & m = G_z = 0 \\ \frac{2\pi}{m} (r_{<}/r_{>})^m & G_z = 0, m \neq 0 \\ 4\pi I_m^{G_z}(r_{<}) K_m^{G_z}(r_{>}) & m \cdot G_z \neq 0 \end{cases} \quad (3.29)$$

where $r_{>} = \max(r, r')$, $r_{<} = \min(r, r')$, $I_m^{G_z}$ and $K_m^{G_z}$ are the modified cylindrical Bessel and MacDonal functions I_m and K_m of order m : $I_m^{G_z}(r) = I_m(G_z r)$, $K_m^{G_z}(r) = K_m(G_z r)$. The radial component of the Coulomb potential in the vacuum $V_\mu^V(\mathbf{r})$ is obtained in terms of the radial charge density as:

$$V_{G_z, m}^V(r) = \int_0^\infty r' G_{m, G_z}(r, r') \rho_{G_z, m}(r') dr', \quad r > R_{\text{vac}}. \quad (3.30)$$

Note, that the integration range is between $0 \leq r' \leq R_{\text{vac}}$. Thus it includes the interstitial region, where the charge density has a three-dimensional Fourier representation. The corresponding radial components of the interstitial charge density read:

$$\rho_{G_z, m}(r) = \sum_{\mathbf{G}_\parallel} i^m \rho_{G_z, \mathbf{G}_\parallel} e^{-im\varphi_{\mathbf{G}_\parallel}} J_m(G_\parallel r), \quad (3.31)$$

with J_m denoting the cylindrical Bessel functions of order m and $\varphi_{\mathbf{G}_\parallel}$ is the polar coordinate of the in-plane component \mathbf{G}_\parallel of a reciprocal vector. Therefore, the integration over the interstitial region is reduced to a \mathbf{G}_\parallel -summation on the vacuum boundary for each (m, G_z) -component. On the interstitial-vacuum boundary a value of the vacuum potential V_b^V is obtained.

In the next step we construct the potential \tilde{V} in the interstitial region, having the following Fourier components:

$$\tilde{V}_{\mathbf{G}} = \frac{4\pi}{G^2} \rho_{\mathbf{G}}, \quad \text{and} \quad \tilde{V}_{\mathbf{0}} = 0, \quad (3.32)$$

with the interstitial-vacuum boundary value \tilde{V}_b . Applying the Fast Fourier Transform (FFT) to \tilde{V} we get it on a real grid in the interstitial. The second auxiliary interstitial potential \mathcal{V} we use solves the boundary problem:

$$\Delta \mathcal{V}(\mathbf{r}) = 0, \quad r \in \text{IR}, \quad \mathcal{V}_b = V_b^V - \tilde{V}_b, \quad (3.33)$$

where \mathcal{V}_b is a boundary value of \mathcal{V} . This potential is easily found analytically on the real grid. After the real grid summation and applying backward FFT to $\tilde{V} + \mathcal{V}$ we get the Fourier components of the real interstitial potential $V_I(\mathbf{G})$.

3.3.5 Basis Functions

As characteristic for the FLAPW method, optimally adjusted basis functions are used in three different regions of space:

$$\varphi_{\mathbf{G}}(k_z, \mathbf{r}) = \begin{cases} e^{i(\mathbf{G}+k_z)\mathbf{r}} & \text{in IR} \\ \sum_L \left(A_L^{\alpha\mathbf{G}}(k_z) u_l^\alpha(r) + B_L^{\alpha\mathbf{G}}(k_z) \dot{u}_l^\alpha(r) \right) Y_L(\hat{\mathbf{r}}) & \text{in MT}^\alpha \\ \sum_m \left(A_m^{\mathbf{G}}(k_z) u_m^{G_z}(k_z, r) + B_m^{\mathbf{G}}(k_z) \dot{u}_m^{G_z}(k_z, r) \right) & \\ \times e^{im\varphi} e^{i(G_z+k_z)z} & \text{in VR} \end{cases} \quad (3.34)$$

In the interstitial region the basis functions $\varphi_{\mathbf{G}}(k_z, \mathbf{r})$ are usual plane-waves with $\mathbf{k} = (0, 0, k_z)$.

In the sphere MT^α the basis functions for each atom α have the well-known form of products of spherical harmonics $Y_L(\hat{\mathbf{r}})$, $L = (l, m)$, and of the radial wavefunctions $u_l^\alpha(r)$ and their energy derivatives $\dot{u}_l^\alpha(r)$, which solve for each angular momentum $l \leq l_{\max}$ certain types of radial Schrödinger like scalar-relativistic equations, with the spherical part of the potential $V_0^{\text{MT}^\alpha}(r)$ and suitably chosen energy parameters E_l [98].

In the vacuum region the space coordinate \mathbf{r} is written in terms of cylindrical coordinates (r, φ, z) and the summation over m goes up to the angular expansion parameter m_{\max} , which ensures that the oscillations of the plane-waves on the cylindrical vacuum boundary continue smoothly to the vacuum side. Since the vacuum potential is rather flat, relativistic effects on the basis functions can safely be ignored, and the cylindrically symmetrical part of the vacuum potential $V_0(r)$ and the vacuum energy parameter E_v , determined in every iteration, enter in solving the radial Schrödinger equation for every pair (m, G_z) giving rise to the vacuum radial basis wavefunctions $u_m^{G_z}(k_z, r)$ and their energy derivatives $\dot{u}_m^{G_z}(k_z, r)$.

The sets of augmentation coefficients A and B both for the MT spheres and the vacuum region are determined such that the basis functions and their spatial derivatives are continuous across the MT spheres, interstitial and vacuum region boundaries. The equations and normalization conditions for the radial functions $u_m^{G_z}(k_z, r)$ and $\dot{u}_m^{G_z}(k_z, r)$, and expressions for A - and B coefficients are given in section 4.2.4.

All the basis functions with reciprocal lattice vector \mathbf{G} that fulfill the condition $|k_z + \mathbf{G}| < K_{\max}$ are included. The corresponding representation of the charge density and potential involves all vectors \mathbf{G} with $|\mathbf{G}| < G_{\max}$. Typically, $G_{\max} \approx 3 \cdot K_{\max}$ in order to describe multiplication of the interstitial potential with the step function. The vacuum parameter m_{\max} is defined in the same manner as l_{\max} in the spheres [98]: $m_{\max} \simeq K_{\max} \cdot R_{\text{vac}}$.

In the case of carrying out spin-polarized calculations for magnetic systems, the basis functions and all the matrix elements discussed below, carry an additional index $\sigma = \uparrow, \downarrow$, which is dropped here for simplicity.

3.3.6 Eigenvalue Problem

The wavefunction $\Psi_{k_z}^\nu(\mathbf{r})$ for a certain k_z -point and an energy band ν is expanded in terms of basis functions as:

$$\Psi_{k_z}^\nu(\mathbf{r}) = \sum_{\mathbf{G}} c_\nu^{\mathbf{G}}(k_z) \varphi_{\mathbf{G}}(k_z, \mathbf{r}), \quad (3.35)$$

where the expansion coefficients $c_\nu^{\mathbf{G}}(k_z)$ and corresponding eigenvalues $\epsilon_\nu(k_z)$ are found by minimizing the Rayleigh-Ritz functional:

$$\epsilon_\nu(k_z) = \frac{\langle \Psi_{k_z}^\nu | \mathcal{H} | \Psi_{k_z}^\nu \rangle}{\langle \Psi_{k_z}^\nu | \Psi_{k_z}^\nu \rangle} \quad (3.36)$$

with respect to the expansion coefficients. \mathcal{H} is the Hamiltonian of the system. Minimization of (3.36) leads to the generalized eigenvalue problem:

$$\{\mathbf{H}(k_z) - \epsilon_\nu(k_z) \mathbf{S}(k_z)\} c_\nu^{\mathbf{G}}(k_z) = 0, \quad (3.37)$$

where the appearance of the overlap matrix $\mathbf{S}(k_z)$ is due to the nonorthogonality of basis functions. The components of the Hamiltonian and overlap matrices are given by following expressions:

$$H^{\mathbf{G}'\mathbf{G}}(k_z) = \int \varphi_{\mathbf{G}'}^*(k_z, \mathbf{r}) \mathcal{H} \varphi_{\mathbf{G}}(k_z, \mathbf{r}) d^3r, \quad (3.38)$$

$$S^{\mathbf{G}'\mathbf{G}}(k_z) = \int \varphi_{\mathbf{G}'}^*(k_z, \mathbf{r}) \varphi_{\mathbf{G}}(k_z, \mathbf{r}) d^3r. \quad (3.39)$$

The integration goes over the entire unit cell. Exact expressions for the Hamiltonian and overlap matrix elements are given in the next Chapter.

3.3.7 Timing

In order to give the reader an impression about the computational cost for computing the vacuum region we have analyzed the timing of the Hamiltonian and overlap matrix setup, the charge density and potential generation. The timing was measured for a bare Au(6,0) tube with 12 atoms per unit cell with the computational parameters as described in section 7.2. The set-up of the Hamiltonian and overlap matrices in the vacuum region takes about 10% of the overall time spend to set up these matrices, which amounts to 2.5% of the entire eigenvalue problem including the diagonalization. The construction of the vacuum charge density takes 0.9% of the total time per iteration and a fraction of 2% of the total time per iteration is needed for the vacuum potential within the LDA (including Coulomb and exchange-correlation potential). In total, for a 12 atom Au(6,0) tube the total time spend for calculating the vacuum region amounts to 5% of the entire CPU time for one iteration with 11 k -points in one half of the Brillouin zone.

We have also performed comparative calculations of a gold monowire, once calculated with the 1D code presented in this thesis as well as with a bulk code, where a wide variety of methods are readily available applying a frequently practiced super-cell approach to

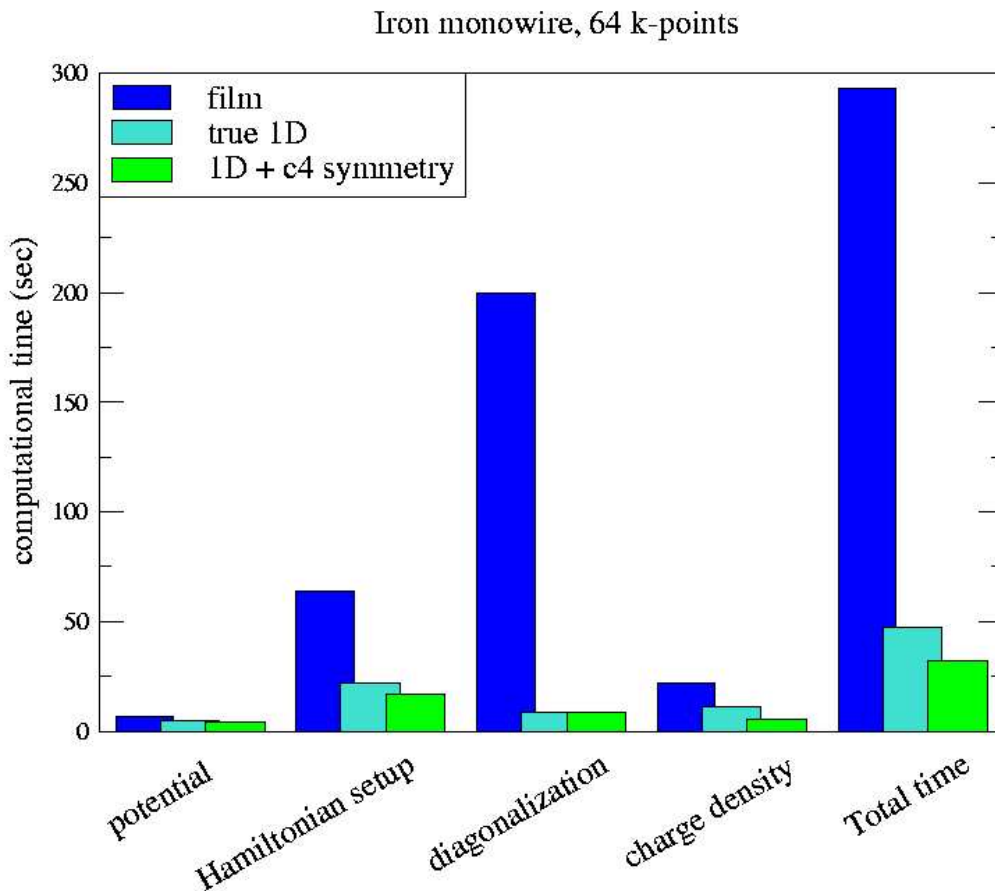


Figure 3.7: Time, consumed by different parts of the program while calculating an iron monowire, compared to the super-cell film program. The comparison is made for one-dimensional and film model realizations of the FLEUR code. 64 k -points in one half of the Brillouin zone were used. Separation between the neighboring monowires for film calculations was set to 19 a.u. The rest of the parameters and hardware used were the same.

simulate the 1D geometry. In order to provide an interpretable comparison, we have used on the same computer hardware also for the super-cell calculations the FLAPW bulk code as implemented in the FLEUR code. In both approaches we have exploited the following symmetry elements: inversion, z -reflection and $p4m$ symmetry group. For the truly one-dimensional calculations we have chosen for the computational parameters D_{vac} and \tilde{D} the values of 4.8 a.u. and 5.9 a.u., respectively. The angular expansion parameter m_{max} of 50 for the charge density and potential, and 20 for the basis functions proved to provide the required accuracy. In the super-cell approach, we followed the work of Delin and Tosatti [14] in choosing the geometrical set-up to simulate the 1D wires. Thus, we used a tetragonal super-cell and the distance between the neighboring monowires was set

to 19 a.u.. For the calculations we used 64 k -points in one half of the Brillouin zone. The rest of the parameters were the same for both calculations. We found that per self-consistency iteration the 1D-method is 150 times faster than the super-cell approach, and the Hamiltonian construction and the diagonalization part of the 1D code is 270 times faster than that of the bulk super-cell code.

For completeness we compare the timing also with the super-cell approach using the film geometry [50] (a truly two-dimensional method with semi-infinite vacuum on both side of a slab of a finite thickness) of the FLEUR code. In this super-cell geometry the one-dimensional wires are simulated by two-dimensional rectangular unit cell where the wires are again separated by 19 a.u.. The parameters D_{vac} and \tilde{D} were set to 4.8 a.u. and 5.9 a.u., respectively. All other computational parameters where chosen as in the bulk and 1D-geometry. We found that per self-consistency iteration the 1D-method is 15 times faster than the super-cell approach with 64 k -points in one half of the Brillouin zone, and the Hamiltonian construction and the diagonalization part of the 1D code is 25 times faster than that of the film super-cell code.

Finally, we would like to mention, that the code was parallelized for CRAY T3E and IBM SP4 supercomputers.

Chapter 4

Eigenvalue Problem

The solution of the eigenvalue problem has to be carried out separately for every Bloch vector. And, of course, the basis set and the Hamiltonian matrix have to be set up for each Bloch vector. However, we will not always add the k -index to the basis functions and the Hamiltonian matrix.

There is one important fact that we have not mentioned so far. Even though plane-waves form an orthogonal basis set, the FLAPW functions do not. The plane-waves in the interstitial-region are non-orthogonal, because the muffin-tin are cut out, i.e. the integration, in terms of which orthogonality is defined, does not stretch over the whole unit cell, but only over interstitial region. An additional contribution comes from the muffin-tin. Even though the $u_l(r)Y_L$ and $\dot{u}_l(r)Y_L$ are mutually orthogonal, in general each plane-wave couples to all functions in the spheres.

Due to the non-orthogonality of the basis functions the overlap matrix \mathbf{S} , defined by (4.1), is not a diagonal, but a hermitian matrix.

$$S^{\mathbf{G}\mathbf{G}'} = \int \varphi_{\mathbf{G}'}^*(\mathbf{r})\varphi_{\mathbf{G}}(\mathbf{r})d^3r \quad (4.1)$$

In (the more convenient) Dirac notation the eigenvalue problem has the following form.

$$\mathcal{H}|\phi_i\rangle = \epsilon_i|\phi_i\rangle \quad (4.2)$$

Where $|\phi_i\rangle$ denotes the eigenfunction corresponding to the i^{th} eigenvalue ϵ_i . Substituting the expansion of the eigenfunctions

$$|\phi_i\rangle = \sum_{\mathbf{G}} c_{i\mathbf{G}}|\varphi_{\mathbf{G}}\rangle \quad (4.3)$$

we obtain

$$\sum_{\mathbf{G}} c_{i\mathbf{G}}\mathcal{H}|\varphi_{\mathbf{G}}\rangle = \epsilon_i \sum_{\mathbf{G}} c_{i\mathbf{G}}|\varphi_{\mathbf{G}}\rangle \quad (4.4)$$

Multiplying this from the left with $\langle\varphi_{\mathbf{G}'}|$ we find

$$\sum_{\mathbf{G}} c_{i\mathbf{G}}\langle\varphi_{\mathbf{G}'}|\mathcal{H}|\varphi_{\mathbf{G}}\rangle = \epsilon_i \sum_{\mathbf{G}} c_{i\mathbf{G}}\langle\varphi_{\mathbf{G}'}|\varphi_{\mathbf{G}}\rangle \quad (4.5)$$

which can be written in matrix form

$$\{\mathbf{H} - \epsilon_i \mathbf{S}\} \mathbf{c}_i = 0 \quad (4.6)$$

where the eigenvector \mathbf{c}_i is the coefficient vector corresponding to the i^{th} eigenvalue. (4.6) is called a generalized eigenvalue problem.

However, this problem can be reduced to a standard eigenvalue problem using the Cholesky decomposition. It can be shown (e.g. Stoer [109]), that any hermitian and positive definite matrix can be decomposed into a matrix product of a lower triangular with only positive diagonal elements matrix and its transposed. Clearly, the overlap matrix satisfies these conditions and can be written

$$\mathbf{S} = \mathbf{L}\mathbf{L}^T \quad (4.7)$$

Therefore (4.6) becomes

$$\mathbf{H}\mathbf{c}_i = \epsilon_i \mathbf{L}\mathbf{L}^T \mathbf{c}_i \quad (4.8)$$

multiplying from the left with \mathbf{L}^{-1} and introducing a unit matrix we get

$$\mathbf{L}^{-1}\mathbf{H}(\mathbf{L}^{-1})^T \mathbf{L}^T \mathbf{c}_i = \epsilon_i \mathbf{L}^T \mathbf{c}_i \quad (4.9)$$

defining

$$\mathbf{P} = \mathbf{L}^{-1}\mathbf{H}(\mathbf{L}^{-1})^T, \quad \mathbf{x}_i = \mathbf{L}^T \mathbf{c}_i \quad (4.10)$$

we finally have

$$\mathbf{P}\mathbf{x}_i = \epsilon_i \mathbf{x}_i \quad (4.11)$$

Thus the generalized eigenvalue problem has been reduced to a simple eigenvalue problem. The eigenvectors \mathbf{c}_i can be obtained by the back-transformation

$$\mathbf{c}_i = (\mathbf{L}^T)^{-1} \mathbf{x}_i \quad (4.12)$$

4.1 Relativity in Valence Electron Calculations

Relativistic effects are important for the correct numerical description of core or valence electrons. Both core and valence electrons have finite wavefunctions near the nucleus, where the kinetic energy is large. This kinetic energy enhancement becomes more significant for heavier elements. Additionally, only relativistic effects, in particular the spin-orbit-coupling, introduce a link between spatial and spin coordinates. Thus, information about the orientation of spins relative to the lattice can only be gained if relativity is taken into account. For fully relativistic description of the electronic structure all relativistic effects (mass-velocity, Darwin-term, spin-orbit coupling) have to be taken into account. However, in many applications an approximation is used, where the spin-orbit interaction is neglected. This approximation is called the scalar relativistic approximation.

4.1.1 The Kohn-Sham-Dirac Equation

In the relativistic density functional theory the Kohn-Sham equation has the form of a single-particle Dirac equation:

$$\{c\boldsymbol{\alpha} \cdot \mathbf{p} + (\beta - 1)mc^2 + V^{eff}(\mathbf{r})\} \boldsymbol{\Psi} = E\boldsymbol{\Psi} \quad (4.13)$$

$$\boldsymbol{\alpha} = \left(\left(\begin{array}{cc} 0 & \sigma_x \\ \sigma_x & 0 \end{array} \right), \left(\begin{array}{cc} 0 & \sigma_y \\ \sigma_y & 0 \end{array} \right), \left(\begin{array}{cc} 0 & \sigma_z \\ \sigma_z & 0 \end{array} \right) \right)^{tr} = \left(\begin{array}{cc} 0 & \boldsymbol{\sigma} \\ \boldsymbol{\sigma} & 0 \end{array} \right) \quad (4.14)$$

$$\beta = \left(\begin{array}{cc} \mathbf{I}_2 & 0 \\ 0 & -\mathbf{I}_2 \end{array} \right) \quad (4.15)$$

Here, σ_x σ_y σ_z are the Pauli matrices and $\boldsymbol{\sigma}$ is the vector of Pauli matrices, \mathbf{p} is the momentum operator, and I_n denotes an $(n \times n)$ unit matrix. V^{eff} is the effective potential, that contains electron-nucleon Coulomb potential, Hartree potential and exchange-correlation potential. In the case of non-zero spin-polarization, V^{eff} becomes spin-dependent. Finally, $\boldsymbol{\Psi}$ is a relativistic four-component wavefunction.

The straightforward way to solve this problem would be to expand each of the four components of $\boldsymbol{\Psi}$ in terms of the FLAPW basis. However, if all four components were treated with the same accuracy, this would result in a basis set which contains four times as many functions as in the non-relativistic (non-magnetic) case. Since the numerical effort of the Hamiltonian diagonalization scales with the dimension of the matrix to the power of three, this would increase the computing time needed for the diagonalization by a factor of 64.

The FLAPW implementation we use introduces some approximations to make relativistic calculations more efficient. One of these approximations is the scalar relativistic approximation, which has been suggested by D.D. Koelling and B.N. Harmon [46], where the spin-orbit term is neglected, and spin and spatial coordinates become decoupled. Hence, the Hamiltonian matrix reduces to two matrices of half the size, which can be diagonalized separately. This saves a factor of four in computing time. The scalar relativistic approximation will be briefly discussed in the next section. It should be noted, that relativistic effects are only significant close to the nucleus, where the kinetic energy is large. It is therefore reasonable to treat the interstitial region and the vacuum non-relativistically. Thus, merely within the muffin-tins the electrons are treated relativistically. And only the large component of $\boldsymbol{\Psi}$ is matched to the non-relativistic wavefunctions at the boundary between the muffin-tins and the interstitial region, because the small component is already negligible at this distance from the nucleus. The small component is attached to the large component, and cannot be varied independently. However, this is a sensible approximation for two reasons: firstly, even inside the muffin-tin sphere the large component is still much bigger than the small component, and plays a more important role, and, secondly, the two components are determined by solving the scalar relativistic equations

for the spherically averaged potential. Therefore, they are very well suited to describe the wavefunctions.

4.1.2 The Scalar Relativistic Approximation

As it was already pointed out in the previous section, the electrons are only treated relativistically inside the muffin-tin spheres. Thus, the first problem that has to be addressed is the construction of the relativistic radial function. This is done by solving the scalar relativistic equation, including only the spherically averaged part of the potential. The starting point is the following Dirac equation:

$$\left\{ c\boldsymbol{\alpha} \cdot \mathbf{p} + (\beta - 1)mc^2 + V(r) \right\} \boldsymbol{\Psi} = E\boldsymbol{\Psi} \quad (4.16)$$

The solution of (4.16) is discussed in many textbooks, e.g. E.M. Rose [92]. Due to spin-orbit coupling m and m_s are not good quantum numbers any more, and they have to be replaced by the quantum numbers κ and μ (or j and μ), which are eigenvalues of the operators K and the z-component of the total angular momentum j_z (or the total angular momentum \mathbf{j} and j_z) respectively. K is defined by

$$K = \beta(\boldsymbol{\sigma} \cdot \mathbf{l} + 1) \quad (4.17)$$

The solutions of (4.16) have the form

$$\boldsymbol{\Psi} = \boldsymbol{\Psi}_{\kappa\mu} = \begin{pmatrix} g_{\kappa}(r)\chi_{\kappa\mu} \\ if_{\kappa}(r)\chi_{-\kappa\mu} \end{pmatrix} \quad (4.18)$$

Where $g_{\kappa}(r)$ is the large component, $f_{\kappa}(r)$ is the small component, $\chi_{\kappa\mu}$ and $\chi_{-\kappa\mu}$ are spin angular functions, which are eigenfunctions of \mathbf{j} , j_z , K and \mathbf{s}^2 with eigenvalues j , μ , κ ($-\kappa$) and $s = 1/2$ respectively. The spin angular functions can be expanded into a sum of products of spherical harmonics and Pauli spinors. Where the expansion coefficients are the Clebsch-Gordon coefficients. The radial functions have to satisfy the following set of coupled equations:

$$\frac{\partial}{\partial r}g_{\kappa}(r) = -\frac{\kappa + 1}{r}g_{\kappa}(r) + 2Mc f_{\kappa}(r) \quad (4.19)$$

$$\frac{\partial}{\partial r}f_{\kappa}(r) = \frac{1}{c}(V(r) - E)g_{\kappa}(r) + \frac{\kappa - 1}{r}f_{\kappa}(r) \quad (4.20)$$

with

$$M = m + \frac{1}{2c^2}(E - V(r)) \quad (4.21)$$

This can be written in matrix form.

$$\begin{pmatrix} -\frac{\kappa + 1}{r} - \frac{\partial}{\partial r} & 2Mc \\ \frac{1}{c}(V(r) - E) & \frac{\kappa - 1}{r} - \frac{\partial}{\partial r} \end{pmatrix} \begin{pmatrix} g_{\kappa}(r) \\ f_{\kappa}(r) \end{pmatrix} = 0 \quad (4.22)$$

To derive the scalar relativistic approximation D.D. Koelling and B.N. Harmon [46] introduce the following transformation.

$$\begin{pmatrix} g_\kappa(r) \\ \phi_\kappa(r) \end{pmatrix} = \begin{pmatrix} 1 & 0 \\ \frac{1}{2Mc} \frac{\kappa+1}{r} & 1 \end{pmatrix} \begin{pmatrix} g_\kappa(r) \\ f_\kappa(r) \end{pmatrix} \quad (4.23)$$

Using this transformation (4.22) becomes

$$\begin{pmatrix} -\frac{\partial}{\partial r} & 2Mc \\ \frac{1}{2Mc} \frac{\kappa(\kappa+1)}{r^2} + \frac{1}{c}(V(r) - E) - \frac{1}{2Mc} \frac{\kappa+1}{r} \left(\frac{\partial}{\partial r} - \frac{M'}{M} \right) & \frac{\kappa-1}{r} - \frac{\partial}{\partial r} \end{pmatrix} \begin{pmatrix} g_\kappa(r) \\ \phi_\kappa(r) \end{pmatrix} = 0 \quad (4.24)$$

Where M' denotes the derivative of M with respect to r ($\partial M/\partial r$). Recalling that κ is the eigenvalue of $K = \beta(\sigma \cdot \mathbf{l} + 1)$ the term $(\kappa+1)M'/2M^2cr$ can be identified as the spin-orbit term. This term is dropped in the scalar relativistic approximation, because it is the only one, that causes coupling of spin up and spin down contributions. For numerical reasons the functions $g_l(r)$ and $\phi_l(r)$ are replaced by $p(r) = rg_l(r)$ and $q(r) = cr\phi_l(r)$. Thus, equations (4.24) become:

$$\frac{\partial}{\partial r} p(r) = 2 \left(1 + \frac{1}{2c^2}(E - V(r)) \right) q(r) + \frac{p(r)}{r} \quad (4.25)$$

$$\frac{\partial}{\partial r} q(r) = \left(\frac{l(l+1)}{2 \left(1 + \frac{1}{2c^2}(E - V(r)) \right) r^2} + V(r) - E \right) p(r) - \frac{q(r)}{r} \quad (4.26)$$

$$\frac{\partial}{\partial r} \dot{p}(r) = 2 \left(\left(1 + \frac{1}{2c^2}(E - V(r)) \right) \dot{q}(r) + \frac{1}{2c^2} q(r) \right) + \frac{\dot{p}(r)}{r} \quad (4.27)$$

$$\begin{aligned} \frac{\partial}{\partial r} \dot{q}(r) &= \left(\frac{l(l+1)}{2 \left(1 + \frac{1}{2c^2}(E - V(r)) \right) r^2} + V(r) - E \right) \dot{p}(r) \\ &\quad - \left(\frac{l(l+1)}{4c^2 \left(1 + \frac{1}{2c^2}(E - V(r)) \right) r^2} + 1 \right) p(r) - \frac{\dot{q}(r)}{r} \end{aligned} \quad (4.28)$$

These formulas have been obtained using the definition of M (4.21), $\dot{M} = 1/2c^2$ and the fact that $m = 1$ in Hartree units. In our implementation of FLAPW the radial wavefunctions are normalized according to

$$\left\langle \begin{pmatrix} g_l \\ \phi_l \end{pmatrix} \middle| \begin{pmatrix} g_l \\ \phi_l \end{pmatrix} \right\rangle = \int_0^{R_{MT}} (g_l^2(r) + \phi_l^2(r)) r^2 dr = 1 \quad (4.29)$$

However, $g_l^2(r) + \phi_l^2(r)$ is not the charge density. The radial charge density is defined by

$$\rho_l(r) = \left\langle \left(\begin{array}{c} g_l \\ f_l \end{array} \right) \middle| \left(\begin{array}{c} g_l \\ f_l \end{array} \right) \right\rangle = \int_0^{R_{MT}} (g_l^2(r) + f_l^2(r)) r^2 dr \quad (4.30)$$

The energy derivatives of the radial functions have to be made orthogonal to the radial functions (comp. section 3.1.2).

$$\left\langle \left(\begin{array}{c} g_l \\ \phi_l \end{array} \right) \middle| \left(\begin{array}{c} \dot{g}_l \\ \dot{\phi}_l \end{array} \right) \right\rangle = 0 \quad (4.31)$$

Thus, the scalar relativistic FLAPW basis set is

$$\varphi_{\mathbf{G}_{\parallel} \mathbf{G}_{\perp}}(\mathbf{r}) = \begin{cases} e^{i\mathbf{G}_{\parallel} \mathbf{r}_{\parallel}} e^{i(G_z+k)z} & Int. \\ \sum_m \left(A_m^{\mathbf{G}}(k) u_m^{G_z}(k, r) + B_m^{\mathbf{G}}(k) \dot{u}_m^{G_z}(k, r) \right) & Vac. \\ \sum_{\alpha} A_{lm}^{\alpha \mathbf{G} k} \left(\begin{array}{c} g_l(r) \\ \phi_l(r) \end{array} \right) Y_{lm}(\hat{\mathbf{r}}) + B_{lm}^{\alpha \mathbf{G} k} \left(\begin{array}{c} \dot{g}_l(r) \\ \dot{\phi}_l(r) \end{array} \right) Y_{lm}(\hat{\mathbf{r}}) & MT \end{cases} \quad (4.32)$$

Note, that the Pauli-spinors have been omitted, since the spin up and down problems are solved independently within the scalar relativistic approximation. Rewriting (4.24)

$$\mathcal{H}_{SP} \left(\begin{array}{c} g_l(r) \\ \phi_l(r) \end{array} \right) = E \left(\begin{array}{c} g_l(r) \\ \phi_l(r) \end{array} \right) \quad (4.33)$$

with

$$\mathcal{H}_{SP} = \left(\begin{array}{cc} \frac{1}{2M} \frac{l(l+1)}{r^2} + V(r) & -\frac{2c}{r} - c \frac{\partial}{\partial r} \\ c \frac{\partial}{\partial r} & -2mc^2 + V(r) \end{array} \right), \quad (4.34)$$

a matrix expression for the scalar relativistic Hamiltonian including only the spherically averaged part of the potential can be obtained.

4.2 Construction of the Hamiltonian Matrix

The FLAPW Hamiltonian and overlap matrices consist of three contributions from the three regions of space.

$$\mathbf{H} = \mathbf{H}_I + \mathbf{H}_{MT} + \mathbf{H}_V \quad (4.35)$$

$$\mathbf{S} = \mathbf{S}_I + \mathbf{S}_{MT} + \mathbf{S}_V \quad (4.36)$$

All three contributions have to be computed separately.

4.2.1 Hamiltonian and Overlap Matrices in the Spheres

The contribution from the muffin-tins to the Hamiltonian matrix and the overlap matrix is given by the following expressions:

$$H_{MT}^{\mathbf{G}'\mathbf{G}}(k) = \sum_{\mu} \int_{MT\mu} \left(\sum_{L'} A_{L'}^{\mu\mathbf{G}'}(k) \varphi_{L'}^{\alpha}(\mathbf{r}) + B_{L'}^{\mu\mathbf{G}'}(k) \dot{\varphi}_{L'}^{\alpha}(\mathbf{r}) \right)^* \mathcal{H}_{MT\alpha} \left(\sum_L A_L^{\mu\mathbf{G}}(k) \varphi_L^{\alpha}(\mathbf{r}) + B_L^{\mu\mathbf{G}}(k) \dot{\varphi}_L^{\alpha}(\mathbf{r}) \right) d^3r \quad (4.37)$$

$$S_{MT}^{\mathbf{G}'\mathbf{G}}(k) = \sum_{\mu} \int_{MT\mu} \left(\sum_{L'} A_{L'}^{\mu\mathbf{G}'}(k) \varphi_{L'}^{\alpha}(\mathbf{r}) + B_{L'}^{\mu\mathbf{G}'}(k) \dot{\varphi}_{L'}^{\alpha}(\mathbf{r}) \right)^* \left(\sum_L A_L^{\mu\mathbf{G}}(k) \varphi_L^{\alpha}(\mathbf{r}) + B_L^{\mu\mathbf{G}}(k) \dot{\varphi}_L^{\alpha}(\mathbf{r}) \right) d^3r \quad (4.38)$$

with

$$\varphi_L^{\alpha}(\mathbf{r}) = \begin{pmatrix} g_l(r) \\ \phi_l(r) \end{pmatrix} Y_L(\hat{\mathbf{r}}), \quad Y_L(\hat{\mathbf{r}}), \quad \dot{\varphi}_L^{\alpha}(\mathbf{r}) = \begin{pmatrix} \dot{g}_l(r) \\ \dot{\phi}_l(r) \end{pmatrix} Y_L(\hat{\mathbf{r}}), \quad (4.39)$$

where we distinguish between the atom index μ and the atom type index $\alpha(\mu)$. If the symmetries for the system are included, then some atoms can be mapped onto each other by space-group operations. Clearly, the potential in these atoms has to be the same. As a consequence, the Hamiltonian and the basis functions $\varphi_L^{\alpha}(\mathbf{r})$ do not differ among the atoms of the same type. Due to this fact the muffin-tin potential of an atom type is only stored once for the representative atom, and the matrices (4.41)–(4.44) are also calculated for the representative only. $\mathcal{H}_{MT\alpha}$ is the scalar relativistic Hamiltonian operator. It can be split up into two parts: the spherical Hamiltonian \mathcal{H}_{sp} (4.34) and the non-spherical parts of the potential V_{ns} :

$$\mathcal{H}_{MT\alpha} = \mathcal{H}_{sp}^{\alpha} + V_{ns}^{\alpha} \quad (4.40)$$

The integrations above can be reduced to the summations, involving the following matrix coefficients:

$$t_{L'L}^{\alpha\varphi\varphi} = \int_{MT\alpha} \varphi_{L'}^{\alpha}(\mathbf{r}) \mathcal{H}_{MT\alpha} \varphi_L^{\alpha}(\mathbf{r}) d^3r \quad (4.41)$$

$$t_{L'L}^{\alpha\varphi\dot{\varphi}} = \int_{MT\alpha} \varphi_{L'}^{\alpha}(\mathbf{r}) \mathcal{H}_{MT\alpha} \dot{\varphi}_L^{\alpha}(\mathbf{r}) d^3r \quad (4.42)$$

$$t_{L'L}^{\alpha\dot{\varphi}\varphi} = \int_{MT\alpha} \dot{\varphi}_{L'}^{\alpha}(\mathbf{r}) \mathcal{H}_{MT\alpha} \varphi_L^{\alpha}(\mathbf{r}) d^3r \quad (4.43)$$

$$t_{L'L}^{\alpha\dot{\varphi}\dot{\varphi}} = \int_{MT\alpha} \dot{\varphi}_{L'}^{\alpha}(\mathbf{r}) \mathcal{H}_{MT\alpha} \dot{\varphi}_L^{\alpha}(\mathbf{r}) d^3r \quad (4.44)$$

These matrix elements do not depend on the $A_L^{\mu\mathbf{G}}(k)$ and $B_L^{\mu\mathbf{G}}(k)$ coefficients, therefore, they are independent of the Bloch vector and need to be calculated only once per iteration

in the beginning of the k -points cycle. The functions φ_L^α and $\dot{\varphi}_L^\alpha$ have been constructed to diagonalize the spherical part \mathcal{H}_{sp}^α of the muffin-tin Hamiltonian \mathcal{H}_{MT}^α :

$$\mathcal{H}_{sp}^\alpha \varphi_L^\alpha = E_l \varphi_L^\alpha \quad (4.45)$$

$$\mathcal{H}_{sp}^\alpha \dot{\varphi}_L^\alpha + \dot{\mathcal{H}}_{sp}^\alpha \varphi_L^\alpha = E_l \dot{\varphi}_L^\alpha + \varphi_L^\alpha \quad (4.46)$$

However, $\dot{\mathcal{H}}_{sp}^\alpha$ is smaller than \mathcal{H}_{sp}^α , by a factor of $1/c^2$ and can be neglected:

$$\mathcal{H}_{sp}^\alpha \dot{\varphi}_L^\alpha = E_l \dot{\varphi}_L^\alpha + \varphi_L^\alpha \quad (4.47)$$

Multiplying these equations with $\varphi_{L'}^\alpha(\mathbf{r})$ and $\dot{\varphi}_{L'}^\alpha(\mathbf{r})$, respectively, and integrating over the muffin-tins gives

$$\langle \varphi_{L'}^\alpha | \mathcal{H}_{sp}^\alpha | \varphi_L^\alpha \rangle_{MT} = \delta_{l'l'} \delta_{mm'} E_l \quad (4.48)$$

$$\langle \varphi_{L'}^\alpha | \mathcal{H}_{sp}^\alpha | \dot{\varphi}_L^\alpha \rangle_{MT} = \delta_{l'l'} \delta_{mm'} \quad (4.49)$$

$$\langle \dot{\varphi}_{L'}^\alpha | \mathcal{H}_{sp}^\alpha | \varphi_L^\alpha \rangle_{MT} = 0 \quad (4.50)$$

$$\langle \dot{\varphi}_{L'}^\alpha | \mathcal{H}_{sp}^\alpha | \dot{\varphi}_L^\alpha \rangle_{MT} = \delta_{l'l'} \delta_{mm'} E_l \langle \dot{\varphi}_L^\alpha | \dot{\varphi}_L^\alpha \rangle_{MT}, \quad (4.51)$$

where the normalization condition for φ_L^α has been used. So, only the contributions from the non-spherical part of the potential are left to be determined. Since the potential is also expanded into a product of radial functions and spherical harmonics

$$V^\alpha(\mathbf{r}) = \sum_{L''} V_{L''}^\alpha(r) Y_{L''}(\hat{\mathbf{r}}), \quad (4.52)$$

the corresponding t -integrals consist of product of a radial integrals and an angular integrals over three spherical harmonics, the so-called gaunt coefficients $G_{l'l''}^{m'mm''}$:

$$t_{L'L}^{\alpha\varphi\varphi} = \sum_{l''} I_{l'l''}^{\alpha\varphi\varphi} G_{l'l''}^{m'mm''} + \delta_{l'l'} \delta_{mm'} E_l \quad (4.53)$$

$$t_{L'L}^{\alpha\varphi\dot{\varphi}} = \sum_{l''} I_{l'l''}^{\alpha\varphi\dot{\varphi}} G_{l'l''}^{m'mm''} + \delta_{l'l'} \delta_{mm'} \quad (4.54)$$

$$t_{L'L}^{\alpha\dot{\varphi}\varphi} = \sum_{l''} I_{l'l''}^{\alpha\dot{\varphi}\varphi} G_{l'l''}^{m'mm''} \quad (4.55)$$

$$t_{L'L}^{\alpha\dot{\varphi}\dot{\varphi}} = \sum_{l''} I_{l'l''}^{\alpha\dot{\varphi}\dot{\varphi}} G_{l'l''}^{m'mm''} + \delta_{l'l'} \delta_{mm'} E_l \langle \dot{\varphi}_{lm}^\alpha | \dot{\varphi}_{lm}^\alpha \rangle_{MT} \quad (4.56)$$

with

$$I_{l'l''}^{\alpha\varphi\varphi} = \int (g_{l''}^\alpha(r) g_l^\alpha(r) + \phi_{l''}^\alpha(r) \phi_l^\alpha(r)) V_{l''}^\alpha(r) r^2 dr \quad (4.57)$$

$$I_{l'l''}^{\alpha\varphi\dot{\varphi}} = \int (g_{l''}^\alpha(r) \dot{g}_l^\alpha(r) + \phi_{l''}^\alpha(r) \dot{\phi}_l^\alpha(r)) V_{l''}^\alpha(r) r^2 dr \quad (4.58)$$

$$I_{l'l''}^{\alpha\dot{\varphi}\varphi} = \int (\dot{g}_{l''}^\alpha(r) g_l^\alpha(r) + \dot{\phi}_{l''}^\alpha(r) \phi_l^\alpha(r)) V_{l''}^\alpha(r) r^2 dr \quad (4.59)$$

$$I_{l'l''}^{\alpha\dot{\varphi}\dot{\varphi}} = \int (\dot{g}_{l''}^\alpha(r) \dot{g}_l^\alpha(r) + \dot{\phi}_{l''}^\alpha(r) \dot{\phi}_l^\alpha(r)) V_{l''}^\alpha(r) r^2 dr. \quad (4.60)$$

The gaunt coefficients are given by

$$G_{l'l''}^{mm'm''} = \int Y_{lm}^* Y_{l'm'} Y_{l''m''} d\Omega. \quad (4.61)$$

Finally, the Hamiltonian and overlap matrix elements become:

$$\begin{aligned} H_{MT}^{\mathbf{G}'\mathbf{G}}(k) &= \sum_{\mu} \sum_{L'L} (A_{L'}^{\mu\mathbf{G}'}(k))^* t_{L'L}^{\alpha\varphi\varphi} A_L^{\mu\mathbf{G}}(k) + (B_{L'}^{\mu\mathbf{G}'}(k))^* t_{L'L}^{\alpha\dot{\varphi}\dot{\varphi}} B_L^{\mu\mathbf{G}}(k) \\ &\quad + (A_{L'}^{\mu\mathbf{G}'}(k))^* t_{L'L}^{\alpha\varphi\dot{\varphi}} B_L^{\mu\mathbf{G}}(k) + (B_{L'}^{\mu\mathbf{G}'}(k))^* t_{L'L}^{\alpha\dot{\varphi}\varphi} A_L^{\mu\mathbf{G}}(k) \end{aligned} \quad (4.62)$$

$$S_{MT}^{\mathbf{G}'\mathbf{G}}(k) = \sum_{\mu} \sum_L (A_L^{\mu\mathbf{G}'}(k))^* A_L^{\mu\mathbf{G}}(k) + (B_L^{\mu\mathbf{G}'}(k))^* B_L^{\mu\mathbf{G}}(k) \langle \dot{\varphi}_L^{\alpha} | \dot{\varphi}_L^{\alpha} \rangle_{MT\mu}. \quad (4.63)$$

The Muffin-Tin A- and B-Coefficients

Any plane-wave can be expanded into spherical harmonics via the Rayleigh expansion:

$$e^{i\mathbf{K}\mathbf{r}} = 4\pi \sum_L i^l j_l(rK) Y_L^*(\hat{\mathbf{K}}) Y_L(\hat{\mathbf{r}}), \quad (4.64)$$

where $r = |\mathbf{r}|$, $K = |\mathbf{K}|$ and \mathbf{K} abbreviates $(\mathbf{G} + k)$. Looking from the local frame, \mathbf{K} and the position of the sphere \mathbf{p}^{μ} appear to be rotated, furthermore, the origin of the local frame is shifted. Therefore, the plane-wave has the following form in the local frame:

$$e^{i\mathbf{K}\mathbf{r}} = e^{i(\mathbf{R}^{\mu}\mathbf{K})(\mathbf{r} + \mathbf{R}^{\mu}\mathbf{p}^{\mu})} \quad (4.65)$$

Thus, the Rayleigh expansion of the plane-wave in the local frame is given by

$$e^{i\mathbf{K}\mathbf{r}} = e^{i\mathbf{K}\mathbf{p}^{\mu}} 4\pi \sum_L i^l j_l(rK) Y_L^*(\mathbf{R}^{\mu}\hat{\mathbf{K}}) Y_L(\hat{\mathbf{r}}) \quad (4.66)$$

The requirement of continuity of the wavefunctions at the sphere boundary leads to the equation:

$$\begin{aligned} \sum_L A_L^{\mu\mathbf{G}}(k) u_l(R_{MT\alpha}) Y_L(\hat{\mathbf{r}}) + B_L^{\mu\mathbf{G}}(k) \dot{u}_l(R_{MT\alpha}) Y_L(\hat{\mathbf{r}}) \\ = e^{i\mathbf{K}\mathbf{p}^{\mu}} 4\pi \sum_L i^l j_l(rK) Y_L^*(\mathbf{R}^{\mu}\hat{\mathbf{K}}) Y_L(\hat{\mathbf{r}}), \end{aligned} \quad (4.67)$$

where $R_{MT\alpha}$ is the muffin-tin radius of for the atom type α . The second requirement is that the derivative with respect to r , denoted by $\partial/\partial r = '$, is also continuous:

$$\begin{aligned} \sum_L A_L^{\mu\mathbf{G}}(k) u_l'(R_{MT\alpha}) Y_L(\hat{\mathbf{r}}) + B_L^{\mu\mathbf{G}}(k) \dot{u}_l'(R_{MT\alpha}) Y_L(\hat{\mathbf{r}}) \\ = e^{i\mathbf{K}\mathbf{p}^{\mu}} 4\pi \sum_L i^l K j_l'(rK) Y_L^*(\mathbf{R}^{\mu}\hat{\mathbf{K}}) Y_L(\hat{\mathbf{r}}). \end{aligned} \quad (4.68)$$

These conditions can only be satisfied if the coefficients of each spherical harmonic $Y_L(\hat{\mathbf{r}})$ are equal. Solving the resulting equations for $A_L^{\mu\mathbf{G}}(k)$ and $B_L^{\mu\mathbf{G}}(k)$ yields:

$$\begin{aligned} A_L^{\mu\mathbf{G}}(k) &= e^{i\mathbf{K}\mathbf{p}^\mu} 4\pi \frac{1}{W} i^l Y_L^*(\mathbf{R}^\mu \hat{\mathbf{K}}) \cdot [\dot{u}_l(R_{MT^\alpha}) K j_l'(R_{MT^\alpha} K) - \dot{u}_l'(R_{MT^\alpha}) j_l(R_{MT^\alpha} K)] \\ B_L^{\mu\mathbf{G}}(k) &= e^{i\mathbf{K}\mathbf{p}^\mu} 4\pi \frac{1}{W} i^l Y_L^*(\mathbf{R}^\mu \hat{\mathbf{K}}) \cdot [u_l'(R_{MT^\alpha}) j_l(R_{MT^\alpha} K) - u_l(R_{MT^\alpha}) K j_l'(R_{MT^\alpha} K)], \end{aligned} \quad (4.69)$$

where the Wronskian W is given by:

$$W = [\dot{u}_l(R_{MT^\alpha}) u_l'(R_{MT^\alpha}) - u_l(R_{MT^\alpha}) \dot{u}_l'(R_{MT^\alpha})]. \quad (4.70)$$

Note, that for calculating the diagonal part of the Hamiltonian and overlap matrix, the following representation of the coefficients can be used:

$$A_L^{\mu\mathbf{G}}(k) = C_{lm}^{\mu\mathbf{G}}(k) a_l^{\mu\mathbf{G}}(k), \quad B_L^{\mu\mathbf{G}}(k) = C_{lm}^{\mu\mathbf{G}}(k) b_l^{\mu\mathbf{G}}(k),$$

where a - and b -coefficients depend only on the l -index, but not on m . In the case of $l = l'$ (diagonal case) the sum over m in (4.63) can be rewritten in terms of Legendre polynomials:

$$\begin{aligned} \sum_{m,m'} C_{lm}^{\mu\mathbf{G}}(k) C_{lm'}^{\mu\mathbf{G}'}(k) &\sim e^{i(\mathbf{G}-\mathbf{G}')\tau_\mu} \sum_{m,m'} Y_{lm}(\mathbf{R}^\mu \hat{\mathbf{K}}) Y_{lm'}^*(\mathbf{R}^\mu \hat{\mathbf{K}}') = \\ &= (2l+1) e^{i(\mathbf{G}-\mathbf{G}')\tau_\alpha} P_l\left(\frac{\mathbf{G}\mathbf{G}'}{GG'}\right). \end{aligned}$$

Using the last derived equation in calculating the diagonal elements of the Hamiltonian and overlap matrices allows to achieve a significant speed-up.

4.2.2 Inversion Symmetry

Transformation of the FLAPW Basis Functions in Systems That Possess Inversion Symmetry

Plane-waves transform in a very simple way under the operation $\mathbf{r} \rightarrow -\mathbf{r}$. Let \mathcal{I} be the inversion operator:

$$\mathcal{I} e^{i\mathbf{K}\mathbf{r}} = e^{-i\mathbf{K}\mathbf{r}} = \left(e^{i\mathbf{K}\mathbf{r}} \right)^*. \quad (4.71)$$

Then if the system possesses an inversion symmetry, the FLAPW basis functions preserve it, i.e. $\varphi_{\mathbf{G}}(k, -\mathbf{r}) = \varphi_{\mathbf{G}}^*(k, \mathbf{r})$. This is due to the fact, that if there is an atom at the position $-\mathbf{p}^\mu$, it follows, that there must be an equivalent atom at the position \mathbf{p}^μ . The value of the basis function $\varphi_{\mathbf{G}}(k, \mathbf{r})$ inside the muffin-tin μ is given by:

$$\varphi_{\mathbf{G}}(k, \mathbf{r}) = \sum_L A_L^{\mu\mathbf{G}}(k) u_l(r) Y_L(\hat{\mathbf{r}}) + B_L^{\mu\mathbf{G}}(k) \dot{u}_l(r) Y_L(\hat{\mathbf{r}}). \quad (4.72)$$

The vector $-\mathbf{r}$ lies in the opposite muffin-tin at the position $-\mathbf{p}^\mu$. Let's denote this atom by $-\mu$. Thus, we find:

$$\varphi_{\mathbf{G}}(k, -\mathbf{r}) = \sum_L A_L^{-\mu\mathbf{G}}(k) u_l(r) Y_L(\hat{\mathbf{r}}) + B_L^{-\mu\mathbf{G}}(k) \dot{u}_l(r) Y_L(\hat{\mathbf{r}}). \quad (4.73)$$

The argument of the spherical harmonic is $\hat{\mathbf{r}}$ rather than $-\hat{\mathbf{r}}$, because the vector is expanded in the local frame of the atom $-\mu$. Substituting the explicit form of $A_L^{-\mu\mathbf{G}}(k)$ and $B_L^{-\mu\mathbf{G}}(k)$ from (4.69) yields:

$$\varphi_{\mathbf{G}}(k, -\mathbf{r}) = \sum_L e^{i\mathbf{K}(-\mathbf{p}^\mu)} i^l Y_L^*(-\mathbf{R}^\mu \hat{\mathbf{K}}) Y_L(\hat{\mathbf{r}}) \{A u_l(r) + B \dot{u}_l(r)\}, \quad (4.74)$$

where it was used, that $\mathbf{p}^{-\mu} = -\mathbf{p}^\mu$ and $\mathbf{R}^{-\mu} = -\mathbf{R}^\mu$. A and B abbreviate all terms in (4.69) that are real and do not depend on r or $\hat{\mathbf{r}}$. Using the fact that $Y_L(\hat{\mathbf{r}}) = (-1)^l Y_L(\hat{\mathbf{r}})$ (4.74) becomes:

$$\varphi_{\mathbf{G}}(k, -\mathbf{r}) = \sum_L e^{-i\mathbf{K}(\mathbf{p}^\mu)} (-i)^l Y_L^*(\mathbf{R}^\mu \hat{\mathbf{K}}) Y_L(\hat{\mathbf{r}}) \{A u_l(r) + B \dot{u}_l(r)\}. \quad (4.75)$$

In the last step it can be exploited that $Y_{l-m}(\hat{\mathbf{r}}) = (-1)^m Y_{lm}^*(\hat{\mathbf{r}})$. Substituting $m' = -m$, (4.75) becomes:

$$\varphi_{\mathbf{G}}(k, -\mathbf{r}) = \sum_{lm'} e^{-i\mathbf{K}(\mathbf{p}^\mu)} (-i)^l Y_{lm'}(\mathbf{R}^\mu \hat{\mathbf{K}}) Y_{lm'}^*(\hat{\mathbf{r}}) \{A u_l(r) + B \dot{u}_l(r)\}. \quad (4.76)$$

Hence, we have shown that the FLAPW basis functions transform according to

$$\varphi_{\mathbf{G}}(k, -\mathbf{r}) = \varphi_{\mathbf{G}}^*(k, \mathbf{r}) \quad (4.77)$$

in the interstitial region and the muffin-tins, if the system possesses inversion symmetry

The Hamiltonian Matrix of Systems with Inversion Symmetry

The property of the FLAPW basis functions derived in the previous section causes simplifications of the Hamiltonian and overlap matrices. In systems that possess inversion symmetry these two matrices are real symmetric rather than complex hermitian. The Hamiltonian depends explicitly on \mathbf{r} via the potential. The matrix elements are given by:

$$H^{\mathbf{G}'\mathbf{G}}(k) = \int \varphi_{\mathbf{G}'}^*(k, \mathbf{r}) \mathcal{H}(\mathbf{r}) \varphi_{\mathbf{G}}(k, \mathbf{r}) d^3r \quad (4.78)$$

Substituting $\mathbf{r}' = -\mathbf{r}$ yields:

$$H^{\mathbf{G}'\mathbf{G}}(k) = \int \varphi_{\mathbf{G}'}(k, \mathbf{r}') \mathcal{H}(\mathbf{r}') \varphi_{\mathbf{G}}^*(k, \mathbf{r}') d^3r, \quad (4.79)$$

where (4.77) and $\mathcal{H}(\mathbf{r}) = \mathcal{H}(-\mathbf{r})$ have been used. In addition the Hamiltonian operator is real, i.e. $\mathcal{H}(\mathbf{r}) = \mathcal{H}^*(\mathbf{r})$. Thus, we finally obtain:

$$H^{\mathbf{G}'\mathbf{G}}(k) = \int \varphi_{\mathbf{G}'}(k, \mathbf{r}') \mathcal{H}^*(\mathbf{r}') \varphi_{\mathbf{G}}^*(k, \mathbf{r}') d^3r = \left(H^{\mathbf{G}'\mathbf{G}}(k) \right)^* \quad (4.80)$$

Apparently, the same relation holds for the overlap matrix. The fact, that the two matrices are real means a great simplification in actual calculation. In principle, the diagonalization of a hermitian matrix is no more difficult than in the real case. However, one complex multiplication contains four real multiplication, and therefore the complex problem is far more “expensive” than the real one, and the diagonalization needs the biggest part of the computer-time in each iteration.

4.2.3 Hamiltonian and Overlap Matrices in the Interstitial

The interstitial contributions to the Hamiltonian and overlap matrix have the following form:

$$H_I^{\mathbf{G}\mathbf{G}'}(k) = \frac{1}{\Omega} \int_I e^{-i(\mathbf{G}+k)\mathbf{r}} \left(-\frac{\hbar^2}{2m} \Delta + V(\mathbf{r}) \right) e^{i(\mathbf{G}'+k)\mathbf{r}} d^3r, \quad (4.81)$$

$$S_I^{\mathbf{G}\mathbf{G}'} = \frac{1}{\Omega} \int_I e^{-i(\mathbf{G}+k)\mathbf{r}} e^{i(\mathbf{G}'+k)\mathbf{r}} d^3r. \quad (4.82)$$

The potential is also expanded into plane-waves in the interstitial region:

$$V(\mathbf{r}) = \sum_{\mathbf{G}} V_{\mathbf{G}} e^{i\mathbf{G}\mathbf{r}} \quad (4.83)$$

Without the existence of the muffin-tin spheres and the vacuum region, the integration of the plane-waves would stretch over the entire unit cell, resulting in a simple summation. The kinetic energy part is diagonal in momentum space and the potential part of the Hamiltonian is local and diagonal in real space and of convolution form in momentum space:

$$H_I^{\mathbf{G}\mathbf{G}'}(k) = \frac{\hbar^2}{2m} |\mathbf{G} + k|^2 \delta_{\mathbf{G}\mathbf{G}'} + V_{(\mathbf{G}-\mathbf{G}')} \\ S_I^{\mathbf{G}\mathbf{G}'} = \delta_{\mathbf{G}\mathbf{G}'}$$

However, these matrix elements are not as straightforward to calculate as they appear at first glance, due to the complicated structure of the interstitial region. The integrations have to be performed only in between the muffin-tins. Therefore, a step function $\Theta(\mathbf{r})$ has to be introduced, which cuts out the muffin-tins.

$$\Theta(\mathbf{r}) = \begin{cases} 1 & \text{interstitial region} \\ 0 & \text{muffin-tins} \\ 0 & \text{vacuum region} \end{cases} \quad (4.84)$$

Using this step function, the matrix elements can be rewritten:

$$H_I^{\mathbf{G}\mathbf{G}'}(k) = \frac{1}{\Omega} \int_{\text{cell}} e^{-i(\mathbf{G}-\mathbf{G}')\mathbf{r}} V(\mathbf{r}) \Theta(\mathbf{r}) d^3r$$

$$+\frac{1}{2}(\mathbf{G}' + k)^2 \frac{1}{\Omega} \int_{cell} e^{-i(\mathbf{G}-\mathbf{G}')\mathbf{r}} \Theta(\mathbf{r}) d^3r, \quad (4.85)$$

$$S_I^{\mathbf{G}\mathbf{G}'} = \frac{1}{\Omega} \int_{cell} e^{-i(\mathbf{G}-\mathbf{G}')\mathbf{r}} \Theta(\mathbf{r}) d^3r$$

In momentum space (4.85) becomes:

$$H_I^{\mathbf{G}\mathbf{G}'}(k) = (V\Theta)_{(\mathbf{G}-\mathbf{G}')} + \frac{\hbar^2}{2m}(\mathbf{G}' + k)^2 \Theta_{(\mathbf{G}-\mathbf{G}')} \quad (4.86)$$

$$S_I^{\mathbf{G}\mathbf{G}'} = \Theta_{(\mathbf{G}-\mathbf{G}')} \quad (4.87)$$

where $\Theta_{\mathbf{G}}$ and $(V\Theta)_{\mathbf{G}}$ are the Fourier coefficients of $\Theta(\mathbf{r})$ and $V(\mathbf{r})\Theta(\mathbf{r})$, respectively. Apparently, these coefficients are needed up to a cut-off of $2G_{max}$. The step function can be Fourier transformed analytically. In order to find the Fourier coefficients of the step function we will represent it in the following way:

$$\Theta(\mathbf{r}) = \Theta_{cyl}(\mathbf{r}) + \Theta_{bulk}(\mathbf{r}) - 1,$$

$$\Theta(\mathbf{G}) = \Theta_{cyl}(\mathbf{G}) + \Theta_{bulk}(\mathbf{G}) - \delta_{\mathbf{G},0}$$

where Θ_{cyl} is a function which is equal to zero outside the cylinder and equal to one inside the cylinder, accommodating the muffin-tins and interstitial, $\Theta_{bulk}(\mathbf{r})$ is a step function which is zero in the MT region, and one everywhere else, with the known Fourier components ([56]):

$$\Theta_{bulk}(\mathbf{G}) = \delta_{\mathbf{G},0} - \sum_{\alpha} e^{-i\mathbf{G}\tau_{\alpha}} \frac{4\pi R_{MT,\alpha}^3}{\Omega} \frac{j_1(GR_{MT,\alpha})}{GR_{MT,\alpha}} \quad (4.88)$$

The Fourier coefficients of the cylindrical step function can be found as follows:

$$\begin{aligned} \Theta_{cyl}(\mathbf{G}) &= \frac{1}{\Omega} \int_{\Omega} e^{i\mathbf{G}\mathbf{r}} \Theta_{cyl}(\mathbf{r}) d^3r = \frac{1}{\Omega} \int_{circle} e^{i\mathbf{G}_{\parallel}\mathbf{r}} d^2r \int_z e^{iG_z z} dz \\ &= \frac{T\delta_{G_z,0}}{\Omega} \int_0^{2\pi} \int_0^R r e^{iG_{\parallel}r \cos(\varphi-\varphi_{\mathbf{G}})} dr d\varphi \\ &= \frac{T\delta_{G_z,0}}{\Omega} \sum_m i^m \int_0^{2\pi} \int_0^R e^{im(\varphi-\varphi_{\mathbf{G}})} J_m(G_{\parallel}r) dr d\varphi = \frac{2\pi T\delta_{G_z,0}}{\Omega} \int_0^R r J_0(G_{\parallel}r) dr \end{aligned}$$

Using the relation $\int_0^a x J_0(x) dx = a J_1(a)$, we finally have:

$$\Theta_{cyl}(\mathbf{G}) = \frac{2\pi T R^2 \delta_{G_z,0}}{\Omega} \frac{J_1(G_{\parallel}R)}{G_{\parallel}R} = \frac{2\Omega}{\tilde{\Omega}} \frac{J_1(G_{\parallel}R)}{G_{\parallel}R} \delta_{G_z,0}. \quad (4.89)$$

The Fourier transform of the product of $V(\mathbf{r})$ and $\Theta(\mathbf{r})$ is given by a convolution in momentum space:

$$(V\Theta)_{\mathbf{G}} = \sum_{\mathbf{G}'} V_{\mathbf{G}'} \Theta_{(\mathbf{G}-\mathbf{G}')}$$

This convolution depends on both \mathbf{G} and \mathbf{G}' , therefore the numerical effort increases like $(G_{max})^6$. However, $(V\Theta)_{\mathbf{G}}$ can be determined more efficiently, using Fast Fourier Transform (FFT). Using this scheme the numerical effort scales like $(G_{max})^3 \ln((G_{max})^3)$ with G_{max} .

4.2.4 Hamiltonian and Overlap Matrices in the Vacuum

In this section we will consider the contributions to the Hamiltonian and overlap matrices coming from the vacuum region. First, we will remind the expressions for the basis function, corresponding to a certain reciprocal vector \mathbf{G} , in the vacuum and interstitial regions. In the interstitial region the basis function is a usual plane-wave:

$$\varphi_{\mathbf{G}}(k, \mathbf{r}) = e^{i(\mathbf{G}+k)\mathbf{r}}, \quad (4.90)$$

while in the vacuum the basis function reflects the cylindrical geometry, and, written in cylindrical coordinates, looks like:

$$\varphi_{\mathbf{G}}(k; r, \varphi, z) = e^{i(k+G_z)z} \sum_m e^{im\varphi} \left(A_m^{\mathbf{G}}(k) u_{G_z, m}(k, r) + B_m^{\mathbf{G}}(k) \dot{u}_{G_z, m}(k, r) \right), \quad (4.91)$$

where the summation over m goes up to a parameter m_{max} . The coefficients A and B are defined from the condition of continuity of the basis function and its first radial derivative at the interstitial-vacuum boundary. To find these coefficients we exploit the expression for the plane-wave in cylindrical coordinates:

$$\varphi_{\mathbf{G}}(k, \mathbf{r}) = e^{i(k+G_z)z} \sum_m i^m e^{im(\varphi-\varphi_{\mathbf{G}\parallel})} J_m(G_r r), \quad (4.92)$$

where J_m is a cylindrical Bessel function of the order m and the in-plane part of the reciprocal vector is written in polar coordinates $\mathbf{G} = (G_r, \varphi_{\mathbf{G}\parallel})$. After using the continuity conditions, discussed above, we come to the following equations for the coefficients A and B :

$$\begin{aligned} i^m \cdot e^{-im\varphi_{\mathbf{G}\parallel}} J_m(G_r R_{vac}) &= A_m^{\mathbf{G}}(k) \cdot u_{G_z, m}(k, R_{vac}) + B_m^{\mathbf{G}}(k) \cdot \dot{u}_{G_z, m}(k, R_{vac}), \\ i^m \cdot e^{-im\varphi_{\mathbf{G}\parallel}} G_r J'_m(G_r R_{vac}) &= A_m^{\mathbf{G}}(k) \cdot u'_{G_z, m}(k, R_{vac}) + B_m^{\mathbf{G}}(k) \cdot \dot{u}'_{G_z, m}(k, R_{vac}). \end{aligned} \quad (4.93)$$

Directly from this system we write down the coefficients:

$$A_m^{\mathbf{G}}(k) = i^m e^{-im\varphi_{\mathbf{G}\parallel}} \frac{\dot{u}'_{G_z, m}(k, R_{vac}) J_m(G_r R_{vac}) - \dot{u}_{G_z, m}(k, R_{vac}) G_r J'_m(G_r R_{vac})}{u_{G_z, m}(k, R) \dot{u}'_{G_z, m}(k, R_{vac}) - \dot{u}_{G_z, m}(k, R_{vac}) u'_{G_z, m}(k, R_{vac})} \quad (4.94)$$

$$B_m^{\mathbf{G}}(k) = i^m e^{-im\varphi_{\mathbf{G}\parallel}} \frac{u_{G_z,m}(k, R_{\text{vac}}) G_r J'_m(G_r R_{\text{vac}}) - u'_{G_z,m}(k, R_{\text{vac}}) J_m(G_r R_{\text{vac}})}{u_{G_z,m}(k, R_{\text{vac}}) \dot{u}'_{G_z,m}(k, R_{\text{vac}}) - \dot{u}_{G_z,m}(k, R_{\text{vac}}) u'_{G_z,m}(k, R_{\text{vac}})} \quad (4.95)$$

The vacuum radial basis functions $u_{G_z,m}(k, r)$ and their energy derivatives $\dot{u}_{G_z,m}(k, r)$, solve certain type of Schrödinger-like equation in the vacuum:

$$\left(-\frac{1}{2} \frac{d^2}{dr^2} - \frac{1}{2r} \frac{d}{dr} + \frac{(k + G_z)^2}{2} + \frac{m^2}{2r^2} + V_0(r) - E_v \right) u_{G_z,m}(k, r) = 0, \quad (4.96)$$

$$\left(-\frac{1}{2} \frac{d^2}{dr^2} - \frac{1}{2r} \frac{d}{dr} + \frac{(k + G_z)^2}{2} + \frac{m^2}{2r^2} + V_0(r) - E_v \right) \dot{u}_{G_z,m}(k, r) = u_{G_z,m}(k, r), \quad (4.97)$$

where only the cylindrically symmetrical part $V_0(r)$ of the potential enters, and E_v is the vacuum energy parameter, optimally defined for every iteration. The relativistic effects on the basis functions can be safely ignored, since the vacuum potential is rather flat. The solutions of the equations (4.96)–(4.97) are found with the assumptions that the radial functions decay to zero on infinity, and the following orthogonality conditions are fulfilled:

$$\int_{R_{\text{vac}}}^{\infty} r u_{G_z,m}^2(k, r) dr = 1, \quad (4.98)$$

$$\int_{R_{\text{vac}}}^{\infty} r u_{G_z,m}(k, r) \dot{u}_{G_z,m}(k, r) dr = 0. \quad (4.99)$$

Technically, the equations for the vacuum radial basis functions are more easy to find numerically using the radial solutions of the following equations:

$$\begin{aligned} \left(-\frac{1}{2} \frac{d^2}{dr^2} + \frac{(G_z + k)^2}{2} + \tilde{V}_m(r) - E_v \right) v_{G_z,m}(k, r) &= 0, \\ \left(-\frac{1}{2} \frac{d^2}{dr^2} + \frac{(G_z + k)^2}{2} + \tilde{V}_m(r) - E_v \right) \dot{v}_{G_z,m}(k, r) &= v_{G_z,m}(k, r), \end{aligned} \quad (4.100)$$

with the boundary conditions

$$\int_{R_{\text{vac}}}^{\infty} v_{G_z,m}^2(k, r) dr = 1, \quad \int_{R_{\text{vac}}}^{\infty} v_{G_z,m}(k, r) \dot{v}_{G_z,m}(k, r) dr = 0. \quad (4.101)$$

In equation (4.100) the potential $\tilde{V}_m(r)$ is an m -dependent reconstructed potential $V_0(r)$:

$$\tilde{V}_m(r) = \frac{m^2}{2r^2} + V_0(r) - \frac{1}{8r^2}. \quad (4.102)$$

The equations (4.100) are more easy to solve, moreover, the needed radial basis functions u and \dot{u} can be directly written as:

$$u_{G_z,m}(k, r) = \frac{v_{G_z,m}(k, r)}{\sqrt{r}}, \quad \dot{u}_{G_z,m}(k, r) = \frac{\dot{v}_{G_z,m}(k, r)}{\sqrt{r}}. \quad (4.103)$$

After generating the radial basis functions and A and B coefficients, the overlap and Hamiltonian matrices are constructed by the following expressions:

$$S_V^{\mathbf{G}'\mathbf{G}}(k) = \sum_{m',m} \int_V e^{-i(k+G'_z)z} e^{-im'\varphi} \left(A_{m'}^{\mathbf{G}'}(k) u_{G'_z,m'}(k,r) + B_{m'}^{\mathbf{G}'}(k) \dot{u}_{G'_z,m'}(k,r) \right)^* \cdot e^{i(k+G_z)z} e^{im\varphi} \left(A_m^{\mathbf{G}}(k) u_{m,G_z}(k,r) + B_m^{\mathbf{G}}(k) \dot{u}_{m,G_z}(k,r) \right) d^3r \quad (4.104)$$

$$H_V^{\mathbf{G}'\mathbf{G}}(k) = \sum_{m',m} \int_V e^{-i(k+G'_z)z} e^{-im'\varphi} \left(A_{m'}^{\mathbf{G}'}(k) u_{G'_z,m'}(k,r) + B_{m'}^{\mathbf{G}'}(k) \dot{u}_{G'_z,m'}(k,r) \right)^* \cdot H_V \cdot e^{i(k+G_z)z} e^{im\varphi} \left(A_m^{\mathbf{G}}(k) u_{m,G_z}(k,r) + B_m^{\mathbf{G}}(k) \dot{u}_{m,G_z}(k,r) \right) d^3r \quad (4.105)$$

The overlap matrix can be further rewritten in an easier way:

$$S_V^{\mathbf{G}'\mathbf{G}}(k) = \sum_m \left(\left(A_m^{\mathbf{G}'}(k) \right)^* A_m^{\mathbf{G}}(k) \delta_{G'_z,G_z} + \left(B_m^{\mathbf{G}'}(k) \right)^* B_m^{\mathbf{G}}(k) \delta_{G'_z,G_z} \langle \dot{u}_{G'_z,m'}(k) | \dot{u}_{G_z,m}(k) \rangle \right), \quad (4.106)$$

while the Hamiltonian matrix, in analogy to the spheres, can be rewritten in terms of the t -matrix:

$$H_V^{\mathbf{G}'\mathbf{G}}(k) = \sum_{m',m} \left(A_{m'}^{\mathbf{G}'}(k) \right)^* A_m^{\mathbf{G}}(k) t_{G_z,G'_z}^{uu,mm'}(k) + \left(A_{m'}^{\mathbf{G}'}(k) \right)^* B_m^{\mathbf{G}}(k) t_{G_z,G'_z}^{u\dot{u},mm'}(k) + \left(B_{m'}^{\mathbf{G}'}(k) \right)^* A_m^{\mathbf{G}}(k) t_{G_z,G'_z}^{\dot{u}u,mm'}(k) + \left(B_{m'}^{\mathbf{G}'}(k) \right)^* B_m^{\mathbf{G}}(k) t_{G_z,G'_z}^{\dot{u}\dot{u},mm'}(k), \quad (4.107)$$

where elements of the t -matrix are:

$$\begin{aligned} t_{G_z,G'_z}^{uu,mm'}(k) &= \langle \phi_{G'_z,m'}(k) | H_V | \phi_{G_z,m}(k) \rangle, \\ t_{G_z,G'_z}^{\dot{u}u,mm'}(k) &= \langle \dot{\phi}_{G'_z,m'}(k) | H_V | \phi_{G_z,m}(k) \rangle, \\ t_{G_z,G'_z}^{u\dot{u},mm'}(k) &= \langle \phi_{G'_z,m'}(k) | H_V | \dot{\phi}_{G_z,m}(k) \rangle, \\ t_{G_z,G'_z}^{\dot{u}\dot{u},mm'}(k) &= \langle \dot{\phi}_{G'_z,m'}(k) | H_V | \dot{\phi}_{G_z,m}(k) \rangle, \end{aligned} \quad (4.108)$$

and

$$\phi_{G_z,m}(k, \mathbf{r}) = e^{iG_z z} e^{im\varphi} u_{m,G_z}(k, r), \quad \dot{\phi}_{G_z,m}(k, \mathbf{r}) = e^{iG_z z} e^{im\varphi} \dot{u}_{m,G_z}(k, r). \quad (4.109)$$

We split the Hamiltonian into corrugated and non-corrugated parts:

$$H_V(\mathbf{r}) = H_{nc}(\mathbf{r}) + V_{co}(\mathbf{r}), \quad (4.110)$$

where $V_{co}(\mathbf{r})$ is a corrugated part of the potential:

$$V_{co}(\mathbf{r}) = \sum_{m'', G''_z} e^{im''\varphi} e^{iG''_z z} V_{m'', G''_z}(r), \quad (m'')^2 + (G''_z)^2 \neq 0. \quad (4.111)$$

Using the following relations

$$\begin{aligned} H_{nc}\phi_{G_z, m} &= E_m\phi_{G_z, m}, \\ H_{nc}\dot{\phi}_{G_z, m} &= E_m\dot{\phi}_{G_z, m} + \phi_{G_z, m}, \\ \langle \phi_{G'_z, m'} | H_{nc} | \phi_{G_z, m} \rangle &= \delta_{m, m'} \delta_{G_z, G'_z} E_m, \\ \langle \phi_{G'_z, m'} | H_{nc} | \dot{\phi}_{G_z, m} \rangle &= 2\pi \delta_{m, m'} \delta_{G_z, G'_z}, \\ \langle \dot{\phi}_{G'_z, m'} | H_{nc} | \phi_{G_z, m} \rangle &= 0, \\ \langle \dot{\phi}_{G'_z, m'} | H_{nc} | \dot{\phi}_{G_z, m} \rangle &= \delta_{m, m'} \delta_{G_z, G'_z} E_m \langle \dot{\phi}_{G'_z, m'} | \dot{\phi}_{G_z, m} \rangle_V, \end{aligned} \quad (4.112)$$

we can obtain for the elements of the t -matrix:

$$\begin{aligned} t_{G_z, G'_z}^{uu, mm'}(k) &= I_{G_z, G'_z, G'_z - G_z}^{uu, mm'}(k) + \delta_{m, m'} \delta_{G_z, G'_z} E_m \\ t_{G_z, G'_z}^{u\dot{u}, mm'}(k) &= I_{G_z, G'_z, G'_z - G_z}^{u\dot{u}, mm'}(k) + \delta_{m, m'} \delta_{G_z, G'_z} \\ t_{G_z, G'_z}^{\dot{u}u, mm'}(k) &= I_{G_z, G'_z, G'_z - G_z}^{\dot{u}u, mm'}(k) \\ t_{G_z, G'_z}^{\dot{u}\dot{u}, mm'}(k) &= I_{G_z, G'_z, G'_z - G_z}^{\dot{u}\dot{u}, mm'}(k) + \delta_{m, m'} \delta_{G_z, G'_z} E_m \langle \dot{u}_{G'_z, m'} | \dot{u}_{G_z, m} \rangle_V \end{aligned} \quad (4.113)$$

where

$$\begin{aligned} I_{G_z, G'_z, G''_z}^{uu, mm'm''}(k) &= \int_{R_V}^{\infty} r u_{G_z, m}(k, r) u_{G'_z, m'}(k, r) V_{m'', G''_z}(r) dr, \\ I_{G_z, G'_z, G''_z}^{\dot{u}u, mm'm''}(k) &= \int_{R_V}^{\infty} r \dot{u}_{G_z, m}(k, r) u_{G'_z, m'}(k, r) V_{m'', G''_z}(r) dr, \\ I_{G_z, G'_z, G''_z}^{u\dot{u}, mm'm''}(k) &= \int_{R_V}^{\infty} r u_{G_z, m}(k, r) \dot{u}_{G'_z, m'}(k, r) V_{m'', G''_z}(r) dr, \\ I_{G_z, G'_z, G''_z}^{\dot{u}\dot{u}, mm'm''}(k) &= \int_{R_V}^{\infty} r \dot{u}_{G_z, m}(k, r) \dot{u}_{G'_z, m'}(k, r) V_{m'', G''_z}(r) dr. \end{aligned} \quad (4.114)$$

Among all vacuum contributions to the various parts of the method this is certainly the most time consuming contribution. A significant speed-up is achieved using the following two facts. Firstly, the elements of the t -matrix depend only on m, m', G_z and G'_z , but not on \mathbf{G}_{\parallel} and \mathbf{G}'_{\parallel} . Using this fact allows us to realize the following, rather fast, reconstruction of the A - and B -coefficients:

$$\begin{aligned} \tilde{A}_{m, G_z}^{\mathbf{G}'}(k) &= \sum_{m'} \left(A_{m'}^{\mathbf{G}'}(k) \right)^* \left(t_{G_z, G'_z}^{uu, mm'}(k) + t_{G_z, G'_z}^{u\dot{u}, mm'}(k) \right), \\ \tilde{B}_{m, G_z}^{\mathbf{G}'}(k) &= \sum_{m'} \left(B_{m'}^{\mathbf{G}'}(k) \right)^* \left(t_{G_z, G'_z}^{\dot{u}u, mm'}(k) + t_{G_z, G'_z}^{\dot{u}\dot{u}, mm'}(k) \right), \end{aligned} \quad (4.115)$$

to reduce the double summation in the expression for the Hamiltonian matrix elements to a single summation by m :

$$H_{\text{vac}}^{\mathbf{G}'\mathbf{G}}(k) = \sum_m \left(\tilde{A}_{m,G_z}^{\mathbf{G}'} \cdot A_m^{\mathbf{G}} + \tilde{B}_{m,G_z}^{\mathbf{G}'} \cdot B_m^{\mathbf{G}} \right) (k). \quad (4.116)$$

Secondly, another achievement can be made based on the symmetry considerations. Knowing which particular $(m'', G_z'') = (m' - m, G_z' - G_z)$ components of the potential are not allowed by the symmetry of the system, we skip the summation over the corresponding (m, m', G_z, G_z') -elements of the t -matrix in the A - and B -coefficients reconstruction part, which makes this part negligible in the computational time. The achieved speed-up due to the latter two considerations is approximately of the rate $m_{\text{max}}/2$, which for the calculations, presented in section 7.2 for the gold tube, for example, gives a factor of 25.

Another consideration can be made based on the fact, that for the large m the A - and B -coefficients decay very rapidly together with the t -matrix elements. This allows us to put the non-diagonal (m, m') -part of the t -matrix to zero for $\{|m|, |m'|\} \leq m_{\text{cutoff}}$, reducing therefore the m and m' -summations in the construction of the Hamiltonian matrix. The actual value of the parameter m_{cutoff} should be determined in such a way, so that it does not change calculated properties in the range of the required numerical accuracy. For instance, for the gold monowire calculations, presented in section 7.2, carried out with the angular basis functions expansion parameter m_{max} of 20, the choice $m_{\text{cutoff}} = 10$ proved to give a negligible difference (0.01%) in total energies, eigenvalues and Fermi energies compared to the case of $m_{\text{cutoff}} = m_{\text{max}}$.

4.3 Fermi Energy and Brillouin Zone Integration

When DFT is applied to infinite periodic solids, quantities that are given by integrals of functions, which depend on the band and the Bloch vector, over the Brillouin zone have to be determined. These integrations stretch only over the occupied part of the band, i.e. over the region of the Brillouin zone where the band energy $\epsilon_\nu(k)$ (ν is the band index) is smaller than the Fermi energy. Hence, the integrals are of the form

$$\frac{1}{V_{BZ}} \int_{BZ} \sum_{\nu, \epsilon_\nu(k) < E_F} f_\nu(k) dk, \quad (4.117)$$

where f is the function to be integrated. Example of such quantities are the number of electrons per unit cell

$$N = \frac{1}{V_{BZ}} \int_{BZ} \sum_{\nu, \epsilon_\nu(k) < E_F} 1 dk, \quad (4.118)$$

the electron (charge) density (cf. section 5.2) and the eigenvalue sum

$$\frac{1}{V_{BZ}} \int_{BZ} \sum_{\nu, \epsilon_\nu(k) < E_F} \epsilon_\nu(k) dk. \quad (4.119)$$

Numerically, these integrations are performed on a discrete mesh in the Brillouin zone. The function to be integrated has to be calculated at a set of k -points in the Brillouin zone, each of which is assigned a weight. Thus, the Brillouin zone integration is transformed into a sum over a set of k -points, where only those bands are included, which have an energy below the Fermi energy at the k -point under summation. Thus, the integrals become:

$$\frac{1}{V_{BZ}} \int_{BZ} \sum_{\nu, \epsilon_{\nu}(k) < E_F} f_{\nu}(k) dk \longrightarrow \sum_k \sum_{\nu, \epsilon_{\nu}(k) < E_F} f_{\nu}(k) w(k) \quad (4.120)$$

Alternatively, this integration can be viewed as an integration over the whole Brillouin zone, where the function to be integrated is given by a product of the function f with a step function that cuts out the region of the Brillouin zone, where the band energy is above the Fermi energy. Clearly, the resulting function does not satisfy the condition of being smoothly varying. Therefore, the special k -points method does not converge very quickly, and rather many k -points are needed to obtain accurate results. On the other hand this method is simple to implement, because the weights depend only on k and the band energy (via the step function) at each k -point. Another problem arises from this “sharp” differentiation between occupied and empty bands (parts of bands). Let’s consider a band that is very close to the Fermi energy at a certain k -point. During the iterations the DFT self-consistency cycle energy of this band might rise above or drop below the Fermi energy. This leads to sudden changes in the charge density, which can slow down or even prevent the convergence of the density. These sudden changes are clearly a result of the discretization in momentum space. To avoid this problem, the sharp edges of the step function have to be removed. This can be done, e.g. by using the Fermi function $(e^{(\epsilon - E_F)/k_B T} + 1)^{-1}$ rather than the step function. In other words, the function to be integrated is artificially made smoothly varying. The temperature T can then be adjusted to obtain the best convergence. This method is called temperature broadening.

In the current implementation of the FLAPW method the Fermi energy is determined in two steps. First the bands are occupied (at all k -points simultaneously), starting from the lowest energy, until the sum of their weights equals the total number of electrons per unit cell, i.e. the discretized equivalent of (4.118) is solved at $T = 0$. Then the step function is replaced by the Fermi and the Fermi energy is determined from the requirement that:

$$N = \sum_k \sum_{\nu} w(k, \epsilon_{\nu}(k) - E_F) \quad (4.121)$$

where the weights are given by:

$$w(k, \epsilon_{\nu}(k) - E_F) = w(k) \frac{1}{e^{(\epsilon_{\nu}(k) - E_F)/k_B T} + 1} \quad (4.122)$$

Chapter 5

Charge Density

5.1 Generation of the Starting Density

The starting density for every calculation is approximated as the superposition of spherical charge densities generated for each atom separately from the atomic problem. The starting charge density then is the superposition of the charge densities located at atom sites α : $\rho^\alpha(\mathbf{r}_\alpha + \tau_\alpha)$, $\mathbf{r}_\alpha = \mathbf{r} - \tau_\alpha$.

$$\rho(\mathbf{r}) = \sum_{\alpha} \rho^\alpha(\mathbf{r}_\alpha + \tau_\alpha), \quad (5.1)$$

and has to be expanded as:

$$\rho(\mathbf{r}) = \begin{cases} \sum \rho_\nu(r_\alpha) K_\nu(r_\alpha) & \text{in MT}_\alpha \\ \sum_{\nu} \rho_\nu(r) \Phi_\nu(\mathbf{r}) & \text{in VR} \\ \sum_{\mathbf{G}} \rho_{\mathbf{G}} e^{i\mathbf{G}\mathbf{r}} \sim \sum_{\mathbf{G}} \rho_{\mathbf{G}} \Phi_{\mathbf{G}}(\mathbf{r}) & \text{in IR} \end{cases} \quad (5.2)$$

To find the coefficients in the latter expansion we construct an auxiliary charge density around each atom:

$$\tilde{\rho}_\alpha(r_\alpha) = \begin{cases} A_\alpha e^{-B_\alpha r_\alpha^2} & \text{in MT}_\alpha \\ \rho^\alpha(r_\alpha) & \text{outside MT}_\alpha \end{cases} \quad (5.3)$$

where coefficients A_α and B_α are found from the condition of continuity of the charge density on the muffin-tin boundaries in value and radial derivative. Then the total charge density can be written as:

$$\rho(\mathbf{r}) = (\rho(\mathbf{r}) - \tilde{\rho}(\mathbf{r})) + \tilde{\rho}(\mathbf{r}), \quad \tilde{\rho}(\mathbf{r}) = \sum_{\alpha} \tilde{\rho}_\alpha(r_\alpha), \quad (5.4)$$

where density $\rho(\mathbf{r}) - \tilde{\rho}(\mathbf{r})$ is concentrated only inside the muffin-tins, and, therefore, can be directly calculated on the real grid. However, charge density $\tilde{\rho}$ needs certain attention. This density is smoothly varying through the whole unit cell, therefore, it can be easily expanded in terms of plane-waves:

$$\tilde{\rho}(\mathbf{r}) = \sum_{\mathbf{G}} \tilde{\rho}_{\mathbf{G}} e^{i\mathbf{G}\mathbf{r}}, \quad (5.5)$$

where

$$\tilde{\rho}_{\mathbf{G}} = \frac{1}{\tilde{\Omega}} \int_{\tilde{\Omega}} \tilde{\rho}(\mathbf{r}) e^{-i\mathbf{G}\mathbf{r}} d^3\mathbf{r} = \frac{1}{\tilde{\Omega}} \sum_{\alpha} \int_{\tilde{\Omega}} \tilde{\rho}_{\alpha}(r_{\alpha}) e^{i\mathbf{G}\tau_{\alpha}} e^{-i\mathbf{G}\mathbf{r}} d^3\mathbf{r}. \quad (5.6)$$

Finally, its Fourier coefficients can be presented in the following form:

$$\tilde{\rho}_{\mathbf{G}} = \sum_{\alpha} F_{\alpha}^{\mathbf{G}} \cdot S_{\alpha}^{\mathbf{G}} = \sum_{\mu} F_{\mu}^{\mathbf{G}} \cdot \sum_{\alpha(\mu)} S_{\alpha}^{\mathbf{G}}, \quad (5.7)$$

where $S_{\alpha}^{\mathbf{G}}$ is a structure factor of atom α and $F_{\mu}^{\mathbf{G}}$ is a form factor for an atom type μ :

$$S_{\alpha}^{\mathbf{G}} = e^{i\mathbf{G}\tau_{\alpha}}, \quad F_{\mu}^{\mathbf{G}} = \frac{1}{\tilde{\Omega}} \int_{\tilde{\Omega}} \tilde{\rho}_{\mu}(r_{\mu}) e^{-i\mathbf{G}\mathbf{r}} d^3\mathbf{r}. \quad (5.8)$$

Note, that due to the special form of the auxiliary potential inside the muffin-tin sphere, the form-factor there is calculated analytically. Anyhow, after finding the Fourier components of the charge $\tilde{\rho}$, it is expanded out of the plane-wave representation back in terms of lattice harmonics inside each muffin-tin site, and added to the original charge ρ_{α} .

Latter calculations were done assuming that the system has an in-plane periodicity with the lattice constant \tilde{D} , therefore, at the next step we have to include into consideration the vacuum region. The idea behind this procedure is the following: we leave the charge density in the muffin-tins and in the interstitial region unchanged up to the vacuum boundary, while the vacuum charge is constructed in such a way, that it is continuous at the interstitial-vacuum boundary in its value and radial derivative, and decays fast to zero on infinity.

We start with the cylindrically symmetric component of the vacuum charge density. We force it to have the following form:

$$\rho_0(r) = A \cdot e^{-B \cdot (r - R_v)}, \quad r > R_v, \quad (5.9)$$

where the parameters A and B are defined from the conditions of continuity of the charge density and conservation of the charge. So, the value of the cylindrically symmetric component of the interstitial charge on the boundary is given by the following expression:

$$\rho_0(R_v) = \sum_{\mathbf{G}_{\parallel}} \rho_{0,\mathbf{G}_{\parallel}} J_0(R_v \cdot G_{\parallel}) = A, \quad (5.10)$$

where J_0 is a cylindrical Bessel function of the zero order, $\{\rho_{0,\mathbf{G}}\}$ are the Fourier components of the interstitial charge density. Another condition we have is a condition of the charge conservation, which means that the charge which is carried by the vacuum density should be equal to ρ_{out} :

$$\rho_{out} = \int_{\tilde{\Omega}} \tilde{\rho}(\mathbf{r}) d^3\mathbf{r} - \int_{\Omega} \tilde{\rho}(\mathbf{r}) d^3\mathbf{r}. \quad (5.11)$$

where $\tilde{\Omega}$ is the volume of the rectangular \tilde{D} -unit cell, and Ω is the volume of the cylindrical unit cell. The first integral leaves only the term $\tilde{\Omega}\tilde{\rho}_0$. The second term is easily calculated:

$$\Omega\tilde{\rho}_0 + 2\Omega \sum_{\mathbf{G}_{\parallel} \neq 0} \tilde{\rho}_{\mathbf{G}_{\parallel},0} \frac{J_1(G_{\parallel}R)}{RG_{\parallel}}$$

Finally,

$$\rho_{out} = (\tilde{\Omega} - \Omega)\tilde{\rho}_0 - 2\Omega \sum_{\mathbf{G}_{\parallel} \neq 0} \tilde{\rho}_{\mathbf{G}_{\parallel},0} \frac{J_1(G_{\parallel}R)}{RG_{\parallel}}. \quad (5.12)$$

Vacuum density gives us a charge of:

$$q_{vac} = 2\pi T \cdot A \cdot \int_0^{\infty} (r + R)e^{-B \cdot r} dr = \rho_{out},$$

which reads a simple expression for B :

$$B = \frac{R_v \cdot q + \sqrt{R_v^2 q^2 + 4q}}{2}, \quad (5.13)$$

with $q = \frac{A}{\rho_{out}}$. Other components of the vacuum charge do not contribute to the total charge in the vacuum, and, therefore, their A and B coefficients can be defined by simple matching on the vacuum boundary in the value and derivative, using expressions of the type (5.10) for higher cylindrical harmonics of the interstitial charge.

5.2 Generation of the Charge Density

In this section we will discuss the determination of the charge density from the eigenfunctions. In density functional calculations of an infinite periodic solid the electron density is given by an integral over the Brillouin zone (cf. (2.21)).

$$n(\mathbf{r}) = \frac{1}{V_{BZ}} \int_{BZ} \sum_{\nu, \epsilon_{\nu}(\mathbf{k}) < E_F} |\psi_{\nu}(\mathbf{k}, \mathbf{r})|^2 d\mathbf{k} \quad (5.14)$$

where V_{BZ} is the volume of the Brillouin zone, ν is the band index and E_F is the Fermi energy. In spin-polarized calculations the summation includes also the spin-index σ , while in a non-magnetic calculation a factor of two has to be added to account for the spin-degeneracy. In the case of one-dimensional calculations the three-dimensional Brillouin zone is replaced by a one-dimensional Brillouin zone. In both cases integration methods that sample eigenfunctions and the eigenvalues on discrete \mathbf{k} -point are used to compute the integrals. These methods transform the integration into a weighted sum over the \mathbf{k} -points, where the choice of \mathbf{k} -points and their weights depends on the integration method used. These weights depend not only on the \mathbf{k} -point, but also on the energy of a band, i.e. on the band (index), because each band contributes to the electron density only if its energy is below the Fermi energy.

$$n(\mathbf{r}) = \sum_k \sum_{\nu} |\psi_{\nu}(k, \mathbf{r})|^2 w(\nu, k) \quad (5.15)$$

Within the FLAPW method the eigenfunctions are represented in terms of the coefficients of the augmented plane-waves.

$$\psi_{\nu}(k, \mathbf{r}) = \sum_{\mathbf{G}} c_{\nu}^{\mathbf{G}}(k) \varphi_{\mathbf{G}}(k, \mathbf{r}) \quad (5.16)$$

Inside the muffin-tin spheres each plane-wave is coupled to a sum of spherical harmonics and radial functions. Hence, in a sphere μ an eigenfunction is given by:

$$\psi_{\nu}^{\mu}(k, \mathbf{r}) = \sum_{\mathbf{G}} c_{\nu}^{\mathbf{G}}(k) \sum_L A_L^{\mu\mathbf{G}}(k) u_l^{\alpha}(r) Y_L(\hat{\mathbf{r}}) + B_L^{\mu\mathbf{G}}(k) \dot{u}_l^{\alpha}(r) Y_L(\hat{\mathbf{r}}) \quad (5.17)$$

The $A_L^{\mu\mathbf{G}}(k)$ and $B_L^{\mu\mathbf{G}}(k)$ coefficients can be replaced by band dependent A- and B-coefficients, obtained by performing the contraction over the plane-waves:

$$\psi_{\nu}^{\mu}(k, \mathbf{r}) = \sum_L A_{L,\nu}^{\mu}(k) u_l^{\alpha}(r) Y_L(\hat{\mathbf{r}}) + B_{L,\nu}^{\mu}(k) \dot{u}_l^{\alpha}(r) Y_L(\hat{\mathbf{r}}), \quad (5.18)$$

where

$$A_{L,\nu}^{\mu}(k) = \sum_{\mathbf{G}} c_{\nu}^{\mathbf{G}}(k) A_L^{\mu\mathbf{G}}(k), \quad B_{L,\nu}^{\mu}(k) = \sum_{\mathbf{G}} c_{\nu}^{\mathbf{G}}(k) B_L^{\mu\mathbf{G}}(k). \quad (5.19)$$

5.2.1 “l-like” Charge

Since the wavefunctions are expanded in terms of the spherical harmonics inside the muffin-tin spheres, they can be split up into contributions with a certain l -character:

$$\psi_{\nu}^{\mu}(k, \mathbf{r}) = \sum_l \psi_{\nu,l}^{\mu}(k, \mathbf{r}) \quad (5.20)$$

The particle density of a certain state depends on the square of the wavefunction. Therefore, it contains cross-terms with a mixture of different l 's:

$$n_{\nu}^{\mu}(\mathbf{r}) = \frac{1}{V_{BZ}} \int_{BZ} \sum_l |\psi_{\nu,l}^{\mu}(k, \mathbf{r})|^2 + \sum_{l'l'} 2 \left(\psi_{\nu,l'}^{\mu}(k, \mathbf{r}) \right)^* \psi_{\nu,l}^{\mu}(k, \mathbf{r}) dk \quad (5.21)$$

If, however, the density is integrated over the muffin-tin, the cross-terms vanish because of the orthogonality of the spherical harmonics. Thus, the total electron density inside a sphere can be written as a sum over contributions with definite l -character:

$$n_{\nu}^{\mu} = \sum_l n_{\nu,l}^{\mu}, \quad n_{\nu,l}^{\mu} = \frac{1}{V_{BZ}} \int_{BZ} \int_{MT^{\mu}} |\psi_{\nu,l}^{\mu}(k, \mathbf{r})|^2 d^3r dk, \quad (5.22)$$

where $n_{\nu,l}^{\mu}$ is called a “ l -like” charge. We can also define a k -dependent l -like charge by:

$$n_{\nu,l}^{\mu}(k) = \int_{MT^{\mu}} |\psi_{\nu,l}^{\mu}(k, \mathbf{r})|^2 d^3r \quad (5.23)$$

Substituting (5.18) yields:

$$n_{\nu,l}^{\mu}(k) = \sum_{m=-l}^l |A_{L,\nu}^{\mu}(k)|^2 + |B_{L,\nu}^{\mu}(k)|^2 \dot{N}_l^{\alpha} \quad (5.24)$$

Where

$$\dot{N}_l^{\alpha} = \int_0^{R_{MT^{\alpha}}} (\dot{u}_l^{\alpha}(r))^2 r^2 dr \quad (5.25)$$

and the orthogonality of the spherical harmonics, the normalization conditions for u_l^{α} and the orthogonality conditions for u_l^{α} and \dot{u}_l^{α} have been used.

5.2.2 Determination of the Optimal Energy Parameters

In order to minimize the linearization error, the energy parameters should be chosen as close to the band energies as possible. However, the band energies $\epsilon_\nu(k)$ depend on k whereas the energy parameters E_l^α are constants. In addition, the radial functions contribute to the eigenfunctions of different bands with different energies. Therefore, deviations between $\epsilon_\nu(k)$ and E_l^α have to be accepted. An optimal choice can be obtained from the requirement, that the energy parameters minimize

$$\int_{BZ} \sum_{\nu, \epsilon_\nu(k) < E_F} (\epsilon_\nu(k) - E_l^\alpha)^2 n_{\nu,l}^\mu(k) dk, \quad (5.26)$$

which is the quadratic error weighted with the amount of charge that each band contributes to the l -like charge with the l -character of the energy parameter. Setting the derivative $(\partial/\partial E_l^\alpha)$ equal to zero yields the optimal energy parameter:

$$E_l^\alpha = \left(\int_{BZ} \sum_{\nu, \epsilon_\nu(k) < E_F} \epsilon_\nu(k) n_{\nu,l}^\mu(k) dk \right) / \left(\int_{BZ} \sum_{\nu, \epsilon_\nu(k) < E_F} n_{\nu,l}^\mu(k) dk \right) \quad (5.27)$$

The Brillouin zone integration methods transform this into a sum over a discrete k-point set:

$$E_l^\alpha = \left(\sum_k \sum_\nu \epsilon_\nu(k) n_{\nu,l}^\mu(k) w(\nu, k) \right) / \left(\sum_k \sum_\nu n_{\nu,l}^\mu(k) w(\nu, k) \right) \quad (5.28)$$

5.2.3 Generation of the Charge Density in the Spheres

Substituting (5.18) into (5.14) yields the electron density in the muffin-tin spheres:

$$\begin{aligned} n^\mu(\mathbf{r}) &= \frac{1}{V_{BZ}} \int_{BZ} \sum_{\nu, \epsilon_\nu(k) < E_F} \sum_{L'} \left(A_{L',\nu}^\mu(k) u_{l'}^\alpha(r) + B_{L',\nu}^\mu(k) \dot{u}_{l'}^\alpha(r) \right)^* Y_{L'}^*(\hat{\mathbf{r}}) \\ &\quad \sum_L \left(A_{L,\nu}^\mu(k) u_l^\alpha(r) + B_{L,\nu}^\mu(k) \dot{u}_l^\alpha(r) \right) Y_L(\hat{\mathbf{r}}) dk \end{aligned} \quad (5.29)$$

The particle density inside the muffin-tins is also expanded into spherical harmonics:

$$n^\mu(\mathbf{r}) = \sum_L C_L^\mu(r) Y_L(\hat{\mathbf{r}}) \quad (5.30)$$

The coefficients $C_{L''}^\mu(r)$ can be determined by multiplying (5.29) with $\int d\Omega Y_{L''}(\hat{\mathbf{r}})$:

$$\begin{aligned} C_{L''}^\mu(r) &= \frac{1}{V_{BZ}} \int_{BZ} \sum_{\nu, \epsilon_\nu(k) < E_F} \sum_{L'} \left(A_{L',\nu}^\mu(k) u_{l'}^\alpha(r) + B_{L',\nu}^\mu(k) \dot{u}_{l'}^\alpha(r) \right)^* \\ &\quad \sum_L \left(A_{L,\nu}^\mu(k) u_l^\alpha(r) + B_{L,\nu}^\mu(k) \dot{u}_l^\alpha(r) \right) G_{L''}^{mm'm''} dk \end{aligned} \quad (5.31)$$

with

$$G_{l'l''}^{mm'm''} = \int Y_{lm}^* Y_{l'm'} Y_{l''m''} d\Omega \quad (5.32)$$

where it was used, that the gaunt coefficients are real, i.e.

$$\int Y_{lm} Y_{l'm'}^* Y_{l''m''}^* d\Omega = \int Y_{lm}^* Y_{l'm'} Y_{l''m''} d\Omega \quad (5.33)$$

Finally, applying a Brillouin zone integration method yields:

$$\begin{aligned} C_{L''}^\mu(r) &= \sum_{l'l} \left(\sum_k \sum_\nu \sum_{m'm} (A_{L',\nu}^\mu(k))^* A_{L,\nu}^\mu(k) G_{l'l''}^{mm'm''} w(\nu, k) \right) u_{l'}^\alpha(r) u_l^\alpha(r) \\ &+ \sum_{l'l} \left(\sum_k \sum_\nu \sum_{m'm} (A_{L',\nu}^\mu(k))^* B_{L,\nu}^\mu(k) G_{l'l''}^{mm'm''} w(\nu, k) \right) u_{l'}^\alpha(r) \dot{u}_l^\alpha(r) \\ &+ \sum_{l'l} \left(\sum_k \sum_\nu \sum_{m'm} (B_{L',\nu}^\mu(k))^* A_{L,\nu}^\mu(k) G_{l'l''}^{mm'm''} w(\nu, k) \right) \dot{u}_{l'}^\alpha(r) u_l^\alpha(r) \\ &+ \sum_{l'l} \left(\sum_k \sum_\nu \sum_{m'm} (B_{L',\nu}^\mu(k))^* B_{L,\nu}^\mu(k) G_{l'l''}^{mm'm''} w(\nu, k) \right) \dot{u}_{l'}^\alpha(r) \dot{u}_l^\alpha(r) \end{aligned} \quad (5.34)$$

5.2.4 Generation of the Charge Density in the Interstitial

In the interstitial region the wavefunctions are represented in the following form:

$$\psi_\nu(k, \mathbf{r}) = \sum_{\mathbf{G}} c_\nu^{\mathbf{G}}(k) e^{i(\mathbf{G}+k)\mathbf{r}} \quad (5.35)$$

Starting from (2.8) the electron density is given by:

$$n(\mathbf{r}) = \frac{1}{V_{BZ}} \int_{BZ} \sum_{\nu, \epsilon_\nu(k) < E_F} \sum_{\mathbf{G}' \mathbf{G}''} (c_\nu^{\mathbf{G}'}(k))^* c_\nu^{\mathbf{G}''}(k) dk e^{i(\mathbf{G}'' - \mathbf{G}')\mathbf{r}} \quad (5.36)$$

The electron density in the interstitial region is also expanded into plane-waves:

$$n(\mathbf{r}) = \sum_{\mathbf{G}} n^{\mathbf{G}} e^{i\mathbf{G}\mathbf{r}} \quad (5.37)$$

Hence, the plane-wave coefficients of the electron density are:

$$n^{\mathbf{G}} = \frac{1}{V_{BZ}} \int_{BZ} \sum_{\nu, \epsilon_\nu(k) < E_F} \sum_{\substack{\mathbf{G}' \mathbf{G}'' \\ \mathbf{G}'' - \mathbf{G}' = \mathbf{G}}} (c_\nu^{\mathbf{G}'}(k))^* c_\nu^{\mathbf{G}''}(k) dk \quad (5.38)$$

Apparently, the plane-wave cut-off of the particle density has to be twice the cut-off of the wavefunction expansion (G_{max}) to allow an accurate description. The k - and state-dependent density

$$n_\nu^{\mathbf{G}}(k) = \sum_{\substack{\mathbf{G}' \mathbf{G}'' \\ \mathbf{G}'' - \mathbf{G}' = \mathbf{G}}} (c_\nu^{\mathbf{G}'}(k))^* c_\nu^{\mathbf{G}''}(k) = \sum_{\mathbf{G}'} (c_\nu^{\mathbf{G}'}(k))^* c_\nu^{(\mathbf{G}+\mathbf{G}')} (k) \quad (5.39)$$

is given by a convolution in momentum space. For each coefficient a sum over \mathbf{G} has to be performed. Consequently, the numerical effort put into the determination of $n_\nu^{\mathbf{G}}(k)$ scales proportional to the number of G -vectors squared, i.e. proportional to $(G_{max})^6$. However, $n_\nu^{\mathbf{G}}(k)$ can be calculated more efficiently using the fast Fourier transform (FFT). First, $c_\nu^{\mathbf{G}}(k)$ is Fourier transformed to real space, where it is squared on a real space mesh yielding $n_\nu(k, \mathbf{r})$, then all states are summed up and finally the resulting particle density is back-transformed to momentum space:

$$c_\nu^{\mathbf{G}}(k) \xrightarrow{FFT} \psi_\nu(k, \mathbf{r}) \xrightarrow{square} n_\nu(k, \mathbf{r}) \xrightarrow{\sum_\nu} n(k, \mathbf{r}) \xrightarrow{FFT^{-1}} n^{\mathbf{G}}(k)$$

With this scheme the numerical effort increases proportional to $(G_{max})^3 \ln((G_{max})^3)$, which is a major improvement for large systems. In a last step the plane-waves have to be combined to form the three-dimensional stars.

5.2.5 Generation of the Charge Density in the Vacuum

The density in the vacuum is represented in the following form:

$$n(\mathbf{r}) = \sum_{G_z} e^{iG_z z} \sum_{m_{G_z}} i^m e^{im\varphi} n_{G_z, m}(r) \quad (5.40)$$

while the wavefunctions in the vacuum region are of the following shape:

$$\psi_\nu(k, \mathbf{r}) = \sum_{G_z, \mathbf{G}_\parallel} c_\nu^{\mathbf{G}}(k) e^{i(k+G_z)z} \sum_m i^m e^{im\varphi} \left(A_m^{\mathbf{G}}(k) u_{G_z, m}(k, r) + B_m^{\mathbf{G}}(k) \dot{u}_{G_z, m}(k, r) \right). \quad (5.41)$$

Therefore, the electron density is given by:

$$\begin{aligned} n(\mathbf{r}) &= \frac{1}{V_{BZ}} \int_{BZ} \sum_{\nu, \epsilon(k) < E_F} \sum_{\mathbf{G}'} \sum_{\mathbf{G}''} e^{i(G_z'' - G_z')z} \sum_{m'} \sum_{m''} i^{m'' - m'} e^{i(m'' - m')\varphi} \times \\ &\times \left(c_\nu^{\mathbf{G}'}(k) \left(A_m^{\mathbf{G}'}(k) u_{G_z', m}(k, r) + B_m^{\mathbf{G}'}(k) \dot{u}_{G_z', m}(k, r) \right) \right)^* \times \\ &\times \left(c_\nu^{\mathbf{G}''}(k) \left(A_m^{\mathbf{G}''}(k) u_{G_z'', m}(k, r) + B_m^{\mathbf{G}''}(k) \dot{u}_{G_z'', m}(k, r) \right) \right) dk \end{aligned} \quad (5.42)$$

Taking into account that the radial basis functions do not depend on the \mathbf{G}_\parallel -component of the reciprocal lattice vector \mathbf{G} , we can contract the A - and B -coefficients in the following way:

$$\begin{aligned} A_m^{G_z}(k) &= \sum_\nu \sum_{\mathbf{G}_\parallel} w(\nu, k) c_\nu^{G_z, \mathbf{G}_\parallel}(k) A_m^{G_z, \mathbf{G}_\parallel}(k), \\ B_m^{G_z}(k) &= \sum_\nu \sum_{\mathbf{G}_\parallel} w(\nu, k) c_\nu^{G_z, \mathbf{G}_\parallel}(k) B_m^{G_z, \mathbf{G}_\parallel}(k). \end{aligned} \quad (5.43)$$

Extracting the $\mu = (m, G_z)$ -components of the vacuum charge density, we arrive at the final expression:

$$n_{m, G_z}(r) = \sum_k \sum_{G'_z} \sum_{m'} \times$$

$$\left[\left(A_{m'}^{G'_z} \right)^* A_{m+m'}^{G_z+G'_z} u_{G'_z, m'}(r) u_{G_z+G'_z, m+m'}(r) + \left(A_{m'}^{G'_z} \right)^* B_{m+m'}^{G_z+G'_z} u_{G'_z, m'}(r) \dot{u}_{G_z+G'_z, m+m'}(r) + \right.$$

$$\left. \left(B_{m'}^{G'_z} \right)^* A_{m+m'}^{G_z+G'_z} \dot{u}_{G'_z, m'}(r) u_{G_z+G'_z, m+m'}(r) + \left(B_{m'}^{G'_z} \right)^* B_{m+m'}^{G_z+G'_z} \dot{u}_{G'_z, m'}(r) \dot{u}_{G_z+G'_z, m+m'}(r) \right],$$
(5.44)

where we remember that A, B -coefficients and u, \dot{u} -functions depend also on k .

In principal, the terms of the form

$$\sum_{G'_z} \sum_{m'} \left(A_{m', \nu}^{G'_z}(k) \right)^* A_{m+m', \nu}^{G_z+G'_z}(k) u_{G'_z, m'}(k, r) u_{G_z+G'_z, m+m'}(k, r)$$

represent convolution in the momentum space by m and G_z , and, therefore, could be efficiently computed on the base of two-dimensional FFTs in cylindrical coordinates (z, φ) for every radial vacuum grid point r .

Chapter 6

Potential

6.1 Coulomb Potential

The Coulomb potential consists of two parts, the Hartree term $V_H(\mathbf{r})$ and the external potential of the nuclei $V_i(\mathbf{r})$:

$$V_c(\mathbf{r}) = V_H(\mathbf{r}) + V_i(\mathbf{r}) \quad (6.1)$$

The Hartree potential has to be determined from the charge density via the Poisson equation

$$\Delta V_H(\mathbf{r}) = 4\pi\rho(\mathbf{r}) \quad (6.2)$$

In real space the solution of (6.2) is given by

$$V_H(\mathbf{r}) = \int \frac{4\pi\rho(\mathbf{r}')}{|\mathbf{r} - \mathbf{r}'|} d\mathbf{r}'. \quad (6.3)$$

In reciprocal space, however, the Poisson equation is diagonal, and as a result the solution is very simple:

$$V_H(\mathbf{G}) = \frac{4\pi\rho(\mathbf{G})}{\mathbf{G}^2} \quad (6.4)$$

Therefore, and because of the particular representation of the charge density and the potential in the interstitial and vacuum regions, the solution of the Poisson equation in reciprocal space appears to be convenient. However, due to the localized core and valence states the charge density varies rapidly on a very small length scale near the nuclei. Thus, the plane-wave expansion of ρ converges slowly, and a direct use of (6.4) is impractical if not impossible. This difficulty can be overcome via the pseudo-charge method.

6.1.1 The Pseudo-Charge Scheme

The pseudo-charge method, developed by Weinert [120] is a very elegant technique to calculate the interstitial and vacuum Hartree potential. The underlying idea is to divide the solution of the Poisson equation into two steps. In the first step the true muffin-tin charge is replaced by a convergent pseudo-charge density $\tilde{\rho}$, that leads to the same

potential outside the muffin-tins. Then the interstitial (and vacuum) potential is calculated in reciprocal space. In the second step the muffin-tin potential is determined from the Dirichlet boundary value problem, defined by the exact muffin-tin charge and the interstitial potential on the muffin-tin spheres' boundaries. The potential outside the muffin-tin spheres due to a charge distribution inside the spheres is determined uniquely by its multipole moments q_L :

$$V(\mathbf{r}) = \sum_{l=0}^{\infty} \sum_{m=-l}^l \frac{4\pi}{2l+1} \frac{q_L}{r^{l+1}} Y_L(\hat{\mathbf{r}}). \quad (6.5)$$

However, the multipole moments do not define the charge density uniquely. The charge density is given by:

$$\rho(\mathbf{r}) = \rho_I(\mathbf{r})\Theta(\mathbf{r} \in I) + \sum_{\alpha} \rho_{\alpha}(\mathbf{r})\Theta(\mathbf{r} \in MT^{\alpha}) \quad (6.6)$$

Equation (6.6) can be rewritten

$$\rho(\mathbf{r}) = \rho_I(\mathbf{r}) + \sum_{\alpha} [\rho_{\alpha}(\mathbf{r}) - \rho_I(\mathbf{r})]\Theta(\mathbf{r} \in MT^{\alpha}) \quad (6.7)$$

Thus, the interstitial charge has been extended into the muffin-tins and subtracted there again. The second term in (6.7) can be replaced by a pseudo-charge $\tilde{\rho}^{\alpha}$, which has the same multipole moments (see [120] for details). The resulting pseudo-charge $\tilde{\rho}$ is given by

$$\tilde{\rho}(\mathbf{r}) = \rho_I(\mathbf{r}) + \sum_{\alpha} \tilde{q}^{\alpha}(\mathbf{r}) \quad (6.8)$$

Density $\tilde{\rho}(\mathbf{r})$ is constructed in such a way, that it has rapidly converging Fourier expansion, compared to the original charge density $\rho(\mathbf{r})$. Therefore, the Poisson equation can now be solved using (6.4).

Still, the muffin-tin potential V_{MT}^{α} remains to be determined. For this step the exact muffin-tin charge ρ_{α} has to be used. Since the interstitial potential is already known at this point, the calculation of V_{MT}^{α} constitutes a classical spherically symmetric Dirichlet boundary value problem, which can be solved by the Green function method [39]:

$$V_{MT}^{\alpha}(\mathbf{r}) = \int_{MT^{\alpha}} \rho_{\alpha}(\mathbf{r}') G(\mathbf{r}, \mathbf{r}') d^3r' - \frac{R_{\alpha}^2}{4\pi} \oint_{S^{\alpha}} V_I(\mathbf{r}') \frac{\partial G}{\partial n'} d\Omega' \quad (6.9)$$

The second integral runs over the muffin-tin sphere boundary S^{α} , and the resulting potential necessarily satisfies the boundary conditions. The Green function is given by:

$$G^{\alpha}(\mathbf{r}, \mathbf{r}') = 4\pi \sum_{l,m} \frac{Y_L(\hat{\mathbf{r}}') Y_L(\hat{\mathbf{r}})}{2l+1} \frac{r_{<}^l}{r_{>}^{l+1}} \left(1 - \left(\frac{r_{>}}{R_{MT^{\alpha}}} \right)^{2l+1} \right) \quad (6.10)$$

where $r_{>} = \max\{|\mathbf{r}|, |\mathbf{r}'|\}$, $r_{<} = \min\{|\mathbf{r}|, |\mathbf{r}'|\}$. Finally, the muffin-tin potential has to be expanded into lattice harmonics $K_{\nu}(\hat{\mathbf{r}})$:

$$V_{MT}^{\alpha}(\mathbf{r}) = \sum_{\nu} V_{MT,\nu}^{\alpha}(r) K_{\nu}(\hat{\mathbf{r}}). \quad (6.11)$$

The potential of the nuclei $V_i^\alpha(\mathbf{r}) = \frac{eZ^\alpha}{|\mathbf{r}|}$ is added to the spherical ($l = 0$) component of the potential $V_{MT,0}^\alpha(r)$.

The muffin-tin potential is computed in the same way for bulk, film and one-dimensional geometries. Apparently, the interstitial and vacuum regions have to be treated differently in the film and 1D model, due to the different boundary conditions and different representations of the vacuum potential. Therefore, in the next two sections the solution of the Poisson equation will be outlined separately.

In the case of bulk calculations we have periodic boundary conditions in three dimensions. Therefore, the solution of the Poisson equation,

$$\mathbf{G}^2 V(\mathbf{G}) = 4\pi \tilde{\rho}(\mathbf{G}) \quad (6.12)$$

is very simple. Obviously, this equation can only be solved if $\tilde{\rho}(0) = 0$. Since $\tilde{\rho}(0)$ is the average charge density, this means that charge neutrality is essential. Still, $V(0)$ remains undetermined by (6.12), i.e. one has the freedom to shift the potential by a constant. This is a consequence of the periodic boundary conditions, since they do not fix the reference of the potential. Usually $V(0)$ is chosen to be zero, hence the Coulomb potential in the interstitial-region is given by:

$$V_I(\mathbf{r}) = \sum_{\mathbf{G} \neq 0} \frac{4\pi \tilde{\rho}(\mathbf{G})}{\mathbf{G}^2} e^{i\mathbf{G}\mathbf{r}} = \sum_{s \neq 0} \frac{4\pi \tilde{\rho}_s}{\mathbf{G}_s^2} \Phi_s^{3D}(\mathbf{r}) \quad (6.13)$$

where the first summation is expressed in terms of \mathbf{G} -vectors and the second one in terms of stars.

6.1.2 Solution of the Poisson Equation in the Vacuum and Interstitial

The particular spatial partitioning of the unit cell results in different representations for the charge and potential in the interstitial and vacuum regions. Therefore, a certain transformation from one representation to another should be developed in order to make the junction of the charge and the potential on the interstitial-vacuum boundary.

In the vacuum the following representations are the most suitable for solving the Poisson equation:

$$V(\mathbf{r}) = V_0(r) + \sum_{m, G_z}^{\sim} V_{G_z, m}(r) e^{im\varphi} e^{iG_z z} \quad (6.14)$$

$$\rho(\mathbf{r}) = \rho_0(r) + \sum_{m, G_z}^{\sim} \rho_{G_z, m}(r) e^{im\varphi} e^{iG_z z} \quad (6.15)$$

where we separate $\{m = 0, G_z = 0\}$ components of the density and potential from the rest of the sum over m and G_z , which we indicate with tilde. In (6.15) the cylindrical system of coordinates is used: $\mathbf{r} = (r, \varphi, z)$.

At the next step we make use of the following relation, which allows us to rewrite interstitial density and potential in cylindrical coordinates:

$$e^{i\mathbf{G}\mathbf{r}} = e^{iG_z z} \sum_{m=-\infty}^{+\infty} i^m e^{im(\varphi - \varphi_{\mathbf{G}_{\parallel}})} J_m(G_{\parallel}r), \quad (6.16)$$

where $\varphi_{\mathbf{G}_{\parallel}}$ is an in-plane angle of the reciprocal vector \mathbf{G} , $G_{\parallel} = |\mathbf{G}_{\parallel}|$ and J_m is a cylindrical Bessel function of integer order m . Use of (6.16) reads the following cylindrical representation of the density and potential in the interstitial region:

$$\rho_{G_z, m}(r) = \sum_{\mathbf{G}_{\parallel}} i^m \rho_{G_z, \mathbf{G}_{\parallel}} e^{-im\varphi_{\mathbf{G}_{\parallel}}} J_m(G_{\parallel}r), \quad (6.17)$$

$$V_{G_z, m}(r) = \sum_{\mathbf{G}_{\parallel}} i^m V_{G_z, \mathbf{G}_{\parallel}} e^{-im\varphi_{\mathbf{G}_{\parallel}}} J_m(G_{\parallel}r). \quad (6.18)$$

A way of solving the Poisson equation, based on the latter cylindrical representations on the real radial grid in the vacuum and interstitial region as well, could be proposed. In this case every (m, G_z) -component of the density and potential could be analytically calculated for every cylindrical radial grid point in the interstitial and vacuum regions, and corresponding radial equations for the Coulomb potential, derived later, could be numerically solved. However, this scheme requires much more time, than the method, based on the use of FFTs in the interstitial, which we develop further.

Substituting the cylindrical expansions of the density and potential in the Poisson equation $\Delta V(\mathbf{r}) = -4\pi\rho(\mathbf{r})$ yields:

$$\left(\frac{d^2}{dr^2} + \frac{1}{r} \frac{d}{dr} - G_z^2 - \frac{m^2}{r^2} \right) V_{G_z, m}(r) = -4\pi\rho_{G_z, m}(r), \quad \text{when } G_z^2 + m^2 \neq 0, \quad (6.19)$$

$$\left(\frac{d^2}{dr^2} + \frac{1}{r} \frac{d}{dr} \right) V_0(r) = \left(\frac{1}{r} \frac{d}{dr} r \frac{d}{dr} \right) V_0(r) = -4\pi\rho_0(r), \quad \text{when } G_z = m = 0. \quad (6.20)$$

The Poisson equation is solved using the following boundary conditions at infinity:

$$\lim_{r \rightarrow \infty} V(r) = 0, \quad \lim_{r \rightarrow \infty} \frac{\partial V(r)}{\partial r} = 0. \quad (6.21)$$

Thus, we introduce the zero energy as an absolute reference from which all energies are measured. For example, the work function is just given by the negative of the Fermi energy E_F . The interstitial part of $\rho_0(r)$ reads:

$$\rho_0(r) = \sum_{\mathbf{G}_{\parallel}} \rho_{0, \mathbf{G}_{\parallel}} J_0(G_{\parallel}r), \quad (6.22)$$

while the vacuum part of $\rho_0(r)$ is given on a uniform radial mesh (for $r > R_{\text{vac}}$).

Cylindrically Symmetric Component of the Coulomb Potential $V_0(r)$

There are two equal numerically efficient ways of solving (6.20). The first one is based on the Green function method, where the Green function for (6.20) with the boundary conditions (6.21) is given by:

$$G_0(r, r') = -4\pi \ln r_{>}, \quad r_{>} = \max(r, r'), \quad (6.23)$$

so that the resulting potential can be computed as:

$$V_0(r) = \int_0^\infty r' G_0(r, r') \rho_0(r') dr'. \quad (6.24)$$

Another equivalent way solves the interstitial-vacuum boundary problem. Due to the analytical expression for $\rho_0(r)$ in the interstitial region in terms of Bessel functions (6.22), we use the latter method for the interstitial part of $V_0(r)$. On the other hand, the representation of the vacuum charge density on the radial grid makes it reasonable to apply the Green function method for the vacuum part of $V_0(r)$. In the following we use $V_0^i(r), \rho_0^i(r)$ for the interstitial part, and $V_0^v(r), \rho_0^v(r)$ for the vacuum part of the $V_0(r)$ and $\rho_0(r)$.

First, we divide our charge density $\rho_0(r)$ into two parts $\rho_0'(r)$ and $\rho_0''(r)$. Both charge densities are neutral, and they vary in the vacuum and interstitial regions, respectively. The sum of these two charge densities gives $\rho_0(r)$, therefore, we can solve the Poisson equation (6.20) independently for $\rho_0'(r)$ and $\rho_0''(r)$, with the boundary conditions (6.21) for the solutions $V_0'(r)$ and $V_0''(r)$. The sum of the latter two gives us $V_0(r)$.

1. The part of $\rho_0(r)$, charge density $\rho_0'(r)$ is constructed as:

$$\rho_0'(r) = \rho_0(r) + \bar{\rho}, \quad r < R; \quad \rho_0'(r) = 0, \quad r > R, \quad (6.25)$$

and the charge neutrality condition implies:

$$\int_0^R r \rho_0'(r) dr = 0. \quad (6.26)$$

Equation (6.26) allows us to compute $\bar{\rho}$:

$$\int_0^R r \left(\sum_{\mathbf{G}_{\parallel}} \rho_{0, \mathbf{G}_{\parallel}} J_0(G_{\parallel} r) \right) dr = -\bar{\rho} \int_0^R r dr = -\frac{R^2}{2} \bar{\rho}, \quad (6.27)$$

$$\frac{R^2}{2} \rho_{0,0} + \sum_{\mathbf{G}_{\parallel} \neq 0} \rho_{0, \mathbf{G}_{\parallel}} \int_0^R r J_0(G_{\parallel} r) dr = -\frac{R^2}{2} \bar{\rho}, \quad (6.28)$$

but

$$\int_0^R r J_0(G_{\parallel} r) dr = \frac{1}{G_{\parallel}^2} \int_0^{G_{\parallel} R} r J_0(r) dr = \frac{R J_1(G_{\parallel} R)}{G_{\parallel}}. \quad (6.29)$$

This leads to:

$$\begin{aligned}\bar{\rho} &= -\rho_{0,0} - \sum_{\mathbf{G}_{\parallel} \neq 0} \frac{2\rho_{0,G_{\parallel}} J_1(G_{\parallel} R)}{G_{\parallel} R}, \\ \rho'_0(r) &= \rho_{0,0} + \bar{\rho} + \sum_{\mathbf{G}_{\parallel} \neq 0} \rho_{0,G_{\parallel}} J_0(G_{\parallel} r) = \sum_{\mathbf{G}_{\parallel} \neq 0} \rho_{0,G_{\parallel}} \left(J_0(G_{\parallel} r) - \frac{2J_1(G_{\parallel} R)}{G_{\parallel} R} \right),\end{aligned}\quad (6.30)$$

when $r < R$. After substituting (6.30) into the Poisson equation, it reads:

$$\left(\frac{1}{r} \frac{d}{dr} r \frac{d}{dr} \right) V'_0 = -4\pi \left(\rho_{0,0} + \bar{\rho} + \sum_{\mathbf{G}_{\parallel} \neq 0} \rho_{0,G_{\parallel}} J_0(G_{\parallel} r) \right). \quad (6.31)$$

By checking we conclude that the solution is given by:

$$V'_0(r) = 4\pi \sum_{\mathbf{G}_{\parallel} \neq 0} \rho_{0,G_{\parallel}} \frac{J_0(G_{\parallel} r)}{G_{\parallel}^2} - \pi r^2 (\rho_{0,0} + \bar{\rho}) + A \ln r + B. \quad (6.32)$$

It is clear, as far as:

$$\left(\frac{1}{r} \frac{d}{dr} r \frac{d}{dr} + G_{\parallel}^2 \right) J_0(G_{\parallel} r) = 0 \Rightarrow \left(\frac{1}{r} \frac{d}{dr} r \frac{d}{dr} \right) J_0(G_{\parallel} r) = -G_{\parallel}^2 J_0(G_{\parallel} r),$$

and

$$\left(\frac{1}{r} \frac{d}{dr} r \frac{d}{dr} \right) \frac{r^2}{4} = 1.$$

On the other hand, the second term in (6.32) is a general solution of the equation:

$$\left(\frac{1}{r} \frac{d}{dr} r \frac{d}{dr} \right) (A \ln r + B) = 0.$$

At this point we can use the charge neutrality of the slab: the constants A and B are determined from the condition that the value and derivative of the potential on the vacuum boundary are equal to zero. Note, that the charge density $\rho'_0(r)$ does not give any contribution to the vacuum potential.

$$V'_0(r) = \frac{d}{dr} V'_0(r) = 0, \quad r = R. \quad (6.33)$$

The derivative of $V'_0(r)$ on the vacuum boundary is given by:

$$\frac{d}{dr} V'_0(R) = 4\pi \sum_{\mathbf{G}_{\parallel} \neq 0} \rho_{0,G_{\parallel}} \frac{J'_0(G_{\parallel} R)}{G_{\parallel}} - 2\pi R (\rho_{0,0} + \bar{\rho}) + \frac{A}{R},$$

but since $J'_0(r) = -J_1(r)$,

$$4\pi \sum_{\mathbf{G}_{\parallel} \neq 0} \rho_{0, \mathbf{G}_{\parallel}} \frac{J'_0(G_{\parallel} R)}{G_{\parallel}} = 2\pi R(\bar{\rho} + \rho_{0,0}),$$

and $A = 0$. The second boundary condition gives us

$$B = \pi R^2(\bar{\rho} + \rho_{0,0}) - 4\pi \sum_{\mathbf{G}_{\parallel} \neq 0} \rho_{0, \mathbf{G}_{\parallel}} \frac{J_0(G_{\parallel} R)}{G_{\parallel}^2}.$$

The potential V'_0 finally reads:

$$V'_0(r) = 4\pi \sum_{\mathbf{G}_{\parallel} \neq 0} \rho_{0, \mathbf{G}_{\parallel}} \left(\frac{J_0(G_{\parallel} r)}{G_{\parallel}^2} - \frac{J_0(G_{\parallel} R)}{G_{\parallel}^2} \right) + \pi(\bar{\rho} + \rho_{0,0}) (R^2 - r^2). \quad (6.34)$$

2. The second part of the density $\rho''_0(r)$ is varying in the vacuum, i.e. it is equal to $-\bar{\rho}$ for $r \leq R$ and equal to vacuum density $\rho^v_0(r)$ for $r \geq R$. This density also satisfies the neutrality condition:

$$\int_0^{\infty} r \rho''_0(r) dr = 0,$$

or, equivalently,

$$\int_0^R r \rho''_0(r) dr = \int_{\infty}^R r \rho''_0(r) dr.$$

By integrating $\rho''_0(r)$ we obtain $V''_0(r)$ (given by the interstitial and vacuum parts, $V''_i(r)$ and $V''_v(r)$, respectively) with the boundary conditions:

$$\lim_{r \rightarrow \infty} \frac{d}{dr} V''_0(r) = 0, \text{ and } \lim_{r \rightarrow \infty} V''_0(r) = 0.$$

Substituting the Green function (6.23) into (6.24) reads:

$$V''_v(r) = 2\pi R^2 \bar{\rho} \ln r - 4\pi \ln r \int_R^r t \rho^v_0(t) dt - 4\pi \int_r^{\infty} t \ln t \rho^v_0(t) dt. \quad (6.35)$$

In its turn, the interstitial part of $V''(r)$ is given by

$$V''_i(r) = 4\pi \ln r \int_0^r t \bar{\rho} dt + 4\pi \int_r^R t \ln t \bar{\rho} dt - 4\pi \int_R^{\infty} t \ln t \rho^v_0(t) dt, \quad (6.36)$$

or, as far as

$$\begin{aligned} \int_r^R t \ln t dt &= \left(\frac{R^2}{2} \ln R - \frac{r^2}{2} \ln r \right) - \left(\frac{R^2}{4} - \frac{r^2}{4} \right) \Rightarrow, \\ V''_i(r) &= 2\pi r^2 \bar{\rho} \ln r + 4\pi \int_r^R t \ln t \bar{\rho} dt - 4\pi \int_R^{\infty} t \ln t \rho^v_0(t) dt \\ &= 2\pi R^2 \bar{\rho} \ln R - \pi \bar{\rho} (R^2 - r^2) - 4\pi \int_R^{\infty} t \ln t \rho^v_0(t) dt, \\ \Rightarrow V''_i(r) &= V''_v(R) - \pi \bar{\rho} (R^2 - r^2). \end{aligned}$$

Finally, after adding $V_0'(r)$ and $V_0''(r)$ components of the potential, we obtain:

$$V_0^i(r) = V_i'(r) + V_i''(r) \quad (6.37)$$

$$= 4\pi \sum_{G_{\parallel} \neq 0} \rho_{0,G_{\parallel}} \left(\frac{J_0(G_{\parallel}r)}{G_{\parallel}^2} - \frac{J_0(G_{\parallel}R)}{G_{\parallel}^2} \right) + V_0^v(R) + \pi\rho_{0,0} (R^2 - r^2) \quad (6.38)$$

$$V_0^v(r) = 2\pi R^2 \bar{\rho} \ln r - 4\pi \ln r \int_R^r t \rho_0^v(t) dt - 4\pi \int_r^\infty t \ln t \rho_0^v(t) dt. \quad (6.39)$$

$G_z^2 + m^2 \neq 0$ -Components of the Coulomb Potential in the Vacuum

For the warped components of the Coulomb potential in the vacuum substituting the expansions of the density and the potential (6.14)-(6.15) in the Poisson equation yields (6.19):

$$\left(\frac{d^2}{dr^2} + \frac{1}{r} \frac{d}{dr} - G_z^2 - \frac{m^2}{r^2} \right) V_{G_z,m}(r) = -4\pi \rho_{G_z,m}(r), \quad (6.40)$$

with the boundary conditions of decaying of the potential in its value and derivative on infinity.

The set of equations (6.40) for every $G_z^2 + m^2 \neq 0$ -component of the vacuum Coulomb potential can be solved by using the Green function method. The corresponding equations for the Green functions look like:

$$\left(\frac{d^2}{dr^2} + \frac{1}{r} \frac{d}{dr} - G_z^2 - \frac{m^2}{r^2} \right) G_{G_z,m}(r, r') = -\frac{4\pi \delta(r - r')}{r}. \quad (6.41)$$

Two separate cases should be considered:

1. $G_z \neq 0$:

$$G_{G_z,m}(r, r') = 4\pi I_m(G_z r_<) K_m(G_z r_>), \quad (6.42)$$

where $I_m(r)$ and $K_m(r)$ are modified Bessel functions of the second kind.

2. $G_z = 0, m \neq 0$:

$$G_{0,m}(r, r') = \frac{2\pi}{m} \left(\frac{r_<}{r_>} \right)^m. \quad (6.43)$$

The resulting expression for a corresponding cylindrical harmonic of the vacuum Coulomb potential is given by:

$$V_{G_z,m}(r) = \int_0^\infty r' G_{G_z,m}(r, r') \rho_{G_z,m}(r') dr', \quad (6.44)$$

where $r > R_{\text{vac}}$.

Since the cylindrical harmonic of the charge density, to be integrated, is represented differently in the vacuum and interstitial regions, we divide the cylindrical harmonic of the

vacuum potential into two parts, each part reflecting the influence of the corresponding part of the charge density harmonic: $V_{G_z,m} = V_{G_z,m}^v + V_{G_z,m}^i$, so that

$$V_{G_z,m}^i(r) = \int_0^{R_{\text{vac}}} r' G_{G_z,m}(r, r') \rho_{G_z,m}(r') dr', \quad V_{G_z,m}^v(r) = \int_{R_{\text{vac}}}^{\infty} r' G_{G_z,m}(r, r') \rho_{G_z,m}(r') dr'. \quad (6.45)$$

Now substituting the corresponding Green functions we come to the following expressions:

1. $G_z \neq 0$:

$$\begin{aligned} V_{G_z,m}^i(r) &= 4\pi K_m(G_z r) \int_0^R r' I_m(G_z r') \rho_{G_z,m}(r') dr', \\ V_{G_z,m}^v(r) &= 4\pi I_m(G_z r) \int_r^{\infty} r' K_m(G_z r') \rho_{G_z,m}(r') dr' \\ &\quad + 4\pi K_m(G_z r) \int_R^r r' I_m(G_z r') \rho_{G_z,m}(r') dr'. \end{aligned} \quad (6.46)$$

2. $G_z = 0, m \neq 0$:

$$\begin{aligned} V_{G_z,m}^i(r) &= \frac{2\pi}{mr^m} \int_0^R (r')^{m+1} \rho_{G_z,m}(r') dr', \\ V_{G_z,m}^v(r) &= \frac{2\pi r^m}{m} \int_r^{\infty} \frac{\rho_{G_z,m}(r')}{(r')^{m-1}} dr' + \frac{2\pi}{mr^m} \int_R^r (r')^{m+1} \rho_{G_z,m}(r') dr'. \end{aligned} \quad (6.47)$$

Due to the analytical representation of the charge density in the interstitial region, as given by (6.17), we rewrite equations (6.46)–(6.47) in the following way:

1. $G_z \neq 0$:

$$V_{G_z,m}^i(r) = 4\pi K_m(G_z r) i^m \sum_{\mathbf{G}_{\parallel}} \rho_{G_z, \mathbf{G}_{\parallel}} e^{-im\varphi_{\mathbf{G}_{\parallel}}} \int_0^R r' I_m(G_z r') J_m(G_{\parallel} r') dr', \quad (6.48)$$

which can be calculated analytically in terms of the vacuum boundary values of the special functions:

$$\int_0^R r I_m(G_z r) J_m(G_{\parallel} r) dr = \frac{R}{G^2} \left(G_z I_{m+1}(G_z R) J_m(G_{\parallel} R) + G_{\parallel} I_m(G_z R) J_{m+1}(G_{\parallel} R) \right), \quad (6.49)$$

allowing us to reduce the integration problem to a \mathbf{G}_{\parallel} -summation, reading:

$$\begin{aligned} V_{G_z,m}^i(r) &= 4\pi R K_m(G_z r) i^m \sum_{\mathbf{G}_{\parallel}} \frac{\rho_{G_z, \mathbf{G}_{\parallel}}}{G^2} e^{-im\varphi_{\mathbf{G}_{\parallel}}} \times \\ &\quad \times \left(G_z I_{m+1}(G_z R) J_m(G_{\parallel} R) + G_{\parallel} I_m(G_z R) J_{m+1}(G_{\parallel} R) \right). \end{aligned} \quad (6.50)$$

2. $G_z = 0, m \neq 0$:

$$V_{G_z, m}^i(r) = \frac{2\pi i^m}{mr^m} \sum_{\mathbf{G}_{\parallel}} \rho_{0, \mathbf{G}_{\parallel}} e^{-im\varphi_{\mathbf{G}_{\parallel}}} \int_0^R (r')^{m+1} J_m(G_{\parallel} r') dr'. \quad (6.51)$$

In this case a following integration formula can be used:

$$\int_0^R r^{m+1} J_m(G_{\parallel} r) dr = \frac{\int_0^{G_{\parallel} R} (G_{\parallel} r)^{m+1} J_m(G_{\parallel} r) d(G_{\parallel} r)}{G_{\parallel}^{m+2}} = \frac{R^{m+1} J_{m+1}(G_{\parallel} R)}{G_{\parallel}}. \quad (6.52)$$

The final expression reads:

$$V_{G_z, m}^i(r) = \frac{2\pi i^m R}{m \left(\frac{r}{R}\right)^m} \sum_{\mathbf{G}_{\parallel} \neq 0} \frac{\rho_{0, \mathbf{G}_{\parallel}}}{G_{\parallel}} e^{-im\varphi_{\mathbf{G}_{\parallel}}} J_{m+1}(G_{\parallel} R). \quad (6.53)$$

Integrals of the part of the vacuum potential, coming from the vacuum charge density are directly calculated on the real grid in the vacuum region.

Fourier Components of the Interstitial Coulomb Potential

Up to now we found a way to calculate the vacuum part of the total Coulomb potential. This gives us an opportunity to use its boundary values on the interstitial-vacuum boundary in order to solve the boundary problem and find the interstitial part of the Coulomb potential.

Logically, the largest contribution to the Coulomb potential in the interstitial comes from the interstitial charge. One of the possible solutions for the Poisson equation in the interstitial we even know (having already the Fourier representation):

$$\tilde{V}_{\mathbf{G}} = \frac{4\pi\rho_{\mathbf{G}}}{G^2}, \quad \tilde{V}_{\mathbf{0}} = 0. \quad (6.54)$$

However, the potential \tilde{V} gives wrong values on the interstitial-vacuum boundary, reflecting also the contributions of the charge from the neighboring repeating unit cells to the Poisson equation. But taking into account considerations above, this potential can be treated as a core for the correct Coulomb interstitial potential, to which small corrections can be added in order to ensure the continuity of the total Coulomb potential on the vacuum-interstitial boundary. This idea is realized by introducing an auxiliary potential \mathcal{V} , which, when added to \tilde{V} gives the correct interstitial potential:

$$\tilde{V}(\mathbf{r}) + \mathcal{V}(\mathbf{r}) = V^I(\mathbf{r}). \quad (6.55)$$

Obviously, \mathcal{V} has to satisfy Laplace equation:

$$\Delta\mathcal{V}(\mathbf{r}) = 0, \quad (6.56)$$

which should be solved with the following boundary condition:

$$\mathcal{V}(R_{\text{vac}}) = V^V(R_{\text{vac}}) - \tilde{V}(R_{\text{vac}}), \quad (6.57)$$

where $V^V(R_{\text{vac}})$ and $\tilde{V}(R_{\text{vac}})$ denote the values of the vacuum Coulomb potential V^V and potential \tilde{V} on the cylinder with the radius R_{vac} , being the interstitial-vacuum boundary.

Starting with the representation of \mathcal{V} in terms of cylindrical harmonics, it can be easily checked, that analytical expressions are the following:

$$\mathcal{V}_{m,G_z}(r) = \begin{cases} \tilde{V}_{0,0}(r) - \tilde{V}_{0,0}(R) + V_{0,0}^V(R_{\text{vac}}) + \pi\rho_{0,0}(R_{\text{vac}}^2 - r^2) & m = G_z = 0 \\ \left(V_{0,m}^{\text{vac}}(R_{\text{vac}}) - \tilde{V}_{0,m}(R_{\text{vac}}) \right) \frac{R_{\text{vac}}^m}{r^m} & G_z = 0, m \neq 0 \\ \left(V_{G_z,m}^V(R_{\text{vac}}) - \tilde{V}_{G_z,m}(R_{\text{vac}}) \right) \frac{I_m(G_z r)}{I_m(G_z R_{\text{vac}})} & m \cdot G_z \neq 0 \end{cases} \quad (6.58)$$

Therefore, every (m, G_z) -component of \mathcal{V} can be analytically calculated on a uniform 2D net of grid points in the rectangle with the side \tilde{D} , including the interstitial region, and then Fourier back-transformed, obtaining Fourier representation of \mathcal{V} in terms of coefficients $\mathcal{V}_{\mathbf{G}}$. Finally, by a simple addition of $\mathcal{V}_{\mathbf{G}}$ and $\tilde{V}_{\mathbf{G}}$ for every reciprocal vector \mathbf{G} we obtain the Fourier coefficients of the interstitial Coulomb potential $V_{\mathbf{G}}^I$.

6.2 Exchange–Correlation Potential

The problem of the determination of the exchange correlation potential is quite different from the Coulomb potential. On one hand, V_{xc}^σ is a local quantity, i.e. $V_{xc}^\sigma(\mathbf{r})$ depends only on $n_\uparrow(\mathbf{r})$ and $n_\downarrow(\mathbf{r})$ at the same position \mathbf{r} . Thus, the muffin-tins, the interstitial- and vacuum-region can be treated independently. On the other hand, V_{xc}^σ and ϵ_{xc}^σ are non-linear functions of n_\uparrow and n_\downarrow . Therefore, V_{xc}^σ and ϵ_{xc}^σ have to be calculated in real space in the same way. First, n_\uparrow and n_\downarrow are transformed to real space, where V_{xc}^σ and ϵ_{xc}^σ are calculated. Then V_{xc}^σ and ϵ_{xc}^σ are Fourier back-transformed. Then, V_{xc}^σ is added to the Coulomb potential, yielding the spin-dependent potential V_\uparrow and V_\downarrow . ϵ_{xc}^σ is needed for the determination of the total energy.

6.2.1 Calculation of ϵ_{xc}^σ and V_{xc}^σ in the Interstitial

In the interstitial-region the charge density is expanded into three-dimensional stars with coefficients n_s^σ . Multiplying these by $e^{i\mathbf{R}\mathbf{G}^\sigma}$ yields the plane-wave coefficients n_G^σ . If the space group is symmorphic the star and plane-wave coefficients are identical. However, due to numerical inaccuracy, the calculated coefficients of symmetry-equivalent plane-waves are not exactly equal, and the corresponding star coefficient is obtained from the average of the plane-wave coefficients. In the next step a three-dimensional Fast-Fourier

transform is carried out. Then the exchange-correlation potential is calculated on a real space mesh $\{\mathbf{r}_i\}$. Finally, V_{xc}^σ is back-transformed, and the star coefficients are computed.

$$n_s^\sigma \longrightarrow n_G^\sigma \xrightarrow{FFT} n^\sigma(\mathbf{r}_i) \longrightarrow V_{xc}^\sigma(\mathbf{r}_i) \xrightarrow{FFT^{-1}} V_{xc}^{\sigma,G} \longrightarrow V_{xc}^{\sigma,s}.$$

6.2.2 Calculation of ϵ_{xc}^σ and V_{xc}^σ in the Spheres

The muffin-tin charge is expanded into lattice harmonics and radial functions. The radial functions are stored on a discrete real-space mesh. Thus, the transform to real space affects only the angular part. The charge density is calculated on a set of special angular points $\hat{\mathbf{r}}_i = (\theta_i, \phi_i)$. Again, the exchange correlation potential is calculated in real space. Thereafter, the resulting $V_{xc}^\sigma(\mathbf{r})$ is expanded into spherical harmonics Y_L . The Y_L are orthonormal, therefore the coefficients can be obtained from

$$v_{xc,L}^\sigma(r) = \int Y_L(\hat{\mathbf{r}}) V_{xc}^\sigma(r, \hat{\mathbf{r}}) d\Omega. \quad (6.59)$$

The choice of the points $\{\hat{\mathbf{r}}_i = (\theta_i, \phi_i)\}$, on which $n^\sigma(\mathbf{r})$ and $V_{xc}^\sigma(\mathbf{r})$ are calculated, depends on the integration method, that is used to perform the angular integration. In the current implementation (6.59) is computed by a Gauß-Legendre integration and the angular points are chosen such, that the orthonormality condition of the Y_L holds also for the angular mesh $\{\hat{\mathbf{r}}_i\}$.

6.2.3 Calculation of ϵ_{xc}^σ and V_{xc}^σ in the Vacuum

As we have already mentioned, the exchange-correlation potential $V_{xc}(\mathbf{r})$ in the vacuum, as well as in the interstitial and MT regions, is found on the real grid in cylindrical coordinates (r, φ, z) . For a given radial point r_i in the vacuum the two-dimensional charge density $\rho(r_i; \varphi, z)$ is found with the help of FFT. This means, that $\rho(r_i; \varphi, z)$ and the two-dimensional exchange-correlation potential $V_{xc}(r_i; \varphi, z)$ (as a function of the charge density $\rho(r_i; \varphi, z)$) are found on a linear grid in the (φ, z) plane $\{\varphi, z : 0 \leq \varphi < 2\pi, 0 \leq z < T\}$. Further back Fourier transformation in this plane gives us a set of Fourier coefficients $\{V_{xc}^\mu(r_i)\}$ – the coefficients of the two-dimensional stars $\Phi_\mu(\varphi, z)$ in the expansion of the exchange-correlation potential (see (3.20)). The described algorithm is repeated for every point r_i from the radial grid of points. At the end of the procedure, the exchange-correlation potential is added to the Coulomb potential on the radial grid.

Having a linear angular grid on the segment $(0, 2\pi)$ with the number of points depending only on m_{\max} for the charge density and potential, obviously causes an increase in the distance between the grid points in 3D proportionally to r_i . Therefore it might seem that the accuracy in the description of the exchange-correlation potential (and the charge density) decreases as r_i increases. But actually the accuracy of the representation is only determined by m_{\max} , assuming to be the same for every r_i . Furthermore, the exchange-correlation potential, being especially important in the vacuum, decays very fast into the vacuum. Therefore, beyond some certain radial point r_0 , which is much less

then the ending point of the vacuum, only the cylindrically symmetric component of the potential becomes really important. In a similar spirit, in the film-FLAPW method [50] for the last 150 grid points of the vacuum, only the z -dependent part of the potential can be kept.

In the case of GGA, the exchange-correlation energy is written like:

$$E_{xc}[\rho] = \int \varepsilon_{xc}(\rho(\mathbf{r}), |\nabla\rho(\mathbf{r})|) d\mathbf{r}, \quad (6.60)$$

which defines the exchange-correlation potential as the functional derivative of E_{xc} with respect to the density ρ , i.e.,

$$V_{xc}(\mathbf{r}) = \frac{\delta E_{xc}[\rho]}{\delta\rho(\mathbf{r})} = \frac{\partial\varepsilon_{xc}}{\partial\rho(\mathbf{r})} - \nabla \cdot \frac{\partial\varepsilon_{xc}}{\partial\nabla\rho(\mathbf{r})}. \quad (6.61)$$

Since the energy depends on $|\nabla\rho(\mathbf{r})|$, one finds from (6.61) that in order to obtain V_{xc} one requires not only $|\nabla\rho(\mathbf{r})|$, but also $\Delta\rho(\mathbf{r})$ and $\nabla\rho(\mathbf{r}) \cdot \nabla|\nabla\rho(\mathbf{r})|$ [124]. These quantities, as well as the exchange-correlation energy and potential, are found in the vacuum region on the real space grid in cylindrical coordinates (r, φ, z) . If we denote by \hat{e}_r , \hat{e}_z and \hat{e}_φ the orthogonal basis vectors at a given point in the vacuum, then the gradient of the charge density will be written as:

$$\nabla\rho(\mathbf{r}) = \frac{\partial\rho(\mathbf{r})}{\partial r} \hat{e}_r + \frac{1}{r} \frac{\partial\rho(\mathbf{r})}{\partial\varphi} \hat{e}_\varphi + \frac{\partial\rho(\mathbf{r})}{\partial z} \hat{e}_z \quad (6.62)$$

The following two expressions stand for the absolute value of the gradient and the Laplacian:

$$|\nabla\rho(\mathbf{r})| = \sqrt{\left(\frac{\partial\rho(\mathbf{r})}{\partial r}\right)^2 + \frac{1}{r^2} \left(\frac{\partial\rho(\mathbf{r})}{\partial\varphi}\right)^2 + \left(\frac{\partial\rho(\mathbf{r})}{\partial z}\right)^2}, \quad (6.63)$$

$$\Delta\rho(\mathbf{r}) = \frac{1}{r} \frac{\partial}{\partial r} \left(r \frac{\partial\rho(\mathbf{r})}{\partial r} \right) + \frac{1}{r^2} \frac{\partial^2\rho(\mathbf{r})}{\partial\varphi^2} + \frac{\partial^2\rho(\mathbf{r})}{\partial z^2}.$$

These quantities and a subsequent expression $\nabla\rho(\mathbf{r}) \cdot \nabla|\nabla\rho(\mathbf{r})|$, involve the partial derivatives of the first and second order of the charge density with respect to the spatial coordinates. The radial derivatives of the vacuum charge density components $\frac{\partial}{\partial r}\rho_{m,G_z}(r)$ and $\frac{\partial^2}{\partial r^2}\rho_{m,G_z}(r)$ are found numerically on the linear radial grid. After that, knowing the analytical exponential dependence of the charge density in the vacuum on cylindrical φ and z coordinates, the rest of the mixed derivatives of the first and second order can be found, for instance,

$$\frac{\partial^2\rho(\mathbf{r})}{\partial\varphi\partial r} = -i \sum_{G_z,m} m \frac{\partial\rho_{G_z,m}(r)}{\partial r} e^{im\varphi} e^{iG_z z}. \quad (6.64)$$

The values of the derivatives are calculated on a uniform real space (φ, z) grid for every radial point r_i with the use of two-dimensional Fourier transformations. Finally, the GGA exchange-correlation potential and energy density ε_{xc} are determined on the real space grid making an explicit use of analytical expansions for v_{xc} and ε_{xc} .

Chapter 7

Results

7.1 Monowires of Ti and 4*d* transition elements

There is presently a strong interest in the physics of metal nanowires in low dimensions. A freely standing metallic nanowire is formed when two pieces of material, initially at contact, are pulled away from each other. In this process, a connective bridge elongates and narrows. Experimentally, segments of such nanowires have been formed between tips in particular of Au [49, 91], but very often also in break junctions of Pt and Ir [101]. The one-dimensional character of nanowires causes several new physical phenomena to appear, such as quantized conductance and helical geometries.

In addition to these, another type of stable nanowires also exists. Structurally stable monowires can be grown on stepped surfaces, such as, for example, the recently observed Co monowire on Pt substrate [23], or inside tubular structures. E.g. Ag nanowires of micrometer lengths grown inside self-assembled calix[4]hydroquinine nanotubes [36].

An interesting question is when and how magnetism may appear in nanowires and how this effects the other properties. Those metals, which are magnetic already in bulk, can be expected to be magnetic also as nanowires. But may a normally nonmagnetic in the bulk material become magnetic? It has been suggested that even a jellium confined in a thin cylinder may in principle magnetize for certain radii of the cylinder [129]. However, the moment formation is confined to very special radius of electron densities, and the associated energy gain is very small. That is of course so because exchange interactions are not particularly strong in *sp* band metal (Na or Al), a typical system which might be described by the jellium model. The situation is radically different for transition metals of the 3*d*, 4*d* and 5*d* series. Because of the partly occupied *d* orbitals, their ability to magnetize is much stronger and of a fundamentally different nature compared to jellium. In bulk, the resulting large exchange interactions are overwhelmed by large kinetic energy of the electrons, resulting in very large bandwidths and a nonmagnetic ground state. It is well established that the origin of magnetic ordering in low-dimensional *d* or *f* materials is a direct or indirect exchange interaction between electrons in the partially filled *d* or *f* electronic shells.

In this chapter we concentrate on monoatomic wires of the $3d$ element Ti, and the transition $4d$ -elements, in particular, monowires of Ru, Rh and Pd. For these atoms magnetism in low dimensions was reported. For Pd, monowires consisting of a single strand of atoms, have been recently observed by Rodrigues *et al.* [90]. Rather high magnetic moments for this element for an infinite monowire of atoms as well as 3 atoms long wires, contacted to the Pd leads were also observed. Nevertheless, the magnetic moment of Pd atoms disappears already in a Pd(6,0) nanowire, showing a strong dependence of exchange interaction on the coordination number. For Rh it has been suggested experimentally, that small clusters of this metal may possess permanent magnetic moments [12, 11], while bulk Rh is nonmagnetic. Also tendency towards strong magnetism of the monowires of Rh and Ru was theoretically predicted, both for a freestanding configuration and on the surfaces of Ag and Cu [105].

The well known theorems on the absence of magnetic ordering in one and two dimensions [59, 119] are inapplicable to real systems, hence, do not preclude magnetic effects for the real linear chains and nanowires. This is due to the fact that nonzero temperature ruins ideal 1D or 2D ordering and anisotropy term additionally contributes to the Heisenberg Hamiltonian. However, thermal fluctuations in nanowires are expected to be very large, which would destroy long range magnetic order in the absence of an external magnetic field [66]. Depending on temperature and on external field, there will nevertheless be two different fluctuation regimes: a slow one and a fast one.

Slow fluctuations such as those attainable at low temperatures and/or in presence of a sufficiently large external field take a nanomagnet to superparamagnetic state, where magnetization fluctuates between equivalent magnetic valleys, separated, e.g., by anisotropy induced energy barriers. If the barriers are sufficiently large, the nanosystem spends most of the time within a single magnetic valley, and will for many practical purposes behave magnetic. We may under these circumstances be allowed to neglect fluctuations altogether, and to approximate some properties of the superparamagnetic nanosystem with those of a statically magnetized one. Experimentally, evidence of one-dimensional superparamagnetism with fluctuations sufficiently slow on the time scale of the probe was recently reported for Co atomic chain deposited at Pt surface steps [23].

At the opposite extreme – a situation reached for example at high temperatures and in zero external field – the energy barriers are so readily overcome, that the magnetism will be totally destroyed by fast fluctuations, leading to a conventional paramagnetic state. A complete description of this high entropy state is beyond the scope here.

In this chapter we will only deal with straight undimerized wires. This might appear oversimplifying, since, for instance, it has been calculated that infinite gold wires have a local energy minimum for a zigzag structure [62]. We will investigate this structure for a monowire of iron, presented later in the thesis. Our rationale for this simplification of the wire geometry is that wires – extended between two tips – are inevitably subject to stretching. Simple thermodynamics governing the flow of atoms at the wire-tip drives the thinning and implies a finite string tension. Thus, even if a free-ended wire favored a zigzag structure, this effect will be counteracted in the ultimate wire hanging between tips just before breaking of the contact.

7.1.1 Ti Monowire

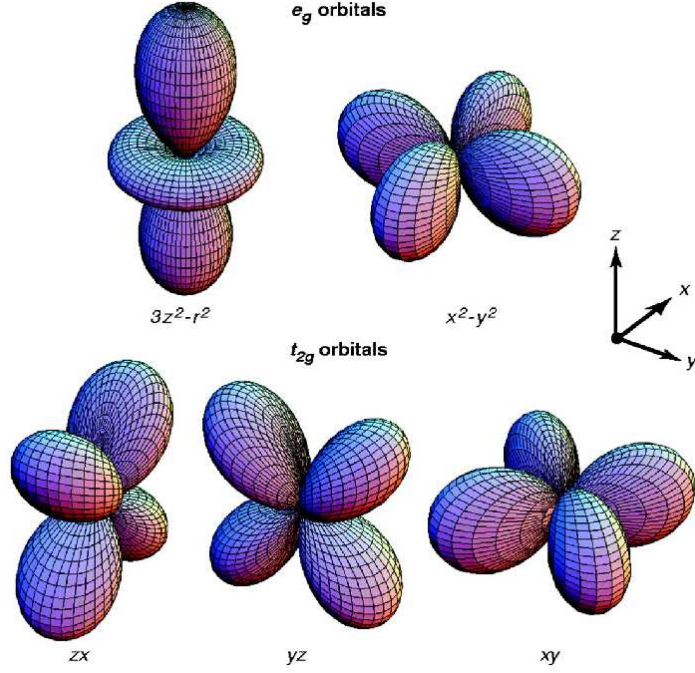
For the Ti monowire we used 16 k -points in one half of the Brillouin zone for calculations without spin-orbit coupling and 32 k -points for calculations with spin-orbit coupling. The monowire was calculated with two Ti atoms in the unit cell, allowing an antiferromagnetic solution. The parameters D and \tilde{D} were chosen to be 4.8 and 6.8 a.u. respectively. The muffin-tin radius was varying from 2.01 to 2.4 a.u. depending on the interatomic distance. The wavefunctions cut-off parameter K_{\max} was chosen to satisfy the relation $K_{\max} \cdot R_{MT} = l_{\max}$, with the $l_{\max} = 8$. The charge density cut-off parameter G_{\max} was set to the value of $3 \cdot K_{\max}$. The values of 36 and 18 were used for the vacuum angular expansion parameters for the charge density and basis functions, respectively. No symmetry restrictions were used. For calculating the optimal ferromagnetic distance we used the muffin-tin radius of 2.01 a.u. and K_{\max} of 4.0 a.u.⁻¹, together with inversion symmetry.

We have calculated the differences in total energies between the nonmagnetic, ferromagnetic and antiferromagnetic solutions in a large range of interatomic distances of 4 – 7 a.u., which are presented in the Fig. 7.2 (right,b). From this graph we conclude, that in a wide range of interatomic distances the atoms of Ti monowire prefer to order themselves ferromagnetically. However, the energy difference between the two magnetic configurations starts to decrease if the interatomic distance becomes larger than 6 a.u., which indicates the possibility that the magnetic ground state of a supported Ti monowire depends on the lattice parameter of the substrate.

The corresponding values of magnetic moments for the ferromagnetic solution are presented in the Fig. 7.2 (right,a). As we will see also for the monowires of other elements, the variation of the magnetic moment with the bond length reveals that the increase is rather steep, almost discontinuous at certain interatomic distances – this happens when one of the narrowed subbands passes through the Fermi level. The stepwise increase of the magnetic moment, which occurs at different bond lengths for the FM and AFM phases, is also the reason for the non-monotonous variation of the magnetic energy difference with the bond length.

Only for the ferromagnetic configuration we have calculated an optimal interatomic distance d_0 of 4.40 a.u., where the minimum of the total energy is reached (see Fig. 7.2 (left)). At this distance the magnetic moment in FM case is $1.05\mu_B$ per Ti atom. This configuration is by 74.3 meV lower in energy than the paramagnetic solution, while no AFM solution was found.

It is interesting to note, that our calculated d_0 is somewhat smaller than d_0 for the monowires of corresponding 4d- and 5d-elements with the same valent configuration: Zr ($4d^25s^2$) and Hf ($5d^26s^2$). We found that for the monowire of Zr the optimal distance (ferromagnetic) d_0 is 4.76 a.u. with the magnetic moment of $0.8\mu_B$ and $E_{NM} - E_{FM} = 42.2$ meV. The monowire of Hf, calculated by Spišák and Hafner in [106], was found to be nonmagnetic with d_0 of 4.91 a.u. This difference can be understood from the analysis of the paramagnetic bandstructure of the Ti MW at the optimal interatomic distance in comparison to corresponding data from [106]. The main difference comes from the fact

Figure 7.1: Five $3d$ -orbitals.

that $4d$ and $5d$ orbitals are more extended compared to $3d$, which, therefore, results in larger equilibrium lattice constants and higher bandwidths with the consequently smaller magnetic moments. On the base of this consideration the difference in the bulk lattice constants for Ti and Zr can be explained, which is around 10% for both the bulk and the monowire.

The first analysis of the $3d$ monowire bandstructure was given by Weinert and Freeman [121]. The symmetry of an isolated monowire is $D_{\infty h}$, as is the symmetry of the special k -points $\Gamma(k=0)$ and $X(k=\frac{\pi}{T})$. The symmetry of all other k -points is $C_{\infty v}$. Since $D_{\infty h}$ is the direct product of $C_{\infty v}$ and the inversion, there are no added degeneracies at Γ or X , hence, we will label each band by its representation along Δ . As we see from the from the Ti bandstructure 7.3, the s and d atomic functions split into three sets of bands: the doubly degenerate $\Delta_3(d_{xz}, d_{yz})$ and $\Delta_4(d_{x^2-y^2}, d_{xy})$ bands and the two singly degenerate bands $\Delta_1(s, d_{z^2})$. The Δ_4 bands are quite narrow since these functions are perpendicular to the chain, while Δ_3 bands are wider due to interactions along the chain. The Δ_1 band is composed of s and d_{z^2} orbitals extending along the chain which defines the z direction. For the early transition metals, the s and d_{z^2} bands are quite distinctly separated. With increasing band filling, the d_{z^2} states are lowered in energy with respect to the s states and the two bands merge into a single $(s - d_{z^2})$ hybridized band.

Charge density plots of different d -orbitals and corresponding bands are presented in Fig. 7.1 for the pure states and in Fig. 7.4 for the corresponding bands, associated with

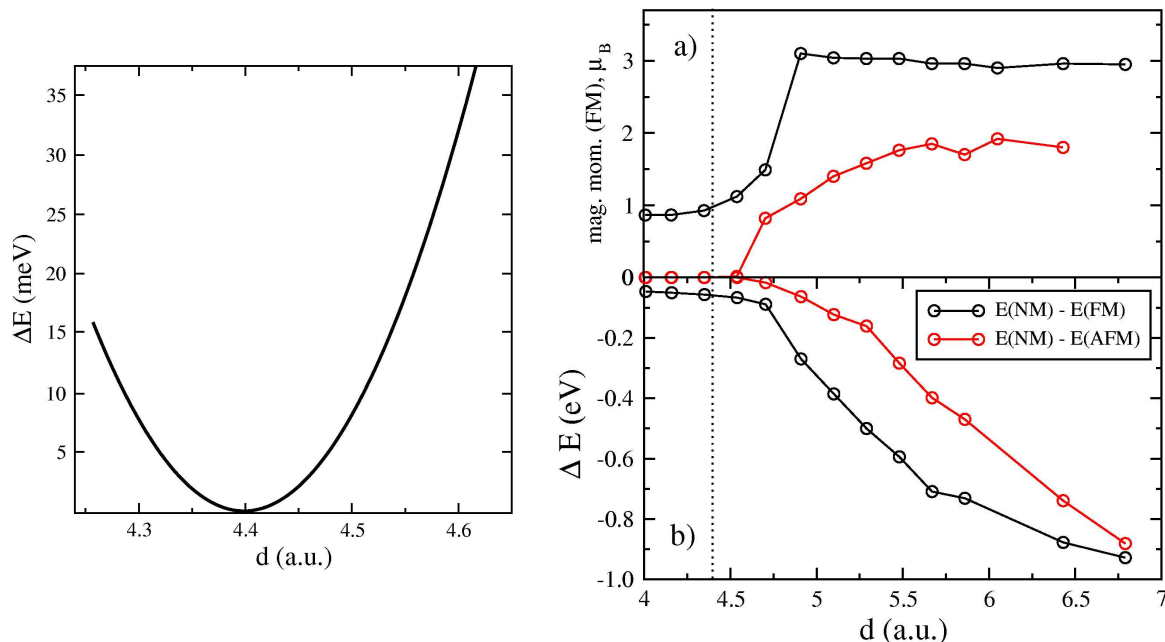


Figure 7.2: Left: ferromagnetic total energy versus interatomic distance $E_{\text{tot}}(d) - E_{\text{tot}}(4.4 \text{ a.u.})$. From this plot the optimal distance can be found to be 4.40 a.u. Right (a): magnetic moment per Ti atom for the ferromagnetic and antiferromagnetic case, depending on d . For the antiferromagnetic case magnetic moments inside the muffin-tin spheres are given; (b) differences in energies between the paramagnetic and ferromagnetic solutions $E_{NM} - E_{FM}$ (black) and between the paramagnetic and antiferromagnetic solutions $E_{NM} - E_{AFM}$ (red) are presented depending on the interatomic distance d (b). With increasing interatomic distance the difference in energies $E_{FM} - E_{AFM}$ vanishes.

the chain, together with the spin-density plot at the Fermi energy.

By symmetry, all the bands have zero slope at the zone boundary, causing van Hove singularities (infinities) in the densities of states (DOS), whereas in 3D cases, these van Hove singularities yield a finite DOS (see Fig. 7.5,(b),(c)). Although these infinities will in reality be broadened by thermal and phonon effects, they should still give large contributions to the optical absorption. For Zr, the paramagnetic DOS at the Fermi energy for all the 4d elements was found to be the highest. Anyway, as our calculations show, the DOS at the Fermi energy for Ti MW is also rather high (Fig.7.5,(a)), and, therefore, if the Stoner picture for magnetic ordering is applicable, Ti monowire should be ferromagnetic with a high magnetic moment. The paramagnetic bandstructure, Fig. 7.3,(a), also allows us to suggest the following: the symmetric shape of the Δ_4 -band in the one-dimensional chains, which contrasts the asymmetric DOS of the hexagonal close packed and face centered cubic transition metals could lead to a variation of the magnetic ground state from ferromagnetism (FM) to antiferromagnetism (AFM) and back to ferromagnetism with increasing band filling. This differs from the behavior of the bulk 3d metals, where fer-

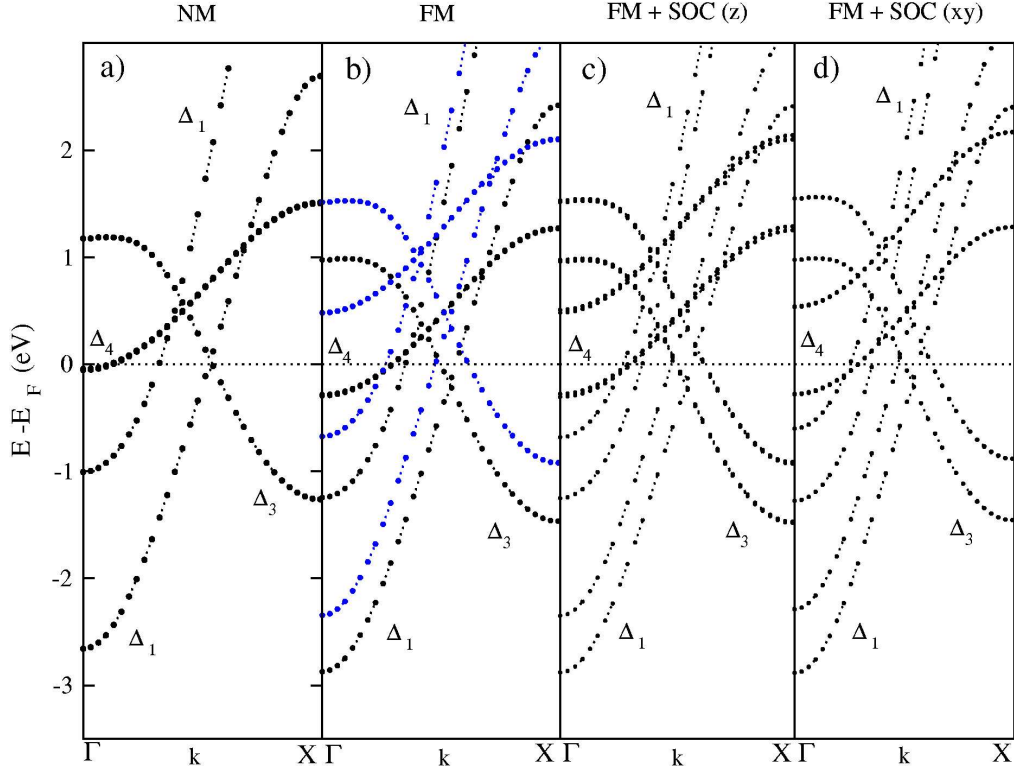


Figure 7.3: Bandstructures of the Ti monowire at the optimal (ferromagnetic) interatomic distance of 4.40 a.u. (a) paramagnetic bandstructure, (b) ferromagnetic bandstructure (c) ferromagnetic bandstructure with SOC, magnetization along the axis of the wire, (d) ferromagnetic bandstructure with SOC, magnetization perpendicular to the wire axis. By Δ_1 , the s - and d_{z^2} -bands are denoted, by Δ_3 the d_{xz}, d_{yz} -bands, and by Δ_4 the $d_{x^2-y^2}, d_{xy}$ -bands.

romagnetism exists for metals with a more than half-filled band and antiferromagnetic order is stabilized for metals with a less than half-filled band, but the early $3d$ metals are nonmagnetic.

7.1.2 Monowires of $4d$ transition elements

In Fig. 7.6 we present the results of our calculations on the monowires of the $4d$ -transition metals from Y to Pd. We show the equilibrium interatomic distances d_0 , magnetic moments and the magnetization energy ΔE_M , defined as a total energy difference between the nonmagnetic and ground state magnetic solutions: $\Delta E_M = E_{FM(AF)} - E_{NM}$ (computed at d_0). Calculations were carried out with the computational parameters, close to those, described in section 7.1.1 for a monowire of titanium atoms.

In general, the chemical bonding in a monowire is, of course, quite different from the

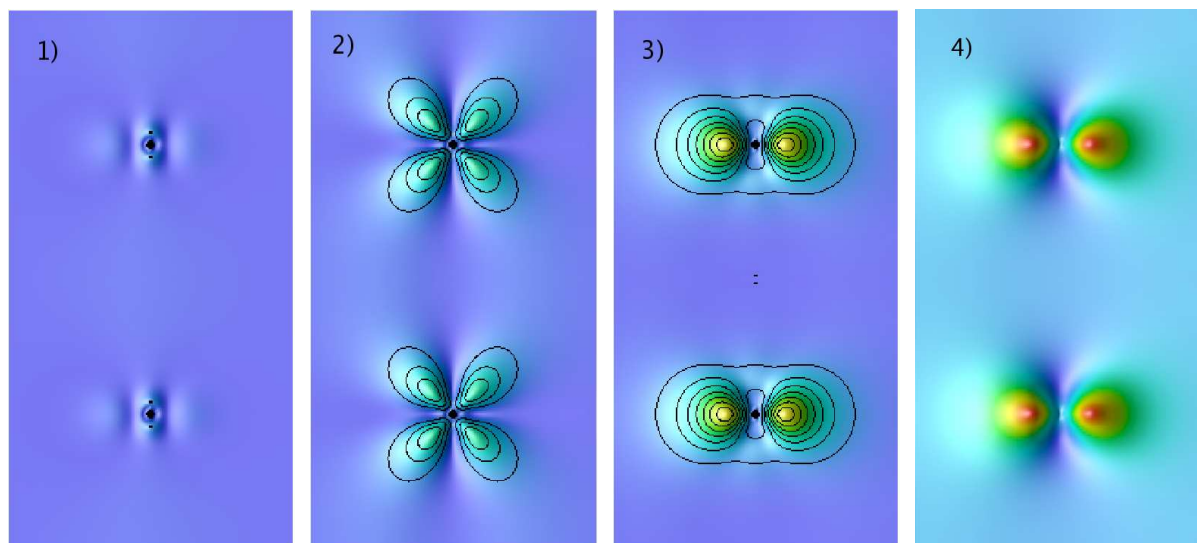


Figure 7.4: Charge density plots for the states (1) Δ_1 around -2.7 eV from the paramagnetic calculation in Fig. 7.3, (a); (2) for the state Δ_3 around 1.25 eV; (3) for the state Δ_4 around the Fermi energy, and (4) the spin density plot from the ferromagnetic calculation Fig. 7.3, (b), around E_F .

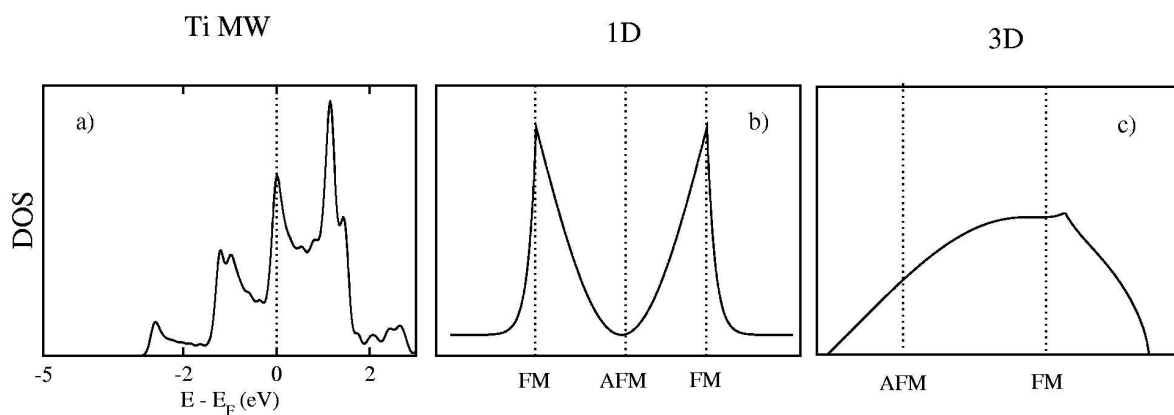


Figure 7.5: Densities of states plots. (a) DOS plot for a Ti MW at the equilibrium lattice constant of 4.4 a.u. (b) model DOS plot for a metal monowire, showing van Hove singularities coming from the flat band edges. When one of the van Hove singularities crosses the Fermi energy, monowire prefers to order ferromagnetically, rather than antiferromagnetically, due to Stoner criterion. Antiferromagnetic ordering is preferable for the metals with a half-filled band (see section 7.1.2) (c) model DOS plot for a 3D system. Ferromagnetism exists for metals with a more than half-filled band and antiferromagnetic order is stabilized for metals with a less than half-filled band.

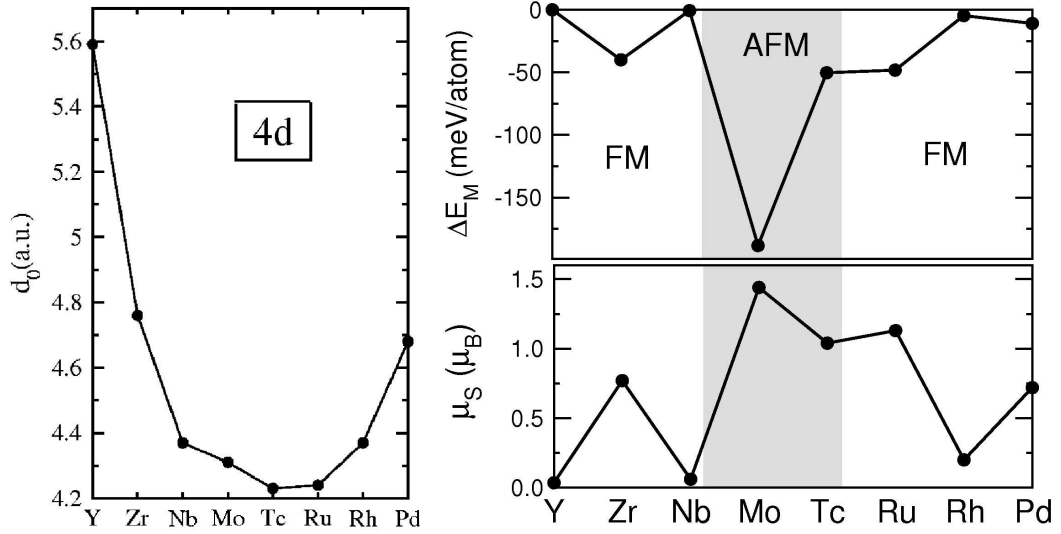


Figure 7.6: Left: equilibrium interatomic distance d_0 for the monowires of the 4d-transition metals from Y to Pd. Right (top): magnetization energy ΔE_M . Right (bottom): spin moment for the ground state magnetic solution (total for the FM and inside the metal muffin-tin sphere for the AFM chains)

bulk material. In a monowire, there are only two nearest neighbors, and, therefore, a smaller equilibrium lattice constant than in the bulk can be expected. This is exactly the case for the monowires of the 3d, 4d and 5d elements, as can be seen from the calculations in [14, 15, 76], where the trend towards decreasing of the equilibrium lattice constant in the case of lowering the dimensionality of the system is clearly shown.

We would like to point out, however, that, strictly speaking, a monowire suspended on a tip or deposited on a surface will not have a quasi-stable configuration at the bond length which minimizes the total energy. In the case of a tip-suspended monowire, the interatomic distance, which minimizes a string tension rather than the total energy will be observed [14]. For a monowire, deposited on the surface, the interatomic distance will be determined by the surface used [106]. Therefore, it is preferable to consider the development of the magnetic properties of a monowire in a certain range of interatomic distances. Nevertheless, for simplicity, the bond length, which minimizes the total energy will be called in this section the equilibrium bond length d_0 .

The distances d_0 were calculated for the magnetic configuration, favorable in total energy around the equilibrium lattice constant. Clear parabolic dependency of the d_0 on the band filling is in a good agreement with Spišák and Hafner [106]. The trend of the bond weakening in going from the middle of the series with atoms with highly open shells to atoms with nearly closed d -shells at the end of the series was explained by Friedel [89] assuming a constant density of states of d -electrons. The shortest bond is formed between the Tc atoms, which have an almost half-filled d -shell. Deviations from the ideal parabolic

behavior reflect the one-dimensional nature of the monowires.

An important side-question is whether there exists a substantial magnetorestrictive effect in the wires, i.e. if the appearance of a magnetic moment causes an equilibrium interatomic distance to change. Although the calculated magnetic moments in the wires can become quite large sometimes, magnetism almost does not influence the equilibrium distance. The calculated equilibrium bond lengths of the magnetic wires are indeed larger, but not very much, typically, hundredths of an Å.

Comparing the DOS of each individual chemical element in 3D, 2D, and 1D, it can be found that the main difference that comes into picture on lowering the dimensionality is the reduction in the bandwidth. The bands become sharper, a manifestation of the reduced coordination, as we descend in dimensionality. For the cases with magnetic ground state, the exchange splitting increases en route. In metallic monowires, due to the one dimensionality of the system, the Stoner stability criterion against magnetism is violated leading to a magnetized monowire when a flat band edge approaches the Fermi energy. In case of transition metals, a strong Hund's rule magnetic moment may appear, creating a robust superparamagnetic state for temperatures not too high, transformable to a genuine magnetic state under an external field.

In the 4*d* series, Y is nonmagnetic, Zr, Ru, Rh and Pd wires are predicted to order ferromagnetically, Mo and Tc have an antiferromagnetic ground state. Niobium, being a border-line case, has a FM ground state with a magnetic moment of $0.05 \mu_B$, and orders antiferromagnetically under a very modest tensile strain. All the elements order ferromagnetically under a sufficiently large tensile strain, and for those with a nearly full *d*-band a stable or metastable FM state coexists with metastable AFM configuration at a higher energy. The magnetic moments of the FM wires are quite modest, the largest moment is found for Ru with about $1.1 \mu_B$, while the moments are substantially larger in the wires with an AFM ground state. In general, the transition from FM to AFM and back to the FM state with increasing the band filling can be perfectly explained on the basis of a scheme presented in Fig. 7.5. For Zr, which has the same valence configuration as Ti, the DOS for the monowire look similar to those of the Ti MW, with a peak at the Fermi energy coming from the Δ_4 -band at the Γ -point, causing, by the Stoner criterion, the FM ground state. When moving further along the 4*d* series, the DOS at the Fermi level is rather low, resulting in the AFM ground state for Mo and Tc. For the elements with an almost filled *d*-shell (Ru and Rh), a Δ_4 -based van Hove singularity at the Fermi energy appears again, this time due to the flat band edge at the *X*-point. The case of Pd will be considered further, as an appearance of magnetism in this monowire seems to be in a contradiction to the full *d*-shell. The paramagnetic DOS for the 4*d* monowires at the nonmagnetic equilibrium interatomic distances can be seen in [106].

In the following we concentrate on the monoatomic wires of the 4*d*-transition elements Ru, Rh and Pd, investigating ferromagnetism in these chains.

Monowires of Ru, Rh and Pd

Experimentally, it has been suggested that small Rh clusters may possess a permanent magnetic moment [12, 11], although bulk Rh is nonmagnetic. Also monoatomic overlayers of Rh and Ru on Ag(001) were predicted to be magnetic [95]. Very recently, experiments have shown the magnetic nature of linear chains of Pd obtained in a break junction [90].

The equilibrium bond lengths for monowires of Ru and Rh were calculated by Spišák and Hafner [106] using a projector augmented-wave method (PAW), for Ru, Rh and Pd by Nautiyal *et al.* [76] with the FLAPW WIEN97 package and by Delin and Tosatti [15] with the FP-LMTO method and WIEN97 package. Our calculated equilibrium ferromagnetic lattice constants of 2.24 Å (Ru), 2.31 Å (Rh) and 2.48 Å (Pd) agree very nicely with the data from these references: 2.23 Å (Ru), 2.27 Å (Rh) in Ref. [106]; 2.24 Å (Ru), 2.27 Å (Rh), 2.44 Å (Pd) in Ref. [76]. Moreover, in Ref. [15] the ferromagnetic d_0 is reported to be 2.27 Å for Ru, 2.31 Å for Rh and 2.56 Å for Pd, using FP-LMTO method. The difference in the magnetic moments calculated in these references of $0.98\mu_B$, $0.92\mu_B$ and $1.1\mu_B$ for Ru, $0.26\mu_B$, $0.16\mu_B$ and $0.3\mu_B$ for Rh ([106], [76], [15], respectively); $0.60\mu_B$ and $0.66\mu_B$ for Pd ([76] and [16], respectively), probably reflects the difference in computational methods and parameters used. Our values for the equilibrium magnetic moments are in a very good agreement with these references. We predict the following magnetic moments for these MWs at the equilibrium interatomic distances of 2.24 Å (Ru), 2.31 Å (Rh) and 2.48 Å (Pd): $1.13\mu_B$ for Ru, $0.2\mu_B$ for Rh, and $0.72\mu_B$ for Pd.

The MWs of the considered elements are predicted to be magnetic in a wide range of bond lengths. Spišák and Hafner [106] predict an energy difference of 39 meV between the total energies of the nonmagnetic and ferromagnetic solutions ($E_{NM} - E_{FM}$) for the Ru MW at the equilibrium bond length of 2.23 Å, and the difference of 6 meV for the Rh monowire at the d_0 of 2.27 Å. The same energy differences constitute 77 meV and 10 meV in [15]. For the Pd MW Ref. [15] gives 12 meV for the $E_{NM} - E_{FM}$ energy difference. This agrees very nicely with our results: 50.5 meV for Ru, 9.9 meV for Rh and 13.4 meV for Pd MWs (at 2.24 Å, 2.31 Å and 4.68 Å, respectively). For these distances no antiferromagnetic solution was found. However, Spišák and Hafner predicted that, for larger interatomic distances a metastable antiferromagnetic solution appears for the MWs of Rh and Ru, and a stabilization of the ferromagnetic configuration at further increase of the interatomic distance. In Ref. [16] antiferromagnetic Pd MW configurations were also tested, but were found to be energetically unstable compared to the ferromagnetic configuration.

It is well-known, that the inclusion of spin-orbit interaction for the MWs of $5d$ elements is crucial for their magnetic properties, and in some cases the SO interaction makes the magnetic ordering vanish, and, in principal, can destroy the stability of the magnetic ground state ([76, 14]). However, SO interaction is also important for the MWs of $4d$ elements. From the general point of view, appearance or disappearance of magnetism in the MWs of $4d$ and $5d$ elements can be attributed to the situation, where the flat band edges are getting close to the Fermi energy, and, in some sensitive cases, the SO coupling causes a splitting of the bands resulting in removing or appearance of the bands at the

Fermi energy. The SO interaction might also cause slight changes in the equilibrium lattice constants and energy differences between magnetic and nonmagnetic states. Therefore, inclusion of the spin-orbit coupling is very important for a correct description of the magnetic properties of the considered MWs.

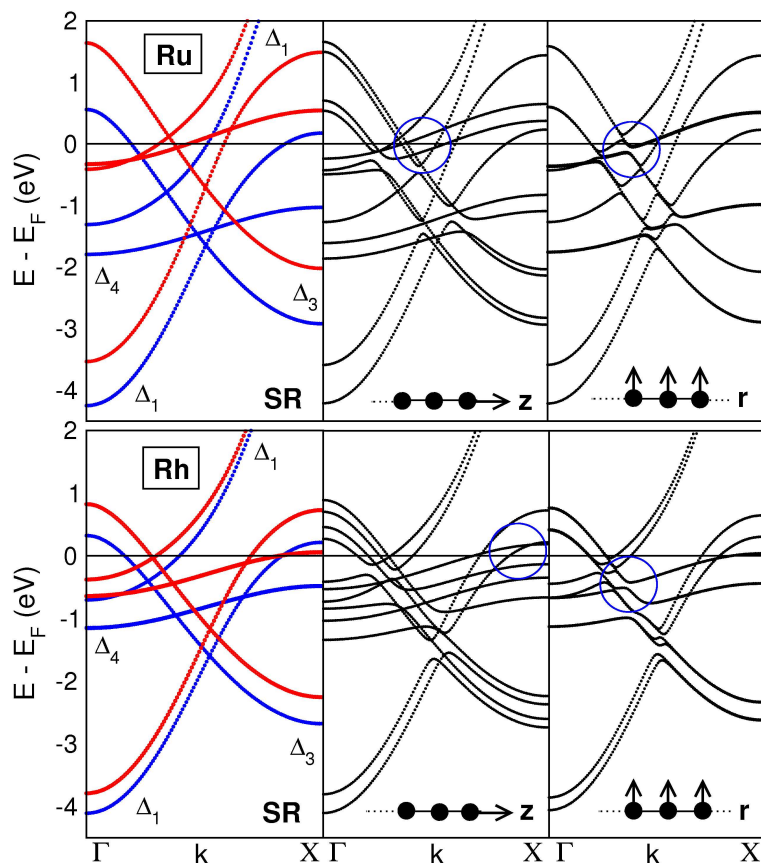


Figure 7.7: Bandstructures of Ru and Rh chains at an interatomic distance of $d=2.54$ Å, calculated without SOC (left panel) and with SOC for two different magnetization directions (middle and right panels). Spin-up and spin-down in the SR case are indicated with blue and red line, respectively. Blue circles mark areas with bands which give rise to orbital moments, as described in the text.

Monowires of Ru and Rh. The spin-polarized bandstructures of the Ru and Rh chains at the interatomic distance of 2.54 Å calculated without SO interaction (SR) are presented in Fig. 7.7 (left panel). In analogy to the Ti monowire, all the bands can be divided into three groups: $\Delta_3(d_{xz}, d_{yz})$, $\Delta_4(d_{x^2-y^2}, d_{xy})$ bands and the two bands $\Delta_1(s, d_{z^2})$, where, compared to the Ti MW, d_{z^2} band is lowered in energy with respect to the s states and the two bands merge into a single s - d_{z^2} hybridized band with an anticrossing around the Fermi level. Figure 7.7 shows that the major contribution to the central peak at the Fermi energy in the densities of states comes from the d -states, while the DOS around

the peak are due to s - d hybridized bands.

At the Γ and X points, both crucial points by symmetry, all band dispersions are horizontal, giving rise to very sharp band edge van Hove singularities. Since the bands have mostly d character at the edges, the exchange energy gain will be rather large, as compared to the nonmagnetic situation, if a d -band splits so that one of the spin-channel band edges ends up above the Fermi level, and the other one below. Strictly speaking, SO coupling will mix the two spin-channels so that, in general, an eigenvalue will have both majority and minority spin character. However, in the present calculations (Fig. 7.7, middle and right panels) this mixing is very small. Thus, if a band edge ends up sufficiently near the Fermi level, we may expect a magnetic moment to develop, which is the case for both elements. The bands, responsible for magnetism, are Δ_4 bands, close to the Fermi energy at X point. The bands of Rh are in general deeper than those of Ru due to one additional electron in the d shell, and, therefore, according to the Hund's rule, the magnetism of Rh MW is suppressed compared to Ru monowire, which can be seen also from the spin splitting of the bands in Fig. 7.7.

The magnetic moment per metal atom in the monowire, as a function of the interatomic distance is shown in Fig. 7.9 (top of the left panel). The black line refers to the scalar-relativistic (SR) calculations; blue and red lines refer to the calculations with the SO coupling included, with the magnetization along the wire direction (z -case) and perpendicular to the wire direction (r -case), respectively. The first thing to note is that Ru and Rh exhibit a magnetic moment for values of the bond length at or close to equilibrium. Another thing to notice is that the magnetic profiles change when SO is included, especially for Rh. This leads, in particular, to disappearance of magnetism in the case of the radial magnetization for this chain. For both elements the magnetic moments reach a plateau value for the values of interatomic distance larger than 2.75 Å. The value of this plateau magnetic moment is close to that of the isolated atom.

Monowire of Pd. The development of the magnetic moment (without and with SO interaction included) with the interatomic distance can be seen in Fig. 7.9. The magnetic moment rapidly reaches the maximum value of around $0.7\mu_B$ at 2.4 Å and preserves this value over a large region of distances, when, after 2.8 Å it monotonically decreases to a zero value at around 3.4 Å, where monowire undergoes a metal-insulator transition, opening a s - d gap, becoming a chain of isolated atoms. However, experimental data ([90]) suggest that well before these bond lengths the monowire is already broken.

In the bulk and also at surfaces (for instance, Ag(111), Ag(001), Au(001)), the $4d$ bands of Pd are rather wide, and, therefore, spin polarization does not occur. On the other hand, as an atom, Pd has a completely filled $4d$ shell. Therefore, two limiting cases are nonmagnetic and appearance of magnetism for the Pd monowire needs investigation. Certain insights can be made based on the fact, that large Pd clusters are expected to be magnetic [73], whereas small Pd clusters are not [93]. We should suppose, that with increasing of the interatomic distance the interatomic hybridization causes a certain s - d transfer, and, hence, the $4d$ shell becomes partly unfilled and symmetry breaking through spin polarization becomes possible. Hund's rule makes it reasonable to assume that spin polarization will also be energetically favorable. In other words, reducing of the number

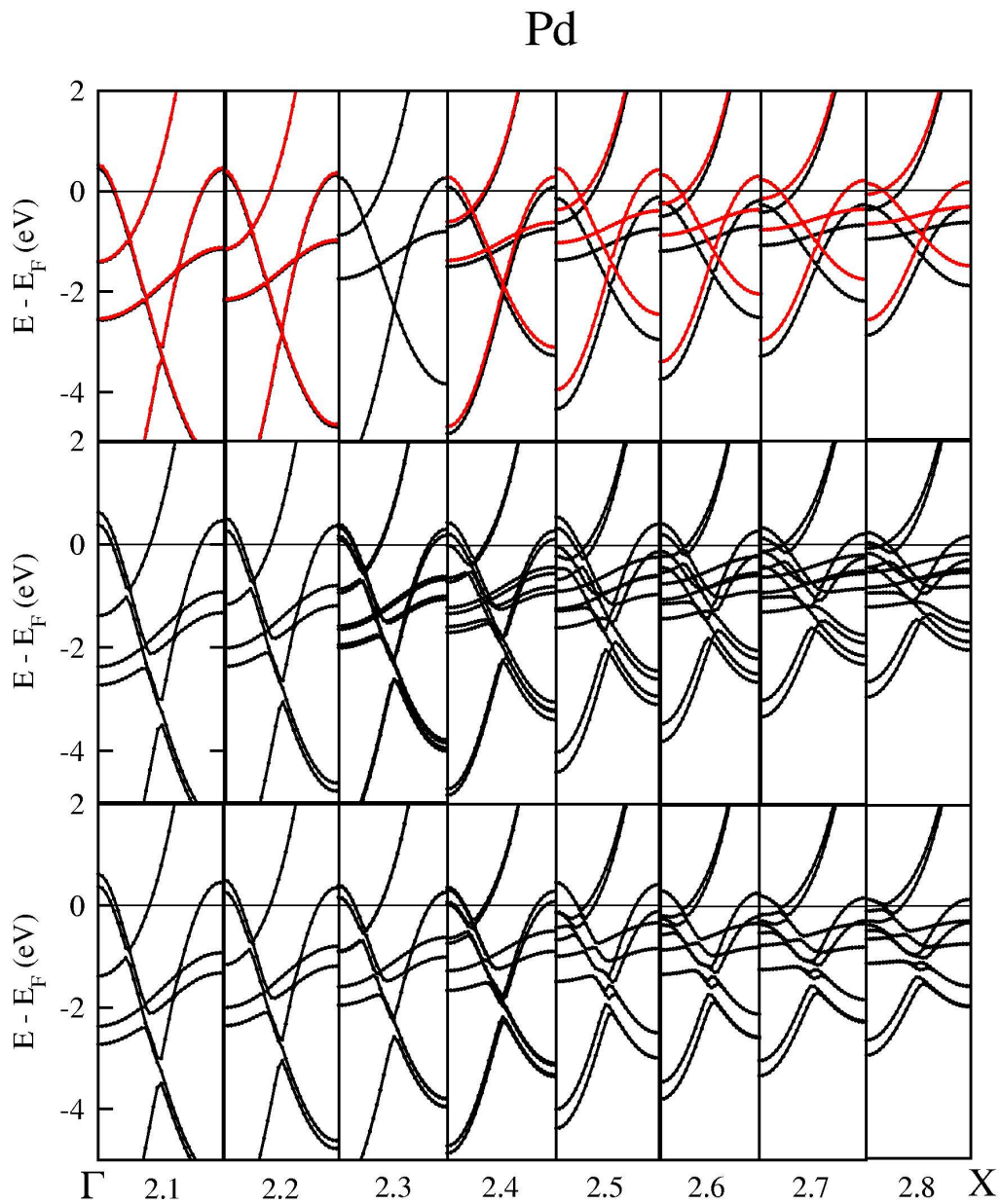


Figure 7.8: Bandstructures for a Pd monowire for increasing interatomic distance. Top: ferromagnetic bandstructures, middle: including spin-orbit coupling with magnetisation along the wire direction, bottom: including spin-orbit coupling with magnetization perpendicular to the wire axis. The values of interatomic distance are given in angstroms.

of the nearest neighbors causes narrowing of the $4d$ bands, so that the bandwidth becomes efficiently small and gain in exchange energy due to spin polarization is larger than the

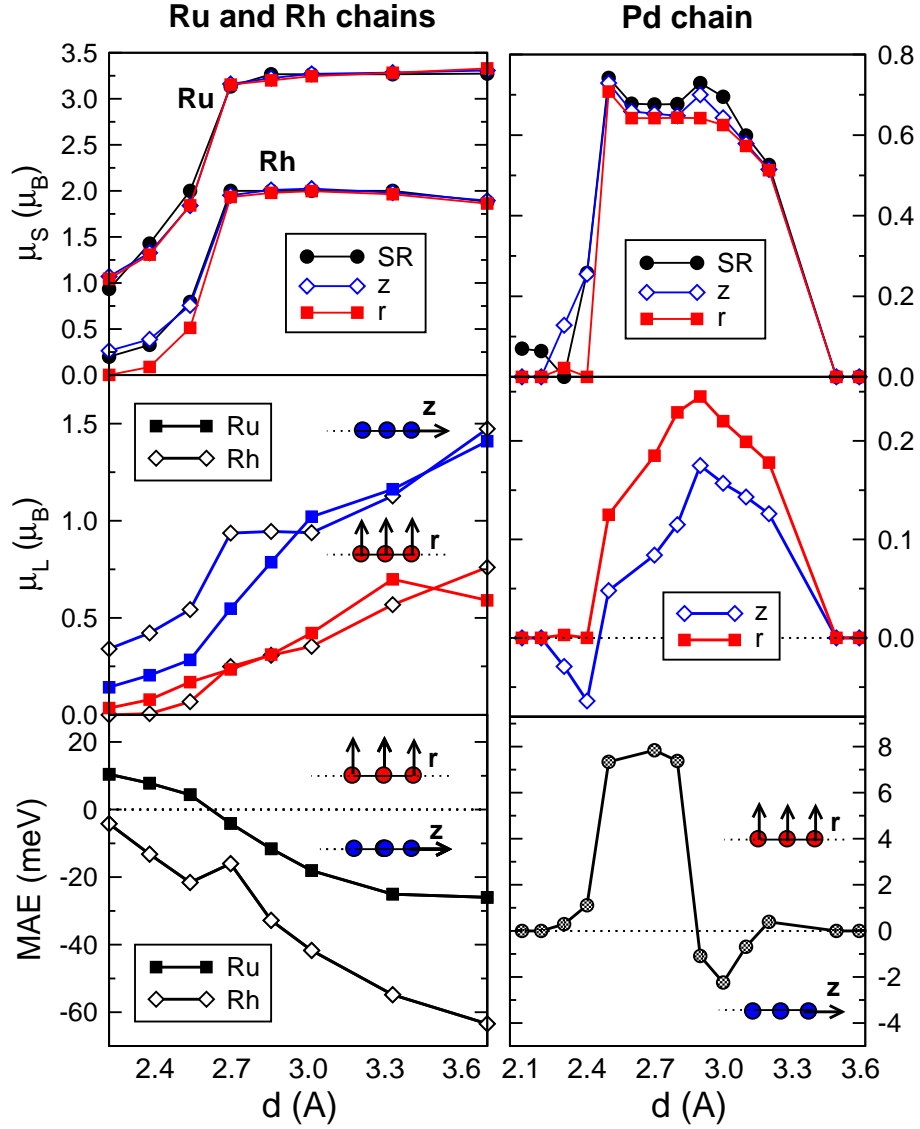


Figure 7.9: Ferromagnetism in monoatomic chains of Ru, Rh and Pd: MAE, spin (μ_S) and orbital (μ_L) magnetic moments as a function of interatomic distance d . Notice, that the scale along the y -axis is different for the left and right panels.

increase in kinetic energy.

However, we want to investigate the development of the bandstructure for the Pd MW depending on the interatomic distance in order to ensure the consideration, that one-dimensionality of the system is crucial for the emerging of the magnetism in this chain. Fig. 7.8 shows the bandstructure of a Pd MW for several bond lengths, illustrating the transition from paramagnetic to ferromagnetic and then to insulating state with the increasing interatomic distance. The Δ_1 bands are of the highest dispersion. Of these two,

s character dominates around the Γ point, while d character is more pronounced at the Brillouin zone boundary X . The Δ_4 bands lie far below the Fermi energy with both spins completely occupied and give no contribution to magnetism. The last group of bands, Δ_3 , has a band edge close to the Fermi level around Γ -point. In the magnetic regime the bands Δ_1 and Δ_3 are very close to the Fermi energy, which drastically increases density of states at the Fermi level, thus, resulting in divergent van Hove singularities after a certain point. A spin splitting of these bands can, therefore, reduce the total electron band energy, somewhat analogous to a band Jahn-Teller, or a Peierls instability effect. Interestingly, after 2.5 Å even the s -dominated band is prone to the spin splitting.

Orbital Moments and Magneto-Crystalline Anisotropy Energies. Reducing the dimensionality of a system causes an increase of the orbital moments and magneto-crystalline anisotropy energies (MAE). From the experimental point of view, a separate determination of the magnetic (μ_S) and orbital (μ_L) moments is rather complicated, thus, correct estimation of the orbital moments by *ab initio* calculations is important for comparison with the experimental values in the case of low-dimensional materials. On the other hand, the MAE acts as an energy barrier, responsible for the stabilization of a certain direction of the magnetisation of the system. Changes in the magnetisation direction can cause significant changes in the electronic and transport properties of the material, especially in the case of heavy elements.

The tendency towards increasing of the orbital moments and MAE was, in principal, confirmed by *ab initio* calculations [48], although the obtained values for a given system differ significantly depending on the computational method. Also, DFT alone is not sufficient to describe the magnetic anisotropies and orbital moments correctly. In order to improve small values of obtained DFT-orbital moments, different ways were proposed.

First of all, introduced by Brooks in [5], orbital polarization terms (OP) were added by Komelj [48] to improve DFT for monowires. OP approach was, however, criticized by Solovyev *et. al.* [103], who applied an LDA+U method [3] to improve the DFT values for orbital moments. However, these proposed methods, describing the tendency towards increasing of the orbital moments and MAEs and their magnitudes correctly, disagree among each other and with the values, obtained experimentally [23].

In Fig. 7.9 (middle and down rows) we present the values of the orbital moments and MAEs for MWs of Ru, Rh and Pd, depending on the interatomic distance, calculated with our DFT method. The values of the μ_L for the monowires of these metals are indeed higher than in the bulk or film, however, they are still quite small compared to expected, close to atomic, values (Pd as alone has $\mu_L = 0$). Without SOC there are no contributions in the GGA functional that lead to an orbital polarization. Inclusion of SOC results in a splitting of the bands and orbital moments arise. In order to investigate the origin of the orbital magnetism, we analyze the bandstructures of Ru and Rh chains at the interatomic distance of 2.54 Å (Fig. 7.7), offering large exchange and spin-orbit splittings for both magnetization directions.

The directional dependence of the magnetization can be specified including the SOC. In case of the axial magnetization (middle panel of Fig. 7.7), two bands Δ_4^\pm with angular momenta $m_l = \pm 2$ are formed from the doubly degenerate spin-down Δ_4 band. The

electron occupation of these bands is responsible for the actual value of the orbital moment $\mu_L(\mathbf{z})$. If the Δ_4^+ -band is fully occupied, and the Δ_4^- -band is unoccupied, an orbital moment of +2 can be obtained. Since only partial occupation is achieved, the orbital moments are $0.28 \mu_B$ and $0.54 \mu_B$ for Ru and Rh, respectively. In the latter case, the higher value of $\mu_L(\mathbf{z})$ is due to the full electron occupation of Δ_4^+ -band, in contrast to the Ru chain (marked areas in the middle panel of Fig. 7.7). For radial magnetization (right panel), the generally smaller values of the in-plane orbital moments, $\mu_L(\mathbf{r})$, are due to the partial occupation of SO-split Δ_4 - Δ_3 mixed bands (inside marked areas). As a consequence of the larger band filling the value of $\mu_L(\mathbf{r})$ is smaller for Rh than for Ru ($0.07 \mu_B$ compared to $0.17 \mu_B$). In a Pd chain the fully occupied Δ_4 bands lie well below the Fermi energy, giving a small contribution to $\mu_L(\mathbf{z})$, while the larger values of $\mu_L(\mathbf{r})$ are due to the SO-split Δ_3 -bands at the Fermi energy [16]. In general, the peculiar behavior of the orbital moments in $4d$ transition-metal MWs is due to an interplay of partial occupation of spin-orbit split Δ_3 and Δ_4 bands and their relative position with respect to the Fermi energy, attributed to the band filling. The larger slope of the Δ_3 bands in comparison to the Δ_4 bands results in larger values of the z -orbital moment.

For Ru and Rh chains with increasing bond distance d the orbital moments gradually rise. For $d > 3.3 \text{ \AA}$ giant values of $1.5 \mu_B$ for $\mu_L(\mathbf{z})$ and $0.7 \mu_B$ for $\mu_L(\mathbf{r})$ for both MWs are reached. The origin for enhanced values of μ_L lies in the splitting of the Δ_4 , Δ_3 -bands at E_F into bands with different angular momenta m_l due to the inclusion of SOC. An increase of d leads to a narrowing of the bands, and, eventually, bands with different angular momentum, m_l , become almost fully occupied or fully unoccupied, giving rise to a large value of the orbital moment.

Combination of high values of the spin and orbital moments with the large difference between $\mu_L(\mathbf{r})$ and $\mu_L(\mathbf{z})$ results in giant values of the MAE. Already at 2.9 \AA it reaches 40 meV per atom and gets as large as 60 meV for a Rh chain with $d = 3.3 \text{ \AA}$. When the value of $\mu_L(\mathbf{z})$ is close to the value of $\mu_L(\mathbf{r})$, a switch in the magnetization direction occurs as can be observed at $d = 2.6 \text{ \AA}$ for Ru and $d = 2.85 \text{ \AA}$ for Pd.

In this situation, when the orbital moments are rather high and the electronic structure strongly depends on the direction of the magnetic moment, magneto-crystalline anisotropy energy becomes a parameter, which defines the electronic and transport properties of the system. MAE profiles of Ru, Rh and Pd show, that, depending on the interatomic distance, the magnetisation of the system can easily change its direction from along the wire direction to the perpendicular one. As far as the bandstructures and the orbital moments of the MWs of these elements differ significantly depending on the magnetisation direction, we claim, that in order to analyze the experimentally observed values of the magnetic moments and conductances, one should necessarily take into account MAE profiles for these systems. In principle, the changes in the conductance of the system can be empirically estimated based on the changes in the number of band-crossings at the Fermi energy [14], while this number, for a given distance, differs depending on the magnetisation direction (Figs. 7.8-7.7). Finally, based on these profiles, desired magnetic and transport properties of the system can be achieved by a precise interatomic distance control, for instance, in a controllable break junction. This provides us with a unique

advantage in the search for new generation of magnetic storage devices.

7.2 Gold (6,0) Nanowire

Frequently metallic wires are produced by forming a break junction, i.e. by pulling off two pieces of material. During this process a one-dimensional bridge appears, which then elongates, narrows and breaks. Experimentally such bridges were formed for Au [91], Pt [81] and Ir [101]. With respect to the bulk materials these free-standing nanowires are of course unstable, but when some "magic geometries" are reached, wires with lengths of about 15 nm and long lifetimes were reported. Structurally more stable metallic nanowires can form on stepped surfaces or inside tubular structures.

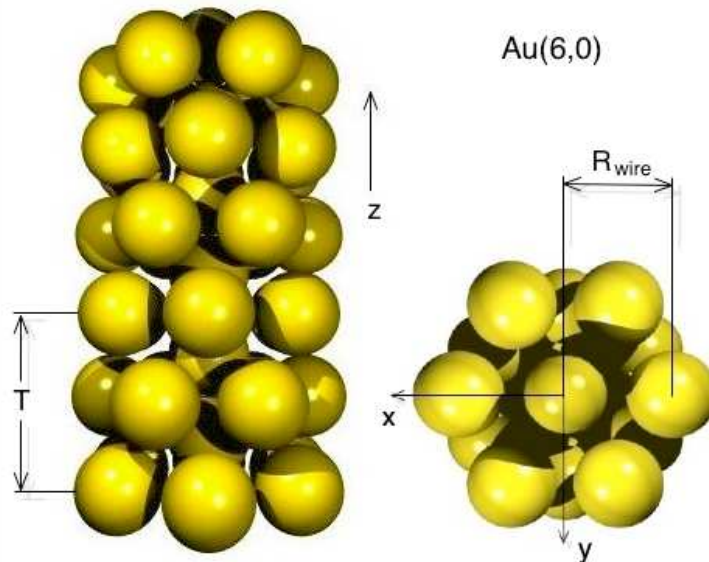


Figure 7.10: Geometrical structure of a Au(6,0) nanowire. Left: side view. Right: top view. The unit cell contains 12 atoms in the outer shell and 2 atoms in the central strand.

Recently, several experimental [78, 49, 82] and theoretical [14, 16, 113] studies have been published on structural and physical properties of different gold nanowires. Here, we want to report on calculations of an Au(6,0) nanowire with our new code. For the educational purposes we also perform calculations of an Au(6,0) nanotube and an Au monowire, and compare the obtained results with those available in the literature.

7.2.1 Computational Details

GGA and LDA calculations are carried out using the values of 3.6 a.u.^{-1} and 10.8 a.u.^{-1} for the cut-off parameters K_{max} and G_{max} , respectively. For the GGA calculations we

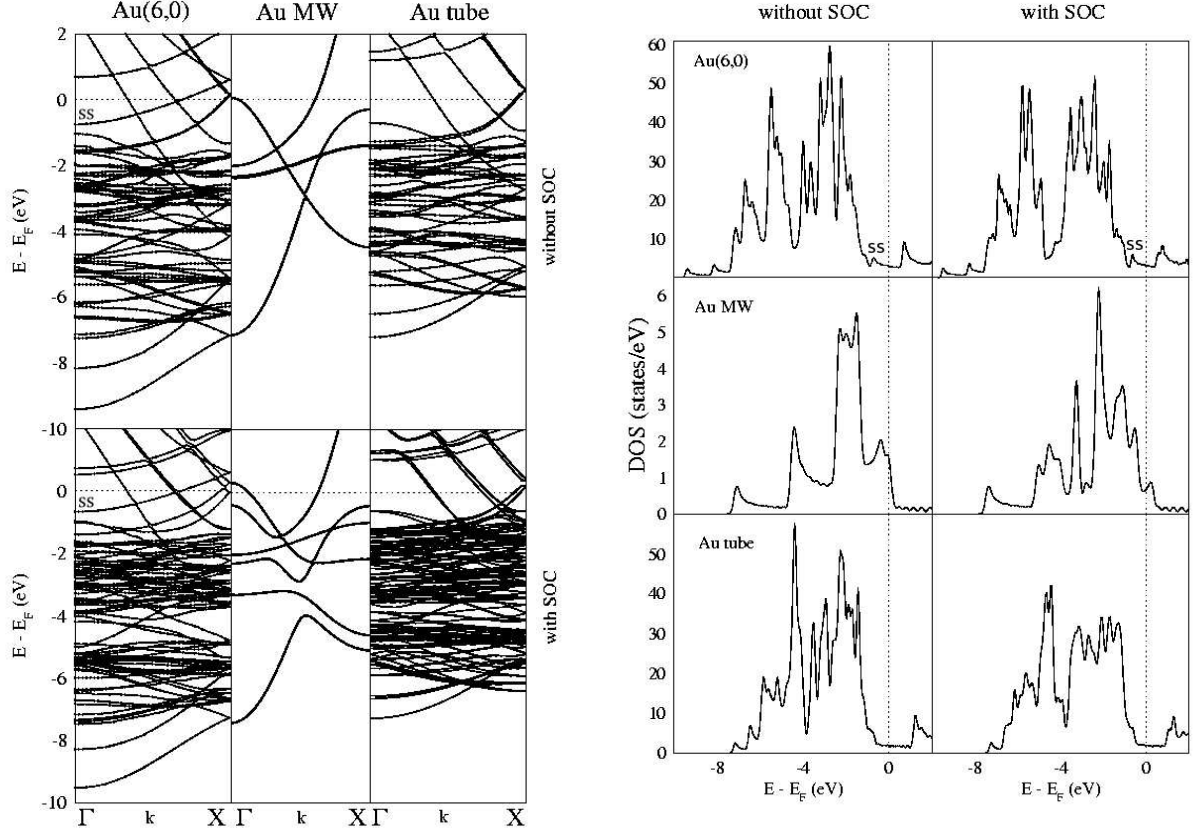


Figure 7.11: Bandstructures of a Au(6,0) nanowire (left), a free Au MW (middle) and an Au(6,0) tube (right) for the atomic positions as calculated for the Au(6,0), $R_{\text{wire}} = 5.21$ a.u., $T=8.84$ a.u. within the GGA, with (bottom panels) and without (top panels) spin-orbit coupling effects included. The band marked 'ss' is discussed in the text.

Figure 7.12: Densities of states (DOS) of Au wires, calculated without (left panels) and with spin-orbit interaction (right panels). 'ss' denotes the peak in the DOS coming from the energy band 'ss' in Fig. 7.11 at the Γ -point. Top: DOS of the Au(6,0) nanowire. Middle: DOS of the free Au MW. Bottom: DOS of the Au(6,0) tube. DOS are calculated for the geometries discussed in the text.

used the revPBE functional [130] and the Vosko, Wilk and Nusair functional [118] was applied for the LDA calculations. The muffin-tin radii for the gold atoms were fixed at 2.0 a.u. during the calculations. For the basis functions as well as the charge density and potential in the vacuum region we used the angular expansion parameters $m_{\text{max}} = 24$ and $m_{\text{max}} = 50$, respectively. The vacuum parameters $D_{\text{vac}} = 15.0$ a.u. and $\tilde{D} = 16.6$ a.u., and a grid spacing $dr = 0.08$ a.u. and 250 grid points for the representation of all real space quantities in the vacuum region were sufficient to reach the numerical accuracy.

Structural optimization was done using 11 k -points in one half of the Brillouin zone, the bandstructures and densities of states were calculated using 41 k -points in one half of the Brillouin zone. The Au(6,0) nanotube and the free-standing Au MW were calculated with the same computational parameters.

7.2.2 Geometrical Structure

The structure of the wire, having 14 gold atoms in the unit cell, is shown in the Fig. 7.10. It consists of a central strand of Au atoms and an outer shell Au(6,0) tube. Every atom of the central MW was placed in between the planes of outer hexagons along the symmetry axis of the nanowire. We did not consider the possibility of dimerization or creation of zig-zag structures for the inner Au MW inside the Au(6,0) tube.

Within GGA we found an optimized period T in z -direction of 8.84 a.u. and a wire radius R_{wire} of 5.21 a.u. (the wire radius, R_{wire} , is defined in Fig. 7.10), while the LDA calculations led to the optimized T value and wire radius of 8.86 a.u. and 5.16 a.u., respectively. This is in a good agreement with [113], where $R_{\text{wire}} \approx 5.3$ a.u. and $T = 8.82$ a.u. Optimized geometrical parameters ($T=8.84$ a.u. and $R_{\text{wire}}=5.21$ a.u.) were used for the GGA electronic structure calculations of the Au MW and Au(6,0) nanotube.

Structural relaxation of the Au(6,0) nanowire with spin-orbit coupling (SOC) effect included led to changes in the optimized geometrical parameters of less than 1%.

7.2.3 Electronic Structure

The GGA-bandstructures for the Au(6,0) nanowire (left), an Au MW (middle) and an Au(6,0) tube (right) at the positions as in the Au(6,0) nanowire, are shown in Fig. 7.11. Top panel presents the bandstructures without SOC interaction included, the bandstructures with SOC effects included are shown in the bottom panel of Fig. 7.11. All the calculated structures show strong metallicity due to the s -bands of gold.

With 'ss' in the bandstructures of the Au(6,0) nanowire we marked a surface state at the Γ -point below the Fermi energy. As one can conclude from the comparison between the band structures of the Au tube, Au MW and Au nanowire, the appearance of this surface state is due to the hybridization of the states coming from the outer Au(6,0) nanotube and the inner Au MW. The charge density plots for this state are presented in Sec. 7.2.4.

The bandstructures for the Au(6,0) wire and Au(6,0) tube with SOC effects included (Fig. 7.11, bottom panel (left)) shows multiple band splitting as compared to the bandstructure without SOC, giving rise to the pronounced band splitting at the Fermi level. For the bandstructure of the Au(6,0) nanowire calculated with and without spin-orbit interaction, the total number of conducting channels for ballistic transport is equal to six, which coincides with the number given in [113].

The bandstructure of the Au(6,0) nanowire (top left) coincides rather nicely with the bandstructure for this structure given in [113]. The bandstructures of the Au MW are in good comparison to those in [14] and [62].

In top of Fig. 7.12 the densities of states (DOS) of the Au(6,0) nanowire are shown, obtained with and without spin-orbit coupling. Including SOC, the figure shows an increase of the pseudo-gap between the two subgroups of d -bands, the first of them lies between -4 eV and -2 eV, while the other one is located in the energy interval between -7 eV to -5 eV. By 'ss' we denote the peak in the DOS, which comes from the surface state 'ss' in Fig. 7.11 at the Γ -point. The spin-orbit interaction changes also the DOS around the Fermi level, emphasizing this peak.

The total density of states for the gold monowire and the Au(6,0) tube, calculated with GGA at the positions as in the Au(6,0) nanowire with and without spin-orbit interaction, are shown at the bottom of Fig. 7.12. From the DOS we can observe, that due to the hybridization of the states, coming from the outer Au tube and inner Au MW, the pseudo-gap between the two subgroups of d -bands is larger for the Au(6,0) nanowire, than for the Au(6,0) tube or Au MW. The same reason stands for the appearance of the surface state 'ss' in the case of the Au(6,0) nanowire.

7.2.4 Charge Density

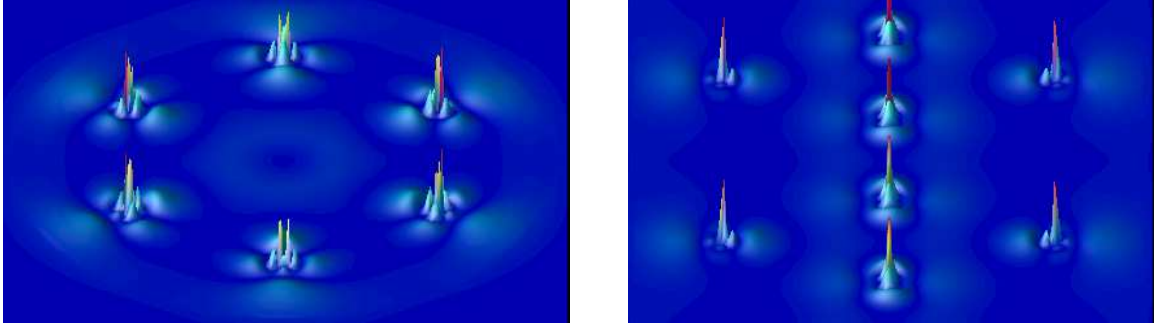


Figure 7.13: Charge density plots for the Au(6,0) wire for the energy band denoted by 'ss' at the Γ -point in Fig. 7.11. Left: Charge density plot in xy -plane (perpendicular to the z -axis), cutting through the centers of the atoms in the outer hexagon ring. Right: Charge density plot in xz -plane, cutting through the centers of the inner strand atoms and 2 atoms in the outer shell hexagon ring.

In Fig. 7.13 we present the charge density plots at the Γ -point for the energy band which is denoted by 'ss' in Fig. 7.11. The charge density plot in the xy -plane (perpendicular to the z -axis), cutting through the centers of the gold atoms in one of the outer shell hexagons, is presented in the top panel of the Fig. 7.13. The plot in the bottom panel shows the charge density in the xz -plane, cutting through the centers of the inner strand of gold atoms and two atoms in the outer hexagon of the gold wire. In Fig. 7.13 the surface state ('ss') character of the state at the outer atoms is clearly visible. For this state a d_{z^2} type orbital at the outer Au atoms is found with a slow decay into the vacuum. For inner strand atoms this state has p_z character.

The calculated work functions for the Au tube is 4.9 eV and 4.8 eV for the Au(6,0) nanowire, compared to the work function of the Au(111) surface of 5.31 eV [102]. The decrease of the work function can be addressed to the curvature effects.

7.3 Hybrid Structure $Fe@Au(6,0)$

Among all 1D structures, metallic nanowires and carbon nanotubes filled with various materials are of great interest in nanoscience and nanotechnology because of their interesting properties. The importance of carbon nanotubes for the research and applications is due to their particular physical properties, mechanical stability and chemical tunability. Single-walled (SWCNTs) and multi-walled (MWCNTs) carbon nanotubes show conductive or semiconductive behavior with low defect scattering depending on their chirality [17], having a wide range of applications such as p - n junctions [58] or field-effect transistors [110, 63, 33]. Recent theoretical and experimental investigations open a new field for carbon nanotubes in the area of spintronics [115, 20]. It was proposed to combine carbon nanotubes with transition-metals which are coated on the surface of the tube or put inside the tube hollow [70, 126]. It was shown that carbon nanotubes in principle can offer highest possible magnetoresistance ratios and the spin-scattering length for certain types of nanotubes reaches 130 nm [115, 65]. The combination of this fact with the pronounced magnetism of the transition metals in low dimensions makes such hybrid structures perfect candidates for the future generation spin-dependent transport devices [126].

On the other hand, metallic nanowires, due to their one-dimensional nature, are the origin of several new phenomena to appear, such as quantized conductance, charge and spin separation, helical geometries and magic structures [49, 29, 113]. Starting from the monowires (MWs) [78, 14, 62, 96], in particular, monowires made out of transition-metals [80, 23], or complicated helical metallic wires became a target of concentrated attention in one-dimensional research, especially with respect to structural stability and transport properties [114, 29, 127, 79]. Recently a significant experimental progress has been made moving metallic helical tubes to the frontier [82, 81]. This stimulated the interest in the magnetic behavior of these structures and recently several theoretical and experimental studies were reported on this topic. [14, 80, 129, 16] Therefore, another alternative for spintronics on the nanoscale in one dimension, based on the combination of a metallic (nonmagnetic) carrying tube and transition-metal atoms could be proposed.

In this section we want to report on our calculations of the atomic and electronic structure, magnetic properties and the charge density, of the $Fe@Au(6,0)$ hybrid structure, showing, that such hybrid structure, if used for electron transport, will show a significant spin-polarization leading to strongly spin-polarized transport properties.

The calculations were carried out within the local density approximation using the functional of Vosko, Wilk and Nusair [118] and within the generalized gradient approximation using the revPBE functional [130]. For self-consistency calculations of the hybrid structure we used 80 k -points in one half of the first Brillouin zone. For the gold and

Table 7.1: (Equilibrium) Fe-Fe distance, total spin magnetic moment in the unit cell μ_m^{tot} (divided by the number of Fe atoms), spin magnetic moment μ_m^{MT} in the MT sphere of Fe and magnetocrystalline anisotropy energy per Fe atom in three different types of Fe monowires and their dimers calculated with LDA and GGA. Fe-1: bare Fe monowire, Fe-2: bare monowire of Fe at the positions as in the Fe@Au(6,0), Fe-3: monowire of Fe inside the Au(6,0) tube. Monomer is denoted by 'm', dimer is denoted by 'd'. The Fe-Fe distance for the dimers is found by relaxation of the two Fe atoms in the double unit cell of the monomer. The magnetocrystalline anisotropy energy (MAE) is defined as the energy difference $\Delta E = E(\hat{e}_z) - E(\hat{e}_r)$ between the magnetization aligned along the wire axis and the radial direction of the wire. In the case of the hybrid structure Fe@Au(6,0) two possible in-plane alignments of the magnetization are possible: along the x and y axis. Corresponding MAEs are denoted by X and Y , respectively.

		Fe-Fe distance (a.u.)		μ_m^{tot} (μ_B)		μ_m^{MT} (μ_B)		MAE (meV/ Fe atom)		
		LDA	GGA	LDA	GGA	LDA	GGA	LDA	GGA	
Fe-1	m	4.14	4.28	3.25	3.32	2.92	3.01	1.4	5.5	
	d	3.90	4.02	3.26	3.31	2.90	3.00	2.7	4.1	
Fe-2	m	4.43	4.42	3.34	3.35	3.01	3.05	5.1	7.6	
	d	3.92	4.10	3.31	3.30	2.97	3.03	8.9	7.3	
Fe-3	m	4.43	4.42	3.32	3.39	2.88	2.97	X	-32.	-31.
								Y	-32.	-31.
	d	4.14	4.20	3.28	3.37	2.86	2.96	X	-24.	-26.
								Y	-37.	-34.

iron atoms the radii of MT spheres were chosen to be 2.0 a.u. Basis functions of all \mathbf{G} -vectors were included up to a length determined by the condition $|\mathbf{G} + k_z| < K_{\text{max}}$ with $K_{\text{max}} = 3.6 \text{ a.u.}^{-1}$. This corresponds to a vacuum angular expansion parameter for the basis functions of $m_{\text{max}} = 20$. For the plane-wave expansion of the charge density and potential a parameter $G_{\text{max}} = 3 \cdot K_{\text{max}} = 10.8 \text{ a.u.}^{-1}$ proved to give reliable results. The angular expansion of the vacuum charge density and potential was terminated at $m_{\text{max}} = 50$.

In order to investigate the magnetic structure of the hybrid system and the case of dimerization, we also performed a set of calculations on free-standing MWs of iron atoms, both within LDA [118] and GGA [130]. For these calculations we used 64 k -points in one half of the first Brillouin zone. The parameters G_{max} and K_{max} were set to 11.4 a.u.^{-1} and 3.8 a.u.^{-1} , respectively.

The results of the calculations on the hybrid structure Fe@Au(6,0) and the Fe MWs are summarized in Table 7.1.

7.3.1 Geometrical Structure

The geometrical structure of the system is shown in Fig. 7.10, having 12 gold atoms and 2 iron atoms per unit cell. It consists of the Au(6,0) outer tube and an inner strand of

iron atoms, which replaces the inner monowire of gold atoms in the Au(6,0) nanowire. For the GGA calculations the period of the structure and the radius of the outer shell of gold atoms were chosen to be the ones of the (6,0) gold nanowire optimized with GGA: 8.84 a.u. and 5.21 a.u., respectively. For the LDA calculations we use the optimal LDA values of 8.86 a.u. and 5.16 a.u. From total energy and force calculations we concluded that the inner Fe strand changes the geometrical parameters by less than 1%. As for the plain Au system, including the effects of the spin-orbit interaction did not cause any significant structural changes: the geometrical parameters changed by less than 1%, and the magnetic spin moment per iron atom changed by 0.5%.

We also considered three different types of iron MWs: the bare MW, a MW with the interatomic Fe-Fe distance equal to that of the central strand of Au atoms in the Au(6,0) nanowire (denoted by Fe@Au-MW) and an iron monowire inside the Au(6,0) tube (Fe@Au(6,0)-MW). For the free-standing MW the optimized Fe-Fe distance is 4.14 a.u. (LDA) and 4.28 a.u. (GGA), respectively, compared to 4.31 a.u. in [76] (GGA) and 4.26 a.u. in [104] (GGA).

Although we focus primarily on straight and linear monowires, we have observed that for the iron atoms inside the gold tube the zig-zag configuration appears to be energetically more favorable as compared to the unperturbed hybrid structure (as it was predicted for the free-standing iron MWs [104]). We concentrated our effort on considering the possibility of a Peierls dimerization of the Fe atoms along the chain. Thus, we double the unit cell with lattice constant a . Keeping the lattice constant fixed at $2a$, we investigate the total energy $E(\delta)$ as a function of the iron atom relaxation δ off the ideal high symmetry position along the chain axis. In most cases the dimerization was found to be preferable with a gain in total energy of around 30 meV resulting in changes in the Fe-Fe distance due to dimerization in the range of $\delta=5-12\%$ depending on the system (compared to 20meV and 16% in [104]). For more details see Table 7.1.

The calculated work function for the Fe@Au(6,0) structure is 4.5 eV, which is 0.3 eV smaller than the work function of the Au(6,0) tube, filled with the Au monowire.

7.3.2 Magnetic Properties

In one-dimensional systems, the calculated magnetic moments of the iron atoms are much larger than the corresponding bulk value of $2.2 \mu_B$ and the spin-polarization for the electrons at the Fermi level is quite large. The calculated hybrid structure has an average magnetic moment of around $2.92 \mu_B$ per MT sphere of iron atom and $3.34 \mu_B$ per Fe atom in the entire unit cell (cf. Table 7.1). The magnetic moment of the gold atoms in all the calculations is around $0.02 \mu_B$. For the iron MWs we found a magnetic moment of around $2.97 \mu_B$ per MT sphere of iron atom and $3.30 \mu_B$ per Fe atom in the entire unit cell (which is in a good comparison to the values in [104, 76]).

The decrease of the magnetic moment in the MT spheres of iron atoms in the hybrid structure comparing to the free-standing MWs gives the measure for the interaction between the iron atoms of the central strand and the atoms of the outer gold tube.

We checked the possibility of the structures to become antiferromagnetic (AFM). For

the bare MW the ferromagnetic state (FM) is more favorable by 0.37 eV (LDA) and 0.33 eV (GGA) per Fe atom (similar values were obtained in [104]). For the Fe@Au(6,0) structure this difference is 0.38 eV (LDA) per atom of iron and dimerization does not appear. We conclude that AFM solution is energetically very unfavorable and it is not considered any further.

The calculated orbital magnetic moments μ_L for the iron monowires lie in the range of 0.2–0.3 μ_B (similar values were obtained for the iron MWs in [18]).

Magnetocrystalline anisotropy energies (MAE), being defined as energy differences $\Delta E = E(\hat{e}_z) - E(\hat{e}_r)$ between the magnetization aligned along the wire axis and the radial direction of the wire, were also calculated. For the hybrid structure Fe@Au(6,0) two possible in-plane alignments of the magnetization can lead to the stationary solutions: along the x and y axis. Corresponding MAEs, $\Delta E_X = E(\hat{e}_z) - E(\hat{e}_x)$ and $\Delta E_Y = E(\hat{e}_z) - E(\hat{e}_y)$, are denoted by X and Y in the Table 7.1. The coordinate system is chosen such, that the x -axis points to the center of the gold atom in the outer hexagon ring and the y -axis points in between the two gold atoms in the hexagon ring. While in the case of free-standing MWs the magnetization is aligned along the wire axis with the MAEs between 1 meV to 7 meV, surprisingly in the case of the hybrid structure the situation changes drastically. The influence of the outer heavy gold atoms with the magnetic moment of just 0.02 μ_B per atom causes the changes in the magnetization direction to in-plane along the x -axis. The further creation of the dimer changes the easy axis again to the y -axis. The average energy differences for the hybrid structure are around 30 meV per iron atom. In order to confirm the role of the encasing Au atoms with a magnetic moment of just 0.02 μ_B on the magnetization direction, we carried out calculation where we switched off the spin-orbit interaction of the Au atoms by hand and we ended up at the results obtained for the single Fe wire: the easy axis of the magnetization is again along the wire, the hard axis is along the x direction, and the energy difference is 3.0 meV per iron atom (LDA) close to the value of 5.1 meV obtained for the single Fe wire (LDA). The shape anisotropy caused by the classical dipole interaction between the magnetic moments of the atoms prefers the in-chain direction as easy axis. The hard axis pointing radially from the wire is 0.1 meV higher in energy.

The magnetocrystalline anisotropy energy was calculated applying the force theorem.

7.3.3 Electronic Structure

The bandstructure of the free-standing (6,0) gold tube calculated with GGA is shown in the right panel of the Fig. 7.11. In Fig. 7.14 the back-folded GGA bandstructure of the free-standing iron monowire used to fill the gold tube is shown for spin up and spin down states (indicated by arrows). For this calculation the Fe-Fe distance in the monowire was kept to that of the gold monowire. It is clearly visible, that the minority d -states determine the electronic structure at the Fermi level. A profound symmetry analysis of the bandstructure and the charge density distribution for the Fe MW one can find in [121].

Fig. 7.15 exhibits the atom-resolved band structure of the hybrid system, as calculated in GGA, reflecting the basic features of the iron monowire: the majority of flat spin-down

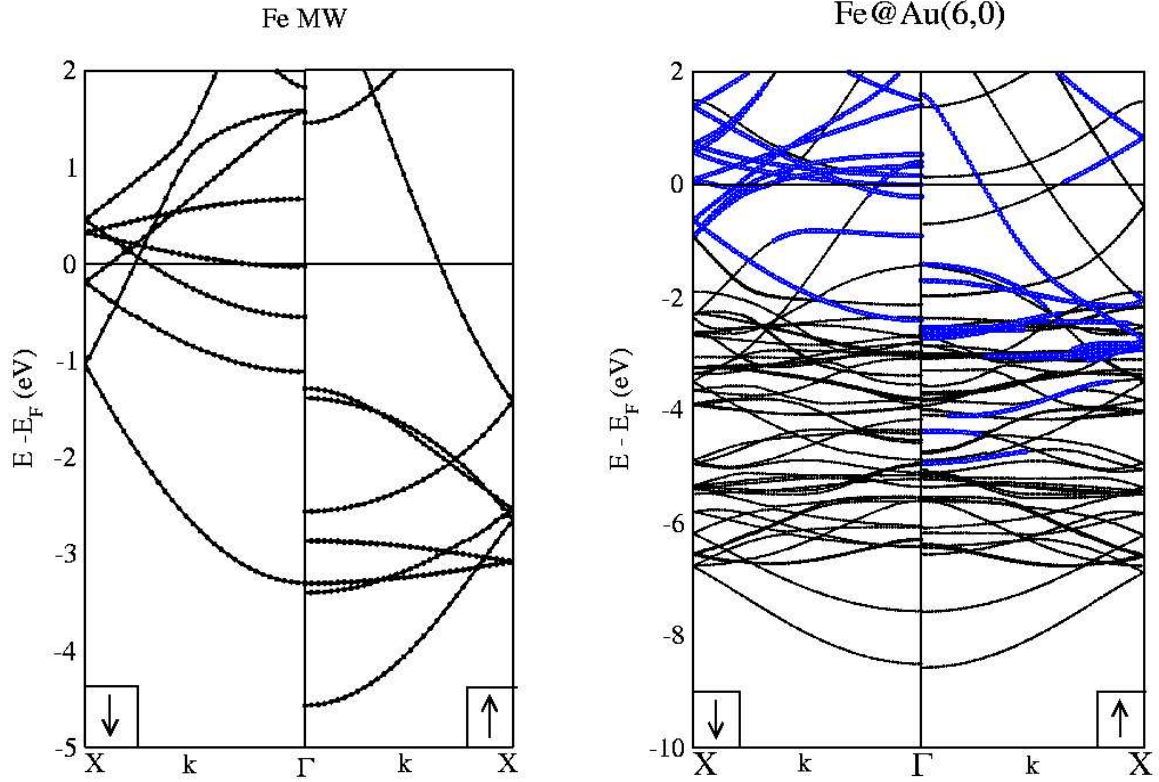


Figure 7.14: Bandstructure of a Fe monowire with a lattice constant consistent with the gold tube for spin down and up channels (GGA). For minority spin, d -bands are concentrated around the Fermi level.

Figure 7.15: Band structure of the Fe@Au(6,0) system. Spin down and spin up are indicated by arrows. Open (blue) circles denote states located predominantly on iron atoms. It can be seen that narrow d -bands of Fe are responsible for large spin polarization at the Fermi level

Fe d -bands, concentrated around the Fermi energy. From the plot of the total density of states (Fig. 7.16) we have obtained that the spin polarization at the Fermi level P_{E_F} reaches 74.3% (GGA), and 77.5% in the case of LDA. The spin-polarization P_{E_F} is defined as $(n_{\downarrow}(E_F) - n_{\uparrow}(E_F))/(n_{\downarrow}(E_F) + n_{\uparrow}(E_F))$, where $n_{\downarrow}(E_F)$ and $n_{\uparrow}(E_F)$ are total DOS for spin-down and spin-up channels at the Fermi level.

Respectively, open (blue) circles in Fig. 7.15 indicate those states, which are predominantly localized on the iron sites. According to our definition this means, that the weight of a wavefunction in the Fe muffin-tins is three times larger than in the muffin-tins of Au atoms. The interstitial region is ignored. The atom-resolved band structure (Fig. 7.15) and atom-resolved local DOS (Fig. 7.16) clearly show that a large DOS at the Fermi level

for the spin-down states comes from the d -states of iron. From the bandstructure and wavefunction analysis one can easily notice a large interaction of the iron states with the outer shell of gold for the spin-up channel: the hybridization of s - and d -states of iron and gold, located at the same energy interval, is significant.

In Fig. 7.17 the densities of states (GGA) for three different types of iron MWs (black solid lines) and their dimers (green dashed lines), are shown. For the case c) of the hybrid structure Fe@Au(6,0) we show the atom-resolved LDOS of the iron atoms. Fig. 7.16 represents the GGA densities of states for the hybrid structure (black solid lines) and its dimer (dashed green lines). Panels for spin down and up are marked with arrows. We conclude from Fig. 7.17(a) that the prominent peak of minority DOS at E_F is the dominant driving force for dimerization. Also in the Fe@Au(6,0) structure, a lowering of the DOS due to dimerization can be found (Fig. 7.16(c)).

7.3.4 Charge Density

In the Fig. 7.18 we present the plots of the magnetization density at the Fermi energy $m_m^{E_F}(\mathbf{r}) = \rho_{\downarrow}^{E_F}(\mathbf{r}) - \rho_{\uparrow}^{E_F}(\mathbf{r})$, where $\rho_{\downarrow}^{E_F}(\mathbf{r})$ and $\rho_{\uparrow}^{E_F}(\mathbf{r})$ are the charge densities for the minority and majority spins around the Fermi level, respectively. Fig. 7.18 (top) presents the magnetization density in the xy -plane, cutting through the centers of the gold atoms in an outer hexagon ring. Half of the hexagon is shown with the white lines connecting the gold atoms, as guide to the eyes. Fig. 7.18 (bottom) shows the magnetization density in xz -plane, cutting through the centers of the iron atoms and one of the gold atoms in the outer shell hexagon. From these plots we see the domination of the d -bands of iron in the minority spin around the Fermi level. The magnetization density has a non-uniform distribution spilling out of the wire into the vacuum and should be, therefore, experimentally accessible, e.g. by the spin-polarized scanning tunneling microscopy (SP-STM). The magnetization density carries the signature of Au p -orbitals for the outer shell atoms and Fe d -orbitals for the inner atoms, signifying the hybridization of the minority Fe d -states with the Au p -states. Thus, the magnetization density at the Fermi energy is dominated by minority states.

The obtained results show that such hybrid structure as Fe@Au(6,0), if used for electron transport, will show a significant spin-polarization leading to strongly spin-polarized transport properties.

7.4 One-Dimensional Multiple Benzene-Vanadium Sandwiches

In the last two decades some physical chemists have applied molecular beam technique to organometallic compounds and have opened up "gas-phase" organometallic chemistry [22]. This movement has proven to be very important to reduce empirical aspects in the conventional organometallic chemistry. In fact, many novel compounds have been synthesized by applying the cluster formation methods such as a modified laser vaporization

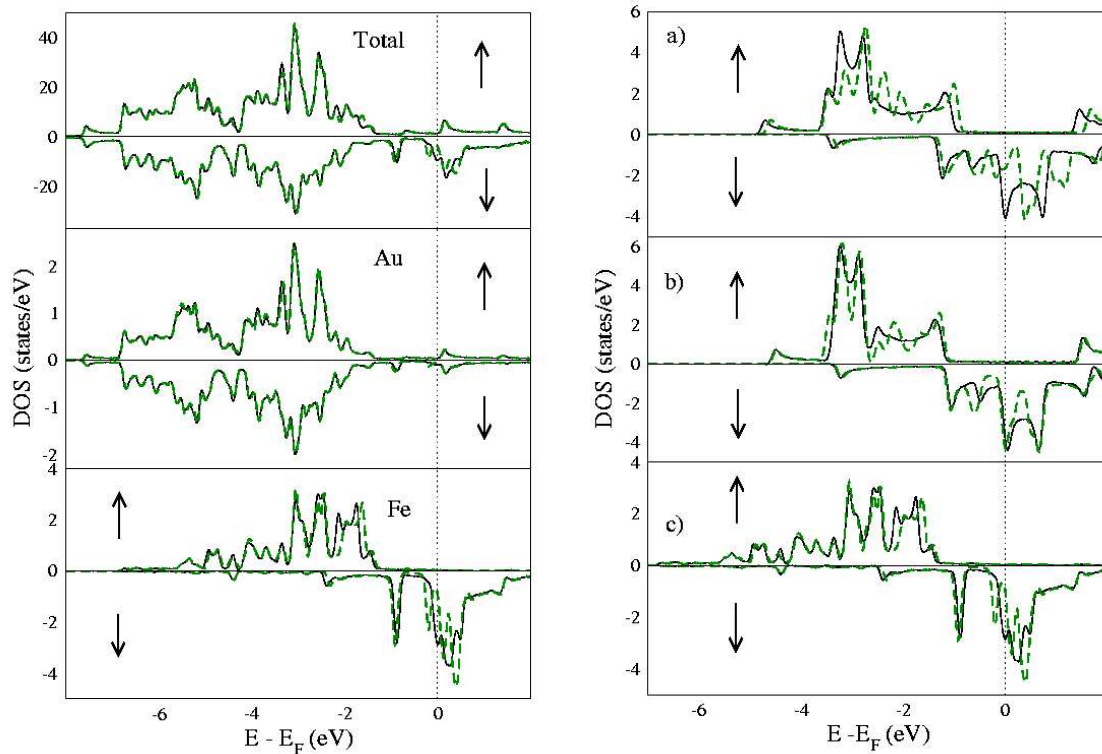


Figure 7.16: Densities of states (solid black lines) for Fe-filled (6,0) gold nanotube (spin up and down are indicated by arrows) and its dimer, calculated with GGA (corresponding DOS for the dimers are shown with dashed green lines). Top: total density of states. Middle: atom-resolved LDOS for the gold atoms. The Au LDOS is almost unaffected by the dimerization of the Fe strand. Bottom: atom-resolved DOS for the iron atoms. The large negative spin polarization is seen at the Fermi level.

Figure 7.17: Densities of states for three different types of iron monowires and their dimers (spin up and down are indicated by arrows). DOS for the non-dimerized MWs are shown with the solid (black) lines, DOS for the dimers are shown with the dashed (green) lines. a) total DOS for the bare MW and its dimer at the GGA interatomic distances of 4.28 a.u. and 4.02 a.u., respectively. b) total DOS of the bare Fe MW at the positions as in the Fe@Au(6,0) system and its dimer (GGA, 4.42 a.u. and 4.10 a.u., respectively). c) atom-resolved LDOS for the iron atoms inside the Fe@Au(6,0) hybrid structure and its dimer (GGA, 4.42 a.u. and 4.20 a.u., respectively).

method [37, 75, 6, 30]. These include atomic clusters, nanostructured materials, atomic chains, mono- and multi-layer films. The unique properties of these materials are a direct consequence of their topology and reduced dimensionality. Atomic clusters of specific size and composition can be produced in a supersonic beam expansion while nanoparticles

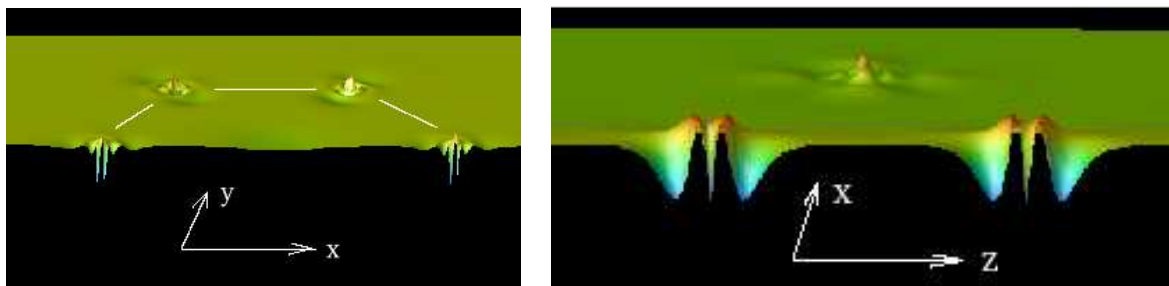


Figure 7.18: Spin-density plots for the Fe@Au(6,0) wire for the states around the Fermi energy. Left: Spin density plot in xy -plane (perpendicular to the tube axis), cutting through the centers of the atoms in the outer hexagon ring of gold. Right: Spin-density plot in xz -plane, cutting through the centers of the inner strand atoms of iron and one of the atoms of gold in the outer shell hexagon ring.

with a narrow size distribution are being synthesized using gas condensation techniques. Atomic chains, monolayers and multilayers, on the other hand, are produced using molecular beam epitaxy on specially prepared surfaces. All these materials have one common characteristic - their length scales are small enough to exhibit quantum phenomena.

Interchain or multilayered organometallic polymers have been inspiring chemistry and physics for a long time [61, 77]. Synthesis of organometallic compounds in gas phase presents a novel guideline to chemists because they can be prepared without solvent and oxidation in air. Especially, the application of the laser vaporization to the gas-phase synthesis of organo-metallic compounds enables us to prepare the constituents in considerable density in a short time because there are no interfering effects of solvents, aggregation phenomena, and counterions. This new approach should open up an entirely different aspect of organometallic chemistry and physics, which can be studied quite nicely in the gas phase, and indeed several groups independently have succeeded in the synthesis of novel organometallic complexes. The technique used to produce and detect the gas-phase organometallic clusters involves a beam source with laser vaporization of metal rods and time-of-flight mass spectrometry whose distinct ability was well-demonstrated in the discovery of C_{60} and metallo-carbohedrene [52].

Furthermore, recently, formation of fullerene-based organometallic compounds suggests that new forms of materials can be synthesized because the fullerenes may prove to be highly versatile ligands due to their intriguing topography and aromaticity [19]. A great deal of effort has been spent in the past decade on modifying fullerenes by coordinating atoms both inside and outside the cage structures [8]. In particular, the finding of superconducting alkali metal fullerenes [31] stimulated considerable interest, suggesting that new forms of materials and superstructures can be synthesized with important chemical and physical properties. Gas-phase studies of transition metals and C_{60} ($M_T - C_{60}$) have been initiated by Freiser and co-workers [21], concerning the possibility of a transition-endohedral complex. As well as organometallic compounds of transition metal elements,

the *f*-block elements of lanthanide (Ln) and actinide (Ac) metals have been of considerable importance in many areas of modern technology [97]. Although these organometallic clusters have been studied extensively as mentioned above, the size range has been rather limited to the small complexes.

By applying the advantages of the laser vaporization method for the metal-molecule complexes, several groups have reported gas-phase studies on metal-benzene complexes. Armentrout and co-workers [67] and Freiser and co-workers [40] have extensively revealed thermochemistry on ML_n^+ complexes, where *M* and *L* are a metal atom and a ligand molecule, respectively. Theoretical calculations have also been carried out. In particular, Langhoff [13] and co-workers have calculated binding energies for all 3*d* transition metal ions (M^+) and benzene complexes and have accounted for the effect of the electron correlation between the metal atoms and benzene molecules. However, almost all the subjects were restricted to small cationic complexes denoted as $M_1(Bz)_x^+$, $x = (1, 2)$ due to the necessity of mass selection and simplification of the calculations.

For 3*d* metal-benzene, $M_n(Bz)_m$, the new organometallic compounds unknown in the bulk, have been newly discovered by Kaya and his co-workers [37]. Two kinds of structures of multiple sandwich and rice-ball were formed, depending on the metal elements [37, 54, 55]. Early transition metals of Sc, Ti and V form the multiple-decker structure of $(n, m) = (n, n + 1)$ [37, 55], while late transition metals of Fe, Co and Ni form the rice-ball structure [54]. With the measurement of the ionization energy E_i of *M*–*Bz*, it was found that the E_i drops significantly with the number of layers, which can be explained by delocalization of *d* electrons through the interaction with the LUMO of benzene [128]. Investigating of these sandwich clusters is of great interest, because they have an ideal one-dimensional structure to have a charge-density-wave (CDW) or spin-density-wave (SDW) states. Particular attention is paid to the CDW conductors because of the strikingly nonlinear and anisotropic electrical properties, gigantic dielectric constants, unusual elastic properties and rich dynamical behavior [112]. A related compound $[Ni(C_3B_2(CH_3)_4H)]_\infty$ has been actually characterized as a microcrystalline material with a remarkably high electrical conductivity of $0.2 (\Omega \text{ cm})^{-1}$ [57]. This value exceeds even that for undoped polyacetylene considerably, and such organometallic sandwich polymers are considered to form a new class of 1D conductors.

On the other hand, it was recently shown by Kaya and co-workers [69] that one-dimensional vanadium-benzene sandwiches are a novel class of high-spin molecular magnets, which display novel properties that make them promising candidates for future applications in high-density information storage and quantum computing [24]. Because of their finite size, these systems display behavior not observed in macroscopic magnetic systems, for example resonant magnetization tunneling phenomena. In recent years, low-dimensional magnetic materials have attracted much attention from both fundamental and applied points of view. Motivated by theoretical predictions [25], much interest has been focused on the area of 1D magnetic nanomaterials, for example, single-chain magnets synthesized using intricately tailored organometallic materials [10]. Paramagnetic complexes are particularly attractive candidates for use as building blocks in low-dimensional magnetic materials because the coordinatively unsaturated metal atom(s) that carry spin

can also serve as junction points in fabrication of 1D, 2D and 3D networks. One of the strategies in producing "designer" molecular magnets and clusters, having particular magnetic properties involves tuning the spin alignment of the constituent paramagnetic metal atoms via choice of the counterions and ligands.

In order to get a good quantitative picture of the equilibrium geometries, electronic structures and magnetic properties of gas phase $V_n(BZ)_m$ complexes, theoretical calculations are necessary, as the above mentioned experimental studies cannot measure equilibrium geometries accurately. In this aspect, there has been a considerable effort towards understanding the geometries of transition-metal-benzene complexes. Mattar and Hamilton [64] have reported DFT-based results on the ground state geometries and spin states of neutral and cationic VBz complexes. Bauschlicher *et al.* [13] reported the equilibrium geometries and dissociation energies of cationic complexes using the modified coupled-pair functional method (MCPF). Ionization energies and optimal geometries were reported by Yasuike and Yabushita [128] for small metal-benzene clusters of early transition metals, calculated with RHF/RHOF and DFT methods.

Geometries and spin multiplicities calculations of $V_n(Bz)_m^+$ complexes were reported by Weis *et al.* [123]. Recently, Pandey *et al.* have reported DFT-GGA calculations on the global geometries, ground state spin multiplicities, relative stabilities and energetics of neutral, cationic and anionic benzene complexes of vanadium [41, 83, 84].

In this section we present our DFT calculations on the set of 1D vanadium-benzene sandwiches $V_n(Bz)_{n+1}$, $n = 0, 1, 2, 3$. We compare obtained results on the optimized structural parameters with those calculated with other methods, present densities of states, charge density plots of the orbitals in this complexes, and investigate the nature of the magnetism in the sandwiches in order to explain experimentally observed behavior of the magnetic moment with increasing n as it was reported by the group of Kaya [69].

7.4.1 Computational Details

We calculate $V_n(Bz)_{n+1}$, $n = 0, 1, 2, 3$ clusters within the 1D super-cell approach, which means that the unit-cell of the system is stretched along z axis, cutting through the centers of vanadium atoms, in order to avoid an interaction, coming from the neighboring molecules. Separation between the centers of the molecules was chosen as following: 8.0 Å ($n = 0$), 10.6 Å ($n = 1$), 13.8 Å ($n = 2$), 17.0 Å ($n = 3$), 20.1 Å ($n = 4$), ensuring negligible interaction between neighboring molecules. We used the GGA with the revPBE functional [130] for the exchange-correlation potential and energy. Parameters D and \tilde{D} were set to 12 a.u. and 13 a.u., respectively. We used $K_{\max} = 3.4$ a.u.⁻¹ and $G_{\max} = 10.2$ a.u.⁻¹. The following muffin-tin radii were chosen: 2.4 a.u. (V), 0.65 a.u. (H) and 1.25 a.u. (C). For the expansion of potential and charge density in the vacuum we used m_{\max} of 48, and $m_{\max}=24$ for the expansion of the basis functions. For separate calculations of benzene we used the basis functions cut-off parameter K_{\max} of 4.00 a.u.⁻¹. These computational parameters proved to give reliable total energies, magnetic moments and equilibrium structural parameters. For calculations of all the complexes we used a D_{6h} symmetry, except for the $V(Bz)$ complex, where we used a C_{6v} symmetry.

7.4.2 $V(Bz)$ Complex

An insight into a mechanism, responsible for the bonding in the molecule $V(Bz)$ can be given on the base of a schematic analysis of the orbitals of benzene and vanadium. The valence electronic configuration of vanadium is $3d^34s^2$. The plots of five atomic $3d$ orbitals d_{z^2} , $d_{x^2-y^2}$, d_{xy} , d_{xz} and d_{yz} are presented in Fig. 7.19 (left), where by blue we denote a positive sign of a wavefunction and by yellow – negative. The π -orbitals of benzene are plotted in Fig. 7.19 (right). The lowest in the group of π -orbitals are three occupied orbitals of benzene (π_1, π_2, π_3), and they are its highest occupied molecular orbitals (HOMO). HOMO orbitals carry six π -electrons of benzene. The upper group of π -orbitals is a group of lowest unoccupied molecular orbitals (LUMO) of benzene. With '+' and '-' positive and negative sign of the wavefunctions is denoted. Of the HOMO, π_1 -orbital has no nodes, and π_2 and π_3 are degenerate in energy and have one node plane. The degenerate LUMO π_4^* and π_5^* have two node planes and π_6^* has three node planes. The reason for the bonding in the molecule is due to the fact that d -orbitals of free atom of V and π -orbitals of benzene are rather close to each other in energy, causing, therefore, a significant interaction. For further use, we will, however, rename the orbitals of V and benzene, taking into account their symmetries, hence, their ability to interact with each other. So, the five $3d$ -orbitals of the metal atom can be divided into one $d\sigma$ (d_{z^2}), two $d\pi$ (d_{xz}, d_{yz}), and two $d\delta$ ($d_{x^2-y^2}, d_{xy}$), and, of course, the $4s$ orbital is classified as $s\sigma$ orbital. Similarly, the six π -orbitals of benzene are one $L\sigma$ (π_1), two $L\pi$ (π_2, π_3), two $L\delta$ (π_4^*, π_5^*) and one $L\phi$ (π_6^*). And, finally, the σ -orbitals of benzene we will denote as Ls . The valence electronic configuration of the free benzene is, therefore, $(L\sigma)^2(L\pi)^4$.

When benzene and vanadium are brought together, overlap and hybridization of the orbitals occurs. The degree of interaction between the $d\sigma$ orbital of V and benzene is negligible, since its direction is to the hole in the middle of the benzene ring. The $d\sigma$ orbital thus remains as the nonbonding atomic orbital in $V(Bz)$, which we also expect to be the highest occupied orbital of the molecule. By the symmetry (Fig. 7.19), the $d\delta$ orbitals of V do not interact with the HOMO of benzene, but with the LUMO $L\delta$. As a result of this interaction we expect two degenerate bonding orbitals, which we will call δ -orbitals of the complex, to appear below the $d\sigma$ orbital. These three highest molecular orbitals of $V(Bz)$ will carry five electrons of V: four electrons at the δ -orbitals, and one electron at the $d\sigma$ orbital. Further, as allowed by the symmetry, the $d\pi$ states of V will interact with the HOMO $L\pi$ states of benzene, creating, as a result, two bonding π -orbitals (and, of course, two antibonding above the Fermi level), which accommodate four electrons of benzene. The $d\pi$ -orbitals of vanadium are more extended in the direction to the benzene ring, and, hence, we expect them to lie rather low in energy, compared to the δ -states. The last two orbitals, $L\sigma$ of benzene and $s\sigma$ of V, which is extended much further than any other atomic orbital of V, interact, causing a bonding Ls -state to appear, where the last two valent electrons of benzene are accommodated. Schematic plot 7.20 represents the latter considerations on the interaction of V and Bz . This scheme, also known as a Hückel scheme, is a result of several previous molecular orbital calculations [128, 2]. However, in order to approve this scheme, we performed a set of *ab initio* calculations.

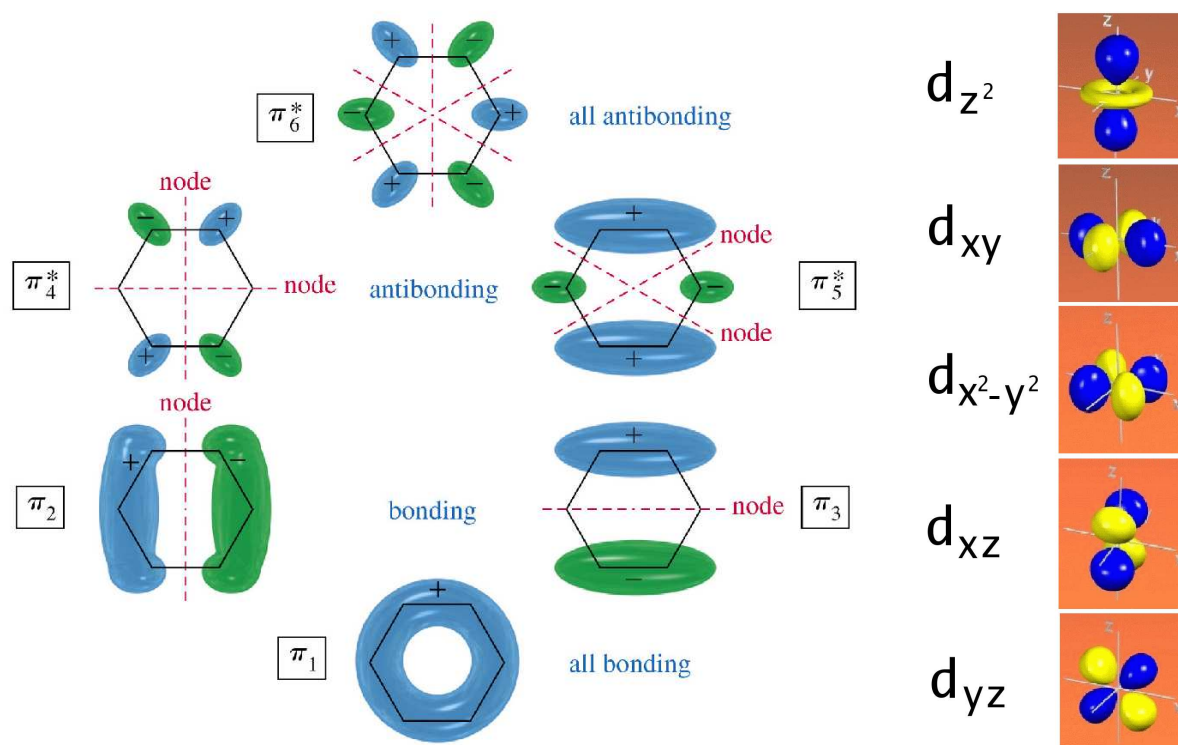


Figure 7.19: Right: schematic orbital configuration for the π -states of benzene. With '+' and '-' positive and negative sign of a corresponding wavefunction is marked. The states π_1, π_2 and π_3 are forming a HOMO group of orbitals. Of these states the latter two have one node plane. A wavefunction of the lowest π -state π_1 does not have any nodes. The orbitals π_4, π_5 and π_6 are the LUMOs of benzene and have a higher number of node planes. Left: $3d$ -orbitals of vanadium, blue color denotes positive sign of a wavefunction, yellow - negative sign.

Geometrical structure of the complex is drawn in Fig. 7.20. In our calculations we supposed that V atom is situated above the centers of the carbon and hydrogen hexagons, and, therefore, the axis (which is defined as the z -axis of the system) which goes through the centers of the V atom and the hexagons, is perpendicular to the planes of hexagons. The planes of the hydrogen and carbon hexagons can be shifted, but they are parallel to each other. It was checked by other authors that this geometrical configuration is optimal for this simple complex, but, for a charged complex $V^+(Bz)$ or more complex sandwiches, which we consider later, other geometrical structures are also possible. For instance, with increasing number of benzenes in the molecule, situation, when they are rotated by $\frac{\pi}{6}$ to each other, can be also stabilized. On the other hand, the vanadium atom could prefer not to lie on the symmetry axis of the system (z) anymore. Finally, in reality, the atoms of carbon and hydrogen are slightly shifted from their symmetrical positions so that they do not lie in the same planes anymore. However, listed above possible topological

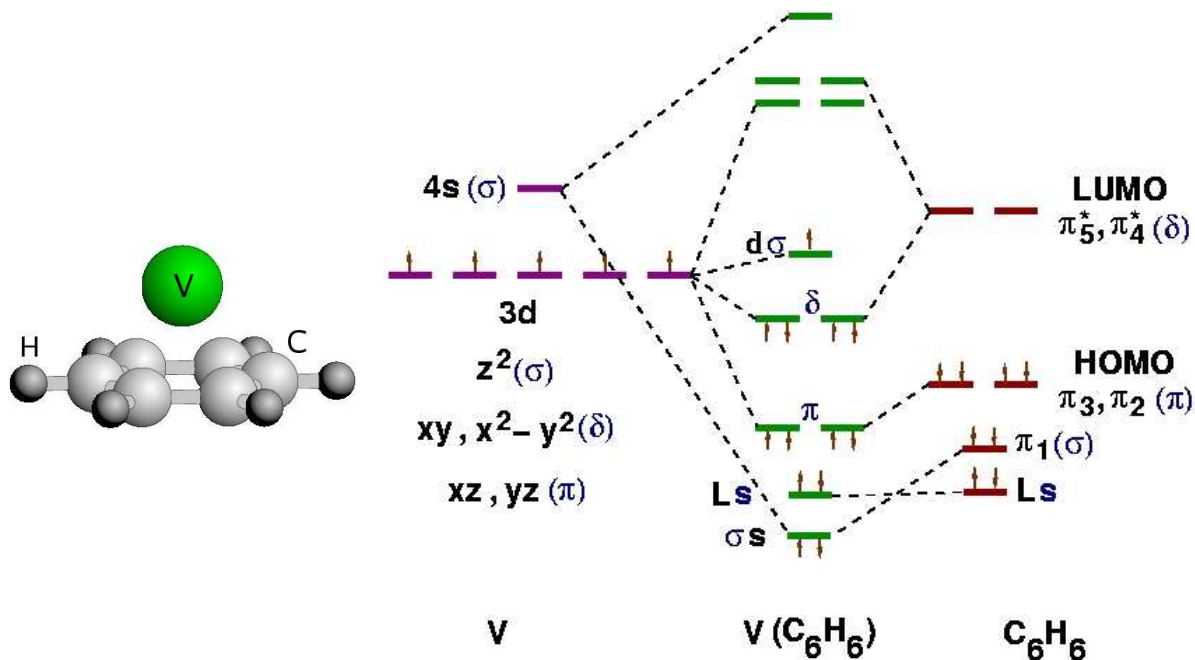


Figure 7.20: Left: Geometrical structure of the $V(Bz)$ complex. The axis z , which goes through the centers of vanadium atom and carbon and hydrogen hexagons, is perpendicular to the planes of the hexagons. Atoms in every hexagon (C,H) are lying in the same plane. Right: schematic orbital interaction scheme for the $V(Bz)$ complex (see text for details).

distortions from symmetrical positions, we consider, are mostly higher in energy than the symmetric configuration, or, the differences in total energies between distorted and symmetrical geometries are negligible [123, 84, 41].

We have performed separately nonmagnetic and spin-polarized optimizations for this complex, restricted by the C_{6v} symmetry. The optimized geometrical parameters for the $V(Bz)$ complex are presented in the Table 7.2, in comparison to the previous calculations. In this table we present the following geometrical parameters: distance between the centers of the V atom and the carbon ring (V-C), distance between the centers of the V atom and the hydrogen ring (V-H), the length of the carbon-carbon bond (C-C) and the length of the carbon-hydrogen bond (C-H). In order to estimate the effect of the V atom on benzene ring we have also performed a separate optimization of benzene, which gave the values of 1.389 Å for the C-C bond and 1.089 Å for the C-H bond. This is in good comparison to the values of 1.386–1.407 Å (C-C) and 1.073–1.087 Å (C-H), given by Bauschlicher in [13], obtained with various methods. A slight overestimation of the C-H bond can be attributed to the use of GGA. However, the changes in the latter bond length due to the V atom are around 0.5% in the case of our calculations and the values, given by other authors, are in the range of 1.073–1.087 Å for the bare benzene. For the C-C bond, nevertheless, the situation is different. We predict that the C-C bond length will increase approximately by 4% when doped with vanadium, which agrees well with data, given by

Table 7.2: Optimized geometry parameters for a $V(Bz)$ complex: distance between the V atom and the center of the carbon ring (V-C), distance between the V atom and the center of the H-ring (V-H), carbon-carbon distance (C-C) and carbon-hydrogen distance (C-H) (Fig. 7.20). NM and FM corresponds to our nonmagnetic and magnetic calculations. (a): data from [84]; (b) data from [64]; (c): data from [13]; (d),(e): data from [123] for triplet and quintet states of $V(Bz^+)$, respectively; (f),(g): data from [41], obtained with different methods.

	NM	FM	(a)	(b)	(c)	(d)	(e)	(f)	(g)
V-C	1.651	1.656	1.97	1.62	1.964	1.67	1.92	1.58	1.45
V-H	1.564	1.571	-	-	-	-	-	-	-
C-C	1.422	1.423	1.42	-	1.42	-	-	1.45	1.48
C-H	1.082	1.081	1.09	-	1.074	-	-	1.09	1.09

other authors (7.2). This increase of the bond length is due to the interaction with the V atom, which leads to the occupation of the LUMO orbitals of benzene with the higher number of nodes. This interaction is also responsible for the shift between the planes of C and H hexagons: the H ring prefers to lie closer to the V atom than the C ring by 0.087 Å (NM) and by 0.085 Å (FM). For the V-C distance we predict the values of 1.651 Å and 1.656 Å for the paramagnetic and magnetic cases, respectively. Presented in the table 7.2 values for this distance, calculated by different authors, however, strongly disagree with our results and among each other. This can be attributed to the differences in electronic configurations for the complex (triplet and singlet states of $V(Bz^+)$ in [123], $V^+(Bz)$ complex in [13]) and different calculational methods used (for instance, GGA-pbw with all-electron 6-311G** basis set, and GGA-pbw with frozen-core LanL2DZ basis set in [41] and [84]). Using the LDA LCAO method, Mattar and Hamilton [64] obtained the value of 1.62 Å for the V-C bond in the neutral complex, which is the closest to our result. However, we believe the most our all-electron FLAPW calculations.

Difference in total energies $E_{NM} - E_{FM}$ of 0.491 eV between the paramagnetic and magnetic solutions at the optimized positions shows, that the magnetic state is much more stable than the nonmagnetic one. The value of the magnetic moment of $1.00\mu_B$ for the complex is consistent with the orbital scheme, we have described previously, and can be understood from the DOS for the molecule, presented in Fig. 7.21. In this plot by black solid line the total DOS are plotted, by solid blue and orange lines the LDOS for the vanadium and carbon atoms, respectively, are plotted for the paramagnetic and magnetic cases (spin-up and spin-down channels are indicated by arrows). Paramagnetic DOS can be understood on the base of the Hückel orbital scheme, explained in the beginning of the section. The nonbonding $d\sigma$ orbital of V is situated at the Fermi level and accommodates one electron. The two degenerate bonding δ -states, created as a result of interaction between the LUMO of benzene and $d\delta$ -orbitals of V are lying slightly lower in energy, accommodating four electrons of V. Large overlap of the $d\pi$ -orbitals of V and $L\pi$ HOMO

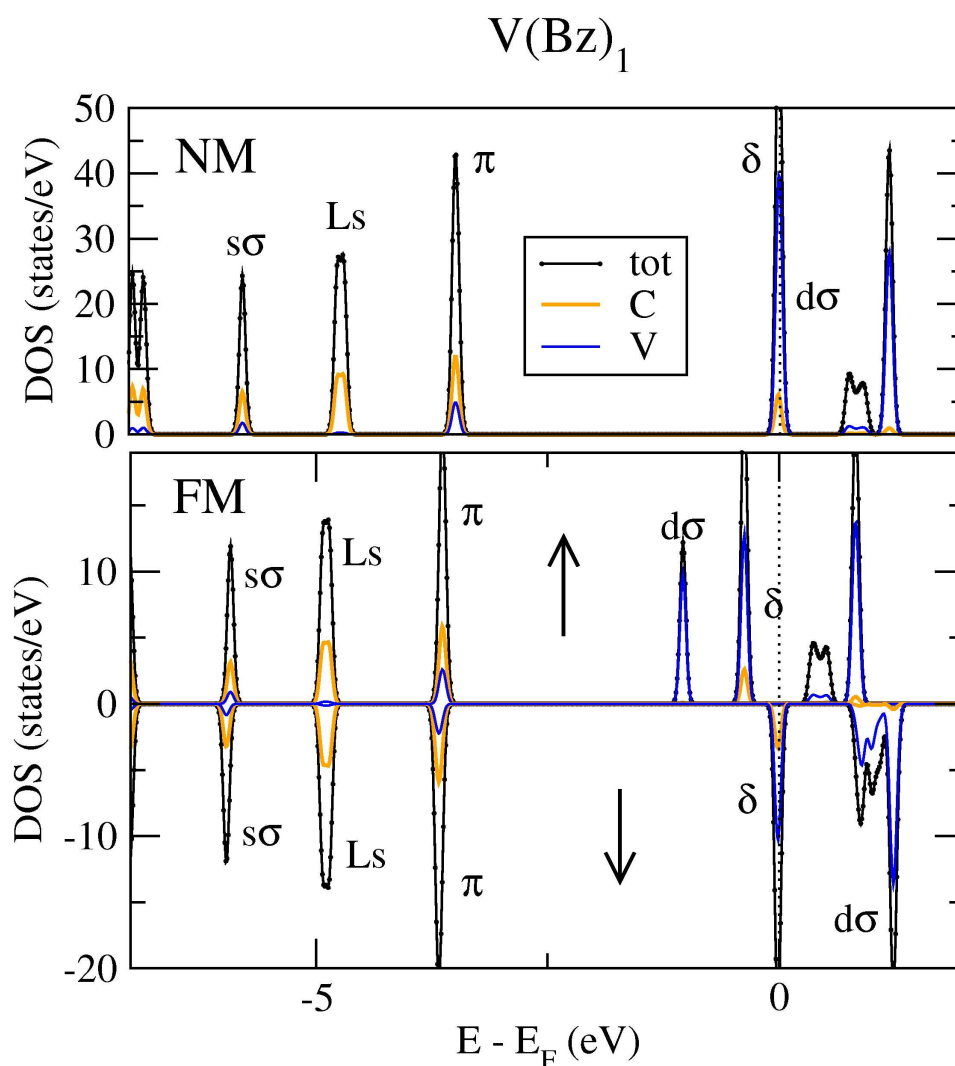


Figure 7.21: Densities of states for the $V(Bz)_1$ cluster: total DOS (black solid line), DOS at the carbon sites (orange solid line) and DOS at the vanadium site (blue solid line). Top: nonmagnetic densities of states. Bottom: spin-polarized DOS for spin-up and spin-down channels (indicated by arrows).

orbitals of benzene is responsible for the low-lying π -states of the molecule, carrying four π -electrons of benzene. The last two valent π -electrons of benzene are situated well below the highest occupied σ -orbitals Ls due to the significant overlap with the $4s$ -orbital of vanadium. The charge density plots of the highest valent states of the cluster $V(Bz)$ can be seen in Fig. 7.22. In the spin-polarized case a large exchange splitting of the states can be seen. This splitting is the largest for the $d\sigma$ state of vanadium, which is located at the Fermi level in the nonmagnetic case, and a smaller splitting can be seen for the δ states. Of five vanadium electrons three have spin up (one at the $d\sigma$ level and two at

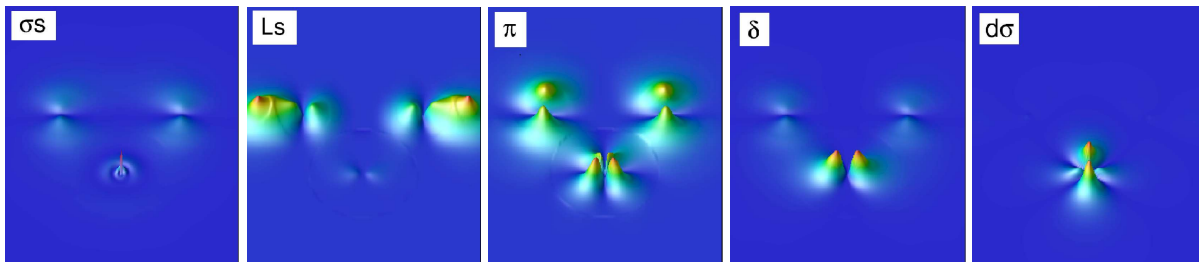


Figure 7.22: Charge density plots for the electronic states of the molecule $V(Bz)$, labelled by the names of the states in Fig. 7.21

the δ level) and two have spin down at the δ level, which results in the total magnetic moment of $1.00\mu_B$ for the system. Our calculations show, that this magnetic moment is entirely located inside the muffin-tin sphere of V ($1.09\mu_B$). The low-lying states of the complex are almost not prone to the exchange splitting, and the magnetic moments of the H atoms ($0.001\mu_B$) and the C atoms ($0.01\mu_B$) are very small, however, magnetic moments of C atoms prefer to couple antiferromagnetically to the magnetic moment of the V atom. Interestingly, the spin-dependent properties of the molecule will be determined by the δ orbitals, which are lying at the Fermi energy.

Our value for the total magnetic moment agrees very well with the experimental average value of $0.8\mu_B$, measured by Kaya and co-workers in [69] for the $V(Bz)_2$ complex at room temperature in the gas phase. However, in the literature the calculated magnetic moment of the $V(Bz)$ complex ranges from $0\mu_B$ to $5\mu_B$. This inconsistency can be attributed to the reasons, discussed previously. First, the magnetic moment depends strongly on the electronic configuration of the complex; secondly, the results strongly depend on the computational method used, and different magnetic states can be favored, depending on the method, even with the same geometrical parameters [123, 84, 83, 41, 13].

7.4.3 $V_1(Bz)_2$ Complex

When two benzene molecules are located at the same distance from V, as in the $V(Bz)_2$ complex, the symmetry-adapted molecular orbitals are produced from the orbitals of a single benzene. These orbitals are classified into the $L(\sigma, \pi, \delta, \phi)_{g,u}$ orbitals. The atomic orbitals of vanadium have g symmetry, and only $L(\sigma, \pi, \delta)_g$ orbitals of benzene can interact with them. An interaction scheme for this complex, in principal, remains the same, as for the $V(Bz)$ complex. Nonbonding $d\sigma$ orbital occupies the Fermi energy with one electron. Lower in energy two degenerate δ -states are situated, created as a result of hybridization of the vanadium $d\delta$ orbitals and $(L\delta)_g$ orbitals of benzene, which carry four vanadium electrons (see Fig. 7.23).

The π group of states consists of two degenerate π_g and π_u orbitals. The hybridization of $d\pi$ states of V and $L\pi_g$ orbitals of benzene is responsible for the appearance of π_g , while

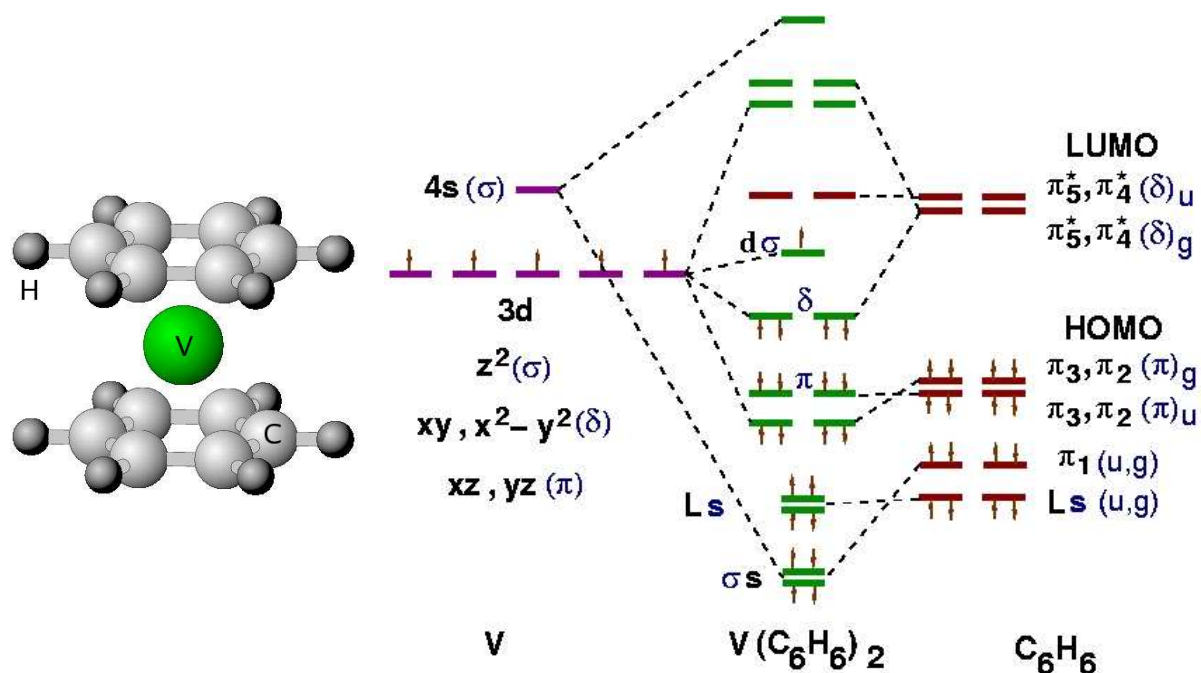


Figure 7.23: Left: Geometrical structure of the $V(Bz)_2$ complex. The axis z , which goes through the centers of vanadium atom and carbon and hydrogen hexagons, is perpendicular to the planes of the hexagons. Atoms in every hexagon (C,H) are lying in the same plane. Right: schematic orbital interaction scheme for the $V(Bz)_2$ complex (see text for details).

the π_u remains nonbonding $L\pi_u$ of benzene. The last two states σ should in principal also split into σ_g and σ_u levels, as the latter one is the $L\sigma_u$ of benzene, non-interacting with the V atom.

Geometrical structure of the system is drawn in Fig. 7.23 (right). We calculate this structure in the frame of D_{6h} symmetry, although for this structure other geometrical configurations are possible [41], as was described earlier. However, it was shown that other possible configurations give negligible total energy differences and do not effect the magnetic properties of the molecules.

Calculated optimal geometrical parameters of this system for nonmagnetic and magnetic cases are listed in table 7.3 in comparison to previously published data. The first thing to notice is that magnetism does not change the equilibrium parameters significantly, compared to the nonmagnetic ones, which is also the case for the $V(Bz)$ semi-sandwich. The difference between the V-C and V-H nonmagnetic and magnetic distances constitutes 1% and 2%, respectively. Another issue to notice is that the C-H distance for this complex, compared to the $V(Bz)$ complex, almost does not change. The C-C distance for the $V(Bz)_2$ system is slightly smaller compared to the $V(Bz)$, which is due to the larger V-C distance in $V(Bz)_2$. In general, all the methods, including ours, give approximately the same C-C and C-H distances, which is not, however, the case for the V-C distance.

Table 7.3: Optimized geometry parameters for a $V(Bz)_2$ complex: distance between the V atom and the center of the carbon ring (V-C), distance between the V atom and the center of the H-ring (V-H), carbon-carbon distance (C-C) and carbon-hydrogen distance (C-H) (Fig. 7.23). NM and FM correspond to our nonmagnetic and magnetic calculations. (a): data from [123]; (b)-(d): RHF/ROHF, R/UHF and DFT R/UB3LYP data from [128]; (e),(f): data from [41].

	NM	FM	(a)	(b)	(c)	(d)	(e)	(f)
V-C	1.799	1.815	1.81	1.708	1.565	1.675	1.69	1.67
V-H	1.786	1.808	-	1.717	1.539	1.667	-	-
C-C	1.415	1.415	-	1.411	1.438	1.426	1.44	1.43
C-H	1.083	1.082	-	1.072	1.088	1.084	1.09	1.09

Our calculated optimal value for this V-C distance of 1.799 Å (nonmagnetic) and 1.815 Å (magnetic), is significantly larger than the corresponding value for the $V(Bz)$ complex. We attribute this fact to the different bonding mechanism, responsible for the geometry of the complex. The second benzene ring of the system causes a certain symmetrical rearrangement of the single benzene orbitals, causing an appearance of the nonbonding orbitals, increasing, therefore, the distance between the benzene rings and the V atom. The same tendency with the same equilibrium distances can be seen in [123]. The only experimental results for the V-C distance of 1.66 Å in the $V(Bz)_2$ complex are given in [74], although the authors report, that their structure determination did not possess a high degree of accuracy. Also, much smaller value for this distance in [74], compared to our calculated one, can be attributed to the fact of presence of the Ag matrix, used for these experiments. In general, it is known that different additional reactants can effect the properties of the complex considerably. For instance [4] the V-C distance drastically decreases when the $V(Bz)_2$ complex is put on the Cu(111) surface. However, obtained by other authors [128, 41] values for the V-C distance reflect the differences in computational methods and electronic configurations used. Finally, as it was also calculated for the $V(Bz)$ complex, the plane of the H-hexagon is shifted towards the V atom by 0.01 Å, compared to the carbon ring.

As for the $V(Bz)$ complex, magnetic solution is much lower in energy than nonmagnetic one, with the difference in total energies $E_{NM} - E_{FM}$ of 0.459 eV. The magnetic moment of the whole system remains the same, with the value of $1.00\mu_B$. Almost the same values, as in the case of $V(Bz)$, stand for the magnetic moments inside the muffin-tin spheres of V, C and H; the antiferromagnetic coupling of the magnetic moments of V and C sites is also preserved.

Basic features of the paramagnetic DOS, Fig. 7.24 (top), precisely reflect the Hückel interaction scheme for this complex, discussed in the beginning of the section. In this plot by black solid line the total DOS are plotted, by solid blue and orange lines the LDOS for the vanadium and carbon atoms, respectively, are plotted for the paramagnetic and

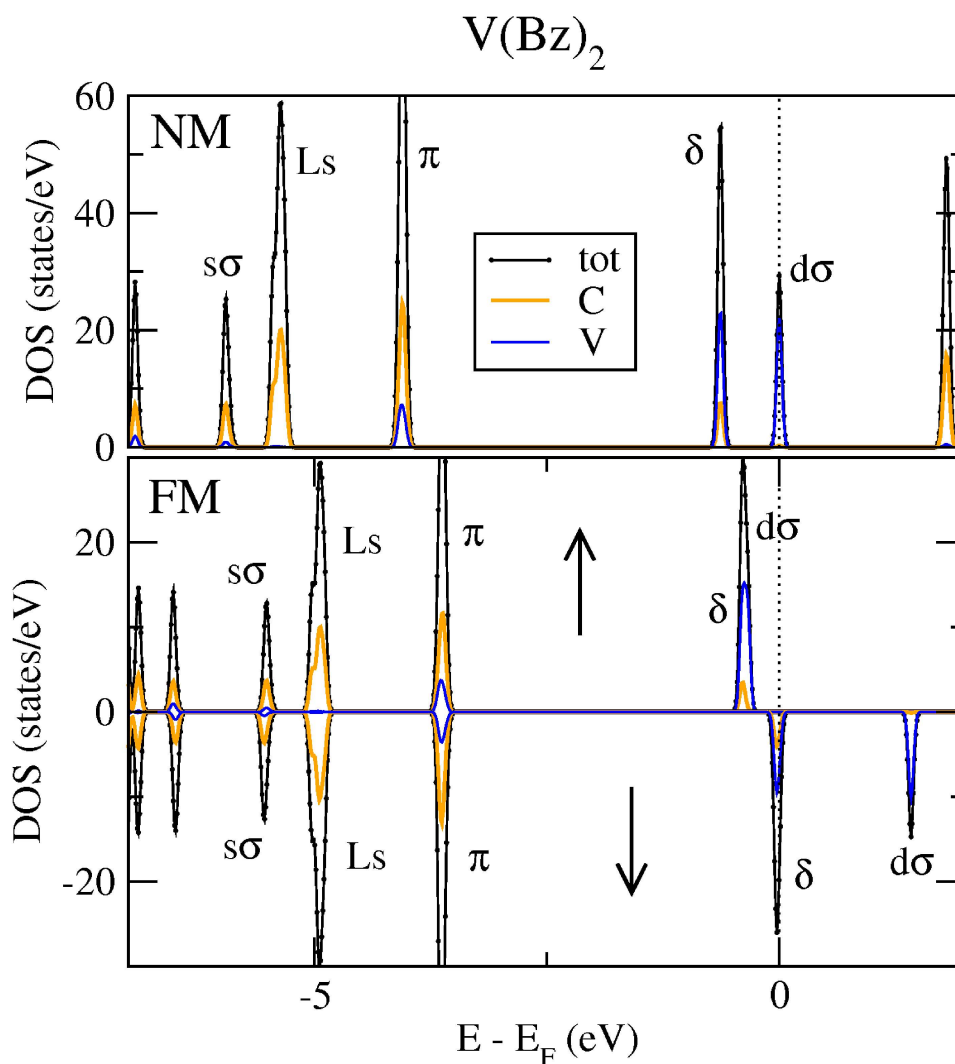


Figure 7.24: Densities of states for the $V(Bz)_2$ cluster: total DOS (black solid line), DOS at the carbon cites (orange solid line) and DOS at the vanadium cite (blue solid line). Top: nonmagnetic densities of states. Bottom: spin-polarized DOS for spin-up and spin-down channels (indicated by arrows).

magnetic cases (spin-up and spin-down channels are indicated by arrows). As in the case of the half-sandwich $V(Bz)$, $d\sigma$ orbital with one electron is located at the Fermi level. However, much lower in the energy, compared to $V(Bz)$ DOS, doubly degenerate hybrid δ is located. This happens due to the larger overlap and stronger bonding of the $d\delta$ orbitals of V with the LUMO of two benzenes $L\delta_g$. According to the symmetry reasons, discussed above, the doubly degenerate π state of $V(Bz)$ slightly splits in $V(Bz)_2$ into two single levels π_g and π_u , of which π_u is nonbonding. The same symmetry splitting, which can be seen in the figure, happens to the $4s\sigma$ - $L\sigma$ hybridized orbital. We, however, did not

distinguish these two $s\sigma_g$ and $s\sigma_u$ levels in the charge density plots for the $V(Bz)_2$ orbitals, presented in Fig. 7.25. Magnetic DOS, Fig. 7.24 (bottom), repeat the main features of the $V(Bz)$ cluster magnetic DOS.

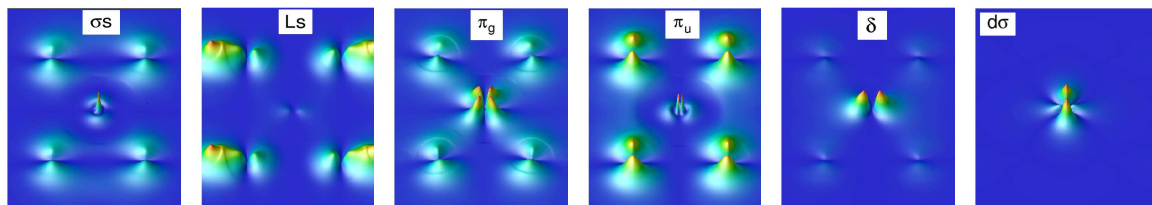


Figure 7.25: Charge density plots for the electronic states of $V(Bz)_2$ -cluster. The plots are labelled by the names of the states in Figs. 7.24, 7.23.

Low lying π , $s\sigma$, Ls states of the molecule are almost not prone to the exchange splitting, while the spin-dependent behavior of the complex is determined by the δ -state at the Fermi energy for spin down channel.

7.4.4 $V_2(Bz)_3$ Complex

A $V_2(Bz)_3$ complex is obtained by putting the $V(Bz)$ half-sandwich on top of the $V(Bz)_2$ molecule (see Fig. 7.26). The orbital interaction scheme, due to the presence of an additional benzene and vanadium becomes rather complicated, although, as the resulting molecule has a symmetric configuration, some suggestions on the resulting orbital arrangement can be made. Resulting orbitals should distinctly split into two groups: one, connected to the outer benzene rings, and the second one, concentrated on the inner benzene ring, equidistant from the two other benzenes. Speaking from the point of view of the system's symmetry, the molecule itself can be imagined as two half-sandwiches, connected by an additional benzene. Taking into account these considerations, we would expect that, due to the bonding and charge transfer between the atoms of V through the central benzene, bonding of the V atoms to the outer benzenes will become weaker and the V-C₂ distance will increase (see Fig. 7.26), compared to the distance in free $V(Bz)$. Expected increase in the V-C₂ distance can be clearly observed from the values, given in table 7.4. We have performed nonmagnetic, ferromagnetic and antiferromagnetic structural optimizations for the complex, however, calculated values did not differ significantly, therefore, only the ferromagnetic distances are presented in the table. In comparison to the V-C distance for the $V(Bz)$ complex (table 7.2), distance from the V atom to the outer C ring V-C₂ increased by 4.6%. This tendency towards increasing can be also seen in almost all the calculations by other authors. Due to the strong interaction of two vanadium atoms via inner benzene, also the carbon-carbon distance C₁-C₁ is considerably larger, than in the $V(Bz)$ or $V(Bz)_2$ complexes and in the outer carbon ring of $V_2(Bz)_3$ (C₂-C₂), which can be attributed to the population of the LUMO orbitals of benzene. The effect of this interaction cannot be, however, noticed for any of the strong

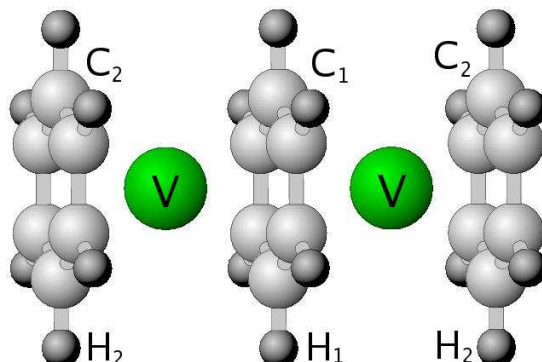


Figure 7.26: Geometrical structure of the $V_2(Bz)_3$ complex. The axis z , which goes through the centers of vanadium atoms and carbon and hydrogen hexagons, is perpendicular to the planes of the hexagons. Atoms in every hexagon (C,H) are lying in the same plane.

carbon-hydrogen bond lengths (C_1-H_1, C_2-H_2). The results of other authors also prove the correctness of the proposed interaction scheme for the complex, presenting it as a sum of $V(Bz)$ and Bz compounds, which is reflected in the ratio of V- C_1 and V- C_2 distances: the V- C_1 distance is larger by approximately 3-5% , than the V- C_2 distance, depending on the method.

We have performed nonmagnetic, ferromagnetic and antiferromagnetic calculations at the optimal positions for the $V_2(Bz)_3$ complex. These calculations confirm that the molecule is magnetic, with the difference in total energies between the ferromagnetic and nonmagnetic solutions $E_{NM} - E_{FM}$ of 0.415 eV per atom of vanadium. A small energy difference between the FM and AFM states of 6.1 meV for the whole complex (FM state is lower in energy) shows, that the magnetic ordering of the molecule can be prone to the thermal fluctuations already at $T_0=100K$. The total magnetic moments of $0.00\mu_B$ (AFM) and $2.00\mu_B$ (FM) for these magnetic states should, in principal, result in an average value of $1.00\mu_B$ for the temperatures larger than T_0 . This fact, together with the spin-rotation effect, can explain an average value of $1.3\mu_B$ for the complex, measured at 154K by Kaya and co-workers [69]. Also, we want to stress, that the energy barrier of 6.1 meV can be easily overcome due to experimental conditions, phonon excitations, etc. [41].

The local magnetic moment of V atom in FM and AFM cases constitutes the same value of $1.02\mu_B$. When vanadium atoms are coupled ferromagnetically, small magnetic moments of carbon atoms of $0.008\mu_B$ are coupled ferromagnetically to each other and antiferromagnetically to the moments of vanadii. In AFM case C magnetic moment of $0.005\mu_B$ in the outer benzene is coupled antiferromagnetically to the closest V atom, while the C moment in the inner benzene vanishes completely. As it was already noticed by Yasuike and Yabushita in [128], the orientation of the magnetic moments in the carbon atoms relatively to the moments of vanadii could considerably effect the difference in total energies between FM and AFM states.

Table 7.4: Optimized geometry parameters for a $V_2(Bz)_3$ complex: distance between the V atom and the center of the inner carbon ring (V-C₁), distance between the V atom and the outer carbon ring (V-C₂), distance between the V atom and the outer H ring (V-H₂), carbon-carbon distance in the outer and inner C rings (C₂-C₂ and C₁-C₁, respectively) and carbon-hydrogen distance in the outer and inner benzenes (C₂-H₂ and C₁-H₁, respectively) (Fig. 7.26). FM corresponds to our ferromagnetic calculations. (a),(b): RHF/ROHF and R/UHF data from [128], respectively; (c)-(f): data from [41], calculated with different methods; (g): data from [123].

	FM	(a)	(b)	(c)	(d)	(e)	(f)	(g)
V-C ₁	1.793	1.791	1.722	1.75	1.73	1.71	1.70	1.76
V-C ₂	1.727	1.660	1.648	1.67	1.65	1.68	1.64	1.76
V-H ₂	1.676	-	-	-	-	-	-	-
C ₁ -C ₁	1.439	1.428	1.448	1.46	1.45	1.47	1.45	-
C ₁ -H ₁	1.081	-	-	1.09	1.09	1.09	1.09	-
C ₂ -C ₂	1.415	1.414	1.429	1.45	1.43	1.45	1.43	-
C ₂ -H ₂	1.082	-	-	-	-	-	-	-

The densities of states and the charge density plots for the corresponding orbitals of the $V_2(Bz)_3$ complex are presented in Figs. 7.27 and 7.28 (paramagnetic, antiferromagnetic and ferromagnetic DOS are given in Fig. 7.27). Due to the inversion symmetry of the system AFM DOS are given only for spin-up channel. In these plots, black solid line is used for the total DOS, orange solid line for the LDOS of C atoms in the inner benzene, green - for the carbons in the outer benzenes and blue - for the LDOS in the muffin-tins of vanadium. We keep the notations for the states of the same origin as in the cases of $V(Bz)$ and $V(Bz)_2$. Not involved in any interactions nonbonding orbitals $d\sigma_1$ and $d\sigma_2$, located on two V atoms, occupy the Fermi level, carrying two d_{z^2} -electrons. Two degenerate δ_2 orbitals, created as a result of the hybridization between the $d\delta$'s of vanadium and LUMO of the outer benzenes are located slightly lower in energy. In Fig. 7.28 we presented the total charge density plots for these three HOMO of $V_2(Bz)_3$, which carry six electrons. The rest of the valent V electrons is accommodated by a much lower in energy, doubly degenerate δ_1 orbitals, which is a hybrid between $d\delta$ of vanadium and a LUMO of the inner benzene. Two hybrids $L\pi_2-d\pi$ and $L\pi_1-d\pi$ are situated very deep in energy, and a mixed set of Ls and $s\sigma$ orbitals comes after. Among the orbitals, which are concentrated on the inner and outer benzenes, the first ones are located characteristically much lower in energy, which shows, that these orbitals, in particular, δ_1 and π_1 , are responsible for the bonding in the molecule. The AFM DOS, symmetric for the both spin channels, shows the exchange splitting between the $d\sigma_1$ and $d\sigma_2$ orbitals. In the FM case, strong exchange splitting can be seen for all the HOMO orbitals of $V_2(Bz)_3$, with the δ_2 orbital for spin-down occupying the Fermi level.

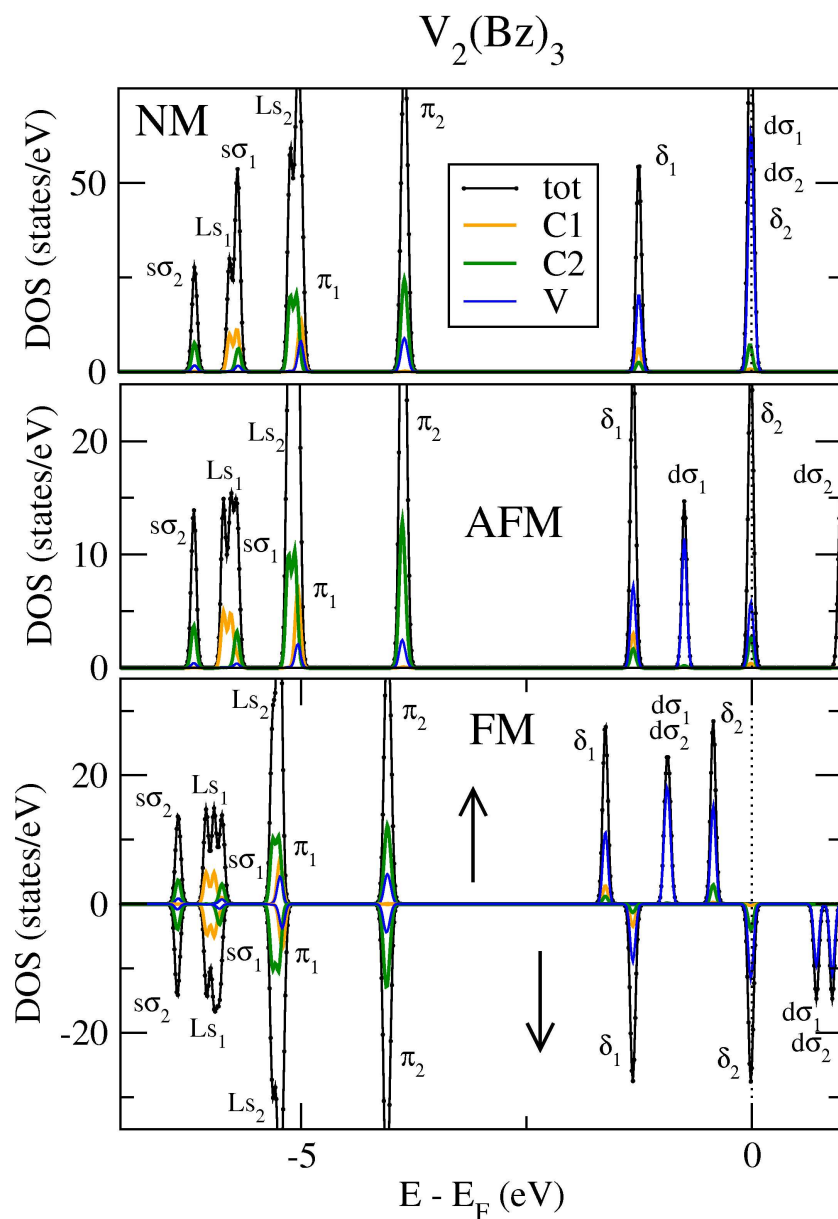


Figure 7.27: Densities of states for the $V_2(Bz)_3$ cluster: total DOS (black solid line), DOS at the outer and inner carbon cites (green and orange solid lines, respectively) and DOS at the vanadium cite (blue solid line). Top: nonmagnetic densities of states. Middle: antiferromagnetic DOS for spin-up channel. Bottom: ferromagnetic DOS for spin-up and spin-down channels (spin-up and spin-down are denoted by arrows). The LDOS at two different vanadium atoms are marked by blue and green solid lines for the antiferromagnetic case.

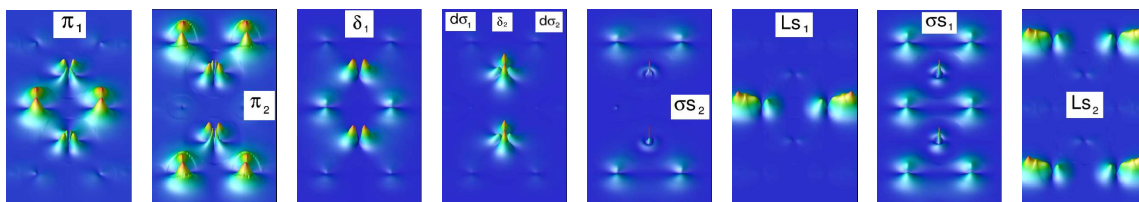


Figure 7.28: Charge density plots for the electronic states of $V_2(Bz)_3$ -cluster. The plots are labelled by the names of the states in Fig. 7.27.

7.4.5 $V_3(Bz)_4$ Complex

In analogy to the previous complex $V_2(Bz)_3$, a $V_3(Bz)_4$ molecule can be considered as a composition of two outer half-sandwiches, connected by an inner complex $V(Bz)_2$ (geometrical structure of the complex is given in Fig. 7.29). Taking into account previously described interaction scheme for the $V(Bz)_2$ complex, we would expect a less degree of bonding in the $V_3(Bz)_4$ complex, compared to $V_2(Bz)_3$, where all the orbitals of the inner benzene were of a bonding character, while $V(Bz)_2$ possesses a set of nonbonding u -orbitals. From these *a priori* considerations, we expect larger equilibrium geometrical parameters for the complex.

Equilibrium geometrical parameters for the system are given in the table 7.5 in comparison to previously published data in [128, 41, 123]. We perform ferromagnetic (FM) and antiferromagnetic (FMB, see Fig. 7.29) optimizations, where in the latter case the magnetic moment of the inner V atom was coupled antiferromagnetically to the moments of the outer vanadii. In both cases we predict a significant increase in the distance V_2 -

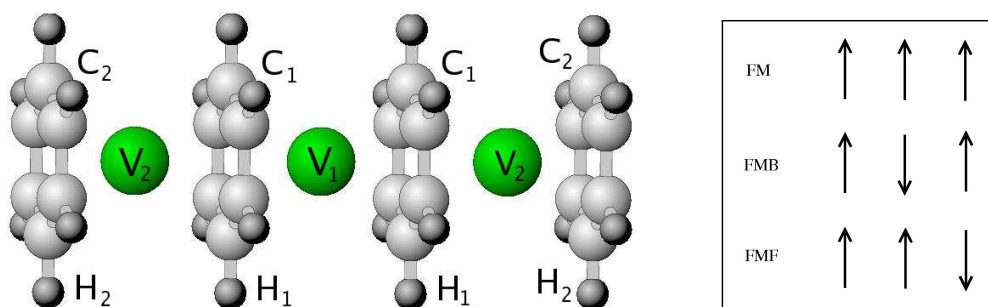


Figure 7.29: Left: geometrical structure of the $V_3(Bz)_4$ complex. The axis z , which goes through the centers of vanadium atoms and carbon and hydrogen hexagons, is perpendicular to the planes of the hexagons. Atoms in every hexagon (C,H) are lying in the same plane. Right: possible magnetic configurations in the complex.

C_1 , compared to the V - C_1 distance in the $V_2(Bz)_3$ complex. This tendency can be also observed in the data of other authors for these distances. Due to the changes in the bonding mechanism of the molecule also an increase in the V_2 - C_2 distance can be seen,

	FM	FMB	(a)	(b)	(c)	(d)
V ₁ -C ₁	1.878	1.885	1.724	1.72	1.68	1.77
V ₂ -C ₁	1.917	1.925	1.841	1.76	1.78	1.75
V ₂ -C ₂	1.831	1.820	1.639	1.66	1.65	1.74
V ₂ -H ₁	1.885	1.910	-	-	-	-
V ₂ -H ₂	1.808	1.794	-	-	-	-
C ₁ -C ₁	1.429	1.431	1.430	1.47	1.47	-
C ₂ -C ₂	1.412	1.412	1.416	1.45	1.45	-

Table 7.5: Optimized geometry parameters for a $V_2(Bz)_3$ complex: distance between the inner V_1 atom and the center of the inner hexagon ring (V_1 - C_1); distance between the outer V_2 atom and the centers of the carbon rings (V_2 - C_1 and V_2 - C_2), distance between the outer V_2 atom and the H rings (V_2 - H_2 and V_2 - H_1), carbon-carbon distance in the outer and inner C rings (C_2 - C_2 and C_1 - C_1 , respectively). FM and FMB correspond to our ferromagnetic and antiferromagnetic calculations, respectively (see text). (a): data from [128]; (b),(c): data from [41]; (g): data from [123].

which results in a smaller C_2 - C_2 distance, already quite close to the unperturbed benzene carbon-carbon distance, while the C_1 - C_1 remains quite large. The parameters of the inner $V(Bz)_2$ complex did not change significantly in the $V_3(Bz)_4$ complex, while a magnetostrictive effect is probably responsible for a larger V_1 - C_1 and respectively smaller V_2 - C_2 and V_2 - C_1 distances in the FMB case. In general, similarly to the previous complexes, the difference between FM and FMB geometrical parameters is almost negligible and it constitutes at most 1%.

Calculated difference in total energies between the ferromagnetic and nonmagnetic solutions is $E_{NM} - E_{FM} = 0.30$ eV per V atom. We considered three possible magnetic configurations at the FM-optimized atomic positions: ferromagnetic FM, FMB (the inner magnetic moment is opposite to the rest of the vanadium magnetic moments) and FMF (one of the outer magnetic moments is opposite to the rest) (see Fig. 7.29). The difference in total energy constitutes 4.1 meV per V atom in favor of the FMB state with respect to the FM solution, with FMF state being 1 meV per V atom higher in energy than the FM state. This is consistent with the experimental data at 56K [43]. However, for the $V_3(Bz)_4$ complex the energy difference of 15 meV (160K) for the whole complex can be easily overcome due to thermal fluctuations at room temperature and the presence of a magnetic field. This leads to a consequent increase in the average value of the magnetic moment with increasing temperature, and was experimentally observed [69]. In the FM case the magnetic moments of the inner and outer vanadii are 0.76 and $1.17\mu_B$, respectively, with the resulting total magnetic moment of $3\mu_B$. The transfer of the spin density from the inner V to the outer ones clearly indicates a delocalization of the d_{z^2} -electrons along the z -axis of the molecule. The magnetic moments of the carbon atoms align antiferromagnetically to the magnetic moments of vanadii, with the values of 0.011

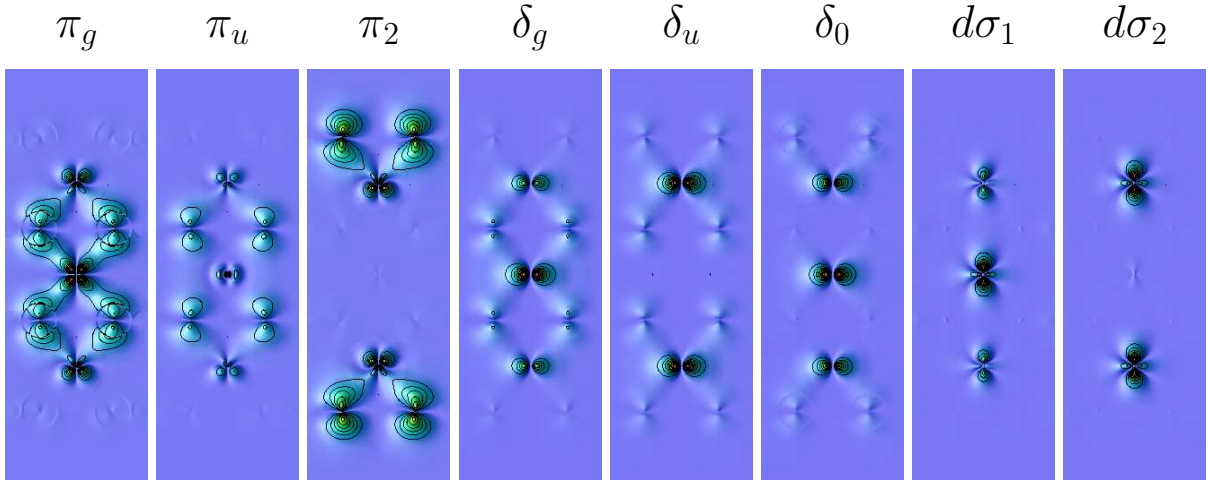


Figure 7.30: Charge density plots for the electronic states of $V_3(Bz)_4$ -cluster. The states are presented from the right to the left in order of their appearance in the nonmagnetic densities of states. The $d\sigma_1$ -state clearly shows a delocalization of the d_{z^2} -electrons of vanadium along the z -axis of the system.

and $0.009\mu_B$ for C_1 and C_2 , respectively. For the FMB configuration, the total magnetic moment of the system constitutes $1\mu_B$, with the absolute value of $1.07\mu_B$ for the magnetic moment inside every muffin-tin sphere of vanadium. In this case the magnetic moment of the outer carbon is $0.008\mu_B$, coupled antiferromagnetically to the magnetic moment of V_2 , and the magnetic moment of C_1 is zero, in analogy to the $V_2(Bz)_3$ complex.

In Fig. 7.30 we show the charge density plots of the orbitals in order of their appearance in the nonmagnetic densities of states. We observe, that the orbitals δ and π , responsible for the bonding in the molecule can be distinctly separated into three groups. The first group includes δ_0 and π_2 orbitals, which represent separate nonbonding δ orbitals of $V(Bz)$ and $V(Bz)_2$ complexes and nonbonding π orbitals of the $V(Bz)$ complex, respectively. The second group is a nonbonding u -group of orbitals, δ_u and π_u , of the outer and inner $V(Bz)_1$ complexes. Finally, the third group is a g -group, associated with the middle $V(Bz)$ molecule. The δ orbitals are in general higher in energy than the π group. Among these, the g -orbitals, responsible for the bonding, are the lowest ones, higher in energy the u -states are situated, and, finally, δ_0 and π_2 – are the highest ones. As we see, the bonding in the molecule is due to the g -group of orbitals, among the π and δ orbitals of the molecule, on the contrary to the $V_2(Bz)_3$ complex, where almost all the δ and π orbitals were of the bonding character. On the base of this fact the elongation of the V-C bonds in the $V_3(Bz)_4$ could be explained. A group of states at the Fermi level includes δ_0 , $d\sigma_1$ and $d\sigma_2$ orbitals, among which the $d\sigma_1$ is a d_{z^2} -orbital of the inner V atom, while $d\sigma_2$ is associated with the outer vanadium. From the charge density plots one can see, that the orbital $d\sigma_1$, concentrated mostly on the inner V atom, is, nevertheless, significantly delocalized along the z -axis of the system. This symbolizes a transition from zero-dimensional

clusters to truly one-dimensional infinite vanadium-benzene nanowires. A large difference in the local magnetic moments of the inner and outer vanadyls for the FM case can be attributed to this fact. For the FMB configuration, however, this delocalization does not occur, which results in the equal local vanadium magnetic moments.

We have also considered a $V_4(Bz)_5$ complex, obtained by a binding of the $V_3(Bz)_4$ cluster and the $V(Bz)$ half-sandwich into a single molecule. This compound is magnetic, and is by 0.23 eV lower in energy than the nonmagnetic cluster. We used optimized ferromagnetic (with all the vanadium magnetic moments aligned) atomic positions to calculate the total energy differences between all the possible magnetic configurations in this molecule. Our calculations show, that the high-spin FM solution with the total magnetic moment of $4\mu_B$ is by 31 meV per V atom lower in energy, than any of the low-spin magnetic solutions. In addition, we considered a case of an infinite wire $(VBz)_\infty$, obtained by an infinite repetition of $V(Bz)$ half-sandwiches. The infinite wire represents the limit of the $V_n(Bz)_{n+1}$ complexes with large n . The energy difference of 57 meV per V atom with respect to the AFM solution is in favor of the FM case, which is 0.11 eV per V atom lower in energy than the NM configuration. This proves, that with increasing number of vanadyls in the molecular $V_n(Bz)_{n+1}$ complexes, the ferromagnetic ordering becomes energetically preferred, leading to the increase in the value of the total magnetic moment of the molecules. This was indeed recently observed experimentally [69].

7.4.6 Conclusions

In this section we considered a set of quasi-one-dimensional multiple vanadium-benzene sandwiches $V_n(Bz)_{n+1}$, systems of a significant interest in the field of organometallics. We calculated optimal geometries, total energies and magnetic structures, and on the base of calculated densities of states we have given the orbital interaction schemes for these complexes. We found out, that the molecules are magnetic, with a large gain in total energy, as compared to the nonmagnetic solution. With increasing number n of vanadyl atoms in the complex, the total magnetic moment of the molecule increases, and the ferromagnetic ordering becomes preferred with respect to the low-spin antiferromagnetic solutions. Also we predict that for $n \geq 3$ a delocalisation of the d_{z^2} -electrons of vanadyls along the axis of the molecules will occur. Our calculations qualitatively explain the results of recent molecular beam magnetic deflection experiments, predicting the molecules to order ferromagnetically [69].

Chapter 8

Conclusions

The full-potential linearized augmented plane-wave (FLAPW) method is a density functional theory based *ab initio* method, which treats all electrons of a system. It is applicable to all elements of the periodic table and to materials relevant for solid state physics with open geometries, low symmetry, structural and chemical complexity. The method proved to be the most precise computational scheme regularly applied in solid state physics capable of calculating ground-state properties such as the total energy, the force exerted on the atoms and the magnetic properties such as spin and orbital moments as well as the magnetic order. So far the method is predominantly used to calculate bulk properties, or surfaces exploiting a film geometry.

In this work we have presented an extension of the FLAPW method to truly one-dimensional systems. The space is partitioned into three regions, the muffin-tin sphere around the atom, a vacuum region surrounding a cylinder and the interstitial region between the atoms and the vacuum region. In each region optimal basis functions for the wavefunctions, charge density and potential are used. The spin-orbit interaction is included to investigate the orbital moments and the magnetic anisotropy. Despite the plane-wave representation in the interstitial region we were able to include a wide class of chiral symmetries, characteristic for one-dimensional systems. The one-dimensional FLAPW method was implemented as extension of the FLAPW code FLEUR and parallelized for supercomputing applications. Due to the efficiently adjusted basis functions and partitioning of space, 1D code allows to achieve a significant speed-up, for instance, approximately by a factor of 150 for monowires, as compared to the super-cell approach in the bulk code.

The accuracy, precision and correctness of the code was validated on a set of 1D structures, already calculated previously with other methods. We focused on the systems of a large current interest in the field of nanophysics. We reported on the calculations of 3*d*- and 4*d*- monowires (Ti; Y, Zr, Nb, Mo, Tc, Ru, Rh and Pd). For these monowires we investigated the ferro- and antiferromagnetic instability, calculated equilibrium interatomic distances, magnetic and orbital moments, magnetocrystalline anisotropy energies. We found that across the 4*d*-transition-metal series, Y and Nb exhibit a nonmagnetic ground-state, Mo and Tc are antiferromagnetic and Zr, Ru, Rh and Pd are ferromagnetic

at equilibrium lattice constants. For the Ru, Rh and Pd monowire, we investigated the easy axis of the magnetization. We found that the easy axis is perpendicular to the wire for Ru and Pd but along-the-wire for Rh.

Further we considered a (6,0) nanowire of gold atoms, and a hybrid structure of an iron monowire inside a gold (6,0) tube, showing that the Fe monowire is prone to the Peierls dimerization. For the hybrid system Fe@Au(6,0) we found a high spin-polarization at the Fermi level, proposing, therefore, this system as a possible candidate for spin-dependent transport applications.

Using a super-cell approach within the one-dimensional FLAPW method we investigated a set of one-dimensional multiple-decker sandwiches of benzene and vanadium, which are for the past 20 years of great interest in the field of organometallics. The calculated structural results obtained are in good agreement with experimental and theoretical results. After the calculation of total energies, magnetic moments, orbital interaction schemes, one can finally conclude, that with the increasing number of the vanadium atoms in the molecule, the magnetic moments of vanadium prefer to order ferromagnetically, which was recently observed experimentally.

In conclusion we developed a versatile electronic structure method for truly one-dimensional systems which can deal with magnetic properties and all elements of the periodic table.

Bibliography

- [1] O.K. Andersen. Linear methods in band theory. *Phys. Rev. B*, 12:3060, 1975.
- [2] M.P. Andrews, H.X. Huber, S.M. Mattar, D.F. McIntosh, and G.A. Ozin. (benzene)vanadium, $(\text{C}_6\text{H}_6)\text{V}$: A half-sandwich with an η^6 -benzene ligand. *J. Am. Chem. Soc.*, 105:6170, 1983.
- [3] V.I. Anisimov, V.P. Andropov, A.I. Liechtenstein, V.A. Gubanov, and A.V. Postnikov. Electronic structure and magnetic properties of 3d impurities in ferromagnetic metals. *Phys. Rev. B*, 37:5598, 1988.
- [4] N. Atodiresei. private communications. 2005.
- [5] M.S.S. Brooks. *Physica B*, 130:6, 1985.
- [6] J.W. Buchanan, J.E. Reddic, G.A. Grieves, and M.A. Duncan. Metal and multi-metal complexes with polyaromatic hydrocarbons: Formation and photodissociation of $\text{Fe}_x\text{-(Coronene)}_y$ cations. *J. Phys. Chem. A*, 102:6390, 1998.
- [7] K. Burke. *Electronic density functional theory: Recent progress and new directions*. Plenum Press, New York, 1997.
- [8] K.A. Caldwell, D.E. Giblin, C.S. Hsu, D. Cox, and M.L. Gross. Endohedral complexes of fullerene radical cations. *J. Am. Chem. Soc.*, 113:8519, 1991.
- [9] D.M. Ceperley and B.J. Alder. Ground state of the electron gas by a stochastic method. *Phys. Rev. Lett.*, 45:566, 1980.
- [10] R. Clérac, H. Miyasaka, M. Yamashita, and C. Coulon. Evidence for single-chain magnet behavior in a $\text{Mn}^{\text{III}} - \text{Ni}^{\text{II}}$ chain designed with high spin magnetic units: A route to high temperature metastable magnets. *J. Am. Chem. Soc.*, 124:12837, 2002.
- [11] A.J. Cox, J.G. Louderback, S.E. Apsel, and L.A. Bloomfield. Magnetism in 4d-transition metal clusters. *Phys. Rev. B*, 49:12295, 1994.
- [12] A.J. Cox, J.G. Louderback, and L.A. Bloomfield. Experimental observation of magnetism in rhodium clusters. *Phys. Rev. Lett.*, 71:923, 1993.

- [13] Jr. C.W. Bauschlicher, H. Partridge, and S.R. Langhoff. Theoretical study of transition-metal ions bound to benzene. *J. Phys. Chem.*, 96:3273, 1992.
- [14] A. Delin and E. Tosatti. Magnetic phenomena in 5d transition metal nanowires. *Phys. Rev. B*, 68:144434, 2003.
- [15] A. Delin and E. Tosatti. The electronic structure of 4d transition-metal monoatomic wires. *J. Phys.:Condens. Matter*, 16:8061, 2004.
- [16] A. Delin, E. Tosatti, and R. Weht. Magnetism in atomic-sized palladium contacts and nanowires. *Phys. Rev. Lett.*, 92:057201–1, 2004.
- [17] M.S. Dresselhaus, G. Dresselhaus, and P. Avouris. *Carbon Nanotubes*. Springer, 2001.
- [18] C. Ederer, M. Komelj, and M. Fähnle. Magnetism in systems with various dimensionalities: A comparison between fe and co. *Phys. Rev. B*, 68:052402, 2003.
- [19] P.J. Fagan, J.C. Calabrese, and B. Malone. *Science*, 252:1160, 1991.
- [20] S. Frank, P. Poncharal, Z.L. Wang, and W.A. de Heer. Carbon nanotube quantum resistors. *Science*, 280:1744, 1998.
- [21] B.S. Freiser. Evidence for an externally bound iron+-buckminsterfullerene complex, FeC_{60}^+ , in the gas phase. *J. Am. Chem. Soc.*, 113:6298, 1991.
- [22] B.S. Freiser. *Organometallic Ion Chemistry*. Kluwer Academic Publishers, Dordrecht, Netherlands, 1995.
- [23] P. Gambardella, A. Dallmeyer, K. Maiti, M.C. Malagoli, W. Eberhardt, K. Kern, and C. Carbone. Ferromagnetism in one-dimensional monatomic metal chains. *Nature (London)*, 416:301, 2002.
- [24] D. Gatteschi, A. Caneschi, L. Pardi, and R. Sessoli. *Science*, 265:1054, 1994.
- [25] R.J. Glauber. *J. Math. Phys.*, 4:294, 1963.
- [26] D. Golberg, F.-F. Xu, and Y. Bando. *Appl. Phys. A*, 76:479, 2003.
- [27] J. Goldberger, R. He, Y. Zhang, S. Lee, H. Yan, H.-J. Choi, and P. Yang. *Nature (London)*, 422:599, 2003.
- [28] C. Guerret-Picourt, Y. Le Bouar, A. Lolseau, and H. Pascard. *Nature (London)*, 372:761, 1994.
- [29] O. Gülseren, F. Erkolessi, and E. Tosatti. Noncrystalline structures of ultrathin unsupported nanowires. *Phys. Rev. Lett.*, 80:3775, 1998.

- [30] B.C. Guo, K.P. Kerns, and Jr. A.W. Castleman. Structure and magnetism of neutral and anionic palladium clusters. *Science*, 255:1411, 1992.
- [31] R.C. Haddon. Conducting films of C₆₀ and C₇₀ by alkali-metal doping. *Nature (London)*, 350:320, 1991.
- [32] D.R. Hamann. Semiconductor charge densities with hard-core and soft-core pseudopotentials. *Phys. Rev. Lett.*, 212:662, 1979.
- [33] S. Heinze, M. Radosavljević, J. Tersoff, and Ph. Avouris. Unexpected scaling of the performance of carbon nanotube schottky-barrier transistors. *Phys. Rev. B*, 68:235418, 2003.
- [34] E. Hernández, C. Goze, P. Bernier, and A. Rubio. *PRL*, 80:4502, 1998.
- [35] P. Hohenberg and W. Kohn. Inhomogeneous electron gas. *Phys. Rev.*, 136:B864, 1964.
- [36] B.H. Hong, S.C. Bae, C.-W. Lee, S. Jeong, and K.S. Kim. Ultrathin single-crystalline silver nanowire arrays formed in an ambient solution phase. *Science*, 294:348, 2001.
- [37] K. Hoshino, T. Kurikawa, H. Takeda, A. Nakajima, and K. Kaya. Structures and ionization energies of sandwich clusters (V_n(benzene)_m). *J. Phys. Chem.*, 99:3053, 1995.
- [38] S. Iijima. Helical microtubules of graphitic carbon. *Nature (London)*, 354:56, 1991.
- [39] J.D. Jackson. *Classical Electrodynamics*. Benjamin, New York, 1967.
- [40] D.B. Jacobson and B.S. Freiser. Reactions of methyliron(1+) and methylcobalt(1+) ions with cyclic hydrocarbons in the gas phase. *J. Am. Chem. Soc.*, 106:3900, 1984.
- [41] A.K. Kandalam, B.K. Rao, P. Jena, and R. Pandey. Geometry and electronic structure of V_n(Bz)_m complexes. *J. Chem. Phys.*, 120:10414, 2004.
- [42] T. Kasuga, M. Hiramatsu, A. Hoson, T. Sekino, and K. Niihara. *Adv. Mat.*, 11:1307, 1999.
- [43] M. Knichelbein. private communications. 2005.
- [44] D.D. Koelling. *Phys. Rev. B*, 2:290, 1972.
- [45] D.D. Koelling and G.O. Arberman. *JPF*, 5:2041, 1975.
- [46] D.D. Koelling and B.N. Harmon. A technique for relativistic spin-polarized calculations. *J. Phys. C*, 10:3107, 1977.

- [47] W. Kohn and L.J. Sham. Self-consistent equations including exchange and correlation effects. *Phys. Rev.*, 140:A1133, 1965.
- [48] M. Komelj, C. Ederer, J.M. Davenport, and M. Fähnle. From the bulk to monatomic wires: An *ab initio* study of magnetism in co systems with various dimensionality. *Phys. Rev. B*, 66:140407, 2002.
- [49] K. Kondo and K. Takayanagi. Synthesis and characterization of helical multi-shell gold nanowires. *Science*, 289:606, 2000.
- [50] H. Krakauer, M. Posternak, and A.J. Freeman. Linearized augmented plane-wave method for the electronic band structure of thin films. *Phys. Rev. B*, 19:1706, 1979.
- [51] E.E. Krasovskii and W. Schattke. The extended-lapw-based $\mathbf{k}\cdot\mathbf{p}$ method for complex band structure calculations. *Solid State Comm.*, 93:775, 1995.
- [52] H.W. Kroto, J.R. Heath, S.C. O'Brian, , R.F. Curl, and R.E. Smalley. C₆₀: Buckminsterfullerene. *Nature (London)*, 318:162, 1995.
- [53] L. Krusin-Elbaum, D.M. Newns, H. Zeng, V. Derycke, J.Z. Sun, and R. Sandstrom. Room-temperature ferromagnetic nanotubes controlled by electron or hole doping. *Nature (London)*, 431:672, 2004.
- [54] T. Kurikawa, M. Hirano, H. Takeda, K. Yagi, K. Hoshino, A. Nakajima, and K. Kaya. Structures and ionization energies of cobalt-benzene clusters (Co_n(benzene)_m). *J. Phys. Chem.*, 99:16248, 1995.
- [55] T. Kurikawa, H. Takeda, A. Nakajima, and K. Kaya. Structures and stabilities of 3d-transition metal-benzene organometallic clusters. *Z. Phys. D*, 40:65, 1997.
- [56] Ph. Kurz. Non-collinear magnetism at surfaces and in ultrathin films. *Ph.D. Thesis, RWTH-Aachen*, 2000.
- [57] M.Y. Lavrentiev, H. Köppel, and M.C. Böhm. Theoretical study of the multimode peierls distortion in the polydecker sandwich compound [Ni(H₅C₃B₂)]_∞. *Chem. Phys.*, 169:85, 1993.
- [58] F. Leonard and J. Tersoff. Novel length scales in nanotube devices. *Phys. Rev. Lett.*, 83:5174, 1999.
- [59] E. Lieb and D.C. Mattis. Theory of ferromagnetism and the ordering of electronic energy levels. *Phys.Rev.*, 125:164, 1962.
- [60] T. Loucks. *Augmented Plane Wave Method*. Benjamin, New York, 1967.
- [61] I. Manners. *Adv. Organomet. Chem.*, 37:131, 1995.

- [62] L. De Maria and M. Springborg. Electronic structure and dimerization of a single monatomic gold wire. *Chem. Phys. Lett.*, 323:293, 2000.
- [63] R. Martel, T. Schmidt, H.R. Shea, T. Hertel, and Ph. Avouris. Single- and multi-wall carbon nanotube field-effect transistors. *Appl. Phys. Lett.*, 73:2447, 1998.
- [64] S.M. Mattar and W. Hamilton. Ground-state geometry of the (η^6 -benzene)vanadium and (η^6 -benzene)vanadium(1+) half-sandwich complexes by local-spin-density linear combination of atomic orbitals techniques. *J. Phys. Chem.*, 93:2997, 1989.
- [65] H. Mehrez, J. Taylor, H. Guo, J. Wang, and C. Roland. Carbon nanotube based magnetic tunnel junctions. *Phys. Rev. B*, 84:2682, 2000.
- [66] N.D. Mermin and H. Wagner. Absence of ferromagnetism or antiferromagnetism in one- or two-dimensional isotropic Heisenberg model. *Phys. Rev. Lett.*, 17:1133, 1966.
- [67] F. Meyer, F.A. Khan, and P.B. Armentrout. Thermochemistry of transition metal benzene complexes: Binding energies of $M(C_6H_6)_x^+$ ($x = 1, 2$) for $M = Ti$ to Cu . *J. Am. Chem. Soc.*, 117:9740, 1995.
- [68] J.S. Miller and A.J. Epstein. Organic and organometallic molecular magnetic materials—designer magnets. *Angew. Chem. Int. Ed. Engl.*, 33:385, 1994.
- [69] K. Miyajima, A. Nakajima, S. Yabushita, M.B. Knickelbein, and K. Kaya. Ferromagnetism in one-dimensional vanadium-benzene sandwich clusters. *J. Am. Chem. Soc.*, 126:13202, 2004.
- [70] M. Monthieux. Filling single-wall carbon nanotubes. *Carbon*, 40:1809, 2002.
- [71] A.M. Morales and C.M. Lieber. A laser ablation method for the synthesis of crystalline semiconductor nanowires. *Science*, 279:208, 1998.
- [72] V.L. Moruzzi, J.F. Janak, and A.R. Williams. *Calculated Electronic Properties of Metals*. Pergamon, New York, 1978.
- [73] M. Moseler, H. Hakkinen, R.N. Barnett, and U. Landman. Structure and magnetism of neutral and anionic palladium clusters. *Phys. Rev. Lett.*, 86:2545, 2001.
- [74] E.L. Muetterties, J.R. Bleeke, E.J. Wucherer, and T.A. Albright. Structural, stereochemical, and electronic features of arene-metal complexes. *Chem. Rev.*, 82:499, 1982.
- [75] S. Nagao, T. Kurikawa, K. Miyajima, A. Nakajima, and K. Kaya. Formation and structures of transition metal- C_{60} clusters. *J. Phys. Chem. A*, 102:6390, 1998.
- [76] T. Nautiyal, T.H. Rho, and Kwnag S. Kim. Nanowires for spintronics: A study of transition-metal elements of groups 8-10. *Phys. Rev. B*, 69:193404, 2004.

- [77] E.W. Neuse and H. Rosenberg. *Metallocene Polymers*. Marcel Decker, New York, 1970.
- [78] H. Ohnishi, Y. Kondo, and K. Takayanagi. Quantized conductance through individual rows of suspended gold atoms. *Nature (London)*, 395:780, 1998.
- [79] M. Okamoto, T. Uda, and K. Takayanagi. Quantum conductance of helical nanowires. *Phys. Rev. B*, 64:033030, 2001.
- [80] T. Ono, Y. Ooka, H. Miyajima, and Y. Otani. $2e^2/h$ to e^2/h switching of quantum conductance associated with a change in nanoscale ferromagnetic domain structure. *Appl. Phys. Lett.*, 75:1622, 1999.
- [81] Y. Oshima, H. Koizumi, K. Mouri, H. Hirayama, K. Takayanagi, and Y. Kondo. Evidence of a single-wall platinum nanotube. *Phys. Rev. B*, 65:121401(R), 2002.
- [82] Y. Oshima, A. Onga, and K. Takayanagi. Helical gold nanotube synthesized at 150 K. *Phys. Rev. Lett.*, 91:205503-1, 2003.
- [83] R. Pandey, B.K. Rao, P. Jena, and M.A. Blanco. Electronic structure and properties of transition metal–benzene complexes. *J. Am. Chem. Soc.*, 123:3799, 2001.
- [84] R. Pandey, B.K. Rao, P. Jena, and J.M. Newsam. Unique magnetic signature of transition metal atoms supported on benzene. *Chem. Phys. Lett.*, 321:142, 2000.
- [85] J.P. Perdew, K. Burke, and M. Ernzerhof. Generalized gradient approximation made simple. *Phys. Rev. Lett.*, 77:3865, 1996.
- [86] J.P. Perdew, K. Burke, and Y. Wang. Generalized gradient approximation for the exchange–correlation hole of a many-electron system. *Phys. Rev. B*, 54:16533, 1996.
- [87] J.P. Perdew and S. Kurth. *Density functionals: theory and applications*. Springer-Verlag, Berlin, 1998.
- [88] J.P. Perdew and A. Zunger. Self-interaction correction to density-functional approximations for many-electron systems. *Phys. Rev. B*, 23:5048, 1981.
- [89] D.G. Pettifor. *Bonding and Structure of Molecules and Solids*. Clarendon Press, Oxford, 1995.
- [90] V. Rodrigues, J. Bettini, P.C. Silva, and D. Ugarte. Evidence for spontaneous spin–polarized transport in magnetic nanowires. *Phys. Rev. Lett.*, 91:096801, 2003.
- [91] V. Rodrigues, T. Fuhrer, and D. Ugarte. Signature of atomic structure in the quantum conductance of gold nanowires. *Phys. Rev. B*, 65:4124, 2000.
- [92] E.M. Rose. *Relativistic Electron Theory*. Wiley, New York, 1961.

- [93] B. Sampedro, P. Crespo, A. Hernando, R. Litrán, J.C. Sánchez López, C. López Cartes, A. Fernandez, J. Ramirez, J. González Calbet, and M. Vallet. Ferromagnetism in fcc twinned 2.4 nm size Pd nanoparticles. *Phys. Rev. Lett.*, 91:237203, 2003.
- [94] L.M. Sandratskii. Noncollinear magnetism in itinerant-electron systems: theory and applications. *Adv. Phys.*, 47:91, 1998.
- [95] S.Blügel. Two-dimensional ferromagnetism of 3d, 4d, and 5d transition metal monolayers on noble metal (001) substrates. *Phys. Rev. Lett.*, 68:851, 1992.
- [96] K. Schmidt and M. Springborg. One-dimensional chains of metal atoms. *Solid State Comm.*, 104:413, 1997.
- [97] H. Schumann, J.A. Meese-Marktscheffel, and L. Esser. Synthesis, structure, and reactivity of organometallic π -complexes of the rare earths in the oxidation state Ln^{3+} with aromatic ligands. *Chem. Rev.*, 95:865, 1995.
- [98] David J. Singh. *Planewaves, pseudopotentials and the LAPW method*. Kluwer, 1994.
- [99] E. Sjöstedt, L. Nordström, and D.J. Singh. An alternative way of linearizing the augmented plane-wave method. *Solid State Comm.*, 114:15, 2000.
- [100] J.C. Slater. Wave functions in a periodic potential. *Phys. Rev.*, 51:846, 1937.
- [101] R.H.M. Smit, C. Untied, A.I. Yanson, and J.M. van Ruitenbeek. Common origin for surface reconstruction and the formation of chains of metal atoms. *Phys. Rev. Lett.*, 87:266102, 2001.
- [102] N. V. Smith, C. T. Chen, and M. Weinert. Distance of the image plane from metal surfaces. *Phys. Rev. B*, 40:7565, 1989.
- [103] I.V. Solovyev, A.I. Liechtenstein, and K. Terakura. Is Hund's second rule responsible for the orbital magnetism in solids? *Phys. Rev. Lett.*, 80:5758, 1998.
- [104] D. Spišák and J. Hafner. Fe nanowires on vicinal Cu surfaces: *Ab initio* study. *Phys. Rev. B*, 65:235405, 2002.
- [105] D. Spišák and J. Hafner. Magnetism of monoatomic wires on vicinal surfaces. *Comput. Mat. Science*, 27:138–150, 2003.
- [106] D. Spišák and J. Hafner. Magnetism of ultrathin wires suspended in free space and adsorbed on vicinal surfaces. *Phys. Rev. B*, 67:214416, 2003.
- [107] M. Springborg. Method for calculating the electronic structures of large molecules; helical polymers. *J. Chem. Phys.*, 87:7125, 1987.

- [108] M. Städele, J.A. Majewski, P. Vogl, and A. Görling. Exact Kohn-Sham exchange potential in semiconductors. *Phys. Rev. Lett.*, 79:2089, 1997.
- [109] J. Stoer. *Numerische Mathematik 1*. Springer-Verlag, Berlin, 1994.
- [110] S.J. Tans, A.R.M. Verschueren, and C. Dekker. Carbon nanotube intramolecular junctions. *Nature (London)*, 393:49, 1998.
- [111] W.M. Temmerman, A. Svane, Z. Szotek, and H. Winter. *Electronic density functional theory: Recent progress and new directions*. Plenum Press, New York, 1998.
- [112] R.E. Thorne. Charge-density-wave conductors. *Physics Today*, 5:42, 1996.
- [113] E. Tosatti, S. Prestepino, S. Kostlmeier, A. Dal Corso, and F.D. Di Tolla. String tension and stability of magic tip-suspended nanowires. *Science*, 291:288, 2001.
- [114] E. Tosatti and S. Prestipino. String tension and stability of magic tip-suspended nanowires. *Science*, 289:561, 2000.
- [115] K. Tsukagoshi, B.W. Alphenaar, and H. Ago. Coherent transport of electron spin in a ferromagnetically contacted carbon nanotube. *Nature (London)*, 401:1744, 1999.
- [116] S. Uryu. Electronic states and quantum transport in double-wall carbon nanotubes. *Phys. Rev. B*, 69:075402, 2004.
- [117] U. von Barth and L. Hedin. A local exchange-correlation potential for the spin polarized case: I. *J. Phys. C*, 5:1629, 1972.
- [118] S.H. Vosko, L. Wilk, and M. Nussair. Accurate spin-dependent electron liquid correlation energies for local spin density calculations: a critical analysis. *Can. J. Phys.*, 58:1200, 1980.
- [119] M.B. Walker and T.W. Ruijgrak. Absence of magnetic ordering in one and two dimensions in a many-band model for interacting electrons in a metal. *Phys. Rev.*, 171:513, 1968.
- [120] M. Weinert. Solution of Poisson's equation: Beyond Ewald-type methods. *J. Math. Phys.*, 22:2453, 1981.
- [121] M. Weinert and A.J. Freeman. Magnetism in linear chains. *J. Magn. Magn. Mater.*, 38:23, 1983.
- [122] M. Weinert, E. Wimmer, and A.J. Freeman. Total-energy all-electron density functional method for bulk solids and surfaces. *Phys. Rev. B*, 26:4571, 1982.
- [123] P. Weis, P.R. Kemper, and M.T. Bowers. Structures and energetics of $V_n(C_6H_6)_m^+$ clusters: Evidence for a quintuple-decker sandwich. *J. Phys. Chem. A*, 101:8207, 1997.

- [124] J.A. White and D.M. Bird. Implementation of gradient-corrected exchange-correlation potentials in Car-Parrinello total-energy calculations. *Phys. Rev. B*, 50:4954, 1994.
- [125] E. Wimmer, H. Krakauer, M. Weinert, and A.J. Freeman. Full-potential self-consistent linearized-augmented-plane-wave method for calculating the electronic structure of molecules and surfaces: O₂ molecule. *Phys. Rev. B*, 24:864, 1981.
- [126] Chih-Kai Yang, Jijun Zhao, and Jian Ping Lu. Magnetism of transition-metal/carbon-nanotube hybrid structures. *Phys. Rev. Lett.*, 90:257203–1, 2003.
- [127] A. I. Yanson, G. Rubio Bollinger, H.E. van den Brom, N. Agrait, and J.M. van Ruitenbeek. Formation and manipulation of a metallic wire of single gold atoms. *Nature (London)*, 395:783, 1998.
- [128] T. Yasuike and S. Yabushita. Ionization energies and bonding scheme of multiple-decker sandwich clusters: M_n(C₆H₆)_{n+1}. *Z. Phys. D*, 40:65, 1997.
- [129] N. Zabala, M.J. Pushka, and R.M. Nieminen. Spontaneous magnetization of simple metal nanowires. *Phys. Rev. Lett.*, 80:3336, 1998.
- [130] Y. Zhang and W. Yang. Comment on "generalized gradient approximation made simple". *Phys. Rev. Lett.*, 80:890, 1998.

Acknowledgments

First of all I would like to thank Prof. Dr. Stefan Blügel for great support and numerous examples of scientific foreseeing and inspiration he has given to me. His constant care was amazing. He has gone through all scientific falls and successes together with me. I am really grateful for that.

A lot of thanks to Dr. Gustav Bihlmayer, who has carefully guided me in our exciting adventures through the code, bugs, algorithms, Buenos Aires and physics.

Special thanks to JP Dr. Stefan Heinze for his constant interest in my work and fruitful ideas, some of which we are still to realize together.

I am very grateful to these people, which managed to create a home atmosphere in the institute, and not only, carrying a great charge of merry mood around me: Jutta Gollnick, Ute Winkler, Marisol Ripoll, Gerrit Vliegthart, Daniele Finarelli, Stefan Cramm, Thorsten Auth, Stephanie Baud. They are responsible for: badminton, Irish Pub parties, football matches, kebab Wednesdays, Aachen weekends, Jülich pizzas and many other things.

My colleagues, Daniel Wortmann, Markus Heide, Vasilie Caciuc, Nikolae Atodiresei, Samir Lounis, Jussi Enkovaara helped a lot by sharing with me their knowledge, advices, ideas, jokes, beers, apples, chewing gums - thanks a lot!

An amazing person and a brilliant scientist, Dr. Eugene Krasovskii, is, basically, guilty for my appearance in Jülich – I am grateful. Another giant, Dr. Phivos Mavropoulos has given me an enormous amount of help in almost everything. Thank you, Phivos.

All the listed people are more (Phivos) or less responsible for my safe daily transportation from Aachen to Jülich for two years - danke sehr.

Of course many hugs to my dear fellows and office-mates Marjana Lezaic and Manni Niesert, who have spent at least two years with me in the same office. Their help, support and understanding is very hard to overestimate. We had a lot of fun together, didn't we?

To my parents – which are α and Ω of everything for me – I dedicate this work.

Curriculum Vitae

Personal data

Name: Yuriy Mokrousov
Date of birth: Apr. 7, 1978
Place of birth: Kiev, Ukraine
Nationality: Ukrainian
Address: Institute of Applied Physics and Microstructure Research Center,
University of Hamburg, Jungiusstrasse 9a, 20355 Hamburg, Germany
E-mail: ymokrous@physnet.uni-hamburg.de

Education

1985–1995 Elementary and high school, Kiev, Ukraine
1995–1999 Studies of physics, National Technical University of Ukraine, Kiev, Ukraine
Diploma thesis: "On the denseness of certain subspaces of a closed linear operator in a Banach space"
1999–2001 Postgraduate studies in applied physics,
National Technical University of Ukraine, Kiev, Ukraine
Master thesis: "Density of the subspaces of analytical vectors and solvability of the abstract Cauchy problem for a linear operator in a Banach space"
since 2002 Ph.D studies in solid state physics, IFF, Forschungszentrum Jülich

Employment

2002–2003 Ph.D. student, Universität Osnabrück
2003–2005 Ph.D. student, Forschungszentrum Jülich